Combination of cohesive elements and remeshing to handle arbitrary crack path propagation : from brittle materials to thermal fatigue analysis of solar system small bodies

Diego Alejandro Uribe Suarez

UNIVERSITÉ CÔTE D'AZUR

ÉCOLE DOCTORALE
SCIENCES FONDAMENTALES ET APPLIQUÉES

Combinaison d'Éléments Cohésifs et Remaillage pour Gérer la Propagation Arbitraire du Chemin de Fissure: des Matériaux Fragiles à l'Analyse de Fatigue Thermique des Petits Corps du Système Solaire

Diego Alejandro URIBE-SUÁREZ

CEMEF, MINES ParisTech - Laboratoire J.-L. Lagrange

Présentée en vue de l'obtention du grade de Docteur en Mécanique Numérique et Matériaux **d'**Université Côte d'Azur

Dirigée par : Pierre-Olivier BOUCHARD
Co-dirigée par : Marco DELBO et Daniel PINO-MUÑOZ

soutenue le : 09 Juillet 2021

Devant le jury, présidé par :
Anna PANDOLFI, Professeur, Politecnico di Milano - Examinatrice
composé de :
Yann MONERIE, Professeur, Université Montpellier - Rapporteur
Justin WILKERSON, Assistant Professor, Texas A&M University - Rapporteur
Pierre-Olivier BOUCHARD, Professeur, CEMEF - Mines ParisTech - Directeur de thèse
Marco DELBO, Directeur de Recherche, Observatoire de la Côte d'Azur - Co-directeur de thèse
Daniel PINO-MUÑOZ, Chargé de Recherche, CEMEF - Mines ParisTech - Co-directeur de thèse

Cemef CENTRE DE MISE EN FORME DES MATERIAUX
MINES ParisTech
Observatoire de la CÔTE d'AZUR
LAGRANGE

Université Côte d'Azur
École Doctorale de Sciences Fondamentales et Appliquées

Thèse de doctorat

pour obtenir le titre de
Docteur en Mécanique Numérique et Matériaux
de l'Université Côte d'Azur

Discipline : Sciences pour l'ingénieur

présentée et soutenue par
Diego Alejandro URIBE-SUÁREZ
CEMEF, MINES ParisTech - Laboratoire J.-L. Lagrange

Combinaison d'éléments cohésifs et remaillage pour gérer la propagation arbitraire du chemin de fissure: des matériaux fragiles à l'analyse de fatigue thermique des petits corps du système solaire

---

Thèse dirigée par
Pierre-Olivier BOUCHARD
Thèse co-dirigée par
Marco DELBO et **Daniel PINO-MUÑOZ**

date de soutenance prévue le 09 Juillet 2021

devant le jury composé de

Yann MONERIE	Professeur	Université Montpellier	Rapporteur
Justin WILKERSON	Assistant Professor	Texas A&M University	Rapporteur
Anna PANDOLFI	Professeur	Politecnico di Milano	Examinatrice
Pierre-Olivier BOUCHARD	Professeur	CEMEF - Mines ParisTech	Directeur de thèse
Marco DELBO	Directeur de Recherche	Observatoire de la Côte d'Azur	Co-directeur de thèse
Daniel PINO-MUÑOZ	Chargé de Recherche	CEMEF - Mines ParisTech	Co-directeur de thèse

Résumé

La présente thèse de doctorat a pour objectif d'améliorer la modélisation du phénomène de rupture dans les matériaux fragiles. Elle porte une attention particulière aux mécanismes de rupture des objets célestes. L'un des problèmes posant le plus de défis aux scientifiques spécialisés dans l'étude de la mécanique de la rupture est la propagation d'une fissure dans un maillage éléments finis, et ce pour des chemins arbitraires. Dans cette étude, ce problème est abordé en utilisant une technique de remaillage avancée utilisant des éléments finis cohésifs permettant la propagation de fissures suivant des directions arbitraires et indépendantes du maillage. La direction de la fissure est calculée suivant le critère du taux de restitution d'énergie maximal, implémentée à l'aide d'un modèle éléments finis et de la méthode $G\theta$. Les effets de différents paramètres numériques et physiques relatifs à la fissure ou à l'énergie libérée lors de la rupture sont investigués.

Bien que différentes preuves de fissures et/ou fragments à la surface de corps célestes de notre système solaire induits par des variations cycliques de la température ont été détaillées, la compréhension de ces mécanismes de propagation dans des objets célestes reste très parcellaire. La fracturation thermique de roches en surface associée à l'impact de micro-météorites peut éventuellement conduire à la rupture complète de fragments de matière et à la production de régolithes. Cette dernière est définie comme la couche de matériau non consolidée qui recouvre la surface des planètes. Afin de comprendre ces mécanismes, l'étude s'attarde sur un exemple précis, celui de l'astéroïde (101955) Bennu. Pour ce faire, elle utilise un modèle thermoélastique couplé avec un modèle linéaire élastique de mécanique de la rupture permettant de considérer les variations cycliques de température liées aux alternances jour/nuit. En utilisant cette méthodologie, il a été observé que les fissures se propagent préférentiellement dans les directions : Nord vers Sud, Nord-Est vers Sud-Ouest et Nord-Ouest vers Sud-Est. Finalement, une analyse de fatigue est effectuée afin d'estimer la vitesse de croissance de la fissure.

Les méthodes détaillées précédemment ont été implémentées dans Cimlib, une librairie C++ dévelopée au CEMEF. Au sein de cette librairie, une méthode permettant la propagation d'une ou plusieurs fissures, suivant des directions arbitraires, en 2D et au sein d'un environnement de calcul en parallèle est à présent disponible. Concernant l'extension de cette méthode à des problèmes 3D, une première approche a été mise au point. Elle permet de propager un front de fissure suivant une direction arbitaire. La structure développée permet d'ouvrir de nouvelles possibilités pour de nombreuses applications, telles que l'étude de la rupture de matériaux composites à l'échelle mesoscopique.

Mots clés: Propagation de fissure; Direction de croissance de fissure; Modèle à zone cohésive; Éléments cohésifs indépendants du maillage; Insertion dynamique; Techniques de remaillage; Astéroïde Bennu; Modèle thermoélastique; Croissance de fissure induite par la fatigue thermique.

Abstract

The present PhD thesis aims at providing a better modeling of fracture phenomenon in brittle materials, with special attention focused on fracture processes taking place in astronomical bodies. One of the most challenging issues in computational fracture mechanics is the propagation of a crack through a finite element mesh for arbitrary crack paths. In this work, this problem is approached by means of an advanced remeshing technique that propagates a crack using cohesive elements through arbitrary directions (mesh-independent). The crack direction is computed using the maximal energy release rate criterion which is implemented using finite elements and the $G\theta$ method. The effects of different numerical and physical parameters regarding the crack path and fracture energy have been investigated.

Even though it has been shown that temperature cycles on airless bodies of our Solar System can cause damaging of surface materials (Thermal cracking), propagation mechanisms in the case of space objects are still poorly understood. Thermal cracking of surface rocks, in addition to the impact of micrometeorties, can eventually lead to rocks' breakup and produce fresh regolith, the latter being the layer of unconsolidated material that covers planetary surfaces. For this reason, the present work combines a thermoelasticity model together with linear elastic fracture mechanics theory to predict fracture propagation in the presence of thermal gradients generated by diurnal temperature cycling and under conditions similar to those existing on asteroid (101955) Bennu. Using the implemented methodologies, it is found that in asteroid Bennu, cracks preferentially propagate in the North to South (N-S), in the North-East to South-West (NE-SW) and in the North-West to South-East (NW-SE) directions. Finally, thermal fatigue analysis was performed in order to estimate the crack growth rate.

Aforementioned methodologies have been implemented in Cimlib, a C++ in-house finite element library developed at CEMEF. Inside Cimlib, a methodology allowing two-dimensional crack propagation through arbitrary directions with the option of handling multiple cracks in the domain and inside a parallel environment was developed. Regarding three-dimensional scenario, a first approach where a crack front was propagated through an arbitrary direction was achieved. Concerning numerical modeling of crack propagation, the developed framework opens new possibilities for various applications such as composites cracking at the meso-scale.

Keywords: Crack propagation; Crack growth direction; Cohesive zone models; Mesh-independent cohesive elements; Dynamic insertion; Remeshing techniques; Asteroid Bennu; Thermoelastic model; Thermal fatigue crack growth.

Pa' mi Apá y Pa' mi Amá!!

Acknowledgements

I would like to express my sincere gratitude to my advisors, Prof. Pierre-Olivier Bouchard, Dr. Marco Delbo, and Dr. Daniel Pino-Muñoz. Thank you very much for giving me the opportunity of being your Ph.D. student, as well as for your guidance, encouragement, support, and patience during my years at CEMEF. Thanks to P.-O. for all your teachings on fracture mechanics theory, I will always remember all the fruitful discussions we had about high-level mathematical developments easily-made by great old-school French engineers, as well as your advice on computer implementations. My special thanks to Daniel for all the lectures you gave me about basic and advanced math, materials science, finite element formulation, computer programming, Linux operating system, working on a cluster, using Git, riding a route bike, snorkeling, and so on. I will never forget that you were always there when I needed help, no matter if it was at night or on the weekend. I learned a lot from you not only from the professional point of view, but also about how you see life. Thanks to Marco for all the help and support you gave me during the development of the application part of my thesis. Thanks for the things you have taught me on planetary science *especially* in space bodies. Thank you for being a super host every time I visited you at OCA. Thank you all for caring about me not just as a Ph.D. student, but also as a person. I deeply and sincerely enjoyed this trip of more than 3 years.

I would like to thank Professor Yann Monerie and Assistant Professor Justin Wilkerson for accepting to review this manuscript. I would also like to thank Professor Anna Pandolfi for being on my dissertation committee. It is my great honor to have all of you on my committee. Some years ago, when I started reading different articles on fracture mechanics, I hardly imagined that all of you would be on my doctoral thesis committee.

I would like to especially thank Sélim Kraria for all his support in the IT department right from Linux basic stuff, SSH connections, Cimlib compilation, external libraries compilation, correct use of Git to usage of computing facilities. Thanks for being very patient with me during these 3 years, without your hard daily work to enhance Cimlib, this work would not be possible. A special thanks goes to Florence Morcamp for being so nice to me every day we saw each other at CEMEF. I enjoyed a lot our hikes in the snow during "Le Colloque National Mécamat" at Aussois in 2019. I enjoyed our talks about everything and the few yoga classes we took during the summer. I also want to thank Mrs. Konstanze Beck from the Welcome Center at Université Côte d'Azur for her kind help in all the administrative procedures related to visa issues.

I would like to thank Victor Grand, Baptiste Flipon, and Franco-German Jaime for all the coffees and laughs we shared. I enjoyed a lot our scientific and not-so-scientific conversations. A special thanks to my good friend, Victor, because during the last year he encouraged me during the tough moments, making my days at CEMEF happier. Thanks for the lunches and all the technical help! I will never forget you. Thanks to Baptiste for sharing all his knowledge and experience, as well as for always being willing to help. I would also like to thank my former

office-mates Luc Védie, Inès Salhi, Hassan Ghraieb, and Gilles Tahan; we shared good moments in the office. Special thanks to Aakash Patil, my current office-mate, I hope you have enjoyed as much as me our time together in the office. Sorry for interrupting our research time to talk about everything and nothing: politics, history, general culture, languages, India, Colombia, spicy food, top Universities, and so on.

Thanks to Feng Gao for all the ping-pong games, as well as for our interesting and endless coffee breaks talking about our countries and our cultures. Thanks to Juhi Sharma and Prashanth Thirunavukkarasu for being such good friends and for the good moments we shared inside and outside the lab. Thanks to Joe Khalil and Ramy Nemer for the nice talks about our countries and our cultures. I learned a lot of things from you guys. I also want to thank all my others friends at CEMEF: Brayan Murgas, Fian Assemien, Matheus Brozovic, Ilusca Janeiro and her husband Reynan Vieria, Sebastian Florez, Karen Alvarado, Alexis Nicolaÿ, Julien Fausty, Shitij Arora, Hazem Eldahshan, Mohamed Mahmoud, Ali-Malek Boubaya.

I would like to thank three good Colombian friends that I made in France: Natalia Mantilla, Jairo Andrés Cubillos, and Helkin Giovani Forero Ballesteros. Thank you for being so kind to me, as well as for all the great moments we shared (e.g., French classes, beach days, cycling, soccer games, parties, chill times).

I want to especially thank Lluís Solà Hernández, *"El Catalán, mi parcero"*, the first friend I made in France. Thanks for all the moments we shared inside and outside the lab. Thanks for introduce me to David Hernando Andrés, Alejandro Lopez Delgado and Pablo Elie Amsallem. I will always have good memories from you guys in my mind. Thanks for being like my family in Nice, the weekends with all of you were amazing.

I would like to especially thank Associate Professor Marcelo Marucho from the University of Texas at San Antonio, who 4 years ago allowed me to go abroad to do an internship in his lab. Honestly, this experience changed my life and laid the foundations for my future. I would also like to thank all the friends I made in San Antonio, Texas USA: Lauren Heather, Christian Hunley, John Eder Sanchez, Aldemar Gordillo Galeano, Cesar Augusto Isaza Merino, Yeray Alexai Rodríguez Núñez, Ulises Santiago, Alfredo Benítez-Lara, Alejandra Londoño-Calderón, Sandra Vergara-Perez and Ernesto Alva-Sevilla. I will never forget the amazing moments I shared with each of you.

Thanks to Professor Juan Hernando Cadavid Restrepo (EAFIT University) for introducing me to continuum mechanics. I would also like to thank Professor Oscar Eduardo Ruiz Salguero (EAFIT University) and Assistant Professor Manuel Julio García Ruiz (Angelo State University) for showing me that mechanical engineers can face any kind of problem from a mathematical and numerical point of view.

I would like to thank in a very special way my schoolteachers: the late Gilberto Llano Ruiz, Luis Hernando Carmona Ramírez, and Dario Ríos, educators at the San José de la Salle School in Medellín, Antioquia, Colombia, and who instilled in me a particular taste for mathematics and physics. I would also like to thank Br. Álvaro Llano Ruiz for being an example of a true educator in my life. You know how much I respect, admire, and appreciate you. I always remember you very fondly as well as your brother Gilberto.

Thanks to my sister *Puli* for being at home with my parents and Martin while I am gone. Thanks to my good friend Carlos Eduardo Pineda Vargas for always supporting me in everything without judging me. Comrade, thanks for being with me in the distance whenever I needed you, more trips and lots of *trova* await us.

Last but not least, to my parents Jorge Enrique Uribe Toro and Maria Yolanda Suárez, I dedicate this thesis, I have no words to express how lucky I am to be your son. You have given me and my sister everything you have, and everything you did not have. Thank you for making me the person that I am today.

Gracias, muchas gracias, muchísimas gracias!![†]

[†]If I forgot to thank someone, I hope you can forgive me.

Table of contents

List of Figures

List of Tables

Context

The identification of the most likely mode of failure and the application of a suitable failure criterion are crucial in the design of structures and machine components. Material damage is in general understood in terms of nucleation and propagation of fractures (cracks). In addition, crack growth modeling plays an essential role in the assessment of engineering structures regarding more accurate prediction of structural damage and failure that can prevent catastrophic failures. The fracture mechanics community recognizes the role of inherent structural flaws (also called cracks or fractures) that affect component's performance and life. These inevitable defects result in high stress concentrations that can lead to failure and threaten safety in both engineering structures [Erdogan, 2000, Zerbst et al., 2015] and natural structures, e.g., domes [Collins et al., 2018] and cliffs [Collins and Stock, 2016]. The presence of fracture and their development can be investigated using laboratory experiments, analytical studies and numerical simulations. The first option is usually expensive, but always necessary at least for getting reliable input data and for the purpose of the validation of the analytical, empirical and numerical models. Analytical studies are typically restricted to simple configurations. Therefore, numerical simulations are often an effective strategy to deal with most complex cases [Liao et al., 2018].

Regarding materials science and engineering, fracture mechanics is thus an active and essential research field. Even though it has been studied for more than 100 years, it still has plenty of open questions waiting to be solved. Fracture is a really complex and very material-specific problem. For this reason, the improvement of fracture initiation and growth prediction, in existing as well as in new materials, is highly worthwhile. Fracture process can take place under static or dynamic conditions, as well as under monotonic or cyclic loadings. When occurring under cyclic loading, the fracture process is known as fatigue. When fracture takes place with no visible prior plastic deformation, it is known as brittle fracture. Meanwhile, if the fracture occurs after a considerable plastic deformation, it is named as ductile fracture. The present study is dedicated to fracture process taking place in brittle materials under both monotonic and cyclic loadings. A suited and proven approach for the study of fracture mechanics is the finite element method (FEM). Over the last years, computers computational power has significantly increased, allowing the study of more and more complex problems like damage and fracture prediction for different real scenarios. Such scenarios often require the application of non-linear finite element (FE) codes in order to solve the physical problem immersed there.

The fracture process can be decomposed into two steps: crack initiation and crack propagation. The first one is essential but not easy. If the goal is to describe this process for a body without an initial pre-crack, damage-based numerical models should be used. These models study the evolution of damage in a continuous way and, at a critical damage value, the crack is initiated as a result of a nucleation process [Alessi et al., 2015, Marigo et al., 2016, Tanné et al., 2018, Eldahshan et al., 2021]. In the fracture mechanics field, the simulation of crack initiation is a challenging task and for this reason, this process is often disregarded. Efforts

are often oriented towards the study of the evolution of pre-existing cracks [Bouchard et al., 2003]. In this case, crack propagation introduces a displacement discontinuity. Dealing with this discontinuity in a finite element mesh is fundamental in fracture mechanics. For this reason, many approaches have been developed to handle it. Proposed approaches range from simple procedures like element erosion [Wulf et al., 1996], where elements are removed once their load carrying capacity has been eroded, to more complex methodologies using enriched finite element methods [Belytschko and Black, 1999, Moës et al., 1999, Jirásek, 2000, Oliver et al., 2006, Fries and Belytschko, 2010] and/or remeshing operations [Bittencourt et al., 1996, Carter et al., 2000, Bouchard et al., 2003, Branco et al., 2015].

The fracture phenomena are not restricted only to man-made structures; they also occur in natural ones like mountains and rocks. Around the world, for example, rockfalls phenomena in steep terrains are common and hazardous. For a long time, different mechanisms such as precipitation, seismic activity, and freezing conditions were thought to be the exclusively triggers of these fracture phenomena. Recently, it has been shown that rockfalls also occur during periods when these triggers are absent. The above has left the door open to a new theory, that these rockfalls may occur as a result of outward expansion due to the solar heating of rock surfaces [Collins and Stock, 2016]. [Collins et al., 2018] showed that thermal stresses, which have been largely neglected in the formation of rocks, can play a key role in triggering fracture phenomena such as exfoliation. The understanding of these fracture phenomena is of vital importance, for example, in locations where infrastructure is commonly supported, as well as for studies of landscape erosion and rockfall hazards [Terzaghi, 1962, Collins and Stock, 2016, Collins et al., 2018].

Thanks to improved technology and observations we can carefully observe these structures not only on earth but also on space objects (planetary objects) such as Mars [Eppes et al., 2015, Viles et al., 2010], our Moon [Ruesch et al., 2020, Li et al., 2017], asteroids [Dombard et al., 2010, Lauretta et al., 2019b, Walsh et al., 2019, DellaGiustina et al., 2019, Molaro et al., 2020a], the nuclei of comets [Attree et al., 2018, Matonti et al., 2019, El Maarry et al., 2] and meteorites [Delbo et al., 2014]. In particular, the small bodies were thought to be kind of pristine [Lauretta et al., 2019b, Libourel et al., 2019]. Small bodies such as asteroids and comets can be considered relicts of the early stages of solar system evolution. This is due to the fact that their material composition as well as their structure are relatively primitive compared to those composing the planets. Therefore, they can provide valuable information of the earliest stages of planet formation [Wada et al., 2018].

All planetary bodies covered with a hard surface are prone to damage via a series of process that determine crack initiation and growth, e.g., quakes, tides, impacts, release of internal stresses, exhumation, thermal effects. It is worth mentioning that thermal cracking effects have been largely underestimated. Therefore, it is interesting to study their effect on the surface evolution of planetary bodies. Nevertheless, fatigue cracking is only one aspect of fracturing on planetary bodies. For instance, [Matonti et al., 2019] showed that surface and interior of the comet 67P/Churyumov-Gerasimenko exhibit shear-fracture and fault networks, ranging from tens to hundreds of meters.

It has been shown that temperature cycles on airless bodies of our Solar System can cause damaging of surface materials [Delbo et al., 2014]. This damaging process, known as thermal cracking, consists in the nucleation and growth of micro-fractures inside the material due to the mechanical stresses induced by the diurnal temperature cycles. In the case of airless bodies, the thermal cracking phenomenon was also neglected, and it is still not well understood. Figure 1 shows a schematic representation of this cycling process. While the celestial body (i.e., asteroids, the nuclei of comets, meteorites) is orbiting the sun, it is rotating around its own axis, leading to strong temperature gradients as well as cyclic thermal loading conditions.

As an example, Figure 2 shows tremendous temperature variation in short period of time on asteroid (101955) Bennu, which rotation period is only 4.28 hours. The diurnal temperature

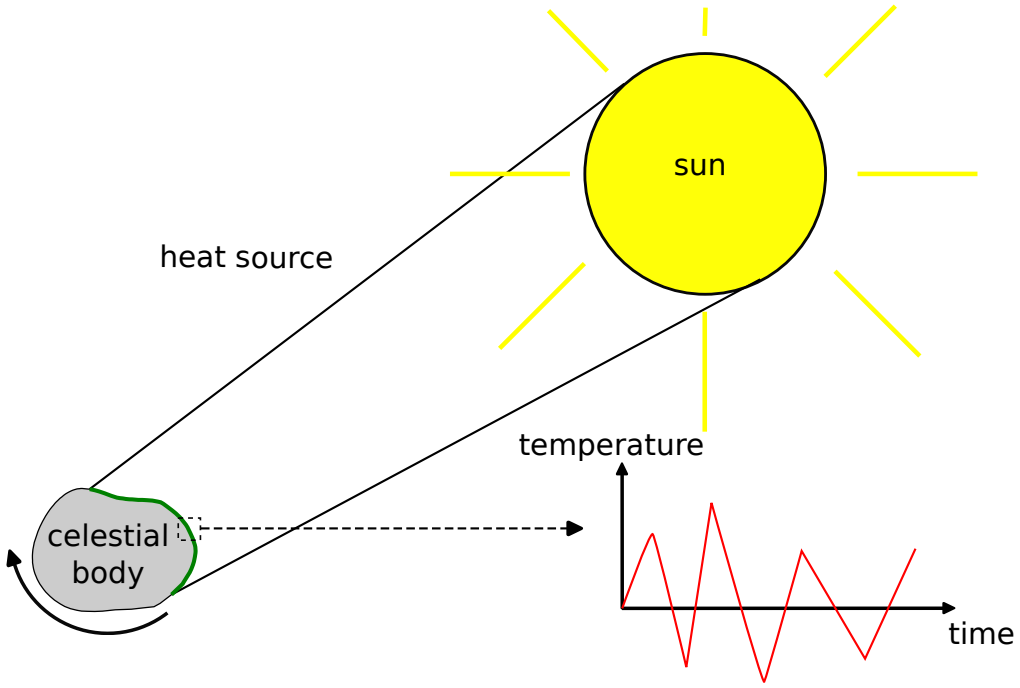

Figure 1: Schematic representation of diurnal temperature cycles

curves are shown for the regions with the lowest and highest thermal inertia on the surface of Bennu. The computation of these temperature curves is well described in [Rozitis et al., 2020].

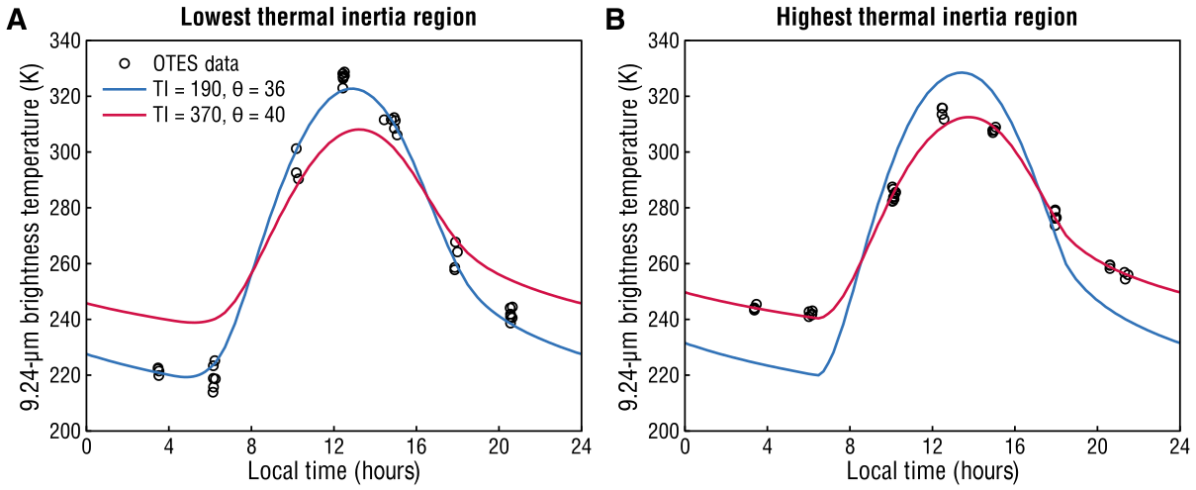

Figure 2: Diurnal temperature curves computed in regions with the lowest and highest thermal inertia on the surface of (101955) Bennu. TI $\rightarrow$ thermal inertia and $\theta \rightarrow$ surface roughness. Figure reproduced from [Rozitis et al., 2020].

In the work of [Ballouz et al., 2020], Bennu's lifetime in near-Earth space since it dynamically and collisionally decoupled from the main asteroid belt (i.e., its age) is estimated to be 1.7 Myr. Following this idea, an interesting question is what would happen to materials like those composing Bennu if they are exposed for very long time to temperature variations like those shown in Figure 2? Will they exhibit any sign of thermal cracking?

Thermal cracking of surface rocks, in addition to the impact of micrometeorites, can eventually lead to rocks' breakup and produce fresh regolith, the latter being the layer of uncon-

solidated material that covers planetary surfaces [Yano et al., 2006, Veverka et al., 2001, Delbo et al., 2014, Murdoch et al., 2015]. Furthermore, several studies propose that also macroscopic fractures, mass-wasting, and material breakdown on asteroids and cometary nuclei could be explained as a consequence of thermal effects [Delbo et al., 2014, Dombard et al., 2010, El Maarry et al., 2, Alí-Lagoa et al., 2015]. For all the reasons above, thermal cracking is now considered an important space weathering mechanism. Figure 3 shows some in situ images of fractures observed on the nucleus of the comet 67P/Churyumov-Gerasimenko. According to [Poulet et al., 2016], these fractures are best explained by thermal insolation leading to thermal fatigue and/or to loss of volatile materials. Images shown in Figure 3 were acquired by the CIVA cameras on-board PHILAE, the landers of ESA's Rosetta mission [Poulet et al., 2016].

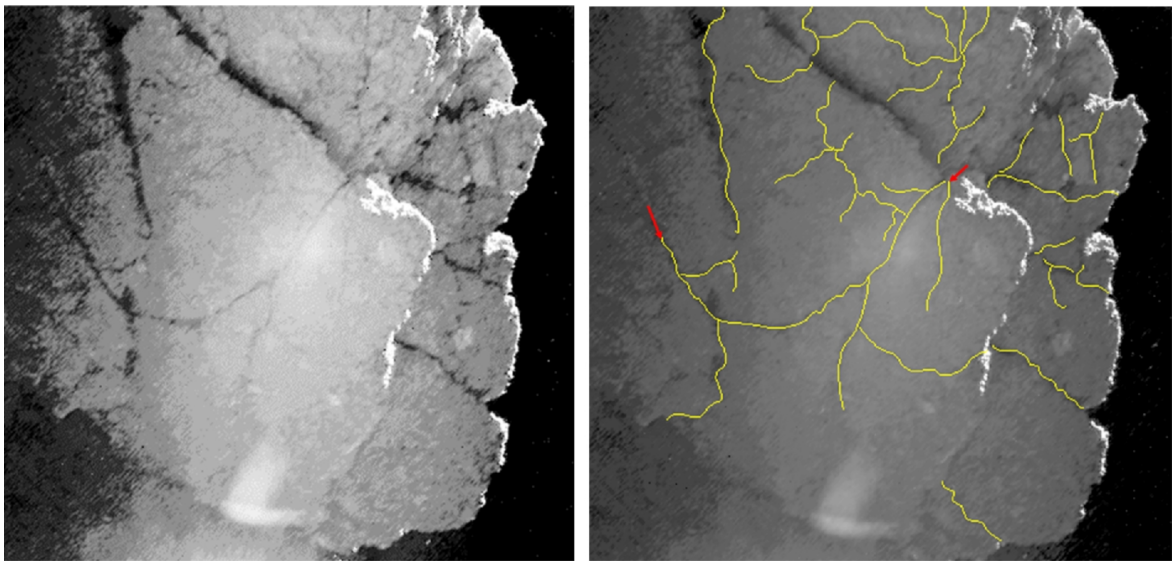

Figure 3: Close-up from CIVA no. 1 showing the fractured block. The left image was stretched to emphasize the fractures. The two red arrows indicate the limits of the fracture having the maximum length (537.6 mm at 1 mm pix^{-1} resolution or 752.6 mm at 1.4 mm pix^{-1} resolution). Figure reproduced from [Poulet et al., 2016].

Regarding astronomical bodies (i.e., comets, asteroids) fracture processes are still poorly understood. This is the context in which this project started. Current work is a collaboration project between CEMEF (Center for Material Forming) - MINES ParisTech and the LAGRANGE laboratory - Observatoire de la Côte d'Azur. This project combines concepts from fracture mechanics theory together with computational mechanics, thermoelasticity, fatigue theory and planetary science. It aims at achieving crack propagation in brittle materials through arbitrary directions combining remeshing operations and dynamic insertion of cohesive elements either in 2D or 3D. This study also tries to provide theoretical foundation for some fracture processes that have been observed in astronomical bodies. Such observed phenomena are thought to be the result of a thermal fatigue induced by the temperature changes driven by the day/night cycles on them. In a particular way, this work tries to analyze and interpret fracture directions on small asteroids with properties similar to those of asteroid (101955) Bennu.

Bennu has recently become the center of important studies because it is the target of the OSIRIS-REx mission [Lauretta et al., 2014, Lauretta et al., 2017]. One of the main objectives of the mission is to return a pristine sample of Bennu to Earth [Lauretta et al., 2019b]. Bennu is also believed to represent objects that may have brought prebiotic molecules and volatiles like water to Earth [Lauretta et al., 2019b]. Bennu is a near-Earth asteroid considered as a rubble-pile and covered in many boulders of varying size [DellaGiustina et al., 2019]. In situ disaggregation and exfoliation of many of these boulders have been shown, pointing out the im-

portant role of thermal fatigue in its landscape evolution. The study of the fatigue phenomenon on Bennu's surface can provide a better understanding of the interaction of the aforementioned landscape evolution with other surface processes such as micrometeoroid impacts [Molaro et al., 2020b]. Another important factor to mention about thermal fatigue is that, its magnitude can be several orders faster than micrometeorite impacts in fragmenting such small rocks on small airless bodies, which further encourages its study [Delbo et al., 2014, El Mir et al., 2019].

With the aim of providing a better understanding of cracking on brittle materials, and particularly on planetary bodies, first, a methodology to tackle one of the most challenging issues in computational fracture mechanics was developed: the propagation of a crack through a finite element mesh for arbitrary crack paths. To overcome this issue, a numerical strategy capable of achieving crack propagation through arbitrary directions (mesh-independent) was implemented inside the in-house finite element (FE) library Cimlib [Digonnet et al., 2007]. This strategy combines advanced remeshing techniques together with dynamic insertion of cohesive elements. The latter ensure that the energy released due to the fracture process is controlled. Next, to understand if and how the surface of dark asteroids (e.g., Bennu) could be cracked by thermal effects driven by the day/night cycles, the developed methodology was combined with a thermoelastic model. To better understand this phenomenon, an attempt was made to numerically reproduce some directions of crack propagation observed in the near-Earth asteroid (101955) Bennu.

- Chapter 1 is devoted to the literature review used as reference for the present work. Basic notions as well as the current state-of-the-art regarding fracture phenomena on solar system small bodies are presented. Some fracture mechanics concepts and the most common crack propagation strategies to deal with the fracture phenomenon using the finite element method are then reviewed.
- Chapter 2 presents in detail the existing finite element formulation as well as all the implementations that were carried out inside Cimlib to achieve crack propagation for arbitrary crack paths in both two- and three-dimensional scenarios (e.g., cohesive zone models, thermoelasticity model, remeshing strategies).
- Crack propagation through a finite element mesh for arbitrary crack paths is a challenging task in computational fracture mechanics. The developed methodology that allows crack propagation using remeshing operations and dynamic insertion of cohesive elements in a mesh-independent way, in both 2D and 3D is presented in Chapter 3.
- Aiming at providing theoretical foundation for the analysis and interpretation of some fracture directions observed on small asteroids, and that are believed to be generated by diurnal temperature cycling, Chapter 4 presents the results obtained when applying the developed and implemented thermo-elastic fracture mechanics model to the case of asteroid (101955) Bennu.
- Finally, some concluding remarks as well as perspectives are presented in Chapter 5.
- Appendix A contains additional details regarding all the implementations performed inside Cimlib.

Publications

Articles in peer-reviewed international journals

As lead author

- **D. Uribe-Suárez**, M. Delbo, P.-O. Bouchard, D. Pino-Muñoz, Diurnal temperature variation as the source of the preferential direction of fractures on asteroids: Theoretical

model for the case of Bennu, *Icarus*, 360 (2021):114347.

- **D. Uribe-Suárez**, P.-O. Bouchard, M. Delbo, D. Pino-Muñoz, Numerical modeling of crack propagation with dynamic insertion of cohesive elements, *Engineering Fracture Mechanics*, 227 (2020):106918.

Participation in international conferences

As presenting author

- **D. Uribe**, D. Pino-Muñoz, M. Delbo, P.-O. Bouchard, Mesh-independent Crack Propagation under Mixed-Mode Loading using Remeshing and Dynamic Insertion of Cohesive Elements, *VI International Conference on Computational Modeling of Fracture and Failure of Materials and Structures (CFRAC 2019)*. Braunschweig (Germany), June 12^{th}-14^{th}, 2019.

Participation in national conferences

As presenting author

- **D. Uribe**, D. Pino-Muñoz, M. Delbo, P.-O. Bouchard, Mesh-independent Crack Propagation under Mixed-Mode Loading using Remeshing and Dynamic Insertion of Cohesive Elements, *Colloque des doctorants en 2éme année de l'EDSFA*. Sophia Antipolis (France), May 20^{th}, 2019.

- **D. Uribe**, P.-O. Bouchard, D. Pino-Muñoz, M. Delbo, Towards a crack propagation criterion and dynamic insertion of cohesive elements applied to thermal fatigue failure of comets/asteroids, *Colloque National Mécamat-Rupture des Matériaux et des Structures*. Aussois (France), January 21^{st}-25^{th}, 2019.

- **D. Uribe**, P.-O. Bouchard, D. Pino-Muñoz, Marco Delbo, Crack Propagation Criteria and Dynamic Insertion of Cohesive Elements Applied to Thermal Fatigue Failure of Comets/Asteroids, *Colloque Quadriennal de Bilan et Prospective Programme national de Planétologie*. Nice (France), September 5^{th}-7^{th}, 2018.

Chapter 1

Introduction

Contents

This introduction chapter is dedicated to the literature review which is used as reference for the present work. This chapter gives a brief overview on the theory required to understand both fracture phenomenon and the different ways it has been approached in the literature. As already stated in the context section, the thermal cracking phenomenon in the case of airless bodies has been neglected for long time and it is still not well understood. The current work aims at understanding if and how, the surface of solar system small bodies, such as dark asteroid (101955) Bennu, could be cracked by thermal effects driven by diurnal temperature variations. For this reason, in section 1.1 some basic notions on space bodies are presented, as well as an overview of the current state-of-the-art regarding fracture phenomena on airless bodies. In order to tackle that problem, section 1.2 describes the basic concepts of fracture mechanics theory, the two common approaches used to deal with fracture analysis are described: local approach based on stress intensity factors (SIF) and global (or energetic) approach based on strain energy release rate. The same section also presents crack growth criteria following both a local and a global approach as well as fatigue crack growth models. Lastly, in this section crack kinking criteria are introduced. Then in section 1.3, the most common crack propagation strategies available in the literature when dealing with propagation of cracks through a finite element mesh are presented. Finally, some remarks regarding the scope and methodology of this work are stated.

1.1 Asteroid fracture phenomena

The initiation of fractures and their growth are key processes in man-made structures and materials. Due to their importance in the everyday life of humans, processes in these structures are the most commonly studied cases in the literature. But these processes also occur in natural objects, such as rocks, boulders, and cliffs [Cao et al., 2019, Al-Mukhtar and Merkel, 2015, Wang et al., 2019, Atkinson, 1982, Vastola, G., 2011, Eppes et al., 2015] and are documented on several objects of our solar system, including Earth [Collins and Stock, 2016, Collins et al., 2018], Mars [Eppes et al., 2015, Viles et al., 2010], our Moon [Ruesch et al., 2020, Li et al., 2017], the nuclei of comets [Attree et al., 2018, Matonti et al., 2019, El Maarry et al., 2], asteroids [Dombard et al., 2010, Lauretta et al., 2019b, Walsh et al., 2019, DellaGiustina et al., 2019, Molaro et al., 2020a], and meteorites [Delbo et al., 2014].

The source of the driving forces that provokes crack nucleation and propagation can be very diverse, ranging from unloading of the pressure stresses under which certain rocks formed in the deep crust of Earth, tectonic stresses, rapid mechanical stresses from impacts, tides and thermal stresses. In the latter case, the presence of water can enhance the cracking phenomena via the known freeze-thaw effect (see e.g. [Hall, 2004] and references therein). The effectiveness of thermal stresses in cracking rocks and other geological units in the absence of water has been long debated: a famous laboratory experiment by [Griggs, 1936] argued against earlier claims that rocks could be fractured by temperature variations only, the process that in general and hereafter is called thermal cracking. However, thermal cracking gained momentum recently and came to great attention to planetary scientists thanks to new measurements, modelling, and observations.

The crack propagation rate is governed, among other variables, by the stress intensity factor (K) (See section 1.2.3.1). K is proportional to the applied stress (σ) and, in thermal problems, σ is proportional to temperature changes (ΔT). On asteroids and atmosphere less space bodies ΔT can be very large of $\sim$100 K [Delbo et al., 2014, Rozitis et al., 2020]. So one could expect thermal cracking to be very important.

More in details, it has been shown that temperature variations resulting from the cycles between day and night can damage materials on airless bodies of our Solar System (for references on this topic, see the introductions of [Molaro et al., 2017, Molaro et al., 2015]). This damaging process consists in the nucleation and growth of micro-fractures inside the material due to

the mechanical stresses induced by the diurnal temperature cycles. In general the mechanical stresses resulting from temperature gradients due to the day and night cycles are smaller than the strength of the material (see e.g. [Delbo et al., 2014, Ravaji et al., 2019, El Mir et al., 2019, Hazeli et al., 2018, Molaro et al., 2017]). In this case the crack can still open and grow in a regime that is said to be sub-critical [Atkinson, 1984]. This phenomenon of sub-critical growth, stable cracking or quasi-static crack propagation occurs when a crack propagates at speeds much lower than the body wave speed even when the stress intensity factor (K) is lower than the fracture toughness (K_c) [Weiss, 2004]. Under this regime, the material is increasingly damaged at each cycle and it is usually spoken of thermal fatigue. Eventually, the application of a large number of cycles can produce important crack growth; the crack tip can reach a boundary of the material, such as a discontinuity or the edge of a rock; this leads to material failure (see e.g. [Dombard et al., 2010, Delbo et al., 2014] for the case of asteroids and meteorites). For example, [Liang et al., 2020] studied volumetric stress distribution in an L6 ordinary chondrite's microstructure subjected to thermal and mechanical loadings through the combination of experiments and micromechanical models. It was found that under thermal cycling, the stress concentrates more uniformly along with particle interfaces. The authors interpret that thermal fatigue crack propagation could result in the debonding of particles from the surrounding matrix.

Hence, on solar system bodies without an atmosphere, thermal fatigue of surface rocks, in addition to the impact of micrometeorites, can eventually lead to rocks' breakup and produce regolith [Dombard et al., 2010, Delbo et al., 2014], the latter being the layer of unconsolidated material that covers planetary surfaces [Yano et al., 2006, Veverka et al., 2001, Murdoch et al., 2015]. In the case of the near-Earth asteroid (101955) Bennu [Lauretta et al., 2019b], [Molaro et al., 2020b] propose that thermal cracking is also able to eject sub-cm-sized particles away from the asteroid surface, thereby offering an explanation for the observed activity of this asteroid [Lauretta et al., 2019a]. Furthermore, several studies also propose that macroscopic fractures, mass-wasting (i.e., gravity-driven movement of regolith down a slope [Millar, 2013]), and material breakdown on asteroids and cometary nuclei could be explained as a consequence of thermal effects [Dombard et al., 2010, El Maarry et al., 2, Alí-Lagoa et al., 2015, Attree et al., 2018, Molaro et al., 2020a].

For all the reasons above, thermal fatigue cracking is now considered a space weathering mechanism. On the other hand, direct evidence of thermal cracking on asteroids (and comets) is still relatively scarce (but strongly growing) and the details of the process in terms of spatial and temporal scales are still poorly understood. One of the first studies that invokes this phenomenon to explain certain *in situ* asteroid observations is the work of [Dombard et al., 2010]. Using images obtained by NASA's Shoemaker mission of the surface of the asteroid (433) Eros, these authors noted boulders that appear to break and erode in place, producing fragments that fill the inside of craters, creating characteristic "ponds" of regolith. Another observational evidence, obtained from images of NASA's OSIRIS-REx mission [Lauretta et al., 2014], is constituted by the detection of exfoliation sheets on some of the boulders on the asteroid (101955) Bennu [Molaro et al., 2020a]. The thickness of the exfoliation sheets is consistent with the depth inside boulders at which thermoelastic simulations show stress concentration as a result of diurnal temperature variations [Molaro et al., 2020a]. However, it has been shown on Earth [McFadden et al., 2005] and Mars [Eppes et al., 2015] that one of the most diagnostic observations of thermal cracking induced by diurnal temperature variations is a preferential meridional direction (north to south) of the fractures on surface rocks. The reason is very simple: during the day the Sun moves in the sky from the east to the west. As a consequence, the temperature gradients are directed essentially in the same direction (west to east). Fractures mainly propagate in a direction perpendicular to that of maximum principal stress. Therefore, this direction of propagation is expected to be essentially from the north to the south, when they are driven by these diurnal temperature cycles. There are hints of predominance of fracture directed in the north to the south and in the north-west to the south-east on the boulders of the

asteroid Bennu [Delbo et al., 2019]. However, a modelling of the crack propagation direction in conditions similar to those existing on Bennu is still lacking. The aim of this work is to provide theoretical foundation for analysis and interpretation of fracture directions on small asteroids with properties similar to those of Bennu.

1.1.1 Asteroids

The objects that are orbiting the sun that are neither planets, nor dwarf planets nor natural satellites are known as small solar system bodies. The group of small solar system bodies whose members mostly orbit in the so-called asteroid main belt that is located between the orbits of Mars and Jupiter, at heliocentric distances ranging between about 2.0 and 3.3 Astronomical Units (AU) are commonly named as asteroids. A wide range of compositions is exhibited by asteroids which vary from irons to undifferentiated rock. Several asteroids appear to be binary and have two components that can be held together as one by mutual gravity. Deep fracturing and even separation of pieces may be caused by impacts, but due to the attraction of mutual gravity, the asteroid may reassemble [Shoemaker, 2003]. The word asteroid is normally used to refer to the solid (rocky, carbonaceous, metallic, etc.) bodies that appear star-like at telescopes. Asteroids have a minimum size above 1 m and they do not exceed a few hundreds of kilometers. A power law adequately describes the size distribution of the asteroid main belt population. Thus, the number of asteroids increases rapidly for decreasing size. The study of the small bodies of our solar system is encouraged by the fact that they can be assumed to be good analogs of the original planetesimals, or even direct survivors of this early population [Cellino, 2021]. Asteroids are classified according to how their spectral reflectance changes versus wavelength [Burbine, 2014].

Inside the group of solar system small bodies, asteroids are not the only one existing class. There are other small objects orbiting the sun. For example, Trans-Neptunian objects (TNO) or Kuiper-belt objects (KBO), are those orbiting at heliocentric distances comparable with or larger than the orbit of Neptune. Centaurs are small bodies orbiting between the main asteroid belt and the orbit of Neptune. There is also another well-known class of solar system small bodies named comets. Inside this group are the objects having a composition rich in ice and volatile elements that can sublimate and produce comas (fuzzy atmosphere) and tails when reaching heliocentric distances sufficiently small [Cellino, 2021, Ye, 2018].

Other kind of objects orbiting the sun are the meteoroids, which are smaller than asteroids and have a maximum size of 1 m. Meteoroids are naturally occurring objects that originate from the fragmentation of planetary body. They typically came from asteroids, but some originate from our moon, comets and other planets such as Mars, after their production, meteoroids are on heliocentric orbits. When they collide with a planet and survive passage through the atmosphere of a different planetary body and reach their surface, they are called meteorites. In this case, and when meteorites or their fragments are collected, these are a source of invaluable information about the composition of the body that produced them. The problem is that it is very difficult to identify the source of meteorites. So it is not always obvious from which planet/asteroid/comet they come from. The thermo mechanical model that will be presented in Chapter 4 uses physical properties from meteorites. For this reason, some information about these objects will be presented below. The light phenomena created when meteoroids pass through other planetary bodies' atmosphere at high speed and burn up are known as meteors [McCoy, 2021, Cellino, 2021].

The top level classification scheme of meteorites presented in [McCoy, 2021] is illustrated in Figure 1.1. This classification emphasizes the meteorites' origin, considered as the most important aspect. In general terms, meteorites can be classified taking into account whether their planetary parent body experienced igneous differentiation or remained undifferentiated since accretion. Igneous differentiation or magmatic differentiation is the process that changes the chemical composition of magmas. The term chondrites is used to refer to undifferentiated

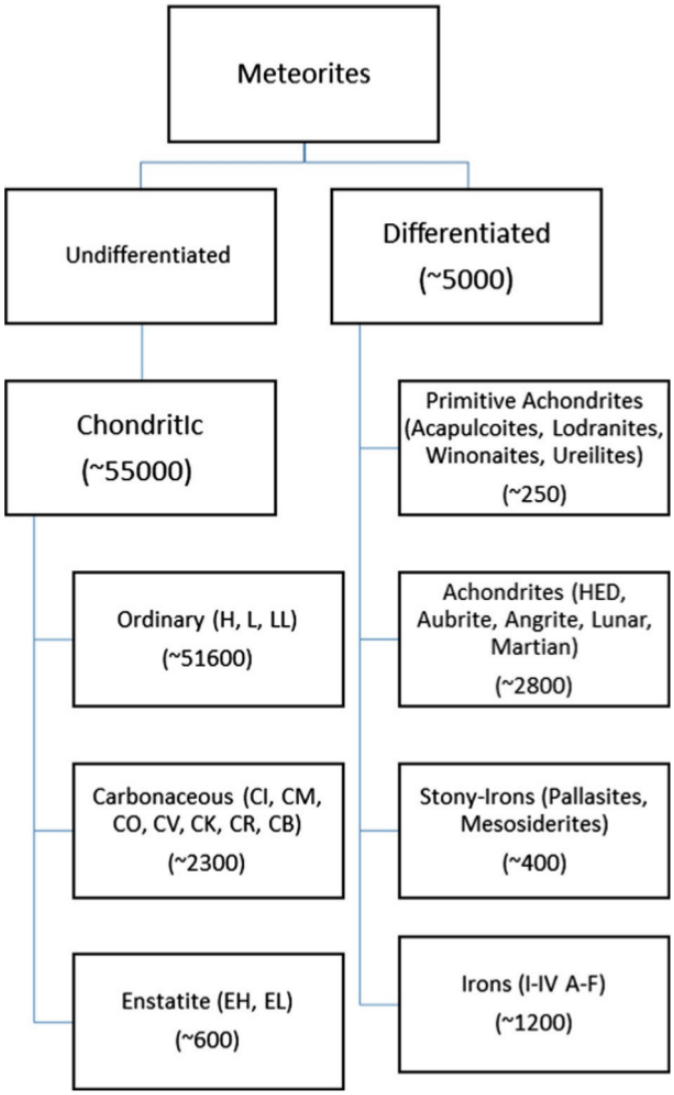

Figure 1.1: Meteorite classification that divides meteorites based on whether their parent bodies experienced igneous differentiation or not. Numbers indicate how many classified meteorites are known in each group. Figure reproduced from [McCoy, 2021].

meteorites. They are called like this because they contain mm-sized igneous spherules called chondrules.

In the group of chondrites, the most common type are the ordinary chondrites which comprise the ∼85% of all meteorites. The ordinary chondrites group is subdivided into H, L and LL groups, based on total iron (Fe) content. It can also be found the carbonaceous chondrites which represent ∼4% of all meteorites. Inside this classification there is a variety of groups, but due to the fact that the earliest-recognized groups CI, CM and CV were carbon-rich, they were named in this way. Generally, these aforementioned groups are named taking into account type specimens. For example, CI designation takes its name from the carbonaceous chondrite Ivuna. There is another classification of chondrites which are known as enstatite chondrites. These constitute ∼1% of all meteorites, they were formed in an oxygen-poor environment, leading to the production of essentially free of ferrous oxide (FeO) enstatite. Similar to the ordinary chondrites, enstatite chondrites are divided into EH and EL chondrites to denote high- and low-total iron respectively. It is thought that the ordinary, carbonaceous and enstatite clans represent common chemical properties, as well as possibly nebular regions, while the groups (e.g., H, CI, EL) represent different parent bodies [McCoy, 2021].

In the case of differentiated meteorites, they comprise less than ∼10% of all meteorites recovered. They are classified as primitive achondrites, achondrites, stony-irons and irons. Even though the primitive achondrites are few in number, they help to sample the gap between undifferentiated chondrites and achondrites, and between stony-irons and irons from fully differentiated asteroids. Primitive achondrites are named for type specimens (i.e., acapulcoites, lodranites, winonaites and ureilites). Their bulk chemical composition is broadly chondritic, but with evidence of melting and melt segregation. Inside the achondrites there are included the howardite-eucrite-diogenite clan, aubrites, angrites, martian and lunar meteorites. These represent ∼5% of all meteorites and they are igneous rocks that were crystallized from melts. There are also the stony-iron pallasites and mesosiderites which are mixtures of metal and differentiated silicates. They are small in number and their origin is still enigmatic. In the final part of the classification it is found the irons, they are metal-dominated but often contain inclusions of sulfides, carbides, phosphides, phosphates and silicates. They represent ∼2% of all meteorites and include at least 13 well-defined groups (i.e., I-IV, A-F) [McCoy, 2021].

One of the main ideas behind this PhD is to numerically reproduce some observed fractures on space bodies which are thought to be induced by large amount of thermal cycles. Current work is specifically focused on asteroid (101955) Bennu, which is depicted in Figure 1.2. As already mentioned in the context section, solar system small bodies can provide valuable information of the earliest stages of planet formation, as they can be considered relicts of the early stages of solar system evolution [Wada et al., 2018]. In the particular case of Bennu, tremendous temperature variation has been reported [Rozitis et al., 2020]. In addition, Bennu has been dynamically decoupled from the main asteroid belt for 1.75 Myr [Ballouz et al., 2020], being this the time that Bennu has been with these temperatures. A natural question would be what would happen to materials like those composing Bennu, if they are exposed for very long time to strong temperature variations? Will thermal cracking appear? Furthermore, fatigue phenomenon on Bennu's surface can provide a better understanding of landscape evolution processes [Molaro et al., 2020b].

Asteroid (101955) Bennu is a low-albedo B-type asteroid. Low-albedo means that Bennu reflects a small amount of the incoming radiation and absorbs the rest. B-type asteroids are a rare type of asteroids that have been linked spectroscopically to CI or CM carbonaceous chondrites, where the 'B' indicates that they are spectrally blue [Yang and Jewitt, 2010, Alí-Lagoa et al., 2013]. Its mean diameter is about 490.06 m. Bennu has been linked to organic-rich hydrated carbonaceous chondrites [Nolan et al., 2013, Lauretta et al., 2019b, Barnouin et al., 2019]. Bennu's bulk composition appears to be hydrated. According to its shape and topography, Bennu's levels of internal shear strength or cohesion are low [Lauretta et al., 2019b]. Its low density is consistent with a "rubble-pile" structure containing 50% macroporosity when the particle density characteristic of CM chondrites is assumed. In this way, asteroid Bennu appears to be a gravitational aggregate. The age of its surface is at 100 million to 1 billion years old [Walsh et al., 2019]. Morphologies observed in fractured boulders on asteroid Bennu suggest the influence of impact and thermal processes [Ballouz et al., 2020, Molaro et al., 2020a, Molaro et al., 2020b]. It has a global geometric albedo of 4.4%, making it one of the darkest objects in the Solar System. The geometric albedo is defined as the amount of radiation reflected from a body relative to that from a flat Lambertian surface, which is a diffuse perfect reflector at all wavelengths [de Pater and Lissauer, 2015]. Magnetite (Fe_3O_4) is present in Bennu's surface, which is an important indicator of past aqueous alteration in the parent body [Yang and Jewitt, 2010, Hergenrother et al., 2013, Clark et al., 2011].

According to the information found in the literature, it is evident that fracture processes in solar system small bodies are still poorly understood. Fracture phenomena on airless bodies have been related to temperature variations resulting from the cycles between day and night. It is possible to find studies that compute thermal stresses on space bodies, or how much a crack

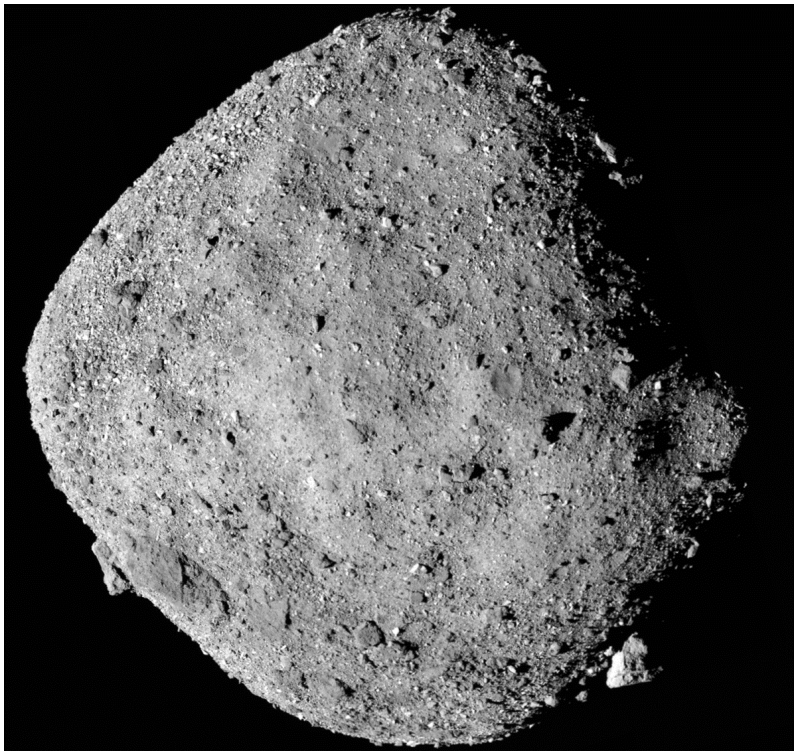

Figure 1.2: Mosaic image of asteroid Bennu composed of 12 PolyCam images collected on December 2, 2018 by the OSIRIS-REx spacecraft from a range of 15 miles (24 km). Credits: NASA/Goddard/University of Arizona.

grow due to thermal fatigue. Nevertheless, there are no studies that really give a theoretical background that allows to explain why some fractures observed on some solar system small bodies, evolve in one direction or another. This lack of models gives origin to the necessity of developing an adapted approach. This approach should combine thermoelasticity theory and fracture mechanics concepts aiming at numerically reproduce some observed fractures on space bodies induced by large amount of thermal cycles. In this specific case, it will be applied to asteroid Bennu. In order to implement this adapted approach, several concepts from different fields should be introduced. A brief overview on fracture mechanics, as well as on the most common numerical methods for crack propagation will be given.

1.2 Fracture mechanics

In order to study and understand advanced concepts in fracture mechanics, a solid background in the fundamentals of Linear Elastic Fracture Mechanics (LEFM) is needed. First, this section describes both the local and global approaches to linear fracture mechanics. Then, some notions in crack propagation are presented: when and where cracks propagate.

1.2.1 Local approach

In an elastic medium, in the vicinity of cracks, the stress fields may be calculated using linear elastic stress analysis. In Figure 1.3 the three types of loading that a crack can experience are shown. These basic fracture modes are (i) Mode I, (ii) Mode II and (iii) Mode III. Mode I is considered to be the most critical with respect to fracture. The stress state near a crack tip (Equations 1.2, 1.3 and 1.4) is usually defined through these fracture modes.

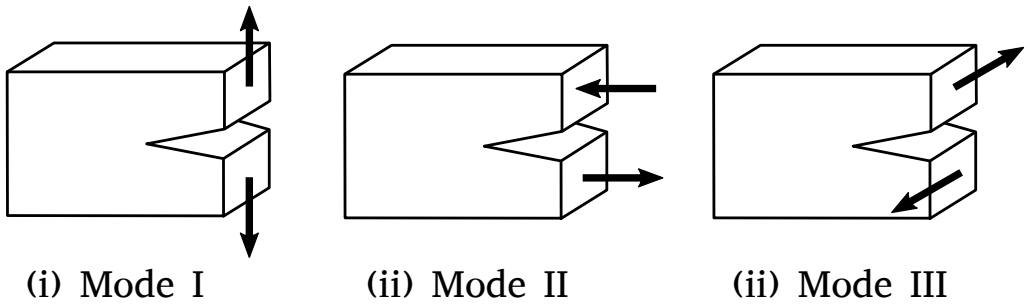

Figure 1.3: Schematic representation of the three fundamental modes of fracture.

A body with a crack can undergo any one of these loading modes, or a combination of two or three of these modes [Anderson, 2005]. When more than one loading mode is present (mixed-mode), the individual contributions to a given stress component are additive:

$$\sigma_{ij}^{(total)} = \sigma_{ij}^{(I)} + \sigma_{ij}^{(II)} + \sigma_{ij}^{(III)} \tag{1.1}$$

Figure 1.4 depicts a material element placed at a distance r from the crack tip and at an angle θ with respect to the crack direction. The in-plane stresses of the element are also shown. The equations describing the stress state close to a crack tip corresponding to Modes I, II and III [Anderson, 2005] are given respectively by equations (1.2), (1.3) and (1.4). It is worth mentioning that each loading mode produces a $\frac{1}{\sqrt{r}}$ singularity at the crack tip and also that K depends on the mode, therefore, the stress intensity factor has a subscript used to indicate the loading mode K_I, K_{II} or K_{III}.

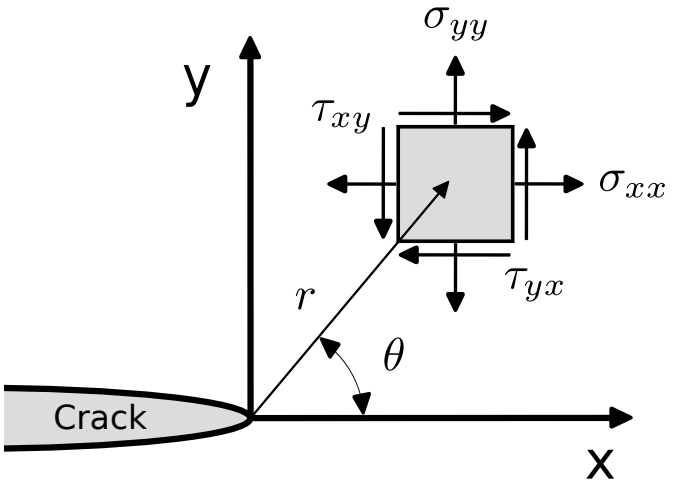

Figure 1.4: Stress state near the crack tip. Figure reproduced from [Anderson, 2005].

$$\begin{aligned}
\sigma_{xx} &= \frac{K_I}{\sqrt{2\pi r}} \cos\left(\frac{\theta}{2}\right)\left[1 - \sin\left(\frac{\theta}{2}\right)\sin\left(\frac{3\theta}{2}\right)\right] \\
\sigma_{yy} &= \frac{K_I}{\sqrt{2\pi r}} \cos\left(\frac{\theta}{2}\right)\left[1 + \sin\left(\frac{\theta}{2}\right)\sin\left(\frac{3\theta}{2}\right)\right] \\
\tau_{xy} &= \frac{K_I}{\sqrt{2\pi r}} \cos\left(\frac{\theta}{2}\right)\sin\left(\frac{\theta}{2}\right)\cos\left(\frac{3\theta}{2}\right) \\
\sigma_{zz} &= \begin{cases} 0 & for\ \ plane\ \ stress \\ \nu(\sigma_{xx} + \sigma_{yy}) & for\ \ plane\ \ strain \end{cases} \\
\tau_{xz} &= \tau_{yz} = 0
\end{aligned} \tag{1.2}$$

$$
\begin{aligned}
\sigma_{xx} &= -\frac{K_{II}}{\sqrt{2\pi r}} \sin\left(\frac{\theta}{2}\right)\left[2+\cos\left(\frac{\theta}{2}\right)\cos\left(\frac{3\theta}{2}\right)\right] \\
\sigma_{yy} &= \frac{K_{II}}{\sqrt{2\pi r}} \sin\left(\frac{\theta}{2}\right)\cos\left(\frac{\theta}{2}\right)\cos\left(\frac{3\theta}{2}\right) \\
\tau_{xy} &= \frac{K_{II}}{\sqrt{2\pi r}} \cos\left(\frac{\theta}{2}\right)\left[1-\sin\left(\frac{\theta}{2}\right)\sin\left(\frac{3\theta}{2}\right)\right] \\
\sigma_{zz} &= \begin{cases} 0 & for\ \ plane\ \ stress \\ \nu(\sigma_{xx}+\sigma_{yy}) & for\ \ plane\ \ strain \end{cases} \\
\tau_{xz} &= \tau_{yz} = 0
\end{aligned}
\tag{1.3}
$$

$$
\begin{aligned}
\tau_{xz} &= -\frac{K_{III}}{\sqrt{2\pi r}} \sin\left(\frac{\theta}{2}\right) \\
\tau_{yz} &= \frac{K_{III}}{\sqrt{2\pi r}} \cos\left(\frac{\theta}{2}\right)
\end{aligned}
\tag{1.4}
$$

In those equations r is the distance between the crack tip and the element of interest, θ gives the direction with respect to the crack axis of this element of interest and ν is the Poisson's ratio. For example, it should be noted that each one of the stress components of the element in equations (1.2), (1.3) and (1.4) is proportional to a single constant K_i ($i = I,\ II$ and III), which is called the **stress intensity factor (SIF)**. The concept of **SIF** was originally developed by [Irwin, 1957] based on the work of [Westergaard, 1939] regarding complete solution for the stress field surrounding a crack. When the **SIF** is known, the entire stress distribution at the crack tip can be calculated using the appropriate equation. Fracture will occur at a critical stress intensity factor K_{Ic}, which is an alternative measure of fracture toughness, i.e., a material's property describing its capability to resist fracture. Accordingly, fracture occurs when $K_I = K_{Ic}$. Here K_I is the driving force for fracture which depends only on the applied load and on the crack geometrical configuration, and K_{Ic} is a material property, i.e., fracture toughness.

Consider the Mode I singular field on the crack plane (i.e., $\theta = 0$), the stresses in the x and y direction are equal and are given by:

$$
\sigma_{xx} = \sigma_{yy} = \frac{K_I}{\sqrt{2\pi r}} \tag{1.5}
$$

For the case where θ is equal to 0, the shear stress is zero, which means that the crack plane is a principal plane for pure Mode I loading. Figure 1.5 shows the behaviour of the normal stress to the crack plane (σ_{yy}) against the distance from the crack tip. Equation (1.5) is only valid in the vicinity close to the crack tip, where the stress field is dominated by the $\frac{1}{\sqrt{r}}$ singularity. Far away from the crack tip, the stresses are dictated by the remote boundary conditions. For instance in Figure 1.5, if the cracked structure is subjected to a uniform remote tensile stress, σ_{yy} approaches σ^{∞}. A region where equations (1.2), (1.3) and (1.4) describe the crack-tip field [Anderson, 2005], can be defined as a singularity-dominated zone.

For some configurations the stress intensity factors may be determined based on remote loads and geometry. Figure 1.6 shows a through-thickness crack in an infinite plate subjected to a remote tensile stress. Here "infinite" means that the width and height of the plate are much larger than the length of the crack ($>> 2a$).

For example, for this configuration the stress intensity factor is equal to:

$$
K_I = \sigma\sqrt{2\pi a} \tag{1.6}
$$

Formulas for calculating the stress intensity factors for different configurations considering the 3 modes (I, II, III) can be found in [Broek, 1982a, Sun and Jin, 2012a, Radaj, 2013a, Radaj,

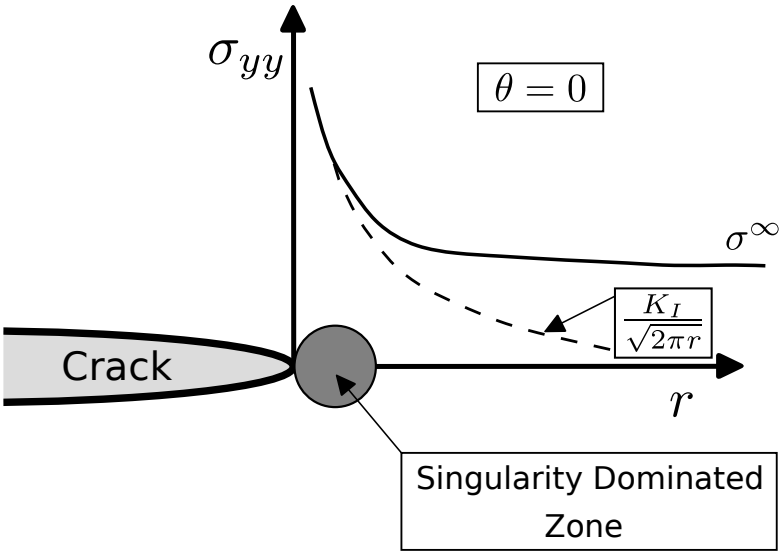

Figure 1.5: Behaviour of stress normal to the crack plane in Mode I with respect to the distance from crack tip. Figure reproduced from [Anderson, 2005]

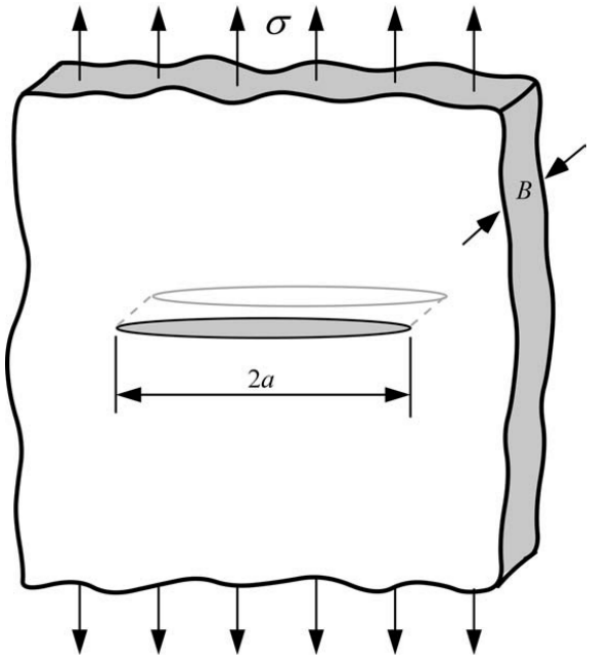

Figure 1.6: Infinity plate with a through thickness crack subjected to uniaxial tension. Figure modified from [Anderson, 2005].

2013b, Brocks, 2018]. For more complex configurations this can be estimated through experiments or numerical simulations [Kobayashi et al., 1964, Tracey, 1971, Blandford et al., 1981]. Since the twentieth century the evolution of fracture mechanics field has been very useful in the understanding of crack initiation and propagation phenomena. The introduction of the stress intensity factor concept by the year 1957, allowed the resolution of practical engineering problems. During the 1960s the linear elastic fracture mechanics (LEFM) had a fast development, with applications to brittle fracture and fatigue crack growth. The linear elastic stress field in the vicinity of a crack tip, including its singularity, can be described through the stress intensity factor. Characterising the mechanical properties of cracked and uncracked test pieces,

may be done using, respectively, the stress intensity factors and the stress fields [Paris and Sih, 1965,Pook, 2000,Pook, 2015]. However, analysing fracture through the stress field requires high accuracy at the crack tip due to the stress singularity. To overcome this issue, an energetic or global approach has also been developed and will be described now.

1.2.2 Global approach

The basic idea behind this approach is that propagation of cracks requires energy. It means that fracture (i.e. crack extension) takes place when the energy for crack growth is enough to overcome the resistance of the material (surface energy, plastic work or others types of energy dissipation). The energy release rate (G) is defined as the rate of change in potential energy with the crack area for a linear elastic material. Fracture will take place when the energy release rate reaches a critical value (G_c), which is known as critical energy release rate and which is a material parameter.

Going back to Figure 1.6, for this configuration (wide plate in plane stress with a crack of length $2a$) the energy release rate is given by equation (1.7):

$$G = \frac{\pi\sigma^2 a}{E} \tag{1.7}$$

Where E is the Young's modulus, σ is the applied stress far way from the crack, and a is the half-crack length. At fracture $G = G_c$, the critical combination of stress and crack size for failure may be described through equation (1.8):

$$G_c = \frac{\pi\sigma_f^2 a_c}{E} \tag{1.8}$$

From equation (1.8) it should be noted that for a constant value of G_c, failure stress σ_f varies according to $1/\sqrt{a}$. Similar to the stress intensity approach, here the energy release rate (G) should be understood as the driving force for fracture, while G_c, the critical energy release rate as an intrinsic property of the material depicting the resistance to fracture. In the field of fracture mechanics, an essential assumption is that fracture toughness (G_c in this case), does not depend on the size and geometry of the cracked body. A fracture analysis based on an energy approach leads to the definition of the strain energy release rate that allows to characterize the loading on a crack and of the critical energy release rate as a material toughness property. According to Griffith, a crack extends if the rate of strain energy release per unit of crack extension ($\frac{dU_s}{da}$), is at least equal to the rate of surface energy requirement ($\frac{dU_\gamma}{da}$):

$$\frac{dU_s}{da} \geq \frac{dU_\gamma}{da} \tag{1.9}$$

Where U_γ is the surface energy, U_s is the strain energy and da is the crack length increment. [Inglis, 1913]'s work states that the increasing of stress at the crack tip dependence was only on the geometrical shape of the crack and not on its absolute size. Based on this, Griffith showed that when a double-ended crack of length $2a$ was introduced in an infinite plate of unit width, and subjected to a uniformly applied stress σ, the strain energy released obtained is [Fischer-Cripps, 2007]:

$$U_s = -\frac{\pi\sigma^2 a^2}{E} \quad Joules \quad (per \quad meter \quad width) \tag{1.10}$$

Atoms on the free surface and the ones below have to adjust to form an equilibrium thereby developing strain in the material close to the free surface. Such deformation requires energy. Such energy is known as surface energy. The total surface energy for 2 surfaces of unit width and length $2a$ is:

$$U_\gamma = 4\gamma a \quad Joules \quad (per \quad meter \quad width) \tag{1.11}$$

In equation (1.11) the factor 4 arises because of there being two crack surfaces of length $2a$. γ is the aforementioned surface energy (fracture surface energy). Commonly γ is larger than the surface free energy because fracture process involves atoms located at small distance into the solid away from the surface [Fischer-Cripps, 2007]. Figure 1.7 shows the variation of the energy when crack length increases. The variation of the strain energy released and the surface energy required as crack length increases is also shown. Note that cracks with length below a_c will not extend spontaneously. Maximun in the total crack energy $(U_\gamma + U_s)$ denotes an unstable equilibrium condition.

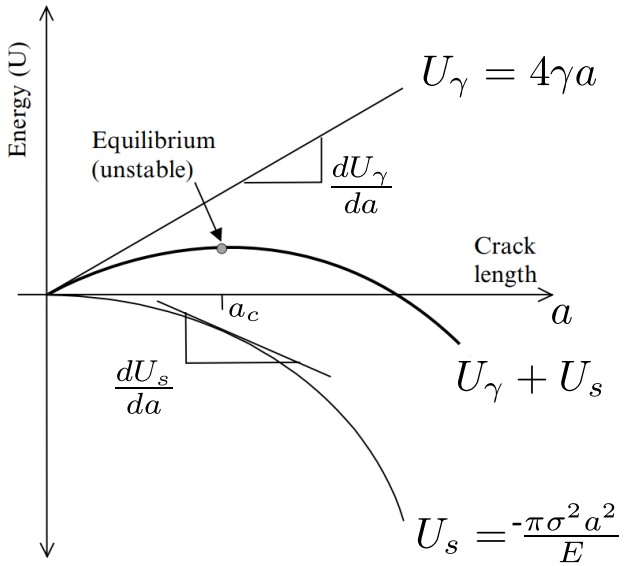

Figure 1.7: Schematic representation of fracture energy balance. Figure reproduced from [Fischer-Cripps, 2007]

For describing the behavior of cracks two parameters have been introduced. One which quantifies the net change in potential energy due to an extension of the crack length (energy release rate), and another that describes the stresses (also the strains and displacements) near the crack tip. While G describes a global behavior, K is a local parameter. These parameters are entirely related in a linear elastic material, so combining equations (1.6) and (1.7) the following relationship can be found:

$$G = \frac{K_I^2}{E'} + \frac{K_{II}^2}{E'} + \frac{K_{III}^2}{2\mu} \quad with \quad \begin{cases} E' = E & for \quad plane \quad stress \\ E' = \frac{E}{1-\nu^2} & for \quad plane \quad strain \\ \mu = \frac{E}{2(1+\nu)} \end{cases} \tag{1.12}$$

Where μ is the shear modulus. Note that in fracture mechanics the energy and stress-intensity approaches are basically equivalent for linear elastic materials. Equation (1.12) also holds for G_c and K_{Ic}.

So far it has been discussed some basic fracture mechanics concepts, as well as the two commonly approaches used when tackling the phenomenon of fracture, mainly in brittle materials. Next step is to determine whether a crack will propagate or not, and if so, in which direction.

1.2.3 Crack growth criteria

Once a crack has initiated, one needs to check if the crack is going to propagate or not (Crack Propagation Criteria), and in which direction (Crack Kinking Criteria). This section covers these topics.

1.2.3.1 Crack propagation criteria

In order to determine if a crack grows or not, local and global criteria are available. The former uses the stress intensity factors while the latter uses the energy release rate. Both criteria use material parameters as reference in order to allow or not crack growth. Another scenario of crack propagation is when this occurs under conditions of cyclic applied loading. This crack growth phenomenon due to cyclic loading is called fatigue crack growth. The latter criterion is important because one of the objectives sought in the current PhD is to be able to perform a thermo-elastic fatigue analysis on solar system small bodies.

Local or global criteria

Local criteria use information from the neighborhood of the crack tip. Regarding crack propagation, usually to decide whether the crack will propagate or not, the stress intensity factors (SIFs), representing the strength of the singularity at the crack tip are used. For example, in mode I loading, the SIF (K_I) is compared against a critical value of a material property (K_{Ic}). When the SIF at the crack tip is greater than the material's toughness ($K_I \geq K_{Ic}$), propagation is allowed. Another way to decide if the propagation is allowed or not, is through the use of an energetic criteria. In this case, the energy release rate (G) is compared against a critical value of a material parameter (G_c). According to this criteron, the propagation takes place when the energy release rate reaches a critical value that is related to the material fracture toughness ($G \geq G_c$). The "greater than" symbols used in $K_I \geq K_{Ic}$ and $G \geq G_c$ only satisfy the computations in a math sense, but they have no physical meaning. The equals signs in $K_I = K_{Ic}$ and $G = G_c$ are enough to satisfy the condition of crack growth, which means there is enough energy to drive crack growth [Zhuang et al., 2014].

If once the propagation starts, the crack arrests and requires more energy to propagate, we are talking about stable propagation. Conversely, if after initiation of the propagation, the crack propagates without any additional loading, we are dealing with an unstable propagation. The latter leads to the complete failure of the material. In the case of stable propagation, computation of the crack propagation velocity can be performed. Equation 5.2 illustrates the two possibilities when talking about crack propagation from an energetic point of view. When $G < G_c$ there is no crack propagation, therefore, there is no crack length increment ($\dot{a} = 0$). Contrary, if $G = G_c$ crack propagation takes place and there is a crack length increment ($\dot{a} > 0$). From these two relationships, it can be inferred that $\dot{G}\dot{a} = 0$. This relation holds for both propagation and not propagation.

$$\begin{cases} \text{if} \quad G < G_c \quad \text{then } \dot{a} = 0 \\ \text{if} \quad G = G_c \quad \text{then } \dot{a} > 0 \end{cases} \quad \Rightarrow \quad \boxed{\dot{G}\dot{a} = 0} \tag{1.13}$$

Where a is the crack length. If G reaches G_c and remains constant ($\dot{G} = 0$), there is a crack length increment ($\dot{a} > 0$), and crack propagation velocity for this case can be found. G can be defined as the decrease in the total potential energy (W_p) during a crack growth (da) (See section 1.2.4.2). As the total potential energy W_p, G is a function of the length of the crack a, and of the loading u, the latter also depending on time. Therefore, during a propagation, $\dot{G}$ can be computed as follows:

$$G = -\frac{\partial W_p}{\partial a} \quad \Rightarrow \quad \dot{G} = -\frac{\partial^2 W_p}{\partial a^2}\dot{a} - \frac{\partial^2 W_p}{\partial a \partial u}\dot{u} \tag{1.14}$$

Finally, using equation (5.2) crack propagation velocity is given by:

$$\dot{a} = \left[-\frac{\frac{\partial^2 W_p}{\partial a \partial u}\dot{u}}{\frac{\partial^2 W_p}{\partial a^2}} \right]^+ = \left[-\frac{\frac{\partial G}{\partial u}\dot{u}}{\frac{\partial G}{\partial a}} \right]^+ \tag{1.15}$$

Readers interested in further details regarding crack propagation velocity and crack growth stability, topics that are out of the scope of the current PhD thesis, can refer to [Suo, 1990] (See also 5.2.2).

Fatigue crack growth models

Fatigue crack growth is the phenomenon taking place when cracks grow due to cyclic loading conditions. The fatigue life of a material subjected to a cyclic load can be split into two stages: (i) a crack initiation and a (ii) crack growth. The first one includes some microcrack growth but in this stage the fatigue cracks are still invisible due to their small size. In the second stage, cracks grow until complete failure [Schijve, 2009]. When dealing with cyclic loading, even if applied loads are far below the critical value, cracks evolve and propagate. Fracture process under fatigue loading implies degradation of the material strength with accumulated damage. If preexisting flaws are assumed in the material, fatigue design uses defect-tolerant approach to define crack propagation life according to empirical crack growth laws based on fracture mechanics theory. The rate at which a crack grows is driven by a fluctuating stress intensity. In a material having a crack, the crack length increment (Δa) is the result of applying a stress intensity range (ΔK) for some number of cycles (ΔN). The rate of growth with cycles can be characterized by the ratio $\Delta a/\Delta N$ or, in a continuous way (i.e., for small intervals) by the derivative of the crack length with respect to the number of cycles da/dN. When stresses are applied in a cyclic manner, an important quantity is the stress ratio R, which is the ratio between the minimum stress and the maximum stress ($\sigma_{min}/\sigma_{max}$). R can be also defined as K_{min}/K_{max}. For a given ΔK, if R increases, then the crack growth rate also increases and vice versa [Dowling, 2013].

The characteristic shape of the fatigue crack growth rate curve is shown in Figure 1.8. Fatigue crack growth rate curve varies between materials. There are three different regimes or regions of fatigue crack growth, namely *I*, *II* and *III*. The division into this three regions depends on the curve shape, the mechanisms of crack extension and various influences on the curve [Janssen et al., 2004]. In Figure 1.8, region *I* is characterized by the existence of a threshold stress intensity range (ΔK_{th}), below which cracks either propagate at very low rate or do not propagate at all. When ΔK_{th} is known, and in order to avoid fatigue crack growth, permissible crack lengths and/or applied stresses can be calculated. Above the threshold value (ΔK_{th}), a rapidly increasing of the crack growth rate takes place when ΔK increases. Inside region *II*, the crack growth rate (da/dN) is generally some power function of ΔK, leading to a linear relation between $\log(da/dN)$ and $\log(\Delta K)$ (e.g., Paris' Law). And lastly in region *III*, the crack growth is rapid, unstable and accelerates until the crack tip stress intensity factor reaches its critical value (K_c) [Farahmand, 2001, Janssen et al., 2004].

Commonly, the curve shown in Figure 1.8 has tails at the upper and lower ends. For small values of ΔK located in region *I*, the lower end tail approaches a vertical asymptote known as the fatigue crack growth threshold (ΔK_{th}). Normally, crack growth does not occur for stress intensity ranges below the threshold ($\Delta K < \Delta K_{th}$). The curve shown in Figure 1.8 has also a tail at the upper end for large values of ΔK (region *III*). In region *III*, when the stress intensity ratio R is equal to 0, it corresponds to zero-to-tension loading. In this case, the tail at the upper end approaches a vertical asymptote which is the critical stress intensity for the material K_c.

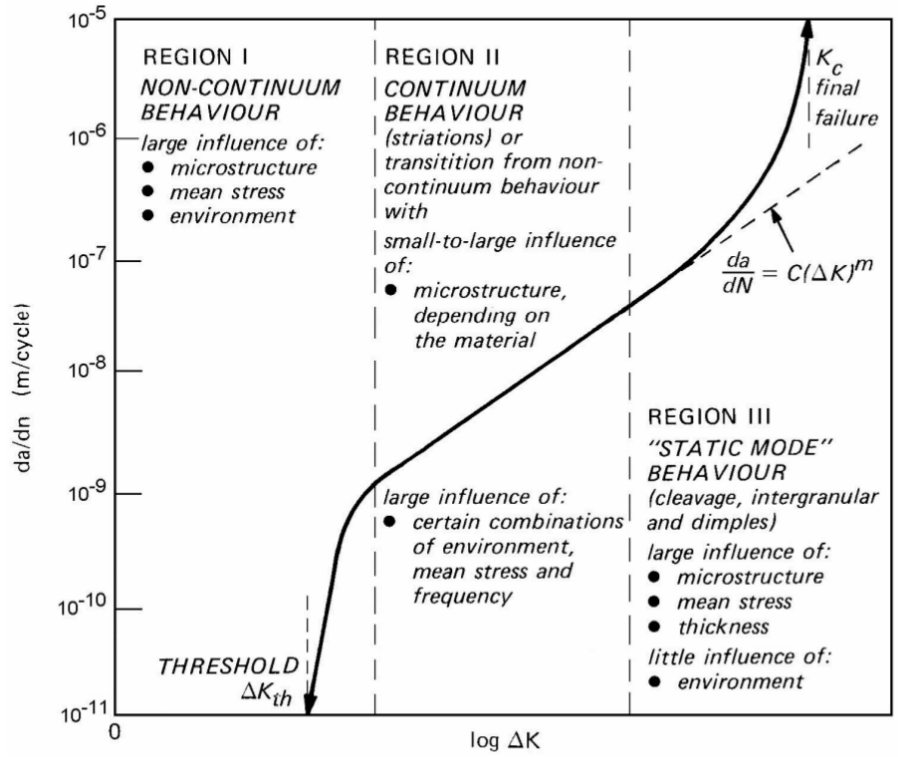

Figure 1.8: Characteristics of the fatigue crack growth rate curve ($\log(da/dN)$vs$\log(\Delta K)$). Figure reproduced from [Janssen et al., 2004].

Paris' law

The most famous method used to predict fatigue crack growth is based on the pioneering work of [Paris et al., 1961,Paris and Erdogan, 1963]. In Paris' work, the rate at which the crack length (a) grows is related to the applied stress intensity factor range (ΔK) through a power law:

$$\frac{da}{dN} = C[\Delta K]^n \tag{1.16}$$

where a is the crack length, N the number of cycles, $\frac{da}{dN}$ the crack growth rate per cycle, ΔK the range of stress intensity factor, C and n are material properties fitted to experimental fatigue data. Thus from equation (1.16), a plot of $\log(da/dN)$ against $\log(\Delta K)$ should be a straight line with a slope of n and $\log(C)$ is the intercept. The limitation of Paris' law is that it is only capable of describing data falling in Region *II*. When the data displays a threshold (Region *I*) or an accelerated growth (Region *I*), Paris' law is not suitable to describe neither region *I* nor region *II* [Beden et al., 2009].

Walker's law

In order to account for the effect of stress ratio R on crack growth rate, [Walker, 1970] presented a generalization of the Paris' law. The Walker's law takes the following form:

$$\frac{da}{dN} = C_0 \left(\frac{1}{(1-R)^{1-\gamma}} \Delta K \right)^n \tag{1.17}$$

where $\frac{da}{dN}$ the crack growth rate per cycle, R is the stress ratio, ΔK the range of stress intensity factor, C_0, n and γ are material properties. C_0 is the intercept constant C for the case of $R = 0$. n is the slope on a log-log scale and γ how strongly the crack growth rate in the material is

affected by the stress ratio R. Walker's law law is not able to describe the tails at the upper and lower ends of growth rate curve [Dowling, 2013].

NASGRO equation

One of the most general approach to describe fatigue crack growth is the NASGRO equation [NASGRO, 2010, Forman and Mettu, 1990]. It accounts for stress ratio R, crack closure and the tails at both the upper (region III) and lower (region I) ends of the crack growth rate curve. The NASGRO equation takes the following form:

$$\frac{da}{dN} = C\left[\left(\frac{1-f}{1-R}\right)\Delta K\right]^n \frac{\left(1-\frac{\Delta K_{th}}{\Delta K}\right)^p}{\left(1-\frac{K_{max}}{K_c}\right)^q} \tag{1.18}$$

where $\frac{da}{dN}$ the crack growth rate per cycle, R is the stress ratio, ΔK the range of stress intensity factor, ΔK_{th} is the fatigue crack growth threshold, K_{max} is the maximum stress intensity factor during the cycle, K_c is the critical stress intensity value of the material. The shapes of the asymptotes in the threshold and critical crack growth regions are controlled respectively by p and q. Finally, f is a crack-opening function empirically formulated by [Newman, 1984].

Once propagation is allowed, next step is to find the direction in which this will take place. For this purpose, the next section focuses on available methodologies that allow to compute the crack propagation direction.

1.2.4 Crack kinking criteria

When crack propagation occurs, the direction of propagation must be defined. There are different criteria to find the direction in which a crack will propagate. Some criteria are based on the local fields at the crack tip, following a local approach, e.g., the maximum circumferential stress criterion [Erdogan and Sih, 1963] or the maximum strain criterion [Wu, 1974, Maiti and Smith, 1984]. Other criteria are based on energetic parameters following a global approach. e.g., the strain energy density [Sih and Macdonald, 1974, Sih, 1973] or the maximum energy release rate criterion [Hussain et al., 1973, Nuismer, 1975]. In the following, two of the aforementioned criteria will be described: The maximal circumferential stress criterion and the maximum energy release rate criterion.

1.2.4.1 Maximal circumferential stress criterion (MCSC)

This criterion proposed by [Erdogan and Sih, 1963] states that a crack in an elastic material is going to propagate in the direction for which the circumferential stress ($\sigma_{\theta\theta}$) is maximun. This criterion is local because the direction of propagation is calculated using the stress field along a small circle of radius r centered at the crack tip. Figure 1.9 shows the representation the stress state on a cylindrical differential element.

For the general mixed-mode problem shown in Figure 1.9, the asymptotic near-tip stress field is given by:

$$\begin{Bmatrix} \sigma_{rr} \\ \sigma_{\theta\theta} \\ \sigma_{r\theta} \end{Bmatrix} = \frac{K_I}{4\sqrt{2\pi r}} \begin{Bmatrix} 5\cos(\frac{\theta}{2}) - \cos(\frac{3\theta}{2}) \\ 3\cos(\frac{\theta}{2}) + \cos(\frac{3\theta}{2}) \\ \sin(\frac{\theta}{2}) + \sin(\frac{3\theta}{2}) \end{Bmatrix} + \frac{K_{II}}{4\sqrt{2\pi r}} \begin{Bmatrix} -5\sin(\frac{\theta}{2}) + 3\sin(\frac{3\theta}{2}) \\ -3\sin(\frac{\theta}{2}) - 3\sin(\frac{3\theta}{2}) \\ \cos(\frac{\theta}{2}) + 3\cos(\frac{3\theta}{2}) \end{Bmatrix} \tag{1.19}$$

Where K_I and K_{II} are respectively the stress intensity factors for mode I and mode II, θ is the angle of the vector that goes from the crack tip to the interest point and r is the distance between the crack tip and the interest point. Following [Erdogan and Sih, 1963], we proceed to maximize $\sigma_{\theta\theta}$ in (1.19) by doing:

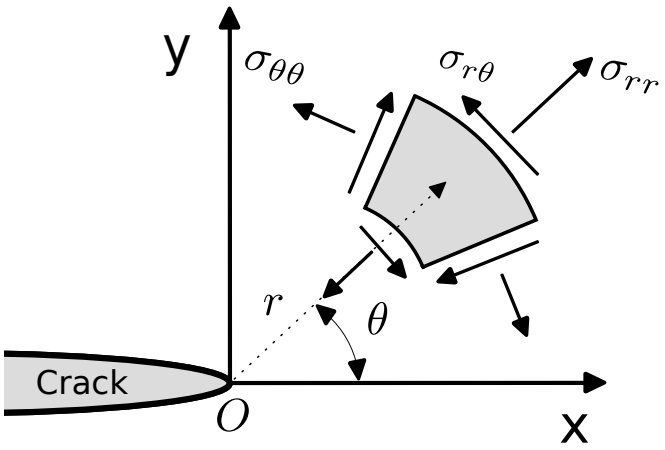

Figure 1.9: Stress components near the crack tip in cylindrical coordinates.

$$\begin{cases} \frac{\partial \sigma_{\theta\theta}}{\partial \theta} = 0 \\ \\ \frac{\partial^2 \sigma_{\theta\theta}}{\partial \theta^2} < 0 \end{cases} \tag{1.20}$$

Then, from the second row of equation (1.19) one obtains:

$$\frac{\partial \sigma_{\theta\theta}}{\partial \theta} = K_I \left[\sin\left(\frac{\theta}{2}\right) + \sin\left(\frac{3\theta}{2}\right) \right] + K_{II} \left[\cos\left(\frac{\theta}{2}\right) + \cos\left(\frac{3\theta}{2}\right) \right] = 0 \tag{1.21}$$

Equation (1.21) can be simplified to:

$$K_I \sin\theta + K_{II} \left(3\cos\theta - 1\right) = 0 \tag{1.22}$$

which can be solved leading to [Nguyen-Xuan et al., 2012]:

$$\theta = 2 \arctan\left(\frac{K_I - \sqrt{K_I^2 + 8K_{II}^2}}{4K_{II}} \right) \tag{1.23}$$

where θ is the actual crack propagation direction, the one that maximizes the circumferential stress in a two-dimensional problem. According to this criterion there is a limit angle corresponding to pure shear: $\theta = \pm 70.53°$.

If the stress intensity factors (K_I and K_{II}) are provided by the FE software, crack propagation direction may be computed by direct application of equation (1.23). In the case where SIFs are not computed by the FE software, the computation of the kinking angle has to be computed based on the circumferential stress $\sigma_{\theta\theta}$ at each integration point of each one of the elements of interests, the ones attached to the crack tip (Figure 1.10). Then the crack propagates toward the integration point that maximises $\sigma_{\theta\theta}$. Crack propagation will be dictated by the location of the integration point with respect to the crack tip. According to [Bouchard et al., 2003], if this method is applied directly, the crack propagation direction would be mesh-dependent due to the fact that this direction would directly depend on the number of elements attached to the crack tip. A smooth $\sigma_{\theta\theta}$ field could be constructed based on near crack tip elements but the final solution would still depend on the mesh refinement at the crack tip.

MCSC is one of the most used criteria in order to compute crack propagation direction because its implementation is very easy. However, it should be mentioned that for the use of this criterion, use of elements that are able to capture the singularity of the stress field at the crack tip is highly recommended. In some cases, the accuracy of the stress field would require the use of special elements such as the Barsoum (or quarter-point) element [Barsoum,

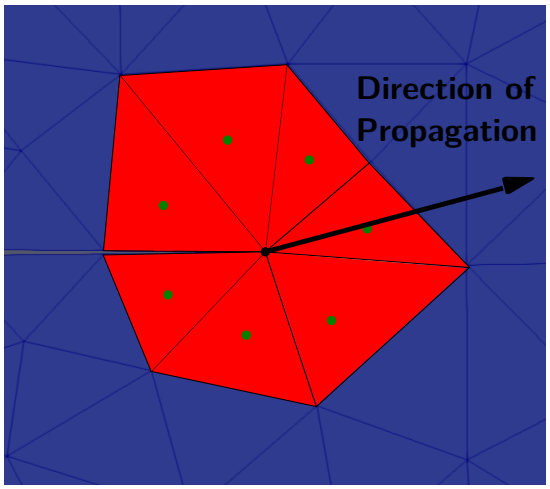

Figure 1.10: Calculation of the direction of propagation with the maximun circumferential stress criterion using the elements attached to the crack tip

1976] which accounts for the stress singularity. Without those elements, the use of an energetic approach may be more appropriate.

1.2.4.2 Maximum energy release rate criterion (MERRC)

According to this criterion, the crack propagation direction will be the one which maximises the energy release rate (G), i.e., the energy required for a unitary crack increase. This criterion is evaluated using all virtual and kinematically admissible displacement fields at the crack tip neighborhood [Hussain et al., 1973, Nuismer, 1975]. The direction of crack propagation (θ_0) can be determined by:

$$\begin{cases} \left(\frac{dG}{d\theta}\right)_{\theta=\theta_0} = 0 \\ \\ \left(\frac{d^2G}{d\theta^2}\right)_{\theta=\theta_0} \leq 0 \end{cases} \tag{1.24}$$

For the computation of G (energy release rate) many techniques are available in the literature, e.g., real crack extension [Watwood, 1970], J-integral [Rice, 1968b], virtual crack extension [Parks, 1974, Hellen, 1975], analytical expression [DeLorenzi, 1982, Delorenzi, 1985] and the $G\theta$ method [Destuynder et al., 1983]. In this work, for the computation of the energy release rate (G), the numerical technique known as $G\theta$ method [Destuynder et al., 1983] will be used. This technique was chosen because it is very accurate and completely mesh independent [Bouchard et al., 2003]. Additionally, its implementation is quite simple and multiple extensions such as the addition of external forces, loads applied to the crack lips as well as the addition of thermal strain (which is highly important in this work) are available.

Gθ method

The $G\theta$ method is a Lagrangian approach proposed by [Destuynder et al., 1983] for calculating the energy release rate. In this method, an infinitesimally small geometrical perturbation of a body (i.e., crack length increment) is introduced in order to computed G. Figure 1.11 shows a homogeneous isotropic linearly elastic body Ω that is subjected to the following prescribed loads: (i) surface tractions f_i applied on a portion Γ of body's boundary ($\partial\Omega$), (ii) body forces F_i and (iii) thermal loads ΔT.

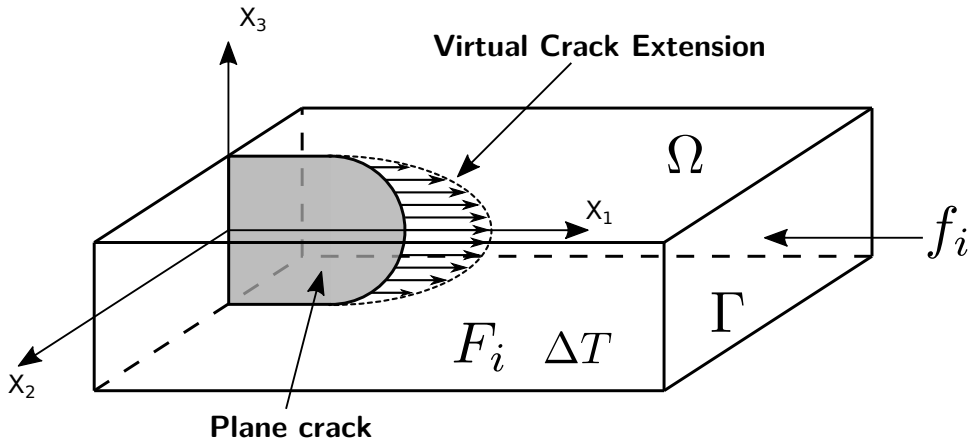

Figure 1.11: Virtual kinematics in the cracked solid Ω.

The $G\theta$ method allows to compute the energy release rate using all virtual and kinematically admissible displacement fields at the crack tip neighborhood. When V_i is defined as any kinematically admissible displacement field (KADF), it follows that the stress tensor σ_{ij} and the displacement field U_i in the loaded state are unique solutions of the following variational equations:

$$\sigma_{ij} = C_{ijkl}\left[\frac{1}{2}\left(U_{k,l} + U_{l,k}\right) - \ \alpha\ \Delta T\ \delta_{kl}\right] \tag{1.25}$$

$$\int_\Omega \sigma_{ij} V_{j,i}\ d\Omega = \int_\Gamma f_i V_i d\Gamma + \int_\Omega F_i V_i\ d\Omega, \qquad \forall V_i \in KADF \tag{1.26}$$

and in equilibrium the total potential energy W_p is given by:

$$W_p = -\frac{1}{2}\int_\Omega \sigma_{ij} U_{j,i}\ d\Omega - \frac{1}{2}\int_\Omega \sigma_{ii}\ \alpha\ \Delta T\ d\Omega \tag{1.27}$$

where C_{ijkl} is the fourth-order elastic constitutive tensor, $U_{i,j}$ is the gradient of the displacement field, $V_{i,j}$ is the gradient of the virtual displacement field, α is the thermal expansion coefficient and ΔT is the temperature difference between the current state and the reference configuration, the latter one being the temperature where there is no strain and δ_{ij} is the Kronecker delta. To determine the variation of the total potential energy in the cracked solid Ω shown in (1.27), $\mathcal{Q}^\eta$ is defined as an arbitrary infinitesimal geometrical perturbation (η) in the vicinity of the crack tip in Ω with no change in its boundary (i.e., no change in the external surface tractions f_i):

$$\mathcal{Q}^\eta(M_i) = M_i^\eta = M_i + \eta V_i(M_i) \tag{1.28}$$

where the virtual field V_i gives the location of each point of the perturbated solid using its initial position (M_i) before the perturbation. For the sake of clarity, we assumed that after this domain perturbation all physical quantities are designated with a superscript η. Thus, Ω^η is the body in the perturbed state, and, if M_i is the position vector of a point in Ω, M_i^η is the same point in the body Ω^η. Following this convention, F_i^η and ΔT^η are the body forces and temperature change in Ω^η and σ_{ij}^η and U_i^η are respectively, the stress and displacement fields defined by the following equations:

$$\sigma_{ij}^\eta = C_{ijkl}\left[\frac{1}{2}\left(\frac{\partial U_l^\eta}{\partial M_k^\eta} + \frac{\partial U_k^\eta}{\partial M_l^\eta}\right) - \ \alpha\ \Delta T^\eta\ \delta_{kl}\right] \tag{1.29}$$

$$\int_{\Omega^\eta} \sigma_{ij}^\eta \frac{\partial V_j}{\partial M_i^\eta}\ d\Omega^\eta = \int_\Gamma f_i V_i d\Gamma + \int_{\Omega^\eta} F_i^\eta V_i\ d\Omega^\eta, \qquad \forall V_i \in KADF \tag{1.30}$$

As η is defined as an arbitrary infinitesimal geometrical perturbation in the vicinity of the crack tip in Ω with no change in its boundary (Γ), the external surface tractions f_i do not change. The total potential energy (W_p^η) of the body Ω^η is given by:

$$W_p^\eta = -\frac{1}{2}\int_{\Omega^\eta} \sigma_{ij}^\eta \frac{\partial U_j^\eta}{\partial M_i^\eta}\, d\Omega^\eta - \frac{1}{2}\int_{\Omega^\eta} \sigma_{ii}^\eta\ \alpha\ \Delta T^\eta\ d\Omega^\eta \tag{1.31}$$

where $\frac{\partial}{\partial M_i^\eta}$ is the gradient operator with respect to the coordinates of point M_i^η. In this work, the elasticity tensor (C_{ijkl}) as well as the thermal expansion coefficient (α) are kept unchanged during the configuration transformation. When the perturbation η is sufficiently small, [Destuynder et al., 1983] showed that the stress field (σ_{ij}) and the displacement field (U_i) on the perturbed configuration may be expressed as:

$$\begin{aligned} \sigma_{ij}^\eta &= \sigma_{ij} + \eta\sigma_{ij}^1 \\ U_i^\eta &= U_i + \eta U_i^1 \end{aligned} \tag{1.32}$$

where σ_{ij}^1 and U_i^1 are the first order variations of the stress and displacement fields during the infinitesimal perturbation η on Ω. As the perturbation is infinitesimal, derivatives and integrals on the perturbed body can be expressed using a first-order limited development in function of the same operations on the unperturbed body:

$$\begin{aligned} \frac{\partial(\ .\ )}{\partial M_j^\eta} &= \frac{\partial(\ .\ )}{\partial x_j}\left(\delta_{ij} - \eta\frac{\partial V_i}{\partial x_j}\right) \\ \int_{\Omega^\eta}(\ .\ )\, d\Omega^\eta &= \int_\Omega(\ .\ )\left(1 + \eta\frac{\partial V_i}{\partial x_i}\right)\, d\Omega \end{aligned} \tag{1.33}$$

Using equation (1.33), all the physical quantities like the stress (σ_{ij}^η), the displacement (U_i^η) and the total potential energy (W_p^η) in the perturbed configuration Ω^η can be translated into the unperturbed configuration Ω (See details in [Destuynder et al., 1983, Suo and Combescure, 1992b]). For example, let W_p^t be the image of W_p^η in the unperturbed configuration Ω, it follows that the variation of the total potential energy due to a small perturbation η in the body's geometry is given by:

$$\frac{\partial W_p}{\partial \eta} = \lim_{\eta\to 0}\frac{W_p^t - W_p}{\eta} \tag{1.34}$$

Due to the fact that the strain energy release rate (G) is the decrease in the total potential energy (w_p) during a growth of crack area (dA):

$$G = \frac{dW_p}{da} = \lim_{\eta\to 0}\frac{W_p^t - W_p}{\eta} \tag{1.35}$$

We have that G under the presence of body forces (F_i) and thermal loads (ΔT) may be expressed as:

$$\begin{aligned} G = \int_\Omega \sigma_{ij}U_{j,k}V_{k,i}\ d\Omega - \frac{1}{2}\int_\Omega \sigma_{ij}\left(U_{j,i} - \alpha\Delta T\delta_{ij}\right)V_{k,k}\ d\Omega \\ + \int_\Omega \sigma_{ii}\alpha T_{,j}V_j\ d\Omega - \int_\Omega F_i U_{j,i}V_j\ d\Omega \end{aligned} \tag{1.36}$$

where $U_{i,j}$ is the gradient of the displacement field, V_i is the virtual displacement field, $V_{i,j}$ is the gradient of the virtual displacement field, $V_{i,i}$ is the divergence of the virtual displacement field, α is the thermal expansion coefficient, ΔT ($\Delta T = T - T_{ref}$) is the temperature difference between the current state and the reference configuration and $T_{,j}$ is the gradient of the temperature. The virtual displacement field V_i representing the virtual kinematics of the crack has the following properties:

- V_i is parallel to the crack plane.
- V_i is normal to the crack front.
- The support of V_i is only needed in the vicinity of the crack.
- $\|V_i\|$ is constant in a defined region around the crack tip.

Readers interested in further details regarding mathematical formulation of the $G\theta$ method can refer to [Destuynder et al., 1983, Suo, 1990, Suo and Combescure, 1992b, Suo and Combescure, 1993].

After introducing important fracture mechanics concepts, some crucial remarks must be stated. It is worth mentioning that the available finite element framework at CEMEF ($P1^+/P1$), which will be detailed in Chapter 2 is not good enough at capturing the singularity of the stress field at the crack tip. To confidently use a local approach when applying both crack propagation and crack kinking criteria, it would be necessary to use either a huge mesh refinement or to implement quarter-point elements, thus requiring quadratic elements. Without those strategies, the use of an energetic or global approach may be more appropriate. The current PhD will therefore tackle crack propagation problems following an energetic approach. Additionally, and taking into account that fracture processes driven by thermal effects is one of the settled goals in this work, crack propagation direction will be computed through an energetic approach (MERRC). Energy release rate (G) will be computed using the $G\theta$ method, which was chosen because its implementation is quite simple and multiple extensions like the addition of thermal strain are available.

It should be also mentioned that due to the fact that systematic fatigue crack growth experiments on solar system small bodies (i.e., asteroids or meteorites) have not been conducted, there is a lack of information regarding fatigue crack growth on these materials. The latter makes difficult to have asteroid or meteorite materials properties. For this reason, among all the presented fatigue crack growth models, Paris' law was considered to be the most suitable model to simulate fatigue crack growth. Due to the fact that there is not much information about the material, it does not have sense to try to use a more complex law which would require more input data about the behavior of the material when subjected to fatigue. In order to define the value of the material's properties required for using Paris' law (C, n) a review of the literature was carried out. It was found that fatigue crack growth data obtained from experiments performed by [Delbo et al., 2014] on two meteorites (carbonaceous chondrite and ordinary chondrite) were satisfactorily predicted using the physical parameters computed in Carrara marble by [Migliazza et al., 2011].

Next step in this work is to review the most remarkable crack propagation numerical methodologies available in the literature. This literature review will help choosing the most suitable numerical technique for this PhD work.

1.3 Numerical methods for crack propagation

When crack propagation takes place, it is desirable to have an extremely accurate stress state close to the crack tip to apply a failure criterion safely and correctly. As it was already stated, fracture process can be decomposed into two steps: crack initiation and crack propagation. The former one is essential but not easy. When aiming at describing this process for a body without initial pre-crack, damage-based numerical models should be used. These models study the evolution of damage in a continuous way, and at a critical damage value the crack is initiated, being the result of a nucleation process [Alessi et al., 2015, Marigo et al., 2016, Tanné et al., 2018]. For crack initation, several criteria have been proposed in the literature. Generally,

these criteria depend on the materials studied. Some of them are based on critical values for mechanical state variables (stress or strain) [Bouchard et al., 2003]. The simulation of crack initiation process is outside of the scope of this work, for this reason, it is not detailed here, and the efforts are oriented to study the evolution of a pre-existing crack.

When a pre-existing crack is assumed, its propagation introduces a discontinuity in the sense of displacements. Dealing with this discontinuity in a finite element mesh is fundamental in fracture mechanics and different methodologies are available in the literature. These methodologies are based on either continuous or discontinuous approaches (e.g., damage-based models, Multiscale Methods, Enriched Finite Element Methods, remeshing techniques). The present work is focused on the latter, in the case where crack propagation is considered as a displacement discontinuity. Among the discontinuous approaches group, different numerical techniques that use or not, remeshing operations when simulating crack propagation can be found. In the following, the most common crack propagation methodologies available in the literature will be briefly described.

1.3.1 Element erosion

Element erosion is perhaps the simplest way to take into account discontinuities in finite element (FE) simulations due to its low computational cost and its straightforward implementation. Discontinuities in a FE simulation are dynamically introduced by removing elements from the FE mesh and/or the associated contributions from the FE formulation based on an appropriate fracture criterion. Element erosion approach is also known as element removal, element deletion or kill element. In this approach some elements are generally removed once their load carrying capacity has been eroded over several load increments in order to avoid convergence problems [Wulf et al., 1996].

For example in the work of [Wulf et al., 1993], when one element fulfills any given failure criterion, it is not erased from the finite element data base, but the stresses in that element become zero. When this happens, there is no more physical relevance of the element. Thus, no more forces will be carried by the element as well as no more contribution to further build-up of stresses will take place. However, it is worth mentioning that there are people that really remove the element from the FE simulation. Figure 1.12 shows the elimination of elements at two different times. The final crack path (shadow red elements) is a straight line without branching [Song et al., 2008]. Even though its implementation is quite simple, this method also presents several limitations, such as volume loss and mesh size and element shape sensitivity issues [Shakoor et al., 2018].

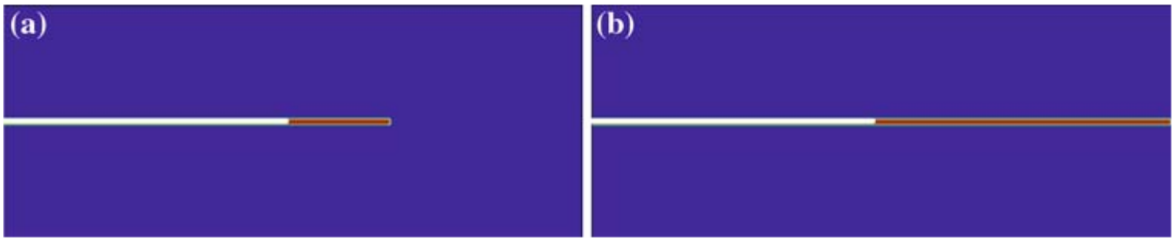

Figure 1.12: 2D crack propagation using element deletion at different time steps. Eliminated elements are shaded in red. Figure reproduced from [Song et al., 2008].

1.3.2 Element-free Galerkin (EFG) methods

The element-free Galerkin method is an interesting methodology developed by [Belytschko et al., 1994a]. It belongs to the group of approaches that work without any remeshing operations.

This method only needs nodal information and boundary descriptions. Thus, the finite element mesh is totally unnecessary. To construct the trial and test functions for the weak form of the problem, moving least-squares interpolants (MLS) are used; throughout the whole domain, dependent variable and its gradient are continuous. To obtain the value of displacements at any point, a set of linear equations should be solved. The number of nodes that influence the approximation at the point determines the size of the system that needs to be solved. In EFG method, the essential boundary condition is enforced through the use of Lagrange multipliers. According to [Belytschko et al., 1994a], EFG does not exhibit any volumetric locking and it appears to be very effective for fracture problems. Simulation of progressively evolving cracks can be simply achieved just by moving the fine mesh of nodes through the rest of the mesh, which is quite simple task because element connectivities do not need to be developed.

Figure 1.13 shows a schematic repesentation of 2D crack propagation using the EFG method. It is worth mentioning that the schematic arrangement of nodes presented in this figure, do not have the usual finite element method connectivity. Indeed, nodal arrangement can be arbitrary, although the local accuracy is influenced by the arrangement.

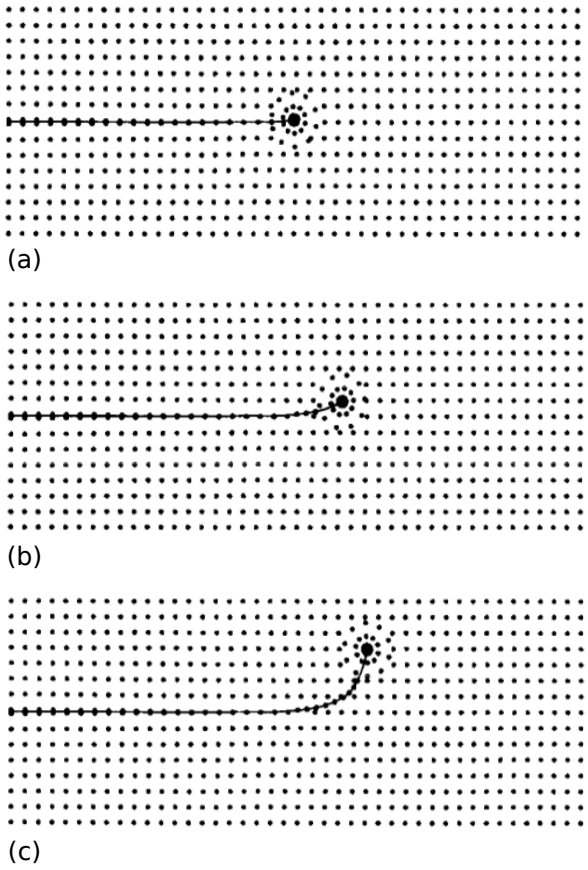

Figure 1.13: 2D crack propagation using EFG method. While crack propagation takes place, at the crack tip, unconnected array of nodal points is adjusted. Figure reproduced from [Belytschko et al., 1996].

EFG method has proved to be well suited when modelling crack propagation in 2D [Belytschko et al., 1994b] and 3D [Krysl and Belytschko, 1999] because the incorporation into the model of the arbitrary surfaces across which the displacement function is discontinuous is straightforward. When there is a crack, it only affects how the nodes influence the displacement at a given point. In this method, when evaluating the displacement in one point, any node that is not visible from this point is omitted (visibility criterion). A straightforward implementation of this criterion results in some interior discontinuities around the crack tip. One of the main

drawbacks of this method is that the boundary conditions are difficult to impose [Ingraffea and de Borst, 2017]. Another drawback of the method is its high computational effort. As it uses MLS, to obtain the displacements at each spatial point a set of linear equations must be solved. Also MLS approximation sometimes causes ill-conditioned equations [Lu et al., 1995, Hegen, 1997, Meng et al., 2019].

1.3.3 Arbitrary Local Mesh Replacement method (ALMR)

Inside the group of the techniques that do not use mesh adaption, there is another approach called Arbitrary Local Mesh Replacement method. Introduced by [Rashid, 1998], the main idea of this method relies on the fact that in the vicinity of the crack tip, the finite element interpolant is replaced by one that is derived from a moving mesh patch. The boundary of this patch is not required to be coincident with the edges of the elements in the background-mesh. The ALMR is a finite-element-based strategy that uses two different meshes: one surrounding the domain close to the crack tip and that moves with it, and an other one that describes the entire domain. In order to solve the crack propagation problem with the ALMR method, first, the body without the crack is discretized into finite elements (background mesh). Then, the crack is represented by the new-free-surface curve (NFS curve). This curve is defined arbitrarily and independently of the background mesh, taking typically, the form of a sequence of line segment as shown in Figure 1.14. This figure also presents the patch mesh, which, in two dimensions, is a circular disk composed of annular rings of elements. Patch mesh is centered at the crack tip and moves with it as the crack propagates, but without suffering distortion. In this method, additional degrees of freedom and a special treatment of partial elements near the patch boundary are required. A disadvantage of the ALMR method is that it requires the superposition of two meshes and, therefore, if the number of cracks increases, then the number of needed meshes also increases. The latter makes more difficult managing automatically the propagation of each crack [Bouchard et al., 2000].

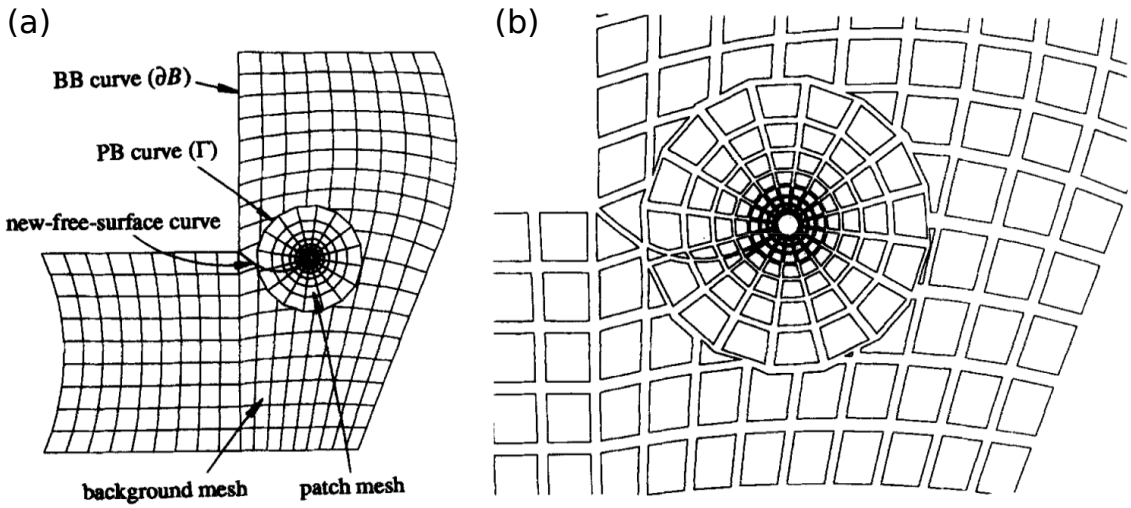

Figure 1.14: a) Representation of a typical finite-element discretization when using the ALMR method. b) Detail of the patch mesh. Figure reproduced from [Rashid, 1998].

1.3.4 Enriched finite element methods

Inside the same group of methodologies that do not perform remeshing in order to propagate a crack, a family of enriched FE methods have been developed. These methods have been widely detailed in the literature [Jirásek, 2000, Oliver et al., 2006, Fries and Belytschko, 2010].

Among these method one can find the Strong Discontinuity Approach (SDA) [Simo et al., 1993, Garikipati, 1996, Oliver and Huespe, 2004], the Extended Finite Element Method (XFEM) [Belytschko and Black, 1999, Moës et al., 1999] and the Generalized Finite Element Method (GFEM) [Duarte and Oden, 1996, Melenk and Babuška, 1996, Melenk, 1995]. When tackling crack propagation problems, a well-known advantage of enriched methods, is the fact that discontinuities might be modeled completely independent of the morphology of the finite element mesh [Belytschko et al., 2009, Shakoor et al., 2018].

As it was already stated, the present of a crack introduces discontinuities, which can be characterized as jumps in the displacement field across the material. Those jumps are termed as strong discontinuities. In the Strong Discontinuity Approach (SDA) [Simo et al., 1993, Garikipati, 1996, Oliver and Huespe, 2004], the displacement jumps due to the presence of the crack are embedded locally in each cracked finite element without affecting neighbouring elements. The SDA bridge both continuous and discrete approaches in order to simulate material failure. In this method, additional degrees of freedom must be added to the finite element model.

According to [Belytschko et al., 2009] the XFEM and GFEM are basically identical methods based on the partition of unity concept [Melenk and Babuška, 1996]. The difference on their names relies on the fact that Texas school adopted the name generalized finite element method (GFEM) in 1995–1996, while in 1999 the Northwestern school coined the name extended finite element method (XFEM). The most famous method among XFEM and GFEM is the well-known Extended Finite Element Method (XFEM). In these methods the displacement-based approximation is enriched near a crack by incorporating both discontinuous and near tip asymptotic fields. Figure 1.15 shows two different enriching strategies near the crack tip presented in [Belytschko and Black, 1999].

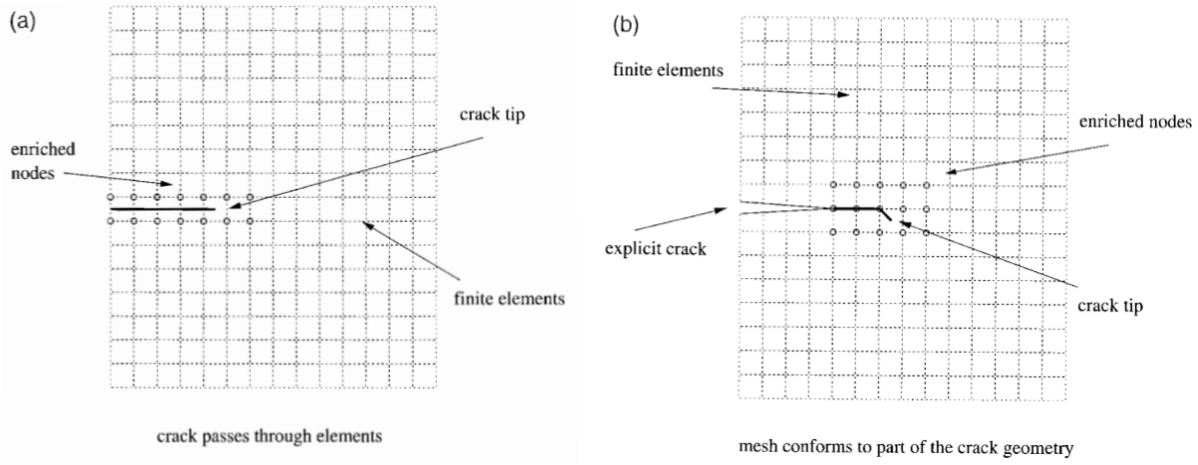

Figure 1.15: Enriching strategies near the crack tip: a) The crack passes through the cells and all the nodes surrounding the whole crack are enriched. b) Part of the crack is explicitly modelled by the mesh. Nodes near the crack tip including the portion of the crack that is not explicitly modelled, are enriched. Figure reproduced from [Belytschko and Black, 1999].

Most of the application involving enriched FE methods have been dedicated to simulate the fracture process in brittle materials. As a disadvantage of such approaches, is the fact that some burdensome modifications to the finite element code are required [Rabczuk et al., 2010]. Furthermore, this formulation might not be suitable in the case of large strain loadings. Actually there are some extensions for ductile fracture but for limited plasticity so that not remeshing is required.

1.3.5 Cohesive zone models (CZMs)

Another common alternative without mesh adaption is the family of cohesive zone models (CZMs) [Barenblatt, 1962, Rice, 1968b]. This approach was developed in order to model the energy dissipation rate, an issue not tackled by the aforementioned methods. Through CZMs the fracture process is modelled as the transition from a sound material to a fully broken one. The physics of the fracture process at the atomic scale is represented through the use of CZMs that also remove crack tip singularity. When using CZMs, fracture process is treated like a gradual phenomenon in which material separation across an extended crack tip region (cohesive zone) takes place. This separation is withstood by cohesive forces. The constitutive behavior of crack opening is governed by a cohesive traction-separation law while the behavior of surrounding material is dictated by the bulk stress-strain relation [Jiang, 2010]. CZMs are independent from the mechanical behavior of the bulk material, the extent of the cracks and the size of the plastic zone [Ortiz and Pandolfi, 1999]. They also offer other advantages, such as straightforward implementation inside conventional finite element codes.

When using cohesive elements (CZMs), a common issue is that an artificial reduction of the stiffness of the material can be induced. This is due to the fact that, in most traction-separation laws, there is an initial region where the traction increases monotonically from zero up to a maximum value. This increase can be linear or not depending on the traction-separation law used. When the traction level increases as a function of the opening displacement, an artificial stiffness that modifies the macroscopic response of the material is introduced into the system [Tomar et al., 2004, Blal et al., 2012]. This problem can be solved through the introduction of Lagrange multipliers in such a way that the opening of the element is only allowed once a critical traction is achieved [Lorentz, 2008]. This solution has the disadvantage that it requires the modification of the finite element formulation. Commonly, cohesive zone models have been used to solve problems involving interfaces, surfaces undergoing decohesion or problems where the crack path is known a priori [Chaboche et al., 2001, Alfano et al., 2007, Turon et al., 2010]. In these cases, cohesive elements can be inserted in a limited zone (known crack path) in the finite element mesh, reducing, but not completely solving the problem regarding artificial reduction of the stiffness.

Figure 1.16 shows the mesh for a three-point bend test specimen when the potential crack path is known a priori [Ortiz and Pandolfi, 1999]. In this case, the mid-section of the specimen is tiled with cohesive elements. When the crack path is not known a priori, some authors use continuum damage theories in order to account explicitly for individual cracks as they nucleate, propagate, branch and possibly link up to form fragments. This is done allowing cracks to form and propagate along element boundaries in accordance with a cohesive-law model. In the work of [Camacho and Ortiz, 1996], when the cohesive model requires it, new surfaces are created through the duplication of existing nodes along previously coherent element boundaries. Figure 1.17 depicts the capabilities of the fracture model presented by [Camacho and Ortiz, 1996]. It should be noted that mesh dependency may appear as a consequence of the fact that cracks are only able to propagate across boundaries between bulk elements. Therefore, the crack path depends on the mesh.

1.3.6 Phase field model

One of the most recently developed methods, among techniques without remeshing, is the phase field model [Francfort and Marigo, 1998, Bourdin et al., 2000, Bourdin et al., 2008]. Even though this method in its core belongs to the continuous approaches, it is presented here because of its ability for simulating crack propagation mainly in brittle materials. In the phase field approach a new variable is included in the problem, the material level of degradation, better known as damage (d). This variable is a bounded scalar field taking values ranging from 0 to 1. When $d = 0$, the material is totally sound and when $d = 1$, the material is fully damaged [Alessi

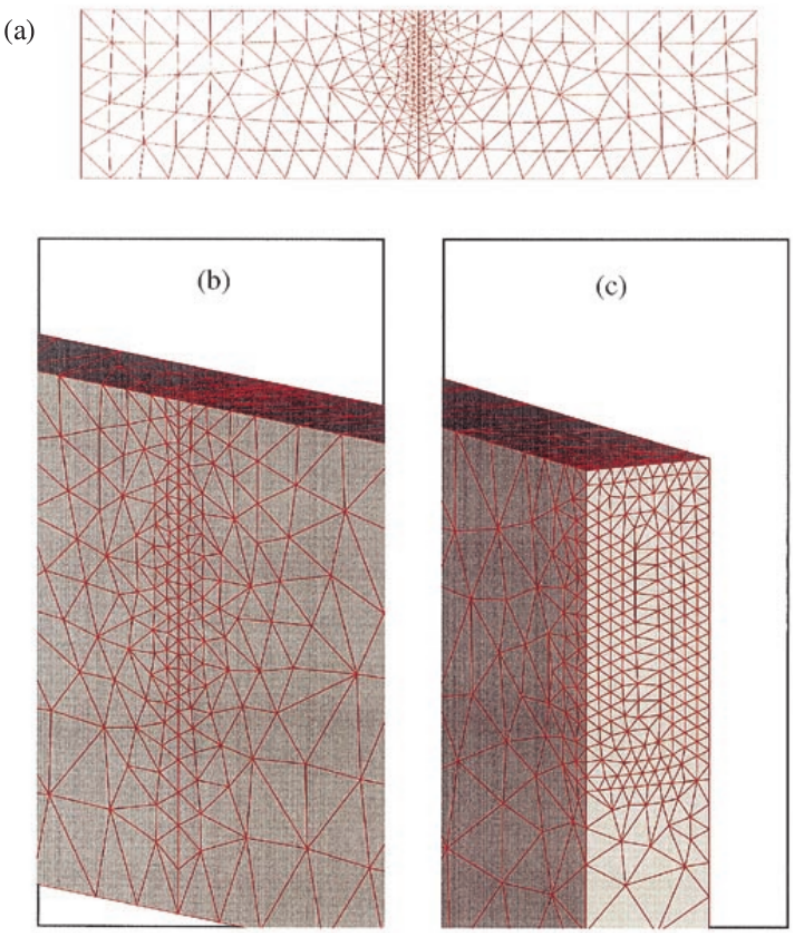

Figure 1.16: Computational mesh for a three-point bend test specimen. The mesh is composed of 8084 nodes, 4410 tetrahedra and 768 cohesive elements. Figure reproduced from [Ortiz and Pandolfi, 1999].

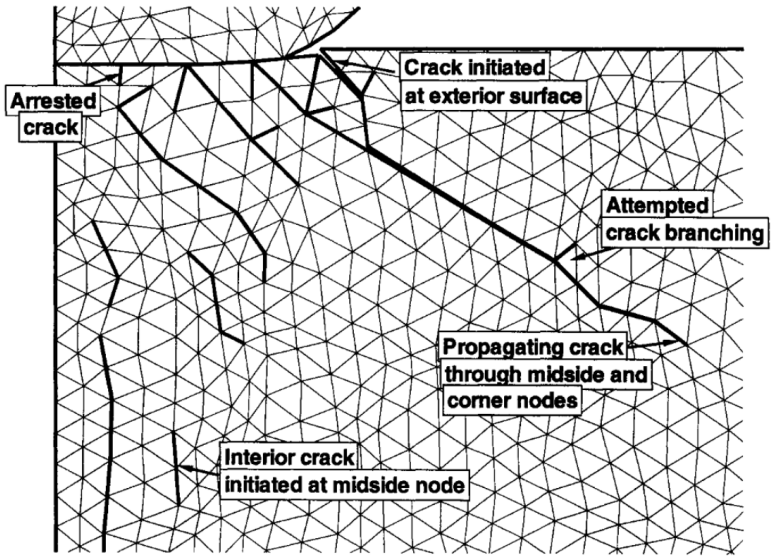

Figure 1.17: Capabilities of the fracture model presented by [Camacho and Ortiz, 1996]: crack initiation at surfaces and in the interior, crack propagation, branching and arrest. Figure reproduced from [Camacho and Ortiz, 1996].

et al., 2018]. Phase field model, introduced by [Francfort and Marigo, 1998], is a variational approach to quasi-static brittle fracture that allows to simulate complex crack topologies as well as crack initiation and propagation together with other phenomenan like coalescence and branching. Phase field model does not require any additional ad-hoc criteria [Kuhn and Müller, 2010, Nguyen et al., 2015]. It is worth mentioning that phase field approach is conceptually very close to non-local damage models.

Phase field approach is a numerical technique to deal with discontinuities based on energy minimization principles. From a mathematical point of view, this method is based on the minimization of total energy with respect to the crack geometry and the displacement field simultaneously [Kuhn and Müller, 2010, Borden et al., 2012, Zhou et al., 2018]. In this method there is a characteristic length scale (l_c) that smears out discontinuities in the interfaces, making the capturing of the interface easier to handle. In the original approach presented by [Bourdin et al., 2008], the peak force reached before the onset of fracture depends on the value of the characteristic length scale (l_c). According to this, higher values of l_c produce lower peak forces and viceversa [Egger et al., 2019]. The phase field method has the notable advantage of avoiding explicit front tracking by making material interfaces spatially diffuse. Another remarkable advantage is its straightforward implementation. Care must be taken when enforcing the irreversibility of the process in order to avoid decreasing of the damage variable d. Figure 1.18 illustrates the 2D crack propagation of the well-known symmetric three point bending test using the phase field method. In this figure, the blue color corresponds to the undamaged material, while the red color represents the fully cracked material [Miehe et al., 2010]. Recently, the phase field method has been successfully used to model the ductile fracture at large scale plastic strains using adaptive isotropic remeshing [Eldahshan et al., 2021].

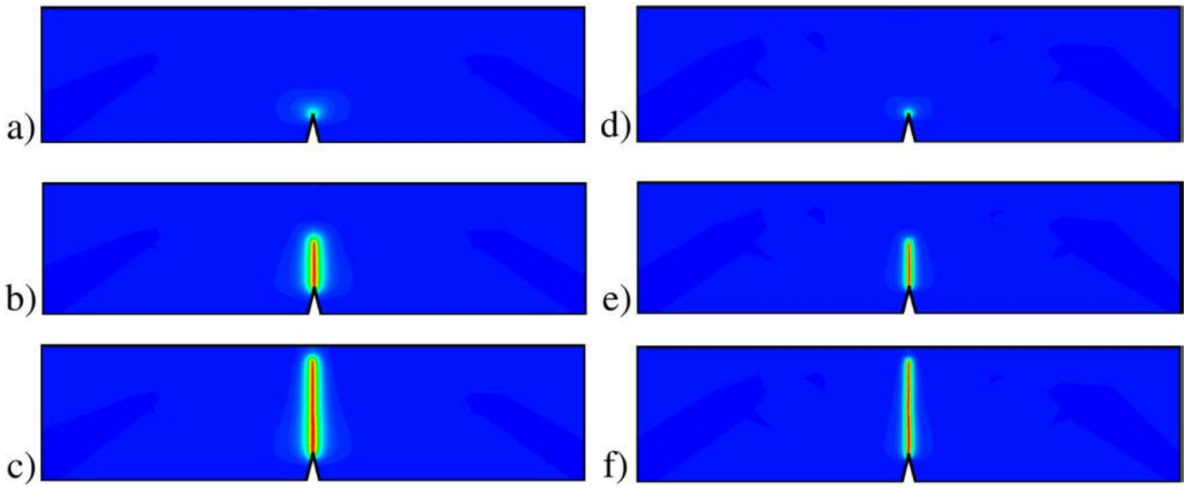

Figure 1.18: Crack path for the symmetric three point bending test at different time steps for two length scales. $l_1 = 0.06\ mm$ for a), b) and c). $l_2 = 0.03\ mm$ for d), e) and f). Figure reproduced from [Miehe et al., 2010].

Even though phase field approach has several advantages, it also presents some limitations which do not seem to be obvious. Due to the fact that isotropic stiffness degradation is assumed by a scalar phase field parameter, the anisotropy that is introduced by a crack is not captured (mesh orientation dependency). In some cases, the phase field approach overestimates the surface energy of a crack (e.g., short cracks and crack initiation). Another drawback of the phase field model is its parameter sensitivity (e.g., length scale) [Strobl and Seelig, 2018, Dally et al., 2020].

1.3.7 Mesh adaption strategies

Mesh adaption is a very natural and efficient way of handling displacement discontinuity as well as crack propagation. Mesh adaption, mesh modification or remeshing operations are words referring to the same concept: they denote global or local adaptive mesh refinement or global or local remeshing without human intervention. Remeshing operations are quite a suitable tool in order to keep a good refinement at the crack tip as it evolves. This is really important due to the fact that crack propagation is highly affected by the mechanical fields in this zone [Bouchard et al., 2000, Coupez et al., 2013].

Several studies regarding crack propagation using remeshing operation can be found in the literature. Among them, it is worth mentioning the work done by [Bittencourt et al., 1996], where a quasi-automatic two-dimensional crack propagation strategy implemented in FRANC2D (FRacture ANalysis Code 2D) is presented. In this work through the use of an underlying winged-edge data structure, the mesh can be automatically modified along the propagation path avoiding the losing of unaffected structural information. In this work crack propagation is driven by linear elastic fracture mechanics theory, and after each propagation of the crack, the finite element mesh is locally regenerated. Another remarkable work is the one presented by [Carter et al., 2000], one of the pioneering works that attempted to model arbitrary non-planar crack growth in three-dimensional solid and shell structures inside the code FRANC3D. In this work the evolution of crack growth in a structure is represented using the computational geometry and topology. This approach is based on the sub-modelling technique, i.e., a global FE mesh containing the crack is created, as well as a more refined sub-model near the crack, which is used to extend the crack [Branco et al., 2015].

Another remarkable technique belonging to the approaches using remeshing operations, is the procedure proposed by [Bouchard et al., 2003]. In this work, through the use of an advanced remeshing technique combined with nodal relaxation, propagation of the crack is achieved. The stress singularity at the crack tip was represented using mid-side nodes (quarter point elements). Figure 1.19 shows a multiple cracks propagation, where the effect of each crack on the propagation of the other one can be observed [Bouchard et al., 2000].

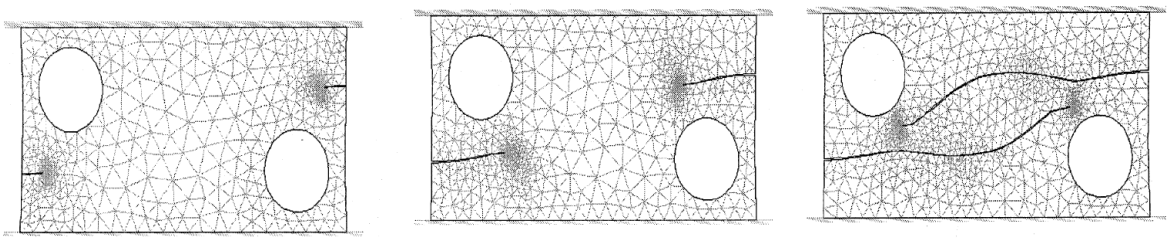

Figure 1.19: Propagation of two cracks in a planar domain with two holes. Figure reproduced from [Bouchard et al., 2000].

It is also worth mentioning the work done by [Ooi et al., 2013] where an efficient methodology for automatic crack propagation using scaled boundary polygon elements is developed. In this work the computational domain is discretized using arbitrary n-sided polygons which lead to flexible mesh generation. Crack growth is determined through the evaluation of generalised dynamic stress intensity factors using standard finite element stress recovery procedures. Finally, crack propagation is adjusted by a remeshing algorithm applicable to any polygon mesh. [Dai et al., 2015] also presented an automatic crack propagation remeshing procedure using the polygon scaled boundary finite element method. The remeshing algorithm presented in this work is simple but flexible because at each time step only minimal changes are performed to the global mesh. Figure 1.20 shows an example of crack propagation using scaled boundary polygon elements. An initial polygon mesh for a rectangular double cantilever beam (RDCB) is shown in Figure 1.20-a) while in Figure 1.20-b) the final polygon mesh after propagation took

place is presented .

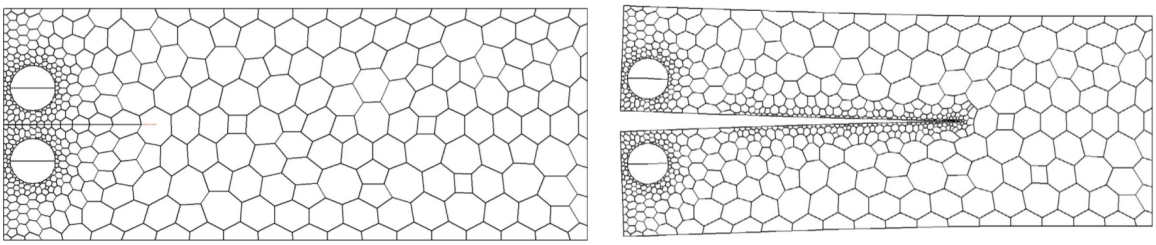

Figure 1.20: Rectangular double cantilever beam subjected to mode-I fracture: a) Initial polygon mesh and b) Final polygon mesh after some propagations. Figure reproduced from [Ooi et al., 2013].

Among the disadvantages of the mesh modification techniques, is should be mentioned that its implementation is difficult, as well as that its computational cost is high. Although challenging, they look to be quite appropriate for accurately modeling crack propagation when this phenomenon is decided to be treated as a discontinuity.

1.3.8 Cohesive zone models combined with remeshing operations

Another available approach in the literature to deal with crack propagation combines remeshing operations and cohesive zone models. Inside this group it is worth mentioning the work of [Pandolfi and Ortiz, 1998, Pandolfi and Ortiz, 2002]. In this work once the effective traction acting on interior faces initially perfectly coherent reaches the cohesive strength of the material, cohesive elements are inserted adaptively. The insertion of cohesive elements changes in this way the geometry of the boundary as well as sometimes the topology of the model. Figure 1.21 shows the dynamic fragmentation of a three-point bend PMMA (Polymethylmethacrylate) specimen. Initially, the specimen has an initial sharp precrack contained within its symmetry plane [Pandolfi and Ortiz, 2002].

It is also worth mentioning the work of [Geißler et al., 2010] where an adaptive insertion of cohesive elements takes place during the simulation, this insertion depends on an extrinsic crack initiation and propagation criterion. To tackle crack propagation through arbitrary directions, a mesh adaptive procedure is presented in this work. Crack propagation direction is predicted using stress-based and energy-based fracture criteria. Another interesting approach is the one developed by [Chiaruttini et al., 2012]. It presents an approach for the numerical simulation of crack propagation based on cohesive models, in the case of structures subjected to mixed mode loadings. In this work, the evolving crack path is remeshed as the crack propagates while special attention is paid to the fields transfer from the old mesh to the new one. Crack propagation direction is defined through the stress intensity factors with an integral computation that is carried out on the crack front. This work has been implemented in the finite element software Z-set that is jointly developed by Onera and Ecole des Mines. This approach is able to tackle arbitrary crack paths. Results obtained using the methodology proposed by [Chiaruttini et al., 2012] are shown in Figure 1.22. The evolution of the crack path on a modified CT specimen with a rigid steel inclusion in the central region is presented there.

Another recent strategy is presented by [Choi and Park, 2019], in which, through a novel stress recovery technique, a domain integral and an element splits remeshing procedure, an accurate crack path under mixed-mode as well as a mesh bias reduction are obtained. In this method, a virtual mesh around the crack tip is generated in order to get an accurate stress evaluation to compute the crack propagation direction through the maximum strain energy release rate. After this, continuum elements are split and cohesive elements are adaptively inserted.

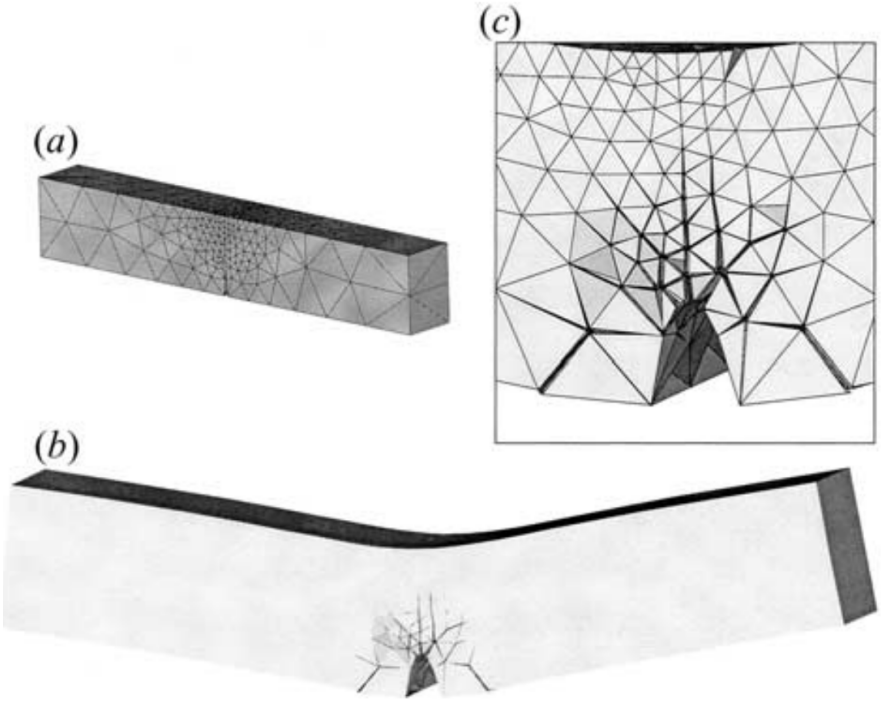

Figure 1.21: Fragmentation results of a three-point bend dynamic test in PMMA: a) initial mesh, b) final configuration and c) Detail of the fracture and fragmentation pattern in the final configuration. Figure reproduced from [Pandolfi and Ortiz, 2002].

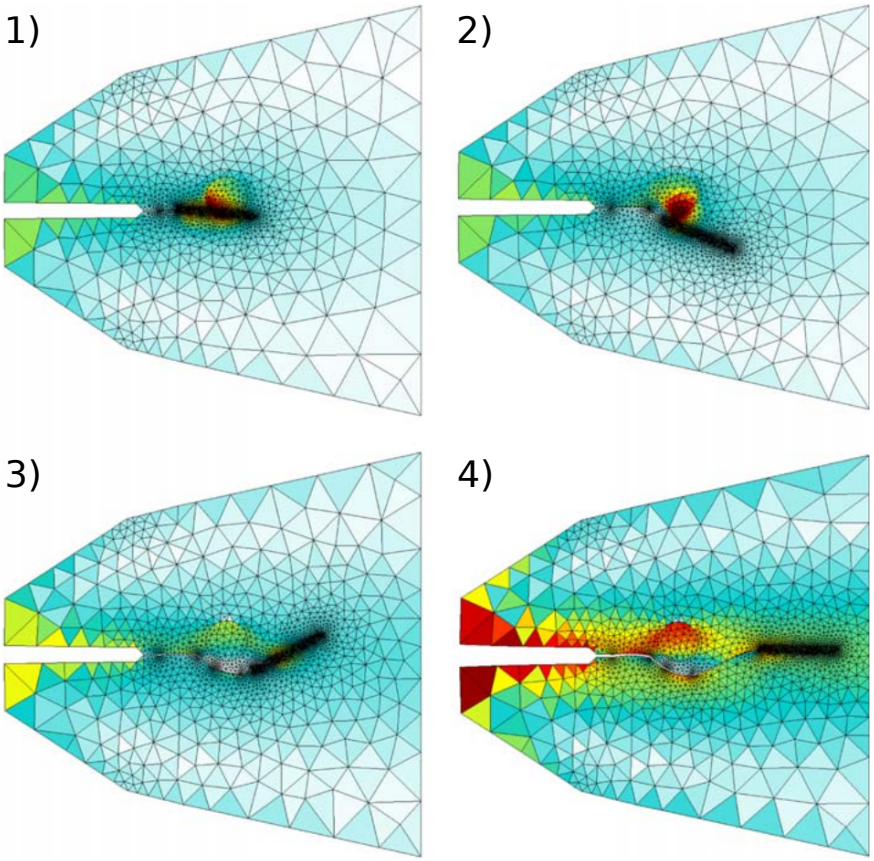

Figure 1.22: Crack path evolution using the adaptive cohesive zone modelling (von Mises isovalues). Figure reproduced from [Chiaruttini et al., 2012].

After describing the most common numerical methods for crack propagation available in the literature along with their advantages and disadvantages, some important remarks must be stated. Inside the presented approaches, most of them require deep modifications of the existing finite element code or even worse, starting an implementation from scratch. Taking into account that there are different methodologies already implemented (e.g., existing FE framework, remeshing strategies) that can be combined and complemented with other simple ones and easy to implement (e.g., cohesive zone models), the use of methodologies that require deep modifications and/or implementation from scratch was not worth it in the context of the present study.

On the one hand, advanced remeshing techniques have been tested and validated at CEMEF through different studies showing quite accurate and reliable results [Coupez et al., 2013, Shakoor et al., 2015, Shakoor et al., 2017]. On the other hand, cohesive zone models (CZMs) offer interesting advantages regarding fracture energy control and reasonable computational cost. In addition, the combination of the aforementioned remeshing capabilities with the insertion of cohesive elements on the fly, i.e., while the crack tip is propagating through the domain, avoids two well-known strong drawbacks of the CZMs: (i) artificial reduction of the stiffness of the material and (ii) the mesh dependency. Consequently, in this PhD, it was chosen to implement a useful and promising methodology, not only capable of addressing the problems defined in the scope of this thesis but also useful in other applications that require simulation of crack propagation (e.g., composites cracking).

Considering that the available finite element framework at CEMEF (See Chapter 2) has some limitations at capturing the singularity of the stress field at the crack tip, in the current PhD, crack propagation problems will be tackled following an energetic approach. Following the premise of avoiding burdensome modifications inside the finite element code, I consider that the most suitable strategy to simulate crack propagation should be based on the methodologies that combined cohesive zone models with remeshing operations.

The next chapter details the implementations that were carried out inside Cimlib to develop the desired methodology.

1.4 Summary of Chapter 1

This first chapter is dedicated to the bibliographical background used as a base for the present work. The first section reviewed basic notions on solar system small bodies. This section also discussed how the fracture phenomena on airless bodies of our solar system have been studied, especially when this phenomenon is thought to be the result of temperature gradients due to the day and night cycles. Taking into account that propagation mechanisms in the case of space objects are still poorly understood, the lacking of a model allowing the simulation of crack propagation direction became evident. Asteroid (101955) Bennu will be considered for application purposes. The reason is that very high spatial resolution observations obtained by NASA's OSIRIS-REx mission are available for Bennu. Therefore, reported observational evidence [Delbo et al., 2019] will be very useful to validate the numerical results obtained with our developed coupled thermoelastic model with the linear elastic fracture mechanics approach presented in Chapter 2.

In the second section a theoretical review on fracture mechanics was given. The two common approaches (i.e., stress intensity factor, energetic) used to perform fracture analyses were explained. Second section also reviewed crack growth criteria. Two notable strategies used to compute crack propagation direction were described: The Maximal Circumferential Stress Criterion (MCSC) and the Maximum Energy Release Rate criterion (MERRC). The choice of the appropriate criterion must consider the accuracy of the computation of either the stress intensity factors or the strain energy release rate [Bouchard et al., 2003]. Fatigue crack growth models were also presented in order to attempt to describe fracture process under fatigue loading.

Finally, the third section reviewed the most common crack propagation strategies available in the literature when dealing with propagation of cracks through a finite element mesh. Among all the presented techniques, the simplest in terms of implementation inside an existing finite element framework is the cohesive zone model approach. Nevertheless, most CZMs approaches suffer from crack-path mesh dependency [Shakoor et al., 2018]. This drawback can be overcome by using another technique that has proved to be well suited when modeling crack propagation: mesh modification strategies. Regarding this point, the remeshing capabilities available at CEMEF can be extensively exploited.

The drawbacks that arise from combining cohesive zone models together with remeshing operations will be handled in Chapter 2. This chapter will show that the presented work can handle crack propagation through arbitrary direction using remeshing operations together with the dynamic insertion of cohesive elements in a mesh-independent way.

1.5 Résumé en français

Ce premier chapitre synthétise les informations essentielles recueillies dans la littérature pour positionner ce travail. La première partie passe en revue les notions de base relatives aux petits corps célestes du système solaire. Elle comprend également une discussion sur les précédentes études des phénomènes de rupture de corps célestes de notre système solaire. Elle s'attarde sur les études attribuant l'origine de ces mécanismes aux variations cycliques de température liées aux alternances jour-nuit. Etant donné que les mécanismes de propagation de fissures dans ce type d'objets restent méconnus, aucun modèle de ce type de phénomène n'a encore été proposé. L'astéroide Bennu (101955) est pris comme exemple de référence. Il a été choisi car des données de très haute résolution spatiale obtenues lors de la mission de la NASA OSIRIS-REx sont disponibles. Ces observations nous permettront [Delbo et al., 2019] de valider le modèle numérique de mécanique de la rupture, développé dans le cadre de ce doctorat et présenté dans le chapitre 2.

La deuxième partie définit les notions essentielles de la mécanique linéaire de la rupture. Les deux approches communes (énergétiques et basées sur le facteur d'intensité des contraintes) utilisées pour analyser la cinétique d'une fissure sont décrites. Ensuite, deux stratégies sont utilisées pour calculer la direction de propagation de la fissure: le critère de la contrainte circonférentielle maximale et le critère du taux de restitution d'énergie maximal. Le choix entre l'une de ces deux méthodes doit être fait en considérant la précision de calcul des fautes d'intensité des contraintes ou de la taux de restitution d'énergie. Des modèles de propagation de fissures liés à des mécanismes de fatigue sont aussi présentés afin de décrire comment le phénomène de rupture peut avoir lieu dans ces conditions.

Finalement, la troisième section décrit les stratégies de propagation de fissures les plus couramments utilisées dans la littérature pour étudier la rupture en utilisant une méthode éléments finis. Parmi toutes les techniques présentées, la plus simple en matière d'implémentation dans un contexte éléments finis est certainement le modèle à zones cohésives, et ce bien que la plupart des approches à zones cohésives pâtissent d'une dépendance au maillage [Shakoor et al., 2018]. En tirant parti des techniques de remaillage disponibles au CEMEF pour modifier le maillage et insérer dynamiquement des éléments, ce type d'approche représente une solution viable pour étudier la propagation de fissure. Le principal défi de combiner un modèle à zone cohésive avec un modèle éléments finis utilisant des stratégies de remaillage sera détaillé dans le chapitre 2. Le travail présenté permet d'illustrer que l'utilisation d'opérations de remaillage couplées à l'insertion d'éléments cohésifs permet une étude du problème et ce, indépendamment du maillage.

Chapter 2

FE framework for crack propagation

Contents

As already said in the Context, the current PhD thesis has two main objectives. First, it aims at modelling crack propagation through a finite element mesh for arbitrary crack paths using advanced remeshing techniques and dynamic insertion of cohesive elements. The second goal is to numerically reproduce some observed fractures on asteroids, which are thought to have been induced by large amount of diurnal thermal cycles. In order to accomplish these goals, the mechanical problem describing the fracture phenomenon driven by loading of both mechanical and thermal nature should be solved.

As presented in Chapter 1, the finite element (FE) method has proved to be very well suited for fracture mechanics problems. The present chapter details the existing finite element formulation, as well as all the implementations that were carried out in order to develop a crack propagation methodology. Section 2.1 presents the equilibrium equations along with the boundary conditions of the mechanical problem. The weak formulation of this problem in which velocity and pressure are the unknowns is presented in section 2.2. An implicit finite element (FE) formulation is used to solve these weak-form equations. In this implicit approach, at each time increment, a global system of equations should be solved in order to find the unknowns at each node of the FE mesh that ensure the equilibrium state. As the problem addressed here is non-linear, a Newton-Raphson method is adopted to find its solution. In order to simulate the fracture process, the implemented cohesive zone models are then presented in section 2.3. As one of the main goals of this PhD is to account for thermal effects when dealing with fracture mechanics problems (i.e., crack propagation direction), the formulation of the implemented thermoelasticity model is described in section 2.4. After this, section 2.5 details the numerical implementation of the $G\theta$ method, which is the methodology used in this work to compute the crack propagation direction in two-dimensional problems. Finally, section 2.6 gives an overview on the mesh adaptation strategies used in this work to simulate crack propagation through a finite element mesh in both two- and three-dimensional problems.

2.1 Mechanical problem

In this section, the basic equations governing the physics of the problem of a body undergoing deformation are described. The theoretical background of this problem relies on the field of continuum mechanics. This field studies the mechanical behavior of a continuous medium when subjected to forces or displacements, as well as the subsequent effects of this medium on its environment. A continuous medium is understood as an infinite set of particles that will be studied macroscopically, i.e., without considering discontinuities that could be present at the microscopic level. Let it be $\Omega \subset R^3$ the domain occupied by a deformable body $\mathscr{B}$ in its reference configuration. Ω is bounded by the border $\partial\Omega \subset R^2$. Developing the equations allowing to describe the displacement, stress and strain fields at each instant t is the way to study the mechanical problem.

2.1.1 Governing equations

The governing equations of a solid occupying the domain Ω_t at time t, and undergoing deformation, are the conservation of momentum and the conservation of mass. The conservation of momentum can be written as:

$$\frac{\partial \sigma_{ij}}{\partial x_j} + f_i = \rho \frac{dv_i}{dt} \tag{2.1}$$

where σ_{ij} is the Cauchy stress tensor, ρ density of the material, f_i is the volume force and $\frac{dv_i}{dt}$ is the material time derivative of the velocity. The mass conservation equation can be expressed as:

$$\frac{\partial \rho}{\partial t} + \frac{\partial (\rho v_i)}{\partial x_i} = 0 \tag{2.2}$$

where v_i is the velocity and $\frac{\partial (\rho v_i)}{\partial x_i}$ is the divergence of the velocity.

2.1.2 Boundary conditions

In addition to the above-mentioned equations, appropriate boundary conditions must be used. The boundary $\partial\Omega$ of the solid Ω is decomposed in different parts ($\partial\Omega = \partial\Omega_v + \partial\Omega_t + \partial\Omega_f$) as shown in Figure 2.1. There are two different types of boundary conditons:

1. Imposed velocity boundary condition: $v_i = \vec{v}_0$ on $\partial\Omega_v$ (Dirichlet B.C.)
2. Stress imposed boundary condition: $\sigma_{ij} n_j = t_i = \vec{t}_0$ on $\partial\Omega_t$ (Neumann B.C.)

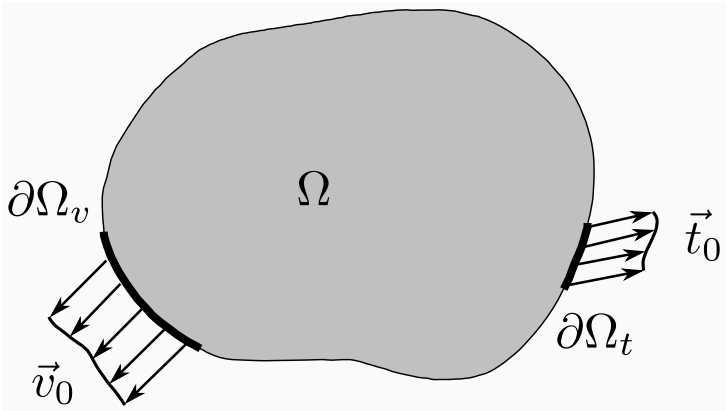

Figure 2.1: Continuum Mechanics Problem.

When the inertia and the volume forces are negligible, the conservation of momentum (equation 2.1) can be reduced to:

$$\frac{\partial \sigma_{ij}}{\partial x_j} = 0 \tag{2.3}$$

The Cauchy stress tensor can be decomposed into its deviatoric and spherical components. Due to this, equation (2.3) can be written as:

$$\frac{\partial S_{ij}}{\partial x_j} - \frac{\partial p}{\partial x_i} = 0 \tag{2.4}$$

where S_{ij} is the deviatoric stress tensor and p is the hydrostatic part of the stress tensor.

Continuity equation can be expressed explicitly in terms of the pressure through the introduction of the bulk modulus (κ) (equation (2.5).

$$\kappa = \rho \frac{\partial p}{\partial \rho} \tag{2.5}$$

Expressing the divergence of the velocity as the trace of the strain rate tensor ($tr(\dot{\varepsilon}) = \dot{\varepsilon}_{ii}$), introducing the bulk modulus (κ) and dropping the advection term, under a Lagrangian configuration, the mass conservation equation can be expressed as:

$$\dot{\varepsilon}_{ii} + \frac{1}{\kappa} \frac{\partial p}{\partial t} = 0 \tag{2.6}$$

2.2 The finite element formulation

The mechanical problem presented in section 2.1 will be solved using the finite element (FE) method. The weak formulation required by the FE method will be derived from the strong form presented previously. The numerical strategy used to solve the problem described by the weak formulation is implemented in Cimlib, a C++ in-house finite element library developed at CEMEF [Digonnet et al., 2007]. The available finite element framework in Cimlib is an implicit formulation (mixed) with first-order elements using linear interpolation functions for both velocity and pressure.

2.2.1 Weak formulation

The set of equilibrium equations with appropriate boundary conditions presented in equation (2.7) define the strong form of the mechanical problem:

$$\begin{cases} \frac{\partial \sigma_{ij}}{\partial x_j} = \frac{\partial S_{ij}}{\partial x_j} - \frac{\partial p}{\partial x_i} = 0 \\ \frac{1}{\kappa}\frac{\partial p}{\partial t} + \dot{\varepsilon}_{ii} = 0 \\ v_i = \vec{v}_0 \ on \ \partial\Omega_v \\ t_i = \vec{t}_0 \ on \ \partial\Omega_t \end{cases} \tag{2.7}$$

Considering the velocity and the pressure as two variables totally independent, let us define appropriate functional spaces:

$$\begin{cases} \mathcal{V} = \{v_i \in \mathcal{H}^1(\Omega)^3, v_i|_{\partial\Omega_v} = \vec{v}_0\} \\ \mathcal{V}^0 = \{v_i^* \in \mathcal{H}_0^1(\Omega)^3, v_i^*|_{\partial\Omega_v} = \vec{0}\} \\ \mathcal{P} = \mathcal{L}^2(\Omega) \end{cases} \tag{2.8}$$

where $\mathcal{V}$ and $\mathcal{V}^0$ are functional spaces of kinematically admissible velocity field, $\mathcal{P}$ is the functional space of the pressure and d is the space dimension. $\mathcal{H}^1(\Omega)$ and $\mathcal{L}^2(\Omega)$ are respectively, the Sobolev and the Lebesgue spaces, which are defined by Eqs. (2.9) and (2.10). $\mathcal{H}_0^1(\Omega)$ is the subspace of $\mathcal{H}^1(\Omega)^3$ such that $v_i^* = 0$ on $\partial\Omega_v$

The Lebesgue space: given Ω is a regular and bounding region in R, the $\mathcal{L}^2$ space is defined as:

$$\mathcal{L}^2(\Omega) = \{u : \Omega \to R, \int_\Omega u^2 d\Omega < \infty\} \tag{2.9}$$

The Sobolev space:

$$\mathcal{H}^1(\Omega) = \{u \in \mathcal{L}^2(\Omega), \frac{\partial u}{\partial x_i} \in \mathcal{L}^2(\Omega)\} \tag{2.10}$$

Lebesgue spaces $\mathcal{L}^p$ are normed vector spaces of functions on a measure space, equipped with the suitable version of the *p-norm*. For example, $\mathcal{L}^2(\Omega)$ is the space of square integrable functions over the domain Ω. A Sobolev space is the set of measurable functions which has a weak derivative up to a given order and which is in $\mathcal{L}^p(\Omega)$.

The weak formulation of the strong form of the problem described by equation (2.7) can be obtained by multiplying the equations by the test functions v_i^* and p^* and by integration over the whole domain Ω together with the use of Green's theorem. As an example, let's take the equation for conservation of momentum (equation 2.3), multiply it by the test function $v_i^* \in \mathcal{V}^0$ and integrate it on the domain Ω:

$$\int_\Omega \frac{\partial \sigma_{ij}}{\partial x_j} v_i^* d\Omega = \underbrace{-\int_\Omega \sigma_{ij} \frac{\partial v_i^*}{\partial x_j} d\Omega}_{1} + \underbrace{\int_\Omega \frac{\partial (\sigma_{ij} v_i^*)}{\partial x_j} d\Omega}_{2} = 0 \tag{2.11}$$

Using the divergence theorem along with the boundary conditions presented in (2.7), the integral labeled as 2 in the right side can be written as:

$$\int_\Omega \frac{\partial(\sigma_{ij}v_i^*)}{\partial x_j}d\Omega = \int_{\partial\Omega} \sigma_{ij}v_i^* n_j d\Gamma = \cancelto{0}{\int_{\partial\Omega_v} \sigma_{ij}v_i^* n_j d\Gamma} + \int_{\partial\Omega_t} t_i v_i^* d\Gamma = 0 \tag{2.12}$$

Using the decomposition of the stress tensor into deviatoric (S_{ij}) and volumetric parts ($p\delta_{ij}$) presented in equation (2.4), the integral labeled as 1 in the right side can be expressed as:

$$\int_\Omega \sigma_{ij}\frac{\partial v_i^*}{\partial x_j}d\Omega = \int_\Omega S_{ij}(v_k)\dot{\varepsilon}_{ij}(v_k^*)d\Omega - \int_\Omega p\frac{\partial v_i^*}{\partial x_i}d\Omega \tag{2.13}$$

Replacing Eqs. (2.12) and (2.13) in equation (2.11), it becomes:

$$\int_\Omega S_{ij}(v_k)\dot{\varepsilon}_{ij}(v_k^*)d\Omega - \int_\Omega p\frac{\partial v_i^*}{\partial x_i}d\Omega - \int_{\partial\Omega_t} t_i v_i^* d\Gamma = 0 \tag{2.14}$$

Equivalently, the weak form of mass conservation equation (equation 2.6) can be obtained. Therefore, the associated variational problem is:

$$find\ (v_i, p) \in \mathcal{V}\ \times\ \mathcal{P}\ \begin{cases} \int_\Omega S_{ij}(v_k)\dot{\varepsilon}_{ij}(v_k^*)d\Omega - \int_\Omega p\frac{\partial v_i^*}{\partial x_i}d\Omega - \int_{\partial\Omega_t} t_i v_i^* d\Gamma = 0 \\ \int_\Omega \left(\dot{\varepsilon}_{ii} + \frac{1}{\kappa}\frac{\partial p}{\partial t}\right)p^* d\Omega = 0 \\ \forall (v_i^*, p^*) \in \mathcal{V}^0\ \times\ \mathcal{P} \end{cases} \tag{2.15}$$

2.2.2 Spatial discretization

To find the solution to the stated problem, the domain Ω is discretized into different geometrically simplicial elements (i.e., triangles, quadrilaterals, tetrahedra, etc). The combination of these simplicial elements forms the "triangulation" of the domain, which defines the discretized domain Ω_h:

$$\Omega_h = \bigcup_{e\in\mathcal{T}_h(\Omega)} \Omega_e \tag{2.16}$$

where $\mathcal{T}_h(\Omega)$ is a finite element mesh of the domain Ω and Ω_e is a simplex of a given mesh size h. The weak-form equations presented in (2.15) are solved through the finite element method. Approach consisting in approximating the continuous spaces $\mathcal{V}$ and $\mathcal{P}$ by the corresponding discrete vectors $\mathcal{V}_h$ and $\mathcal{P}_h$. The approximated spaces are usually included in the continuous ones:

$$\mathcal{V}_h \subset \mathcal{V},\ \mathcal{P}_h \subset \mathcal{P} \mid \lim_{h\to 0}\mathcal{V}_h = \mathcal{V},\ \lim_{h\to 0}\mathcal{P}_h = \mathcal{P} \tag{2.17}$$

In the discretized space, equation (2.15) can be written as:

$$Find\ (v_{h_i}, p_h) \in \mathcal{V}_h\ \times\ \mathcal{P}_h\ \begin{cases} \int_{\Omega_h} S_{ij}(v_{h_k})\dot{\varepsilon}_{ij}(v_{h_k}^*)d\Omega_h - \int_{\Omega_h} p_h\frac{\partial v_{h_i}^*}{\partial x_i}d\Omega_h - \int_{\partial\Omega_{h_t}} t_i v_{h_i}^* d\Gamma_h = 0 \\ \int_{\Omega_h}\left(\dot{\varepsilon}_{ii} + \frac{1}{\kappa}\frac{\partial p_h}{\partial t}\right)p_h^* d\Omega_h = 0 \\ \forall (v_{h_i}^*, p_h^*) \in \mathcal{V}_h^0\ \times\ \mathcal{P}_h \end{cases} \tag{2.18}$$

When discretizing, a continuous problem (Eq. 2.15) is converted into a discrete problem (Eq. 2.18). An appropriate selection of the interpolation functions associated with the unknown variables (v_i and p) is required in order to ensure efficiency and accuracy of the discrete problem solution. The interpolation spaces of the velocity and the pressure cannot be chosen arbitrarily. Compatibility between the two spaces is guaranteed through the Babuška-Brezzi (i.e., *inf-sup*)

condition [Arnold et al., 1984, Brezzi and Fortin, 1991]. The latter, being a condition related to the mathematical convergence characteristics of the finite element formulation. The *inf-sup* (Babuška-Brezzi) condition ensures the solvability, stability and optimality of the finite element solution, as well as allows evaluating whether the problem is well-posed [Bathe, 2001]. A problem is called well-posed if: (i) a solution exists, (ii) the solution is unique and (iii) the solution depends continuously on the given data (in some reasonable topology) [Hadamard, 1902]. The *inf-sup* condition can be mathematically expressed as follows:

$$\inf_{p_h \in \mathcal{P}_h} \sup_{v_{h_i} \in \mathcal{V}_h} \frac{\int_{\Omega_h} p_h \frac{\partial v^*_{h_i}}{\partial x_i} d\Omega_h}{\|p_h\|_{\mathcal{P}_h} \, \|v_{h_i}\|_{\mathcal{V}_h}} > \mathcal{C} > 0 \tag{2.19}$$

where $\| \, . \, \|_{\mathcal{P}_h}$ and $\| \, . \, \|_{\mathcal{V}_h}$ are respectively, the norms of the approximated spaces $\mathcal{V}_h$ and $\mathcal{P}_h$ and $\mathcal{C}$ is a constant that is independent of the mesh. The interpolation degree for the two variables velocity and pressure is imposed by the Babuška-Brezzi condition, as well as it assures the existence and uniqueness of solutions. When this condition is not respected, spurious numerical solutions (e.g. shear locking) come out. This compatibility condition excludes certain choices of interpolation spaces which would seem natural (e.g., $P1/P0$ or $P1/P1$). Obviously, the choice must satisfy this condition. The most common elements satisfying this condition are the MINI element ($P1^+/P1$) [Arnold et al., 1984], the Taylor-Hood element ($P2/P1$) [Hood and Taylor, 1974] and the Crouzeix-Raviart element ($P2^+/P1_{disc}$) [Crouzeix and Raviart, 1973]. In our case, the software CimLib, a C++ in-house finite element library developed at CEMEF [Digonnet et al., 2007], uses the $P1^+/P1$ mixed velocity-pressure element (Figure 2.2), this is the smallest interpolation degree among the compatible elements. This element was introduced by [Arnold et al., 1984] for the computation of Stokes flow. $P1^+/P1$ is an element $P1/P1$ which does not satisfy the *inf-sup* condition (equation 2.19), for this reason the interpolation of the velocity is enriched by the addition of an extra degree of freedom (DOF) associated with the center of gravity of each one of the elements of the mesh.

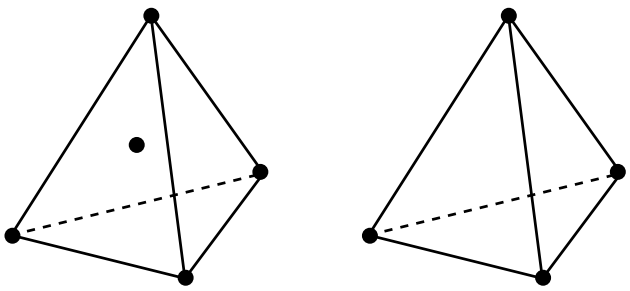

Figure 2.2: Schematic representation of the degrees of freedom in velocity and pressure for the tetrahedral element $P1^+/P1$.

Inside the MINI element formulation introduced by [Arnold et al., 1984], the pressure field is defined linear and continuous, while the velocity field is composed of a linear part (v_i^l) associated with the linear interpolation of the values at the vertices of the element, and a "bubble" part (b_i) corresponding to the additional internal degree of freedom (DOF) added at the center of the element: $v_{h_i} = v_i^l + b_i$. The additional DOF defines a "bubble" which equals unity at element center and zero at element borders. The interpolation function used for the "bubble", can be constructed using a polynomial of degree 4 in the reference tetrahedron [Fortin, 1981]. The discrete spaces are defined as:

$$\begin{cases} \mathcal{V}_h = \mathcal{L}_h + \mathcal{B}_h \\ \mathcal{L}_h = \{v_i^l \in (\mathcal{C}^0(\Omega_h))^3, v_i^l|_{\Omega_e} \in (\mathcal{P}^1(\Omega_e))^3, v_i^l|_{\partial\Omega_e} = \vec{v}_0, \forall e \in \mathcal{T}_h(\Omega)\} \\ \mathcal{L}_h^0 = \{v_i^{l*} \in \mathcal{V}^0 \cap (\mathcal{C}^0(\Omega_h))^3, v_i^{l*}|_{\Omega_e} \in (\mathcal{P}^1(\Omega_e))^3, v_i^{l*}|_{\partial\Omega_e} = \vec{0}, \forall e \in \mathcal{T}_h(\Omega)\} \\ \mathcal{P}_h = \{\mathcal{L}^2(\Omega_h) \cap \ \mathcal{C}^0(\Omega_h), p_h|_{\Omega_e} \in (\mathcal{P}^1(\Omega_e))^3 \forall e \in \mathcal{T}_h(\Omega)\} \end{cases} \tag{2.20}$$

where $\mathcal{C}^0(\Omega_h)$ is the space of continuous functions on the domain Ω_h, $\mathcal{P}^1(\Omega_e)$ is the space of linear functions on element Ω_e. $\mathcal{B}_h$ is the interpolation space of the "bubble" function. In the work of [Coupez, 1996], in order to avoid difficulties in integrating the polynomial of degree 4, $\mathcal{B}_h$ is defined with a piecewise linear function on four sub-tetrahedron Ω_{e_i} $i = 1, 2, 3, 4$ in which the reference tetrahedron Ω_e is decomposed (Figure 2.3):

$$\mathcal{B}_h = \{b_i \in (\mathcal{C}^0(\Omega_h))^3, b_i|_{\partial\Omega_e} = \vec{0}, b_i|_{\Omega_{e_i}} \in (\mathcal{P}^1(\Omega_e))^3, \forall e \in \mathcal{T}_h(\Omega), i = 1, ..., 4\} \tag{2.21}$$

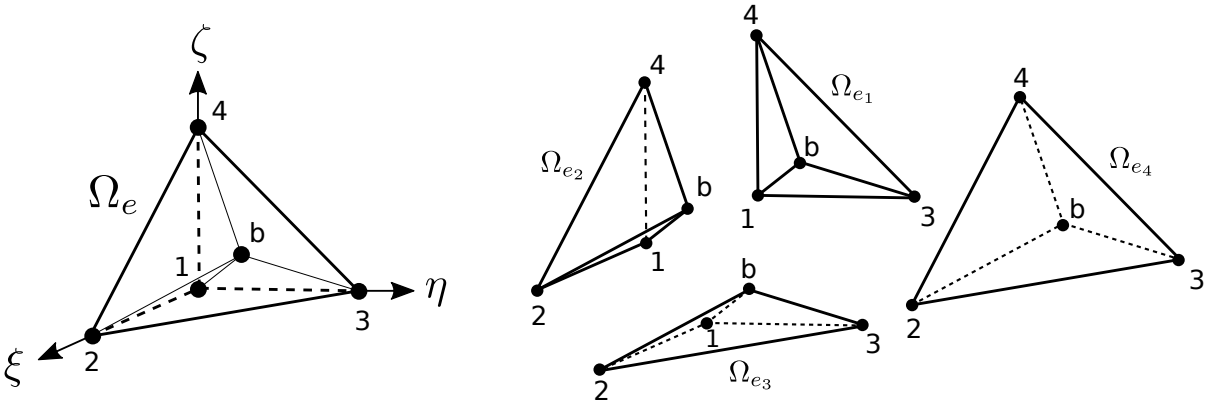

Figure 2.3: Schematic of the decomposition of reference tetrahedron element ($P1^+/P1$) into 4 sub-tetrahedrons Ω_{e_i}.

Accounting for the decomposition of the reference tetrahedron element into 4 sub-tetrahedrons as shown in Figure 2.3, the velocity and pressure fields at a point x_i for each element Ω_e is given by:

$$v_{h_i}(x_i) = \sum_{R=1}^{4} N_R^l(x_i) v_{R_i}^l + N^b(x_i) b_i \tag{2.22}$$

$$p_h(x_i) = \sum_{R=1}^{4} N_R^l(x_i) p_R \tag{2.23}$$

where $N_R^l(x_i) \in \mathcal{L}_h$ are the interpolation functions of the linear velocity and pressure fields associated with the node R, $v_{R_i}^l$ and p_R are the linear velocity and pressure at node R, b_i is a nodal value standing for the difference between the velocity at center of enriched linear tetrahedral element (Ω_e) and the normal linear tetrahedron (Ω_{e_i}). The velocity and pressure interpolation functions associated with the reference element presented in Figure 2.3, are defined as:

$$\begin{cases} N_1^l = \xi \\ N_2^l = \eta \\ N_3^l = \zeta \\ N_4^l = 1 - \xi - \eta - \zeta \end{cases} \quad \text{and} \quad \begin{cases} N^b = 4\xi & in\ \Omega_{e_1} \\ N^b = 4\eta & in\ \Omega_{e_2} \\ N^b = 4\zeta & in\ \Omega_{e_3} \\ N^b = 4(1 - \xi - \eta - \zeta) & in\ \Omega_{e_4} \end{cases} \tag{2.24}$$

In the end and taking into account the "bubble" part, the discrete problem presented in equation (2.18) can be written as:

$$Find\ (v_i^l, b_i, p_h) \in \mathcal{L}_h \times \mathcal{B}_h \times \mathcal{P}_h \begin{cases} \int_{\Omega_h} S_{ij}(v_k^l + b_k)\dot{\varepsilon}_{ij}(v_k^{l*})d\Omega_h - \int_{\Omega_h} p_h \frac{\partial v_i^{l*}}{\partial x_i} d\Omega_h - \int_{\partial\Omega_{h_t}} t_i v_i^{l*} d\Gamma_h = 0 \\ \int_{\Omega_h} S_{ij}(v_k^l + b_k)\dot{\varepsilon}_{ij}(b_k^*)d\Omega_h - \int_{\Omega_h} p_h \frac{\partial b_i^*}{\partial x_i} d\Omega_h = 0 \\ \int_{\Omega_h} \left(\frac{\partial (v_i^l + b_i)}{\partial x_i} + \frac{1}{\kappa}\frac{\partial p_h}{\partial t} \right) p_h^* d\Omega_h = 0 \\ \forall (v_i^{l*}, b_i^*, p_h^*) \in \mathcal{L}_h^0 \times \mathcal{B}_h \times \mathcal{P}_h) \end{cases} \tag{2.25}$$

Due to the fact that the stress deviator depends on the total velocity field $(v_i^{l*} + b_i^*$, which is the result of the local integration of behavior law), the system of equations to be solved is a coupled system of two unknown field variables v_i^{l*} and b_i^*. From the definition of the interpolation space of the bubble functions $\mathcal{B}_h$, the following fundamental properties of the "bubble" functions that helps to decouple the system in equation (2.25) can be deduced [Aliaga, 2000]:

- $b_i = \vec{0}$ on ∂K. This property allows the elimination of the "bubble" from all the integrations on ∂K.
- For all constant tensor C_{ij} in Ω:

$$\int_{\Omega} C_{ij} \frac{\partial b_i^*}{\partial x_j} d\Omega = 0 \tag{2.26}$$

  Leading to the following orthogonal property:

$$\int_{\Omega_h} \frac{\partial v_i^l}{\partial x_j} \frac{\partial b_i}{\partial x_j} d\Omega_h = 0,\ \forall b_i \in \mathcal{B}_h, \forall v_i^l \in \mathcal{L}_h \tag{2.27}$$

These two properties allow to decouple the unknown fields v_i^l and b_i from the discrete variational formulation in equation (2.25), which becomes:

$$Find\ (v_i^l, b_i, p_h) \in \mathcal{L}_h \times \mathcal{B}_h \times \mathcal{P}_h \begin{cases} \int_{\Omega_h} S_{ij}(v_k^l)\dot{\varepsilon}_{ij}(v_k^{l*})d\Omega_h - \int_{\Omega_h} p_h \frac{\partial v_i^{l*}}{\partial x_i} d\Omega_h - \int_{\partial\Omega_{h_t}} t_i v_i^{l*} d\Gamma_h = 0 \\ \int_{\Omega_h} S_{ij}(b_k)\dot{\varepsilon}_{ij}(b_k^*)d\Omega_h - \int_{\Omega_h} p_h \frac{\partial b_i^*}{\partial x_i} d\Omega_h = 0 \\ \int_{\Omega_h} \left(\frac{\partial (v_i^l + b_i)}{\partial x_i} + \frac{1}{\kappa}\frac{\partial p_h}{\partial t} \right) p_h^* d\Omega_h = 0 \\ \forall (v_i^{l*}, b_i^*, p_h^*) \in \mathcal{L}_h^0 \times \mathcal{B}_h \times \mathcal{P}_h) \end{cases} \tag{2.28}$$

2.2.3 Temporal discretization

The system is supposed to be at equilibrium at time t. Then, equilibrium state is disturbed by modifying the external loads, so the new problem consists in determining the velocity and pressure fields that respect the equilibrium at $t + \Delta t$. Through the application of a classical procedure of the finite element method, the elementary contributions can be calculated from the discrete formulation presented in equation (2.28). Then, they are assembled in order to build the matrix system of the problem. The elementary contribution can be written under the following algebraic form defining a non-linear system of equations of the unknown variables v_i^l, b_i, p_h:

$$\begin{cases} R_e^l(v_{e_i}^l, p_{he}) & = R_e^{ll} + 0 + R_e^{lp} & = 0 \\ R_e^b(b_{e_i}, p_{he}) & = 0 + R_e^{bb} + R_e^{bp} & = 0 \\ R_e^p(v_{e_i}^l, b_{e_i}, p_{he}) & = R_e^{pl} + R_e^{pb} + R_e^{pp} & = 0 \end{cases} \tag{2.29}$$

The residuals of the linear velocity, the "bubble" term and the pressure are denoted respectively as R_e^l, R_e^b and R_e^p. The sub-index e indicates that the terms are calculated at each element. The discrete problem presented in equation (2.29) is non-linear. The iterative Newton-Raphson algorithm, which linearizes the equations by the first order Taylor's development is used to solve this non-linear problem. In order to build the local contributions in the linearized problems, the stiffness matrix is introduced:

$$K_e^{xy} = \frac{\partial R_e^{xy}}{\partial z} \tag{2.30}$$

where $(xy) \in \{(ll),(lp),(bb),(bp),(pl),(pb),(pp)\}$; and $z \in \{v_i^l, b_i, p_h\}$. At each iteration of Newton-Raphson algorithm, the solution of the non-linear discrete problem (v_i^l,b_i,p_h) is modified by a correction (δv_i^l,δb_i,δp_h). Such correction is the solution of a global algebraic system obtained through the assembling of the elementary contributions. The global matrix system can be written as follows:

$$\begin{bmatrix} K^{ll} & 0 & K^{lp} \\ 0 & K^{bb} & K^{bp} \\ K^{pl} & K^{pb} & K^{pp} \end{bmatrix} \begin{pmatrix} \delta v_i^l \\ \delta b_i \\ \delta p_h \end{pmatrix} = - \begin{pmatrix} R^l \\ R^b \\ R^p \end{pmatrix} \tag{2.31}$$

The basic functions associated with internal nodes are limited just to one element. The corresponding degrees of freedom are not linked to any other degree of freedom belonging to other element different from the considered one. Therefore, this allows to eliminate the degrees of freedom of the "bubble" at the elementary level before the assembly by condensation. Locally, the following equation can be derived from the second equation of the system shown in (2.31):

$$\delta b_{i_e} = -(K_e^{bb})^{-1} \left[R_e^b + K_e^{bp} \delta p_{h_e} \right] \tag{2.32}$$

Thus, by replacing equation (2.32) in the system shown in equation (2.31), the "bubble" part can be eliminated from this system leading to:

$$\begin{bmatrix} K_e^{ll} & K_e^{lp} \\ K_e^{pl} & K_e^{pp} - K_e^{pb}(K_e^{bb})^{-1} K_e^{bp} \end{bmatrix} \begin{pmatrix} \delta v_{i_e}^l \\ \delta p_{h_e} \end{pmatrix} = - \begin{pmatrix} R_e^l \\ R_e^p - K_e^{pb}(K_e^{bb})^{-1} R_e^b \end{pmatrix} \tag{2.33}$$

Regrouping $C_e = K_e^{pb}(K_e^{bb})^{-1} K_e^{bp}$ and $G_e = K_e^{pb}(K_e^{bb})^{-1} R_e^b$, equation (2.33) becomes:

$$\begin{bmatrix} K_e^{ll} & K_e^{lp} \\ K_e^{pl} & K_e^{pp} - C_e \end{bmatrix} \begin{pmatrix} \delta v_{i_e}^l \\ \delta p_{h_e} \end{pmatrix} = - \begin{pmatrix} R_e^l \\ R_e^p - G_e \end{pmatrix} \tag{2.34}$$

where C_e is the local condensation matrix of the "bubble" and G_e is the second member associated with the same condensation.

In the system shown in equation (2.34) the degrees of freedom associated with the "bubble" term have been totally eliminated. Finally, a mixed formulation in terms of velocity and pressure with only nodal unknowns is obtained: the three components of the velocity field and the component of the pressure field:

$$\begin{bmatrix} K^{ll} & K^{lp} \\ K^{pl} & K^{pp} - C \end{bmatrix} \begin{pmatrix} \delta v_i^l \\ \delta p_h \end{pmatrix} = - \begin{pmatrix} R^l \\ R^p - G \end{pmatrix} \tag{2.35}$$

At each iteration k, the system shown in (2.35) is solved and the velocity and pressure are updated: $v_i^l + \delta v_i^l \rightarrow v_i^l$, $p_h + \delta p_h \rightarrow p_h$. When converged solutions are obtained, i.e., δv_i^l and δp_h $< Tol$, the iterative algorithm stops. After the global problem is solved, the return mapping algorithm [Simo and Taylor, 1985, Simo and Taylor, 1986, Cao, 2013] is used at the element level for the integration of the behavior law. In this work, the adopted constitutive law is purely elastic for the bulk and the fracture process is controlled through the use of cohesive zone models

as presented in the next section. Readers interested in further details regarding the mixed finite element formulation, as well as in stabilization techniques or elastoplastic constitutive laws, can refer to [Aliaga, 2000, Perchat, 2000, Fayolle, 2008, El Khaoulani, 2010].

2.3 Cohesive zone models

A pioneering perspective stating that fracture is a phenomenon taking place accross an extended crack tip (cohesive zone) was proposed back in the 60's [Barenblatt, 1962, Rice, 1968b]. The proposed concept set the ground for cohesive zone models (CZMs). This simple approach asserts that, at the crack tip, it exists a region of finite size where there is a transition from a sound material to a fully broken material [Dugdale, 1960]. Figure 2.4 shows a schematic representation of the cohesive region (process zone), where the fracturing process is taking place in a brittle material. The cohesive zone corresponds to prospective fracture surfaces ahead of a crack that are permitted to separate under loading. Atomic or molecular forces are in charge of preventing the process of separation and creation of crack surfaces [Rice, 1968a]. The force that exerts a resistance to the opening of new surfaces is known as cohesive force, and it is modeled through a phenomenological traction-separation law (cohesive law).

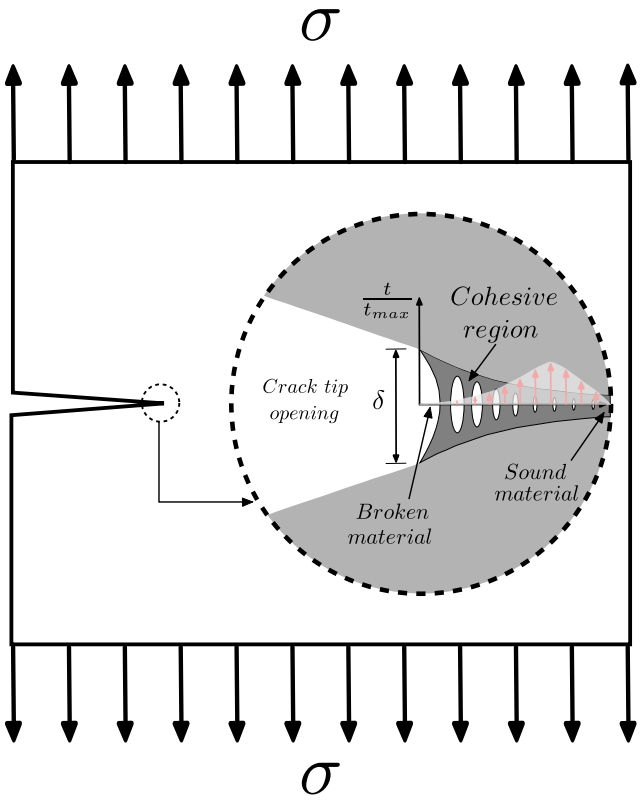

Figure 2.4: Schematic representation of the cohesive zone. Red arrows represent the distribution of traction loading over the cohesive region.

The cohesive region, i.e., the process zone, detailed in Figure 2.4 is a zone located in front of the crack tip. In this zone, different processes like small-scale yielding, micro-cracking and void initiation, growth and coalescence take place [de Borst, 2018]. In the modeling of the fracture process through the use of cohesive zone models, the concept of process zone is highly important. The accuracy of the computation depends directly on the number of elements in this zone. Several authors have proposed different definitions for the process zone length (PZL) [Dugdale, 1960, Barenblatt, 1962, Falk et al., 2001, Turon et al., 2007, Hermes, 2010, Ha et al., 2015]. In this work, unless otherwise stated, the PZL is defined as:

$$PZL = \frac{G_c E}{\pi \sigma_c^2} \tag{2.36}$$

Where G_c is the critical energy release rate, E is the Young's modulus and σ_c is the maximun cohesive stress. The size of the finite element mesh at the crack tip should be smaller than the process zone length.

Using CZMs approaches, a possible crack is modeled by two interface areas connected by cohesive stresses. The degradation process is described by the constitutive law linking the cohesive traction (t) and the opening (separation) of the cohesive region (δ). In the literature many different shapes of the cohesive law are described. For example [Dugdale, 1960] noted that ahead of slits in steel plates subjected to static tension there was a small zone of plasticity, therefore he proposed the use of a constant cohesive law. Polynomial and exponential models were first used by [Needleman, 1987, Needleman, 1990] to study the void nucleation at the interface of particles in matrix metal. [Tvergaard and Hutchinson, 1992] proposed a trapezoidal shape to study crack growth initiation and subsequent resistance in elastic-plastic materials. In order to model the propagation of multiple cracks and delaminations in a composite, [Camacho and Ortiz, 1996] proposed a linear law. [Geubelle and Baylor, 1998] simulate the spontaneous initiation and propagation of transverse matrix cracks and delamination fronts using a bilinear model. It is worth mentioning that the available cohesive laws share some characteristics: when the opening (δ) of the cohesive region increases, the cohesive traction (t) begins to increase until a critical value (σ_c) is reached, then it decreases and vanishes after full fracture. Figure 2.5 depicts some examples of available cohesive laws.

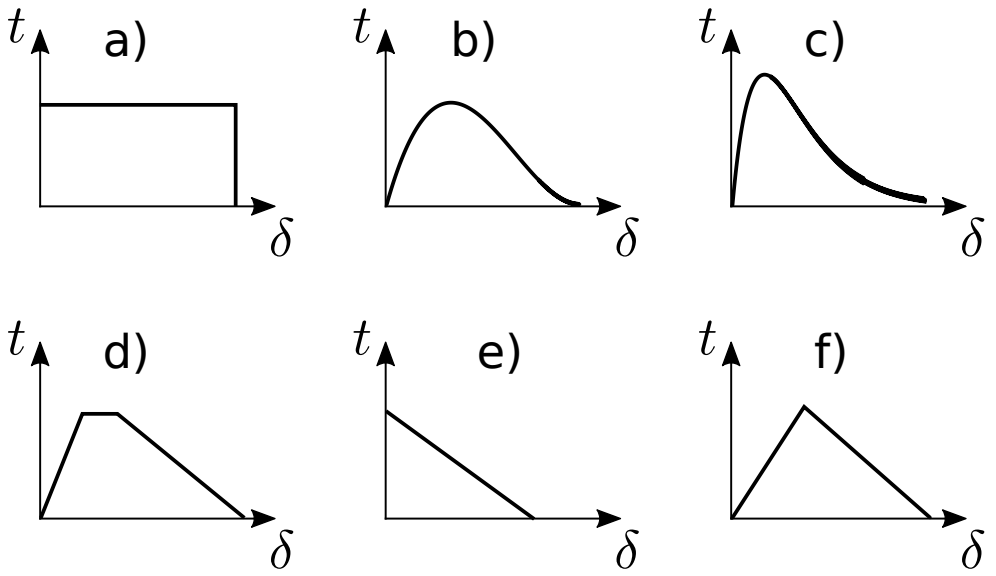

Figure 2.5: Different shapes of the cohesive law: **a)** constant [Dugdale, 1960], **b)** exponential [Barenblatt, 1962], **c)** polynomial [Needleman, 1987], **d)** tri-linear (trapezoidal) [Tvergaard and Hutchinson, 1992], **e)** linear [Camacho and Ortiz, 1996] and **f)** bi-linear [Geubelle and Baylor, 1998].

The cohesive energy which takes into account the creation of two new surfaces and the microdamage phenomena is equal to the area under the cohesive traction-separation curve. Generally, the cohesive energy is equivalent to the fracture energy (G) [Shet and Chandra, 2002]. The critical energy release rate G_c, i.e. the fracture energy required to create the new free surfaces and break the material can be related to the cohesive law in the following way:

$$G_c = \int_0^\infty t d\delta \tag{2.37}$$

Where t is a scalar effective traction and δ an effective opening displacement. The total amount of energy dissipated by the cohesive elements per unit of length can be computed simply using (2.37). Thus, the degradation process can be fine tuned by picking the mathematical form of t.

An engaging feature of a cohesive approach, is that it does not presuppose a particular type of constitutive response in the bulk of the material, the extent of crack growth or the size of the plastic zone. Generally, the cohesive approach assumes that the process zone is located ahead of the physical crack front (tip). Furthermore, it is worth mentioning that the shape and location of successive crack fronts are an outcome of the calculations [Ortiz and Pandolfi, 1999, Sun and Jin, 2012b]. In the following subsections, the two cohesive laws that were implemented in this work will be presented.

2.3.1 Ortiz and Pandolfi's cohesive law

From [Ortiz and Pandolfi, 1999] we can obtain a pair of simple and convenient equations that relate the opening displacement, the maximum cohesive normal traction and the characteristic opening displacement through and irreversible exponential cohesive law. Irreversibility manifests itself upon unloading. Thus, the maximum reached effective opening displacement is the appropriate internal variable to describe the loading-unloading process. In this work the terms loading and unloading are used in the sense of increasing or decreasing the effective opening displacement, respectively. Ortiz and Pandolfi's cohesive law can be derived from the following potential Φ:

$$\Phi = e\sigma_c\delta_c \left[1 - \left(1 + \frac{\delta}{\delta_c}\right) e^{-\frac{\delta}{\delta_c}}\right] \tag{2.38}$$

where δ is the opening displacement, σ_c is the maximun cohesive normal traction and δ_c is the characteristic opening displacement. The interfacial scalar effective traction is given by:

$$t = \frac{\partial \Phi}{\partial \delta} \tag{2.39}$$

The irreversible exponential cohesive law presented here is depicted in Figure 2.6.

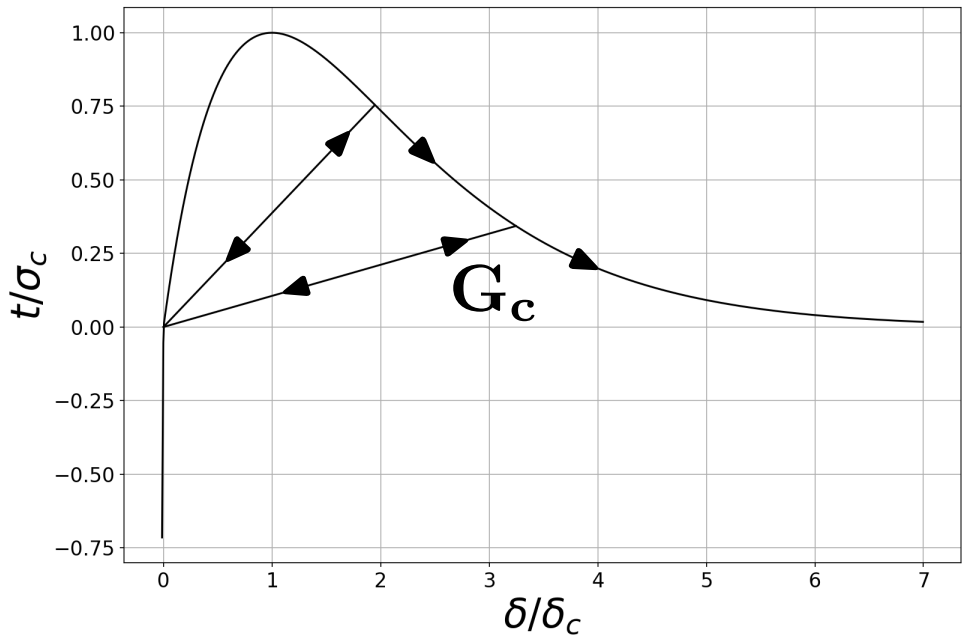

Figure 2.6: Cohesive law in terms of an effective opening displacement δ and effective traction t (loading-unloading envelop).

The loading process is described by equation (2.40), and is characterized by the conditions: $\delta = \delta_{max}$ *and* $\dot{\delta} \geq 0$. Inversely, the unloading process is described by equation (2.41), and is characterized by the conditions: $\delta < \delta_{max}$ *or* $\dot{\delta} < 0$. During the unloading process, the relation between the effective cohesive traction and the effective opening displacement of the interface is linear. This behavior remains linear during reloading until the effective opening displacement reaches the value when unloading started.

$$t = e\sigma_c \frac{\delta}{\delta_c} e^{-\frac{\delta}{\delta_c}} \quad \text{if} \quad \delta = \delta_{max} \quad \text{and} \quad \dot{\delta} \geq 0 \qquad \text{(Loading)} \tag{2.40}$$

$$t = \frac{t_{max}}{\delta_{max}} \delta \quad \text{if } \delta < \delta_{max} \quad \text{or} \quad \dot{\delta} < 0 \qquad \text{(Unloading)} \tag{2.41}$$

where t is the effective cohesive traction, δ is the opening displacement, σ_c is the maximun cohesive normal traction and δ_c is the characteristic opening displacement. In the above cohesive law, there is a parameter named β that can be seen as a factor that assigns different weights to the sliding (δ_s) and normal (δ_n) opening displacements (2.44). δ_s and δ_n are respectively, the opening displacement in the tangential and in the normal direction of the cohesive surface. β can also be seen as the ratio between the shear and the normal critical tractions (2.43).

$$\delta = \sqrt{\beta^2 \delta_s^2 + \delta_n^2} \tag{2.42}$$

$$t = \sqrt{\beta^{-2} t_s^2 + t_n^2} \tag{2.43}$$

Where δ is an effective opening displacement, δ_s and δ_n are respectively, the sliding and normal opening displacements, with t being a scalar effective traction, t_s is the shear traction and t_n is the normal traction [Ortiz and Pandolfi, 1999]. In the case of contact ($\delta < 0$) a penalization technique is implemented, making the cohesive interface acts like a spring with a high constant (K_{pen}) and avoiding in this way, the interference and overlap of the adjacent solid elements (See Figure 2.6):

$$t = K_{pen} \left(e\sigma_c \frac{\delta}{\delta_c} e^{-\frac{\delta}{\delta_c}} \right) \quad \text{if} \quad \delta < 0 \qquad \text{(Contact)} \tag{2.44}$$

where K_{pen} is a penalty coefficient. According to [Roe and Siegmund, 2003], the value of K_{pen} should be around 10 in order to have an significant stiffness.

As we are tackling here a non-linear problem through an implicit finite element (FE) approach, a set of non-linear algebraic equations must be solved. This set of non-linear equations is solved by the Newton-Raphson method, which linearizes the equations by the first order Taylor's development. In order to solve this problem, the tangent stiffness matrix (i.e., the Hessian matrix) for the irreversible exponential cohesive law presented above should be computed. A detailed calculation of the cohesive stiffness matrix is presented in Appendix A.1.

2.3.2 Xu and Needleman's cohesive law

According to [Xu and Needleman, 1993], the simplest constitutive relation for an interface is an elastic one. In this case, the traction through the interface is written as a function of the displacement jump (opening) through the interface. Due to this, the work of separation is path independent. So, through the work of separation and the strength in the normal and tangential directions, and by coupling parameters, the interface can be characterized. The potential ϕ from which the cohesive law is derived is:

$$\phi(d^n, d^t) = \phi_n + \phi_n e^{-\frac{d^n}{\delta_{cn}}} \left\{ \left[1 - r + \frac{d^n}{\delta_{cn}} \right] \left[\frac{1-q}{r-1} \right] - \left[q + \left(\frac{r-q}{r-1} \right) \frac{d^n}{\delta_{cn}} \right] e^{-\left(\frac{d^t}{\delta_{ct}} \right)^2} \right\} \tag{2.45}$$

Where $\phi_n = \sigma_c e \delta_{cn}$, $\phi_t = \sqrt{\frac{e}{2}} \tau_c \delta_{ct}$, $q = \phi_t / \phi_n$, $r = d^{*n}/\delta_{cn}$. d^n and d^t are respectively, the normal and tangential components of the separation between the two interfaces. ϕ_n and ϕ_t are the normal and tangential energies released by the normal and tangetial crack processes. σ_c and τ_c are the normal and shear criticial stresses. δ_{cn} and δ_{ct} are the normal and tangential separation when the stresses are at maximum. Finally, d^{*n} is the value of the normal separation (d^n) after shearing to the state $d^t = \frac{1}{2}\delta_{ct}$ under the condition of zero normal tension (i.e., $T^n = 0$). Generally in the literature $r = 0$ [Rahulkumar et al., 2000, Roe and Siegmund, 2003]. The interfacial tractions (T^n and T^t) are obtained by differentiating Equation 2.45 with respect to the components of the separation (opening) (δ^n and δ^t):

$$\begin{aligned} T^n(d^n, d^t) &= -\frac{\partial \phi}{\partial \delta_n} \\ T^t(d^n, d^t) &= -\frac{\partial \phi}{\partial \delta_t} \end{aligned} \tag{2.46}$$

Thus using equations (2.45) and (2.46) we have:

$$\begin{aligned} T^n(d^n, d^t) &= \left(\frac{\phi_n}{\delta_{cn}}\right) e^{-\left(\frac{d^n}{\delta_{cn}}\right)} \left\{ \left(\frac{d^n}{\delta_{cn}}\right) e^{-\left(\frac{d^t}{\delta_{ct}}\right)^2} + \left[\frac{1-q}{r-1}\right] \left[1 - e^{-\left(\frac{d^t}{\delta_{ct}}\right)^2}\right] \left[r - \frac{d^n}{\delta_{cn}}\right] \right\} \\ T^t(d^n, d^t) &= \left(\frac{\phi_n}{\delta_{cn}}\right) \left(\frac{2\delta_{cn}}{\delta_{ct}}\right) \left(\frac{d^t}{\delta_{ct}}\right) \left\{ q + \left[\frac{r-q}{r-1}\right] \frac{d^n}{\delta_{cn}} \right\} e^{-\left(\frac{d^n}{\delta_{cn}}\right)} e^{-\left(\frac{d^t}{\delta_{ct}}\right)^2} \end{aligned} \tag{2.47}$$

Figure 2.7 shows the tangential and normal behaviour of the cohesive law in the case of uncoupled modeling. Figure 2.7a shows the variation of the normal traction (T^n) as a function of the normal opening (d^n) for $d^t = 0$. The variation of the tangential traction (T^t) as a function of the tangential opening (d^t) for $d^n = 0$ is shown in Figure 2.7b.

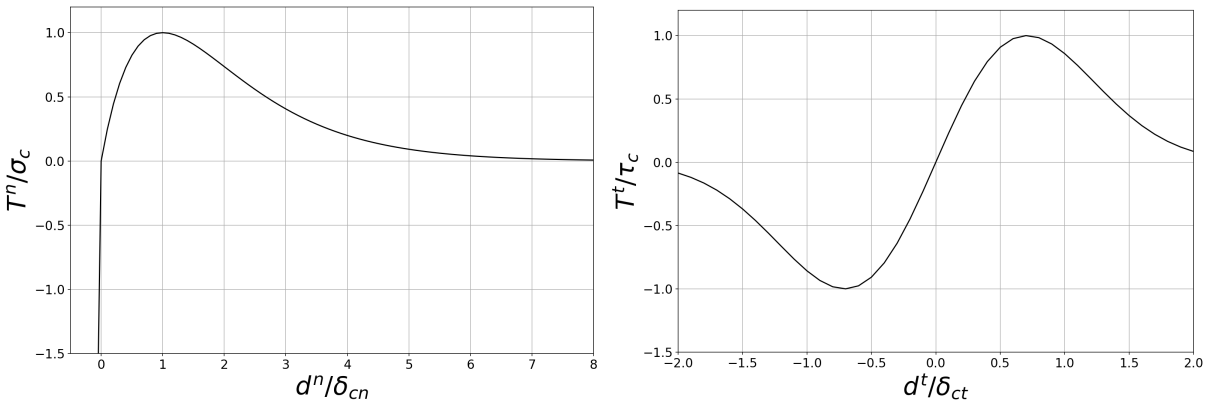

(a) Variation of the normal traction (T^n) as a function of the normal opening (d^n) for $d^t = 0$.

(b) Variation of the tangential traction (T^t) as a function of the tangential opening (d^t) for $d^n = 0$.

Figure 2.7: Relative normal and tangential cohesive traction-separation curves for uncoupled modeling.

For the case where the normal work of separation and the shear work of separation are equal, Figure 2.8 shows the tangential and normal behaviour of the cohesive law when coupling them under mixed mode fracture. If the normal opening displacement increases, then the tangential traction decreases. In the same way, if the tangential opening displacement increases, then the normal traction decreases.

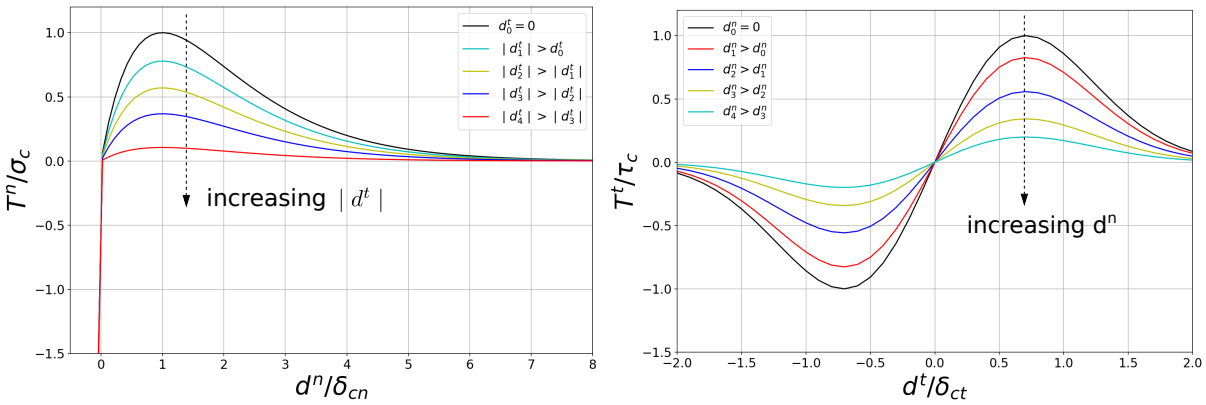

(a) Normal behaviour.

(b) Tangential behaviour.

Figure 2.8: Relative cohesive traction-separation curve for the case of coupled modeling.

Figure 2.9 shows that when unloading takes place, the relation between the cohesive traction and the opening of the interface is linear, this behavior remains linear during reloading until the opening reaches the value when unloading started [Roe and Siegmund, 2003].

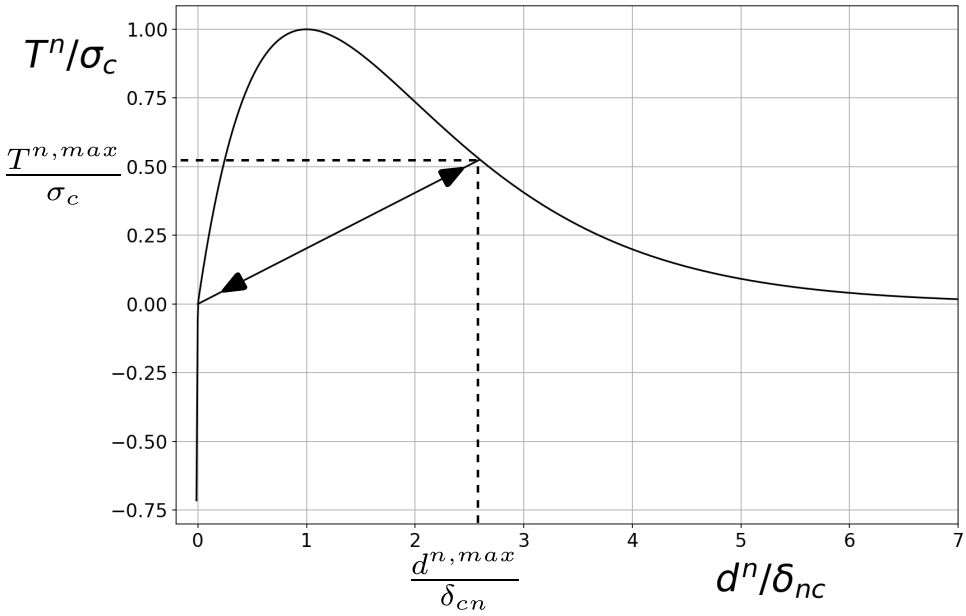

Figure 2.9: Normal traction (T^n) curve in case of loading and unloading.

Then the interface traction follows the constitutive law governed by equation (2.47). To determine the linear relation due to loading or unloading accounting also for the crack mode, three additional variables are computed:

$$\begin{cases} \Psi_t = \frac{|d^t|}{\delta_{ct}} \\ \Psi_n = \frac{\langle d^n \rangle}{\delta_{cn}} \\ \Psi_{oi} = \max_p\{\Psi_i(p)\} \quad \text{with } i \;=\; t \text{ or } n \end{cases} \tag{2.48}$$

Where Ψ_{oi} is the maximum value of Ψ_i during the loading history, p is the time, $|\,d^t\,|$ is the absolute value of the tangential opening and $\langle d^n \rangle$ equal 0 when $d^n \leq 0$ or d^n if $d^n > 0$. The

linear behavior takes places when Ψ_i is less than Ψ_{oi}. Thus, the constitutive law for the traction becomes:

$$T^i = d^i \frac{T^{i,max}}{d^{i,max}} \quad \text{if} \quad \Psi_i < \Psi_{oi} \quad \text{with } i \ = \ t \ or \ n \tag{2.49}$$

where $T^{i,max}$ and $d^{i,max}$ are respectively, the cohesive traction component and the opening of the interface before unloading begins.

As in the case of Ortiz and Pandolfi's cohesive law, if there is contact between the cohesive interfaces ($d^n < 0$), as shown in Figure 2.7a, a penalization term will be added, making the cohesive interface acts like a spring with a high constant (K_{pen}):

$$\begin{aligned} T^n(d^n, d^t) = \left(\frac{\phi_n}{\delta_{cn}}\right) e^{-\left(\frac{d^n}{\delta_{cn}}\right)} \left\{ \left(\frac{d^n}{\delta_{cn}}\right) e^{-\left(\frac{d^t}{\delta_{ct}}\right)^2} + \left[\frac{1-q}{r-1}\right] \left[1 - e^{-\left(\frac{d^t}{\delta_{ct}}\right)^2}\right] \left[r - \frac{d^n}{\delta_{cn}}\right] \right\} \\ + K_{pen} \ \sigma_c \ e \left(\frac{d^n}{\delta_{cn}}\right) e^{-\left(\frac{d^n}{\delta_{cn}}\right)} \qquad \text{if} \quad d^n < 0 \qquad \text{(Contact)} \end{aligned} \tag{2.50}$$

where K_{pen} is a penalty coefficient. Expression of the tangent matrix for the [Xu and Needleman, 1993]'s cohesive law is presented in detail in Appendix A.2.

2.3.3 Viscous regularization

Even though cohesive zone models are very common methods to simulate fracture process in engineering applications, it is well documented that they can induce some instability called solution jumps or elastic snap-back [Volokh, 2004, Jiang, 2010, Needleman, 2014, Sepasdar and Shakiba, 2020]. These instabilities come up just after the peak strength has been reached. When performing quasi-static finite element simulations in an implicit scheme, combined with certain cohesive law parameters and mesh size, at the point of instability, simulations are not able to converge to an equilibrium solution [Gao and Bower, 2004, Hamitouche et al., 2008, Needleman, 2014]. In order to avoid convergence problems in finite element simulations due to displacement jump, different authors suggested adding some viscosity terms [Chaboche et al., 2001, Gao and Bower, 2004]. The work of [Gao and Bower, 2004] showed that, although some additional energy dissipation is introduced into the computations due to the addition of viscosity terms, convergence in the solution is achieved for a small enough time-step and for any nonzero viscosity value.

In order to identify whether instabilities will appear in the computation, [Gao and Bower, 2004] introduced a dimensionless parameter (Λ). This parameter relates the stiffness of the solid with the stiffness of the interface. Λ is equal to:

$$\Lambda = \frac{E\delta_c}{2a\sigma_c} \tag{2.51}$$

Where E is the Young's modulus, σ_c is the maximun cohesive normal traction, δ_c is the characteristic opening displacement and a is the height of the specimen. [Gao and Bower, 2004] showed that, for $\Lambda > e^{-1}$ the interface separation is smooth, meanwhile for the case when $\Lambda < e^{-1}$, the interface separation is unstable. Here $e^{-1} = exp(-1) \approx 0.3679$.

In order to show the effectiveness of the implemented viscous regularization technique, the configuration shown in Figure 2.10 will be used. For simulation purposes, the Young's modulus (E) depicted in Figure 2.10 will take different values leading to different values of the dimensionless parameter Λ. In the first case, $E = 3 \times 10^5 \frac{N}{mm^2}$ and therefore $\Lambda = 1.4545 > \frac{1}{e}$. In this case, the simulation does not exhibit any convergence problem. Figure 2.11 shows the *force-displacement* curve without convergence problems. Then, the following sections briefly present how to include viscous dissipation in the different implemented cohesive laws.

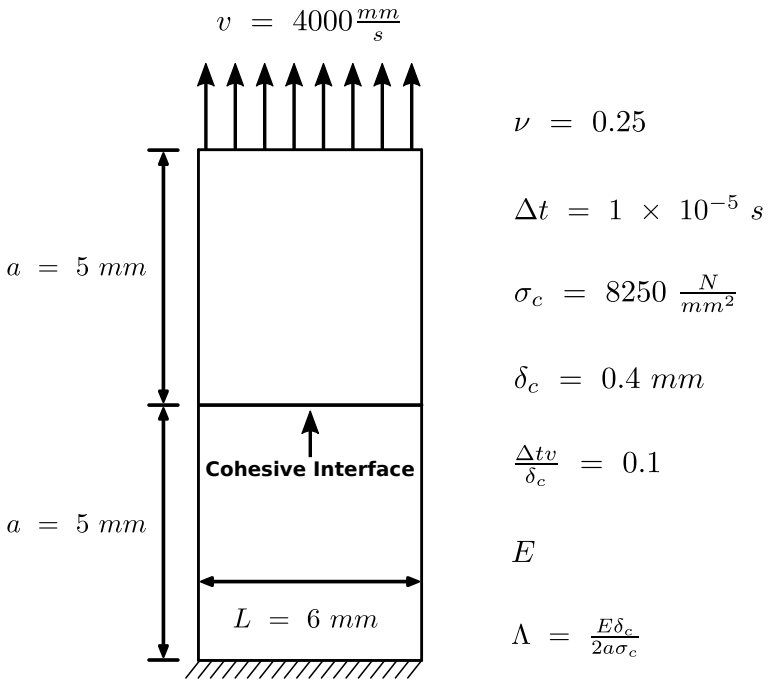

Figure 2.10: Geometry and boundary conditions for the test example.

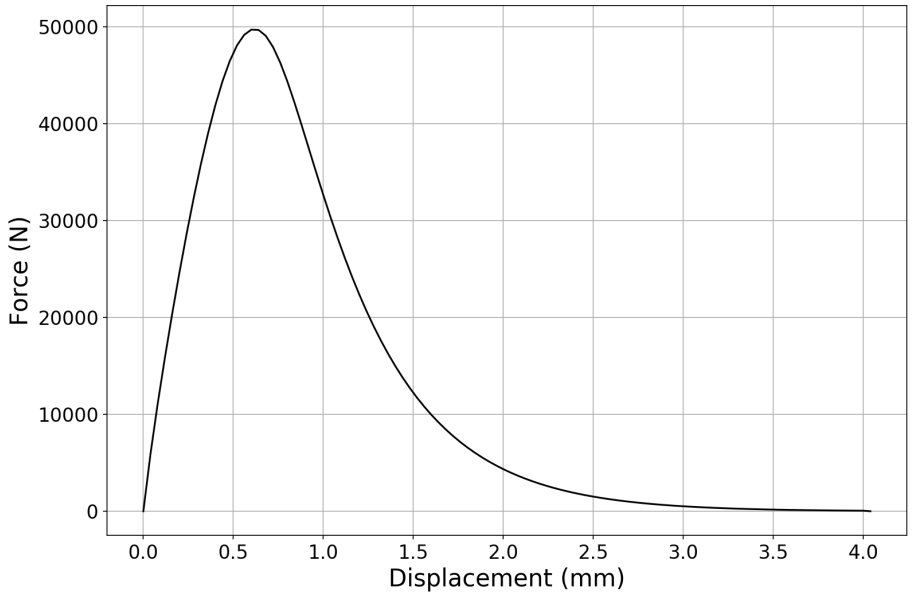

Figure 2.11: *Force-displacement* curve for the case of a stable simulation.

2.3.3.1 Ortiz and Pandolfi's cohesive law

When using this kind of exponential cohesive law, [Sepasdar and Shakiba, 2020] proposed the addition of the following viscosity term:

$$t = e\sigma_c \frac{d}{\delta_c} e^{-\frac{d}{\delta_c}} + \xi \frac{\sigma_c}{\delta_c} \dot{d} \tag{2.52}$$

where ξ is a viscosity-like parameter that governs viscous energy dissipation and $\dot{d}$ is the derivative of the effective opening displacement (d) with respect to the time ($\mathbf{t}$): $\dot{d} = \frac{dd}{d\mathbf{t}}$. The expression of the tangent stiffness matrix for Ortiz and Pandolfi's cohesive law when including viscous dissipation is presented in detail in Appendix A.3.

The test example presented in Figure 2.10 is used again but, in this case the Young's modulus is decreased ($E = 4.2 \times 10^4 \frac{N}{mm^2}$). When E decreases, then Λ also decreases ($\Lambda = 0.2036 < \frac{1}{e}$), making necessary the addition of the terms regarding viscous dissipation.

Figure 2.12 shows the solution of the problem using the aforementioned viscous regularization technique when using Ortiz and Pandolfi's cohesive law. In this figure, the red arrow points out the instability problem when viscous terms equal zero (black curve). It is also shown that the higher the value of the viscosity, the higher the effect on the solution.

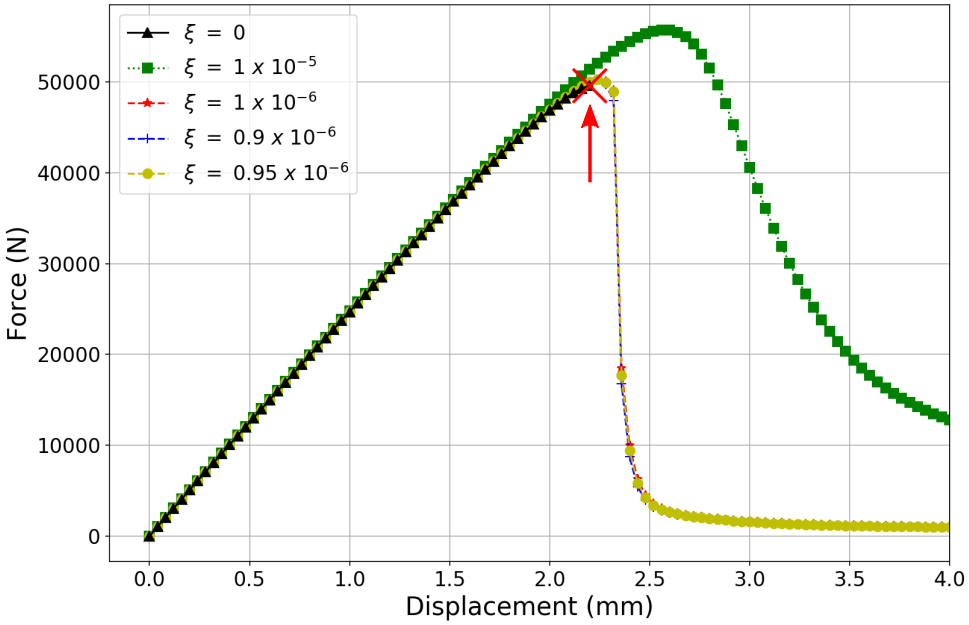

Figure 2.12: *Force-displacement* curve for the case of an unstable simulation using Ortiz and Pandolfi's cohesive law with viscous dissipation.

2.3.3.2 Xu and Needleman's cohesive law

When using the exponential cohesive law presented by [Xu and Needleman, 1993], [Gao and Bower, 2004] proposed the addition of some viscosity term in the following way:

$$T^{*n}(d^n, d^t) = \left(\frac{\phi_n}{\delta_{cn}}\right) e^{-\frac{d^n}{\delta_{cn}}} \left\{ \left(\frac{d^n}{\delta_{cn}}\right) e^{-\frac{d^{2t}}{\delta_{ct}^2}} + \left[\frac{1-q}{r-1}\right] \left[1 - e^{-\frac{d^{2t}}{\delta_{ct}^2}}\right] \left[r - \frac{d^n}{\delta_{cn}}\right] \right\} \left\{1 + \xi_n \frac{d}{dt}\left(\frac{d^n}{\delta_{cn}}\right)\right\}$$

$$T^{*t}(d^n, d^t) = \left(\frac{\phi_n}{\delta_{cn}}\right) \left(\frac{2\delta_{cn}}{\delta_{ct}}\right) \left(\frac{d^t}{\delta_{ct}}\right) \left\{q + \left[\frac{r-q}{r-1}\right] \frac{d^n}{\delta_{cn}}\right\} e^{-\frac{d^n}{\delta_{cn}}} e^{-\frac{d^{2t}}{\delta_{ct}^2}} \left\{1 + \xi_t \frac{d}{dt}\left(\frac{d^t}{\delta_{ct}}\right)\right\} \tag{2.53}$$

Where $T^{*n}(d^n, d^t)$ and $T^{*t}(d^n, d^t)$ are the interfacial tractions when adding some viscosity terms. ξ_n and ξ_t are viscosity-like parameters that govern viscous energy dissipation under normal and tangential loading, respectively. Expression of the tangent stiffness matrix for Xu and Needleman's cohesive law when including viscous dissipation is presented in detail in Appendix A.4.

As in the previous section, the same test example presented in Figure 2.10 is used ($E = 4.2 \times 10^4 \frac{N}{mm^2}$ and $\Lambda = 0.2036$). Again in this case $\Lambda < \frac{1}{e}$, making necessary the addition of the terms regarding viscous dissipation. As it was done previously, the solution for this case using the implemented viscous regularization technique is computed.

Figure 2.13 shows the solution of the problem taking into account the aforementioned viscous regularization technique when using Xu and Needleman's cohesive law. In this figure, the red

circle highlights instability issues in the curves where the value of the viscosity-like parameter is too small to overcome the convergence problems. Figure 2.13 also shows that the higher the value of the viscosity, the higher the effect on the solution. The remarkable difference in the values of the viscosity-like parameter used here compared with the ones used in Figure 2.12, could be explained by the way the viscous term was defined in each one of these cases (See equations (2.52) and (2.53).

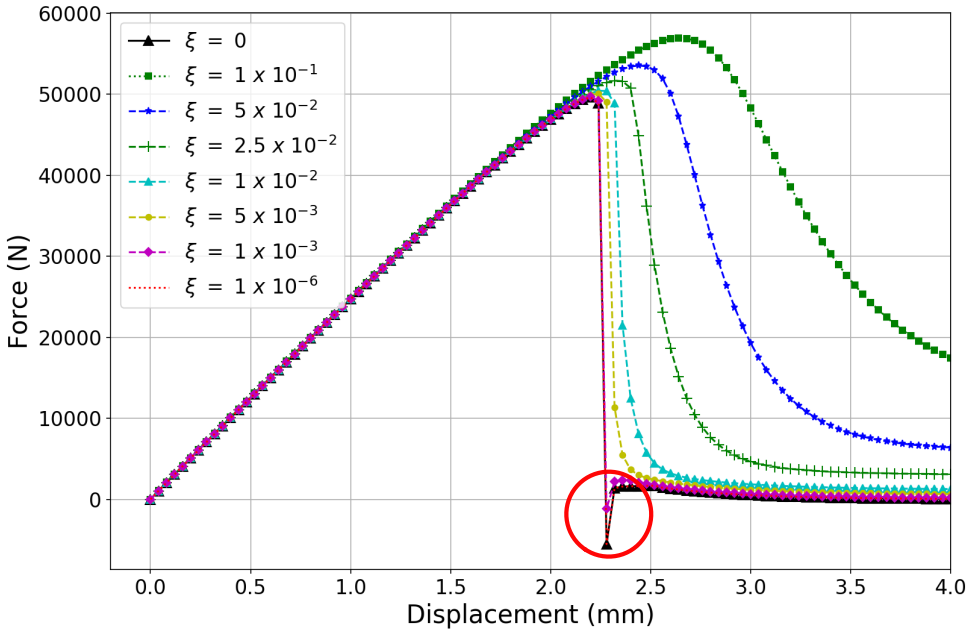

Figure 2.13: *Force-displacement* curve for the case of an unstable simulation using Xu and Needleman's cohesive law with viscous dissipation.

Regarding cohesive zone models including viscous regularization technique, the results presented in this section showed that the performed implementation is appropriate enough when tackling fracture problems in the presence of numerical difficulties. Even though the two-dimensional simulations carried out in this PhD thesis did not require the use of the viscous regularization technique, this implementation was performed thinking about future three-dimensional applications where convergence problems are more common.

2.4 Thermolasticity model

As one of the main applications of the current PhD thesis aims at applying fracture mechanics theory in order to study failure phenomenon on airless bodies of the solar system, an appropriate thermoelasticity model has to be implemented. This is important since it is thought that observed fractures on these bodies are mainly driven by strong temperature variations resulting from the cycles between day and night. In this section the basic background of the implemented thermoelastic model will be presented. First, the way thermal and mechanical equations are related through a weak coupling will be briefly described.

2.4.1 Coupling formulation

Temperature changes (ΔT) produce strains having a nature inherently dilatational (i.e., thermal expansion or contraction) and do not cause any shear. To account for these strains in a mechanical problem, one way is to include the thermal strains originated by the variation of the temperature into the total strain of the body.

Let's decompose the strain into two components:

$$\epsilon_{ij} \;=\; \epsilon_{ij}^{elastic} \;+\; \epsilon_{ij}^{thermal}; \tag{2.54}$$

where $\epsilon_{ij}^{elastic}$ and $\epsilon_{ij}^{thermal}$ are respectively, the elastic and thermal strain tensors. The thermal strain is proportional to temperature changes and defined as:

$$\epsilon_{ij}^{thermal} \;=\; \alpha \Delta T \delta_{ij} \;, \qquad \text{where } \Delta T = T - T_{ref} \tag{2.55}$$

In equation (2.55), α is the thermal expansion coefficient, ΔT is the difference between the computed temperature and the reference temperature, latter one being the temperature where there is no strain and δ_{ij} is the Kronecker delta. This work also assumes an isotropic thermal expansion coefficient. Using equations (2.54) and (2.55), Hooke's law can then be written as:

$$\sigma_{ij} = \lambda \delta_{ij}(\epsilon_{kk} - 3\alpha\Delta T) + 2\mu(\epsilon_{ij} - \alpha\Delta T\delta_{ij}) \tag{2.56}$$

where σ_{ij} is the stress tensor and λ and μ are respectively, the Lamé's first and second parameters. In this PhD thesis a weak thermomechanical coupling is assumed. This means that the temperature is initially obtained from the heat problem and then introduced into the mechanics computation. For the solution of a thermoelastic problem, first, the temperature distribution inside the body is computed by solving the heat transfer problem. Then, the resulting temperature distribution is input to the mechanical problem as an initial strain. A schematic illustration of the steps followed in this work when solving the thermomechanical problem is provided in Figure 2.14. A theoretical example that allows to validate the implemented model is presented in Appendix A.5.

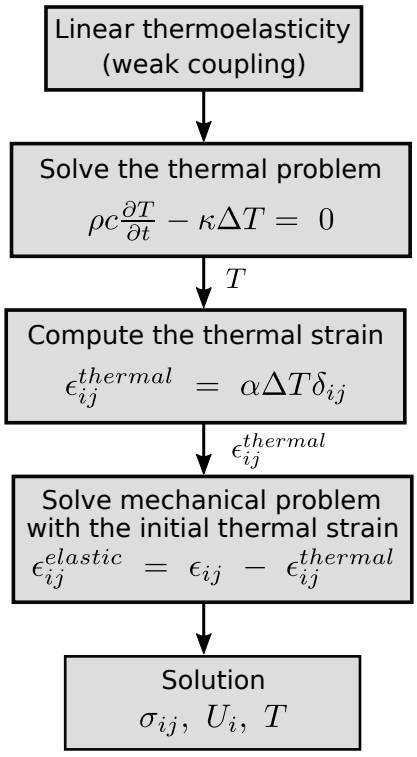

Figure 2.14: Schematic representation of the weak coupling implemented thermoelasticity model.

2.5 Gθ method implementation

As it was already stated, crack propagation requires energy. The amount of energy released during the fracture process is known as energy release rate (G). Commonly, G is widely used in the literature in order to find the crack propagation direction for a given configuration. It can be done through the maximum energy release rate criterion (MERRC), which says that the crack propagation direction will be the one which maximises the energy release rate (G). In this work, for the computation of G (i.e., crack propagation direction), the well-known and famous technique named as the $G\theta$ method presented in section 1.2.4.2 will be used. Its numerical implementation is described below.

The implementation of the $G\theta$ method requires the definition of two contours around the crack tip (i.e., C_1 and C_2). These contours divide this region into three domains C_{int}, C_{ring} and C_{ext} as shown in Figure 2.15.

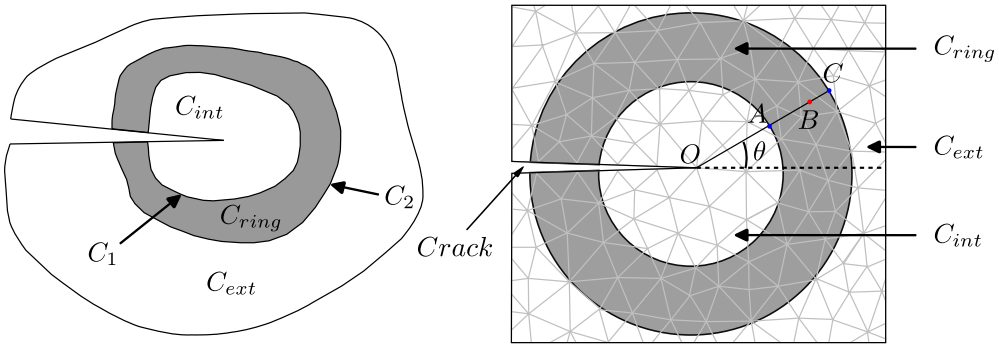

Figure 2.15: Contours and domains used to compute G using the $G\theta$ method.

In order to implement the $G\theta$ method, a virtual displacement field, $\mathbf{V}(v_1, v_2)$, representing the virtual kinematics of the crack should be defined. $\mathbf{V}(v_1, v_2)$ is given by equation (2.57):

$$\mathbf{V} = \begin{cases} v_1 = \left(1 - \frac{AB}{AC}\right)\cos(\theta) \\ \\ v_2 = \left(1 - \frac{AB}{AC}\right)\sin(\theta) \end{cases} \tag{2.57}$$

Where O is the crack tip, B is an integration point of an element belonging to the ring (C_{ring}), A and C are the intersections between OB and C_1 and C_2 respectively (inside and outside contours of the ring); and θ is the virtual direction of propagation measured with respect to the crack axis. In simple words, AB is the distance from the inside contour of the ring to the barycenter of an element belonging to the ring and AC is the width of the ring. G is computed as a function of θ, then the propagation direction is the value of θ associated with the maximum value of G. It is worth mentioning that expression (2.58) will be computed multiple times using different angles searching for the one which maximizes the energy release rate by the crack extension (See next section).

$$\begin{aligned} G = \int_\Omega \sigma_{ij} U_{j,k} V_{k,i}\, d\Omega - \frac{1}{2}\int_\Omega \sigma_{ij}\left(U_{j,i} - \alpha \Delta T \delta_{ij}\right) V_{k,k}\, d\Omega \\ + \int_\Omega \sigma_{ii} \alpha T_{,j} V_j\, d\Omega - \int_\Omega F_i U_{j,i} V_j\, d\Omega \end{aligned} \tag{2.58}$$

where U_i is the displacement field, V_i is the virtual displacement field, F_i are the body forces, α is the thermal expansion coefficient, T is the temperature and ΔT is the temperature difference between the current state and the reference configuration. Hence the values of $\mathbf{V}$ in the three domains are:

- The norm of $\mathbf{V}$ in C_{int} is equal to 1.
- The norm of $\mathbf{V}$ in C_{ring} varies continuously from 1 to 0.
- The norm of $\mathbf{V}$ in C_{ext} is equal to 0.

As is well known, one of the main objectives of this PhD is to carry out crack propagation in brittle materials with some applications on space bodies. For this reason, an important step is to find where the crack is going to propagate, not just under loadings of mechanical nature but also under loadings of thermal nature (space bodies subjected to strong gradient temperatures). In the following, the $G\theta$ method is presented under two scenarios. First, in the case without any thermal load applied. Then, the same method is used to tackle the case with thermal strain.

2.5.1 Case 1: Purely mechanical loading conditions

In this case, the $G\theta$ method is used to compute the maximun G (i.e., crack propagation direction) in the absence of body forces, forces applied directly to the crack faces and thermal loadings. Under these loading conditions, the energy release rate presented in equation (2.58) reduces to:

$$G = \int_{C_{ring}} \left(\sigma_{ij} U_{j,k} V_{k,i} - \frac{1}{2} \sigma_{ij} U_{j,i} V_{k,k} \right) dA \tag{2.59}$$

where $U_{i,j}$ is the gradient of the displacement field, V_i is the virtual displacement field, $V_{i,j}$ is the gradient of the virtual displacement field, $V_{i,i}$ is the divergence of the virtual displacement field and C_{ring} is the integration region. In Figure 2.16-**a**, elements belonging to C_{ring} are marked with a red dot. A discrete set of θ values will be used for a virtual crack propagation. The θ values are selected inside the range $[-70°, 70°]$ [Erdogan and Sih, 1963] with respect to the crack axis. For each one of the θ values, an associated G value will be computed. In Figure 2.16-**a** the virtual ring, including the considered integration points, is depicted. Figure 2.16-**b** shows that G can be computed for each value of θ, which makes the identification of the θ value that maximises $G(\theta)$ straightforward (Figure 2.16-**b**). The direction of propagation will be the value of θ that corresponds to the maximum value of G, i.e., the maximum of the curve $G(\theta)$ in Figure 2.16-**b**.

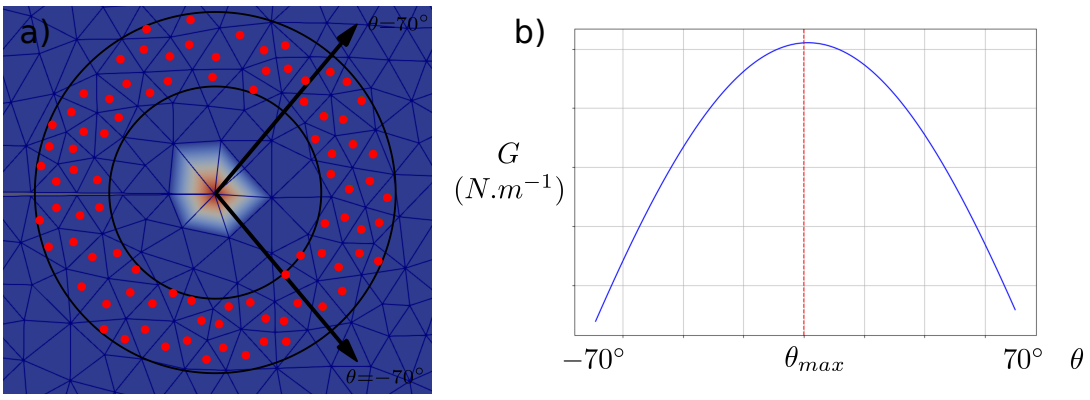

Figure 2.16: a) Ring of elements around the crack tip. b) $G(\theta)$ curve for the maximun energy release rate criterion.

To validate the implemented methodology, a well-known benchmark example will be used: *An edge-crack under mixed-mode loading*. In this benchmark, an edge crack geometry fixed at the bottom and subjected to a top unit shear load is considered. Geometry, boundary conditions as well as material properties are given in Figure 2.17.

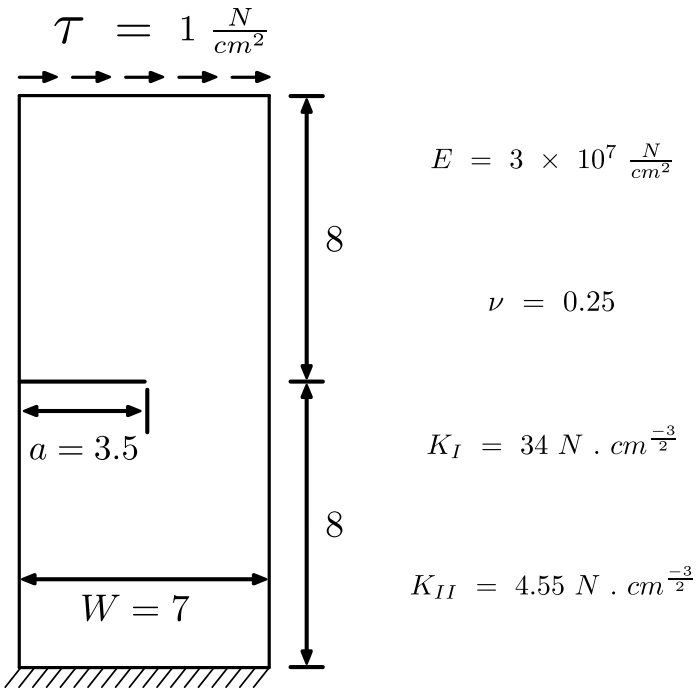

Figure 2.17: Geometry of the plate with an edge crack under shear (dimensions in cm).

In order to prove that the computation of the crack propagation direction through the $G\theta$ method implemented here is accurate, the simulated crack propagation direction was compared against the direction value computed using the theoretical crack growth methodology based on the local stress fields at the crack tip (LEFM) (See section 1.2.4.1).

Before presenting the results regarding validation of the $G\theta$ method under loadings of mechanical nature, it is worth mentioning that the element size of the mesh at the crack tip neighborhood is set to a value equal to 4×10^{-6} cm. The most suitable size of the ring of elements (i.e., thickness) was determined trough a simple sensitivity analysis. According to this, the inner contour (C_1) of the ring of elements was placed at a distance equal to 3 times the average size of the elements attached to the crack tip. While the outer contour (C_2) was placed at a distance equal to 5 times the average size of the elements attached to the crack tip. Here it must be recall the fact that the $G\theta$ method is completely mesh independent [Bouchard et al., 2003]. Additionally, taking into account that the computation of G is carried out far from the crack tip, it was found that refining the mesh does not strongly affect the results as shown in Figure 2.18.

In the benchmark example shown in Figure 2.17, the reference values of $K_I = 34\ N\ cm^{\frac{-3}{2}}$ and $K_{II} = 4.55\ N\ cm^{\frac{-3}{2}}$ are taken from [Wilson, 1969, Stern et al., 1976, Nguyen-Xuan et al., 2012]. Using these values and equation (1.23), the computed exact value of the direction of propagation is $\theta = -14.74°$. Using the implemented $G\theta$ method with a θ step variation of $0.01°$, the angle of propagation identified is approximately $\theta = -14.92°$. Even though this value differs slightly ($0.18°$) from the theoretical one, this is proof that the implemented methodology is able to compute a quite accurate crack propagation direction. To calculate the aforementioned value using the approach presented here, only the direction calculated at the first time step once the crack has reached the threshold that allows its propagation was taken.

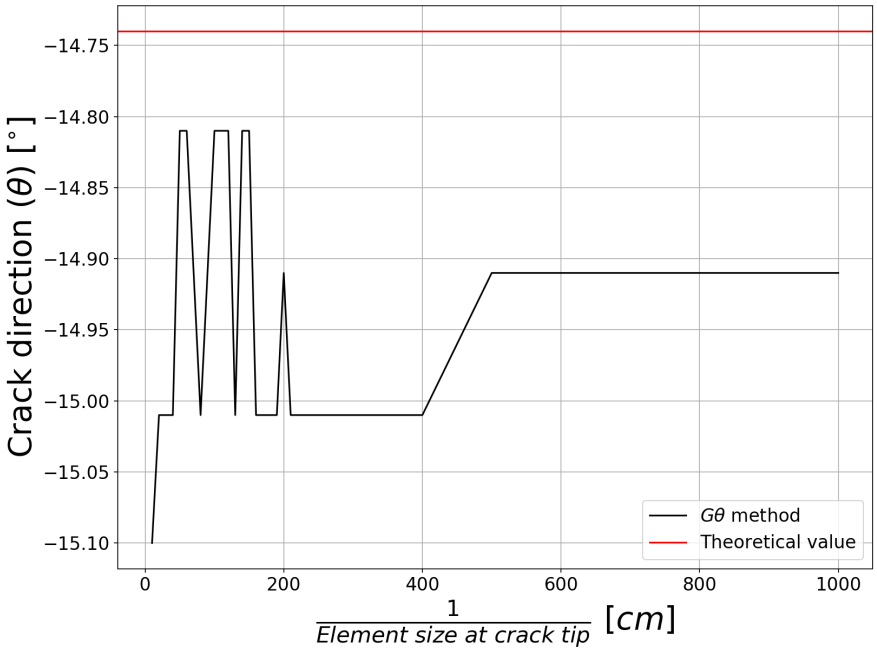

Figure 2.18: Convergence analysis of the crack propagation direction (θ) with respect to the mesh size at the crack tip neighborhood.

2.5.2 Case 2: Combined mechanical and thermal loading conditions

In this case, the implemented $G\theta$ method is tested through the computation of the stress intensity factor in mode I loading (K_I) under the presence of thermal effects. Under this scenario, the energy release rate presented in equation (2.58) reduces to:

$$G = \int_{\Omega} \left(\sigma_{ij} U_{j,k} V_{k,i} - \frac{1}{2} \sigma_{ij} \left(U_{j,i} - \alpha \Delta T \delta_{ij} \right) V_{k,k} + \alpha \sigma_{ii} T_{,j} V_j \right) \, d\Omega \tag{2.60}$$

where $U_{i,j}$ is the gradient of the displacement field, V_i is the virtual displacement field, $V_{i,j}$ is the gradient of the virtual displacement field, $V_{i,i}$ is the divergence of the virtual displacement field, α is the thermal expansion coefficient, ΔT ($\Delta T = T - T_{ref}$) is the temperature difference between the current state and the reference configuration, δ_{ij} is the Kronecker delta, $T_{,j}$ is the gradient of the temperature and Ω is the integration region.

In order to validate the implemented $G\theta$ method when thermal strain is present, the work of [Hellen et al., 1982] was used as reference. In that work the stress intensity factors are calculated at the crack tip in thermally stressed structures. The problem tackled in [Hellen et al., 1982] is a plate of length b fixed at opposite ends with an edge crack of length a. A linear temperature gradient is supposed to exist along the crack direction. K_I is computed for different geometrical relations between the crack length and the plate width (a/b). Geometry, boundary conditions as well as material properties of the benchmark example are given in Figure 2.19.

In [Hellen et al., 1982]'s work, the stress intensity factor K_I is computed using different methodologies such as the virtual crack extension method (VCE) [Parks, 1974, Hellen, 1975], an analytical approach using Green's integral and correction factors (K^*) [Muskhelishvili, 1977, Hellen and Cesari, 1979], J^* integral with a suitable correction term for the thermal effects [Blackburn et al., 1977], as well a analytical approach proposed in [Hellen et al., 1982]. In the comparison that will be presented below, plane strain conditions were assumed and the stress intensity factor (K_I) was normalized by:

$$K_0 = E \; T_0 \; \alpha \; \sqrt{b}/(1-\nu) \tag{2.61}$$

where E is the Young's modulus, ν Poisson's ratio, α is the thermal expansion coefficient, T_0

is the applied temperature and b is the plate width. The result that is obtained using the implemented methodology in current work is in terms of the energy release rate (G), for this reason and assuming plane strain conditions, K_I can be computed through equation (2.62) (see section 1.2):

$$K_I = \sqrt{\frac{G\ E}{1-\nu^2}} \tag{2.62}$$

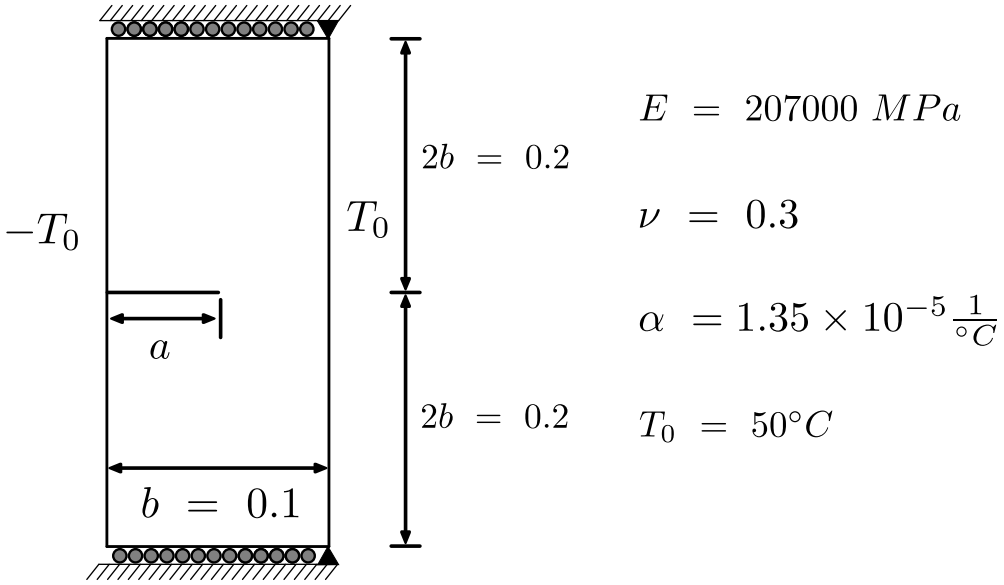

Figure 2.19: Geometry and boundary conditions (units in m).

Figure 2.20 shows the results obtained in [Hellen et al., 1982] and the results coming from the approach proposed in this work ($G\theta$ method). According to [Hellen et al., 1982], the results obtained using the three computational methods (i.e., VCE, K^*, J^* integral) are in very good agreement over the range of the considered crack lengths ($a/b = 0.1$ to 0.8). The foregoing, according to the authors, implies that the calculated K_I values are very accurate. The VCE and K^* results are shown together since they always agreed. Regarding the proposed analytical approach, authors also included this multiplied by a finite width factor presented in [Hellen and Cesari, 1979]. The authors also say that it shows reasonably good agreement compared with computational approaches. Additionally, they argue that this factor can be established from the finite element results. Results obtained using the $G\theta$ method implemented in the current work are also shown in the same figure. A good agreement over the range of the considered crack lengths ($a/b = 0.1$ to 0.8) is observed.

In Figure 2.20 there are some slight differences between the proposed method and the ones used as reference, which can be attributed to the fact that probably, convergence analysis in the solution associated with the mesh size was not tackled in [Hellen et al., 1982]. Following these results, the methodology presented here to compute the stress intensity factor in the presence of thermal strain can be considered accurate enough. Additionally, the current work compares the results of the same problem when including or not including the thermal strain terms directly in the computation of the $G\theta$ method in equation (2.60). This comparison was made to estimate the influence of the thermal terms on the computation of the energy release rate. It should be recall that even if the thermal terms are not included in the computation of fracture energy (G in equation 2.60), they are included in the thermoelasticity model presented in section 2.4. Figure 2.21 shows that the effect of the direct inclusion of thermal strain is not very strong. It is practically imperceptible, especially for longer cracks. This can be one of the reasons why these additional terms are usually neglected in the literature.

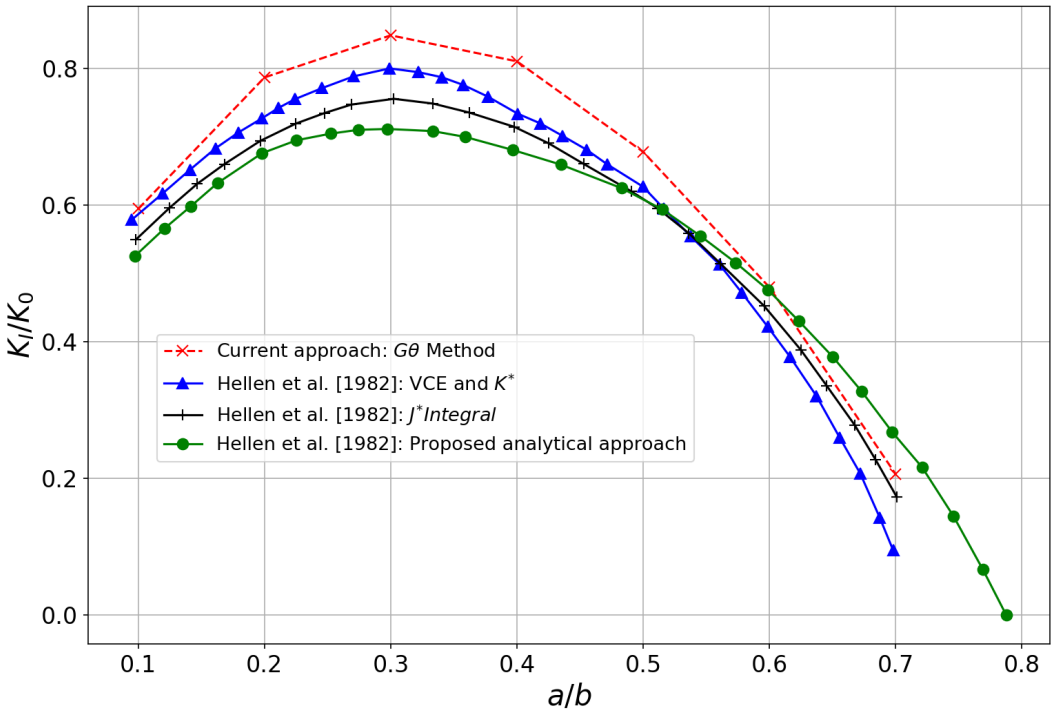

Figure 2.20: Normalized stress intensity factor (K_I/K_0) in an edge-cracked plate with linear temperature gradient for various relations between the crack length and the plate width (a/b) using different approaches.

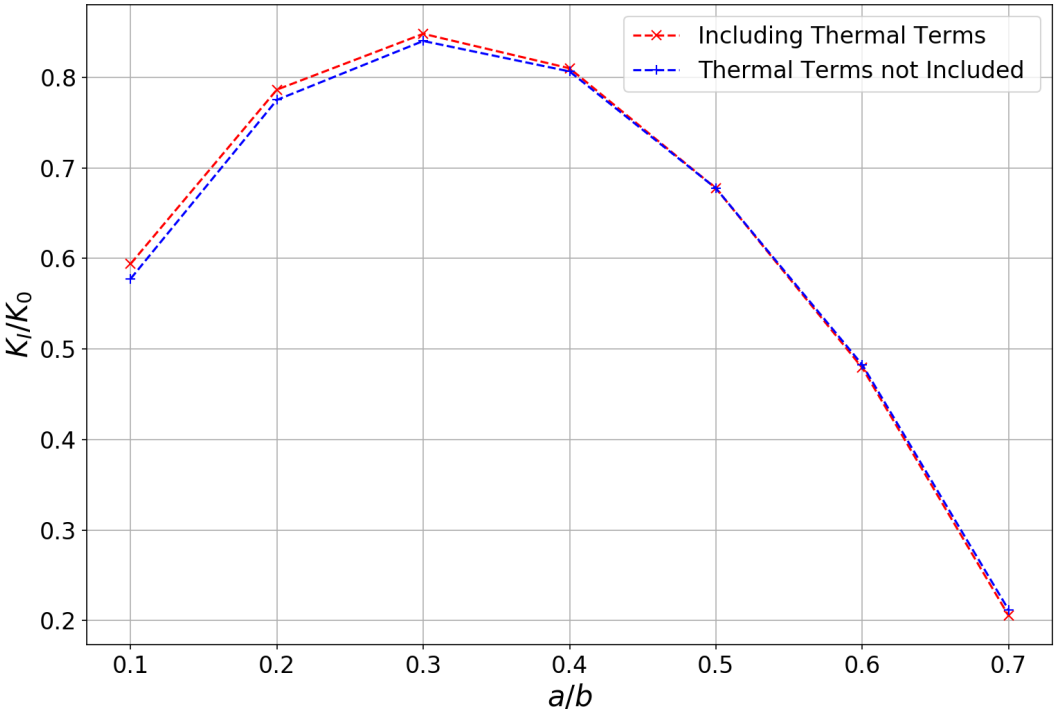

Figure 2.21: Effect of direct inclusion of thermal terms in the $G\theta$ method.

After describing the implemented methodologies in order to compute crack propagation direction under loading of different natures, the next section reviews the remeshing procedures used in this work to ensure mesh-independent crack propagation when using cohesive elements to simulate the fracture process for arbitrary crack paths.

2.6 Mesh modification methodology to perform crack propagation

As it was already stated in this work, when simulating crack propagation through the use of cohesive zone models (CZMs), the two most common problems arising are: (i) that most CZMs approaches suffer from crack-path mesh dependency and (ii) when using them, an artificial reduction of the stiffness of the material can be induced. Common strategies used to overcome these problems were already reviewed in the literature review section (i.e., section 1.3.5). In the current section, the remeshing strategy developed in this PhD to propagate a crack exactly over a computed crack propagation direction will be briefly presented. The methodology that allows the insertion of cohesive elements between two bulk or normal elements in a finite element mesh will also be introduced.

2.6.1 Fitting the mesh to the actual direction of propagation in 2D

Thanks to the advanced remeshing techniques available at CEMEF [Gruau and Coupez, 2005, Shakoor et al., 2015], in this work the finite element mesh can be fit to the crack propagation direction computed using the already presented Maximum energy release rate criterion. When the crack path is unknown, mesh dependency may appear as a consequence of the fact that cracks are only able to propagate across boundaries between bulk elements. Therefore, the crack path depends on the mesh. This issue is depicted in Figure 2.22-**b**, where the predicted crack path and the actual one are shown in blue dashed line and green line respectively. Once the direction of propagation (blue dashed line in Figure 2.22-**a**) is computed using a suitable criterion, Figure 2.22-**b** shows the procedure that has been widely used to insert cohesive elements. These are inserted through the closest edges and nodes to the computed direction. The insertion of cohesive elements in this way exhibits a mesh dependency behaviour, so if the mesh changes, the crack pattern changes slightly as well [Shakoor et al., 2018]. When the crack path is unknown, some authors choose to insert cohesive elements on each interface between bulk elements throughout the material [Xu and Needleman, 1994, Tijssens et al., 2000]. This approach increases the number of degrees of freedom greatly and makes the predicted crack path mesh-dependent [Chiaruttini et al., 2012, Geißler et al., 2010].

Figure 2.22-**c** shows the methodology developed in current work. Before inserting the cohesive elements, a local remeshing procedure in the predicted direction is performed [Shakoor et al., 2015]. In order to perform the fitting of the mesh to the computed direction, a level-set (LS) [Osher and Sethian, 1988] function should be defined in such a way that computed direction is represented as an implicit interface, to which the mesh should be fitted. In this implicit representation, the interface (i.e., crack propagation direction) is carried by a field stored at mesh nodes. In simple words, at each node of the mesh, there is a field storing the distance from this node to the iso-zero value of the level-set (interface). When dealing with two-dimensional crack propagation, defining the level-set function is straightforward, because it just needs two things: (i) computed crack propagation direction and (ii) the coordinates of the crack tip. Using this information, a plane Π representing the implicit interface can be defined. As shown in Figure 2.23, the plane Π can be defined using the normal ($\vec{n}$) to the crack propagation direction (θ) and the coordinates of the crack tip. Finally, the value of the level-set at each node will be equal to the distance from the node to the plane.

Returning again to Figure 2.22, it is worth mentioning that contrary to the process shown in Figure 2.22-**b**, the one shown here is mesh-independent. Inserting cohesive elements **on the fly**, i.e., while the crack tip is propagating through the domain, avoids a well-known strong drawback in the implementation of cohesive zone models into a FE framework: artificial reduction of the stiffness of the material. As it was mentioned in section 1.3.5, this drawback can be overcome by using Lagrange multipliers, but it requires to develop more complex finite element formulations.

Other implications regarding how cohesive elements can be used to model fracture are discussed in [Shakoor et al., 2018].

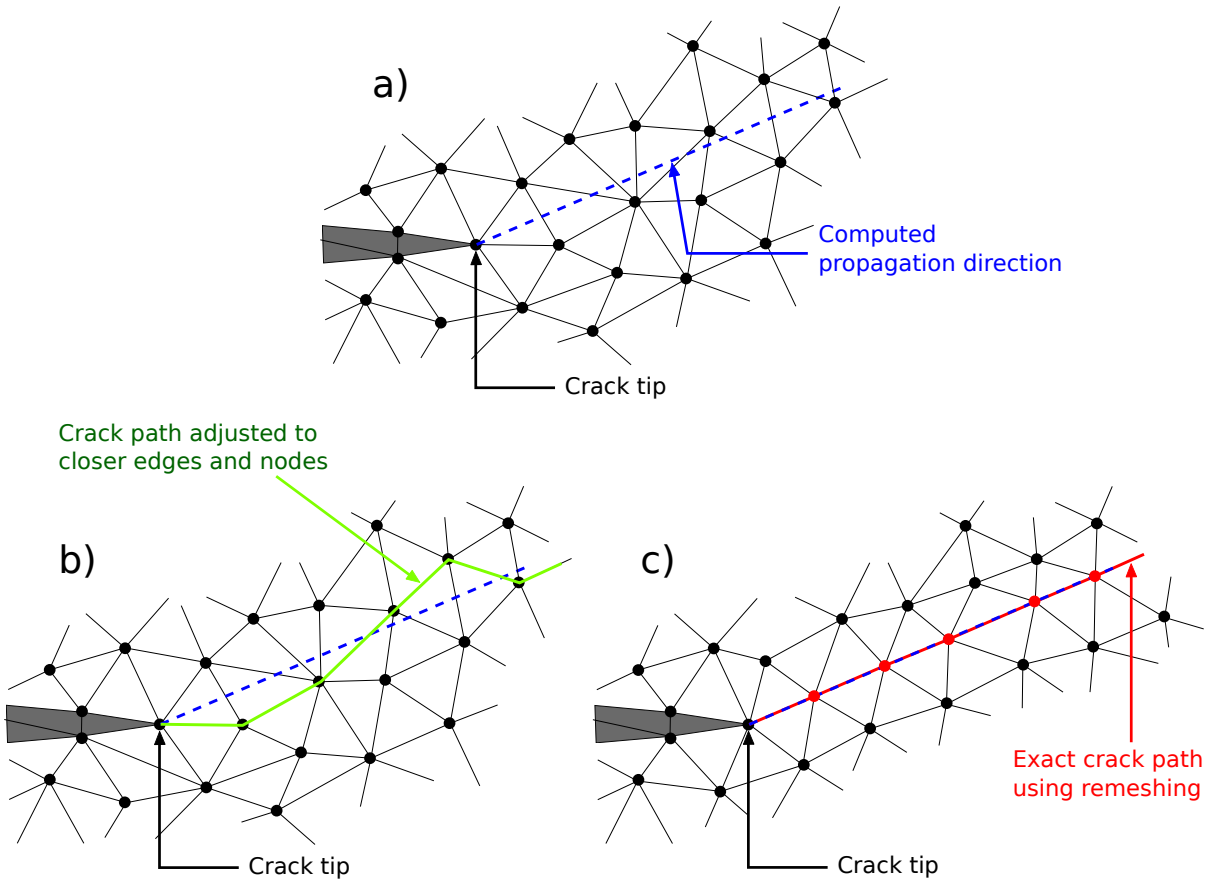

Figure 2.22: **a)** Prescribed crack path (blue dashed line). **b)** Insertion process of cohesive elements previously developed in the literature. **c)** Insertion process of cohesive elements used in this work.

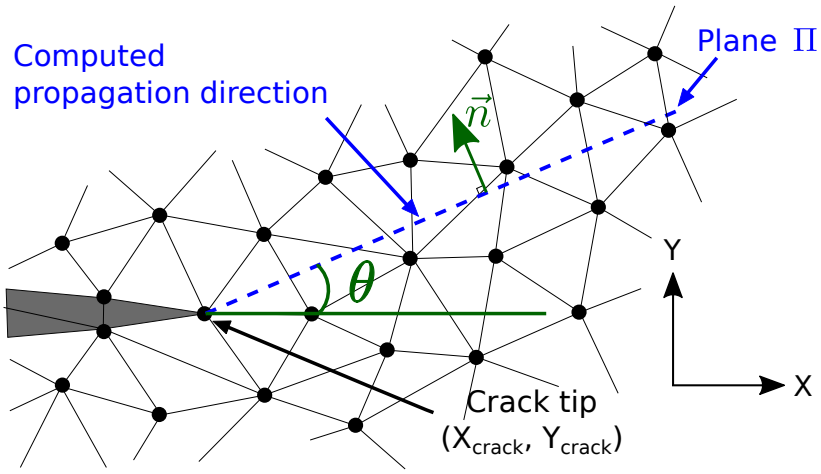

Figure 2.23: Illustration of the definition of the level-set function which is computed using a plane Π. This plane is defined using the normal vector to the propagation direction and the coordinates of the crack tip.

Remeshing procedure introduced by [Shakoor et al., 2015] works well both for 2D and 3D problems. The topology of a 3D crack is more complex. The 2D crack tip is replaced by a

3D crack front whereas the 2D crack edges are now 3D crack surfaces. For this reason, the definition of the level-set function representing the surface over which the crack front will evolve after fitting the mesh, is not trivial.

2.6.2 Computation of the fracture surface in 3D

In this section, a method for computing the fracture surface in 3D is proposed. For the sake of simplicity, an arbitrary propagation direction will be used. Due to the configuration of the loadings, the crack growth direction computed in two nodes located at different positions on the crack front can be different. But another assumption is made in this work, the propagation direction prescribed at each one of the nodes belonging to the crack front is the same *. When the crack front is a straight line as the one shown in Figure 2.24-**b**, the computation of the level-set function is still straightforward. In order to compute it, a point belonging to the crack front is picked up, in this case the point p in Figure 2.24-**c**. Using the coordinates of this point and the normal vector ($\vec{n}$) to the prescribed direction of propagation (θ), a plane Π containing all the nodes belonging to the crack front can be recalculated.

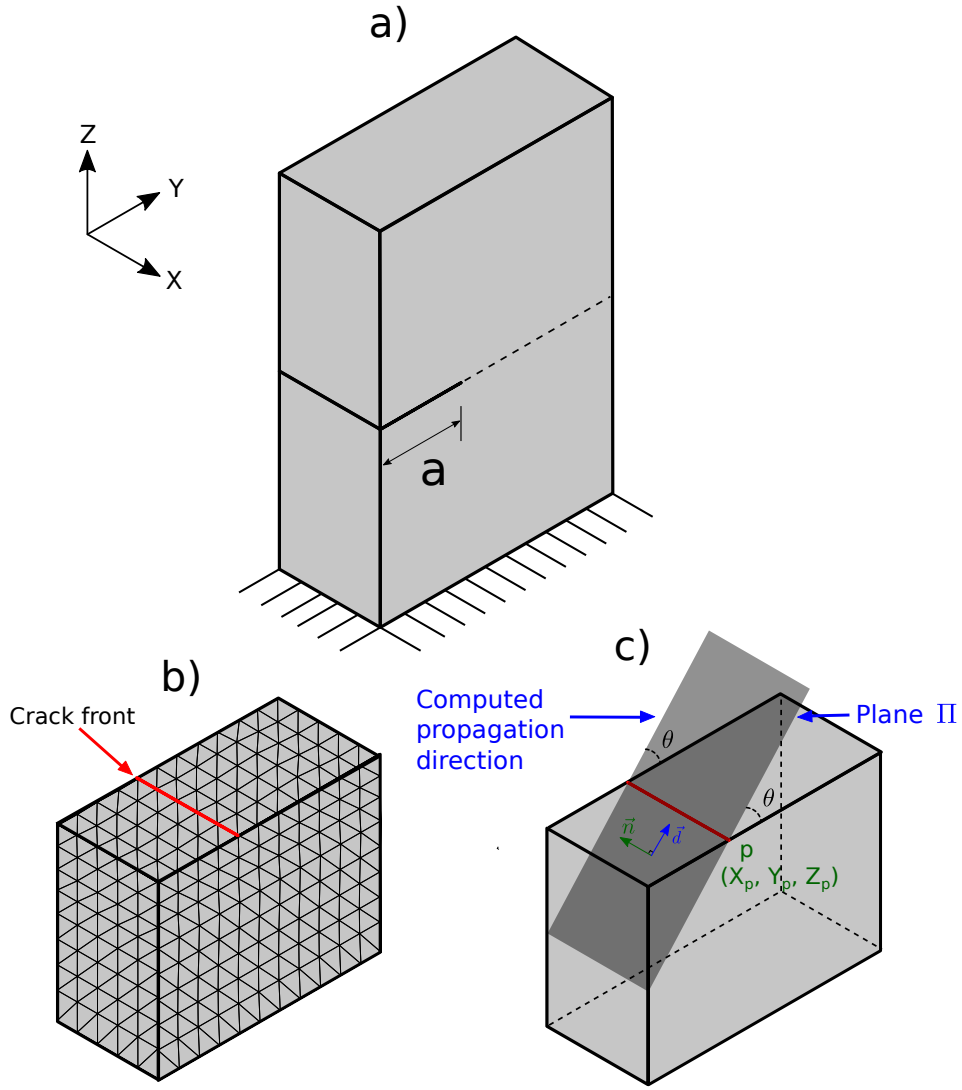

Figure 2.24: **a)** Body with a prescribed crack. **b)** Bottom half part of the domain that allows to see the plane of the rectilinear crack front. **c)** Illustration of how to define a plane Π for the computation of the level-set function when the crack front is a straight line belonging to Π.

*The propagation direction prescribed at each node of the crack front can also be different.

Then, as it was explained before, the distance between each node of the finite element mesh and the plane or interface (i.e., the iso-zero value of the level-set) is calculated. Next step is to proceed with the fitting of the mesh to the iso-zero value of the level-set function.

When the crack front is not a straight line but a curvilinear one as shown in Figure 2.25-**b**, the procedure to define the level-set function whose iso-zero value represents the interface (crack propagation direction) over which the crack front will propagate is not as simple as depicted previously. As it can be seen in Figure 2.25-**c**, the plane Π defined using the normal vector ($\vec{n}$) to the crack propagation direction (θ or $\vec{d}$) does not contain all the nodes belonging to the crack front. Intersection of the iso-zero value of the level-set function and the plane of the crack front is shown as a green dashed line, while the crack front is shown as a red dashed curved line. Plane Π is not anymore the solution we look for in order to define the desired level-set function.

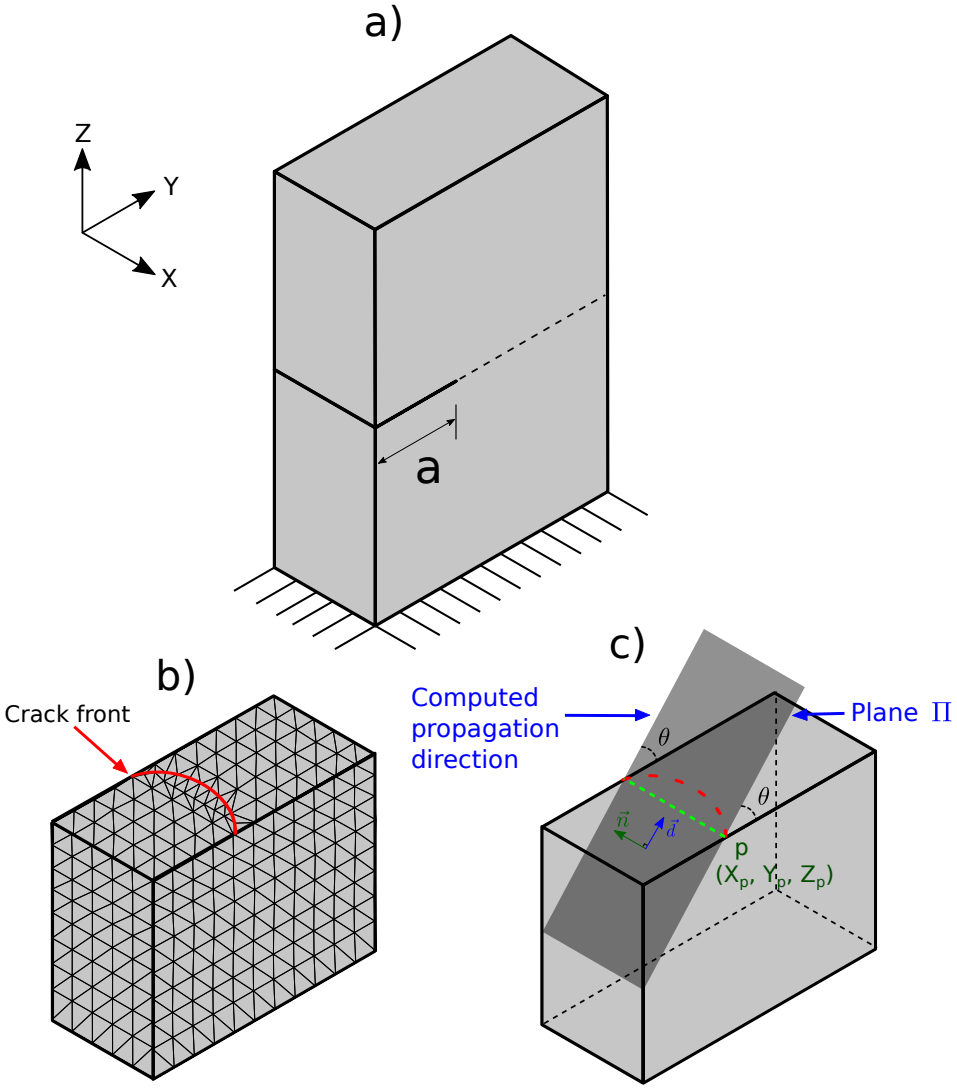

Figure 2.25: **a)** Body with a prescribed crack. **b)** Bottom half part of the domain that allows to see the plane of the curvilinear crack front. **c)** Illustration of how to define a plane Π for the computation of the level-set function, in this case, as the crack front is a not straight line but curvilinear one, the crack front does not completely belong to Π.

Let ϕ be the distance between each node of the finite element mesh and the iso-zero value of the level-set function (i.e., plane Π), $\vec{d}$ the direction in which the crack front will propagate and Γ the crack front. We would like to obtain a level-set such that the following conditions are fulfilled:

$$\begin{cases} |\nabla\phi| = 1 & (2.63) \\ \vec{d}\,.\,\nabla\phi = 0 & (2.64) \\ \phi|_{\Gamma} = 0 & (2.65) \end{cases}$$

Equation (2.63) guarantees that the gradient of the level-set function will be a unitary vector, equation (2.64) guarantees that the crack propagation direction ($\vec{d}$) or iso-zero value of the level-set and the gradient of the level-set function ($\nabla\phi$) are perpendicular. Lastly, equation (2.65) means that the value of the level-set function at the crack front is zero, guaranteeing in this way that all the nodes belonging to the crack front will be contained in the iso-zero value of the level-set. It is worth mentioning that the mathematical problem described by equations (2.63), (2.64) and (2.65) is over-constrained. It means that mathematically, find a function ϕ fulfilling all the defined constraints is not possible. In simple words, a level-set function (ϕ) completely fulfilling the constraints presented in equations (2.63), (2.64) and (2.65) does not exist. However, an approximate solution where the error is minimized can be found. To find this approximate solution, equations (2.63) and (2.64) are combined in a functional, which is minimized using equation (2.65) as Dirichlet boundary condition.

In order to find ϕ that satisfies equations (2.63), (2.64) and (2.65), the following constrained minimization problem should be solved:

$$F(\phi) = \int_{\Omega} \left(|\nabla\phi| - 1\right)^2 d\Omega + \alpha \int_{\Omega} \left(\vec{d}.\nabla\phi\right)^2 d\Omega \tag{2.66}$$

Where $F(\phi)$ is the functional to minimize, ϕ is the value of the level-set function at each node of the mesh, $\vec{d}$ is the crack propagation direction, $\alpha > 0$ is a weighting parameter controlling the effect of this term and Ω is the integration domain.

The previous minimization problem can be solved through a mixed finite element (FE) formulation, which would lead to the introduction of additional variables in the problem (i.e., α). Nevertheless, in this problem we are highly interested in completely fulfilling the constraint described by equation (2.65) and fulfilling as close as possible the second one (2.64). For this reason, in this case, we allow to relax a little bit the second constraint and, therefore, have only one unknown variable (ϕ). Therefore, the goal is to find a function ϕ satisfying the Dirichlet boundary condition $\phi = 0$ on Γ (Crack front) and minimizing F:

$$\min_{\substack{\phi \in \mathcal{H}^1(\Omega), \\ \phi|_{\Gamma}=0}} F(\phi) \tag{2.67}$$

A minimun ϕ^* is characterized by $F(\phi^* + \varepsilon\hat{\phi}) \geq F(\phi^*)$ for all $\hat{\phi}$ and $\varepsilon > 0$, with $\phi^* + \varepsilon\hat{\phi}$ *in* $\mathcal{H}^1(\Omega)$ (i.e., square integrable derivatives). Thus, a minimum ϕ^* must satisfy the Euler-Lagrange condition for stationarity:

$$\frac{\partial F(\phi^* + \varepsilon\hat{\phi})}{\partial\varepsilon}|_{\varepsilon=0} = 0 \quad \forall\hat{\phi} \in \mathcal{H}^1(\Omega) \tag{2.68}$$

The Euler-Lagrange condition in equation (2.68) is a necessary but not sufficient condition to characterize a minimum value of (2.66) [Troutman, 1996]. In this work, the variation $\hat{\phi}$ is allowed such that for sufficiently small ε, the function $\phi^* + \varepsilon\hat{\phi}$ is admissible for equation (2.67). To start the minimization process, ϕ is substituted by $\phi^* + \varepsilon\hat{\phi}$ in equation (2.66):

$$F(\phi^* + \varepsilon\hat{\phi}) = \int_{\Omega} \underbrace{\left(|\nabla\left(\phi^* + \varepsilon\hat{\phi}\right)| - 1\right)^2}_{\text{term 1}} d\Omega + \alpha \int_{\Omega} \underbrace{\left(\vec{d}.\nabla\left(\phi^* + \varepsilon\hat{\phi}\right)\right)^2}_{\text{term 2}} d\Omega \tag{2.69}$$

Then equation (2.70) is differentiated with respect to ε leading to:

$$\frac{\partial F(\phi^* + \varepsilon\hat{\phi})}{\partial \varepsilon} = \frac{\partial}{\partial \varepsilon}\left[\int_\Omega \underbrace{\left(|\nabla\left(\phi^* + \varepsilon\hat{\phi}\right)|-1\right)^2}_{\text{term 1}} d\Omega + \alpha \int_\Omega \underbrace{\left(\vec{d}.\nabla\left(\phi^* + \varepsilon\hat{\phi}\right)\right)^2}_{\text{term 2}} d\Omega\right] \tag{2.70}$$

First, the derivative of the term 1 with respect to ε is computed:

$$\frac{\partial(\text{term 1})}{\partial \varepsilon} = \frac{\partial}{\partial \varepsilon}\left[\left(|\nabla\phi^* + \varepsilon\nabla\hat{\phi}|-1\right)^2\right] \quad = \frac{2\left(|\nabla\phi^* + \varepsilon\nabla\hat{\phi}|-1\right)}{|\nabla\phi^* + \varepsilon\nabla\hat{\phi}|}\nabla\hat{\phi}\left(\nabla\phi^* + \varepsilon\nabla\hat{\phi}\right) \tag{2.71}$$

Then, the derivative of term 2 with respect to ε is computed:

$$\frac{\partial(\text{term 2})}{\partial \varepsilon} = \frac{\partial}{\partial \varepsilon}\left[\left(\vec{d}.\nabla\phi^* + \varepsilon\nabla\hat{\phi}\right)^2\right] \quad = 2\left(\vec{d}.\nabla\phi^* + \varepsilon\vec{d}.\nabla\hat{\phi}\right)\vec{d}.\nabla\hat{\phi} \tag{2.72}$$

Replacing equations (2.71) and (2.72) into (2.70) leads to:

$$\begin{aligned}\frac{\partial F(\phi^* + \varepsilon\hat{\phi})}{\partial \varepsilon} = \int_\Omega \left(\frac{2\left(|\nabla\phi^* + \varepsilon\nabla\hat{\phi}|-1\right)}{|\nabla\phi^* + \varepsilon\nabla\hat{\phi}|}\nabla\hat{\phi}\left(\nabla\phi^* + \varepsilon\nabla\hat{\phi}\right)\right) d\Omega \\ +\alpha\int_\Omega\left(2\left(\vec{d}.\nabla\phi^* + \varepsilon\vec{d}.\nabla\hat{\phi}\right)\vec{d}.\nabla\hat{\phi}d\Omega\right)\end{aligned} \tag{2.73}$$

Next, one sets $\varepsilon = 0$:

$$\frac{\partial F(\phi^* + \varepsilon\hat{\phi})}{\partial \varepsilon}|_{\varepsilon=0} = \int_\Omega \frac{2\left(|\nabla\phi^*|-1\right)}{|\nabla\phi^*|}\nabla\hat{\phi}\nabla\phi^* d\Omega + 2\alpha\int_\Omega \vec{d}.\nabla\phi^*\vec{d}.\nabla\hat{\phi}d\Omega \tag{2.74}$$

Through the previous step, the weak or variational form of the problem is obtained: Find $\phi^* \in \mathcal{H}^1(\Omega)$ such that:

$$\int_\Omega \frac{2\left(|\nabla\phi^*|-1\right)}{|\nabla\phi^*|}\nabla\hat{\phi}\nabla\phi^* d\Omega + 2\alpha\int_\Omega \vec{d}.\nabla\phi^*\vec{d}.\nabla\hat{\phi}d\Omega = 0 \quad \forall\hat{\phi} \in \mathcal{H}^1(\Omega) \tag{2.75}$$

Equation (2.75) can be also written as:

$$\int_\Omega \left[\frac{2\left(|\nabla\phi^*|-1\right)}{|\nabla\phi^*|}\mathbf{I} + 2\alpha\vec{d}\otimes\vec{d}\right] : \left(\nabla\phi^*\otimes\nabla\hat{\phi}\right)\, d\Omega = 0 \quad \forall\hat{\phi} \in \mathcal{H}^1(\Omega) \tag{2.76}$$

where ϕ^* is the minimum of (2.66) that is looked for, $\hat{\phi}$ is an arbitrary variation, $\mathbf{I}$ is the identity, $\vec{d}$ is the direction in which the crack front was assumed to propagate and α is a weighting parameter.
For the sake of simplicity in the notation, from now on:

$$\frac{\partial F(\phi^* + \varepsilon\hat{\phi})}{\partial \varepsilon}|_{\varepsilon=0} = \delta F(\phi^*) = g(\phi^*) \tag{2.77}$$

Additionally, it is also known that:

$$\Delta\phi^* = \phi_1^* - \phi_0^* \tag{2.78}$$

In order to solve the variational problem presented in (2.76), this is linearized using a first-order Taylor polynomial approximation:

$$\frac{\partial g(\phi^*)}{\partial \phi^*}|_{\phi_0^*}\,\Delta\phi^* = -g(\phi^*) \tag{2.79}$$

To solve the linearized problem presented in (2.79), the term $\frac{\partial g(\phi^*)}{\partial \phi^*}$ (i.e., Hessian matrix) must be computed. A detailed calculation of Hessian matrix is presented in Appendix A.6. Using equations (2.76), (2.79) and (A.55), the problem depicted in equation (2.67) can be solved. The solution of this problem will give, as a result, the level-set function to which the mesh will be adjusted in order to propagate the crack front. This minimization problem was solved through the implementation of a non-linear solver in our finite element library CimLib developed at CEMEF [Digonnet et al., 2007].

In order to prove the robustness and accuracy of the implemented non-linear solver, a simple test example as the one shown in Figure 2.25-**c** is used. Given an initial level-set function that was computed using the plane Π, and whose iso-zero value corresponds to the prescribed propagation direction ($\vec{d}$), the goal is to find a level-set function that fits the circular crack front (red dashed line). The iso-zero value of this level-set function should also match as close as possible the prescribed propagation direction ($\vec{d}$). The solution to this problem is shown in Figure 2.26.

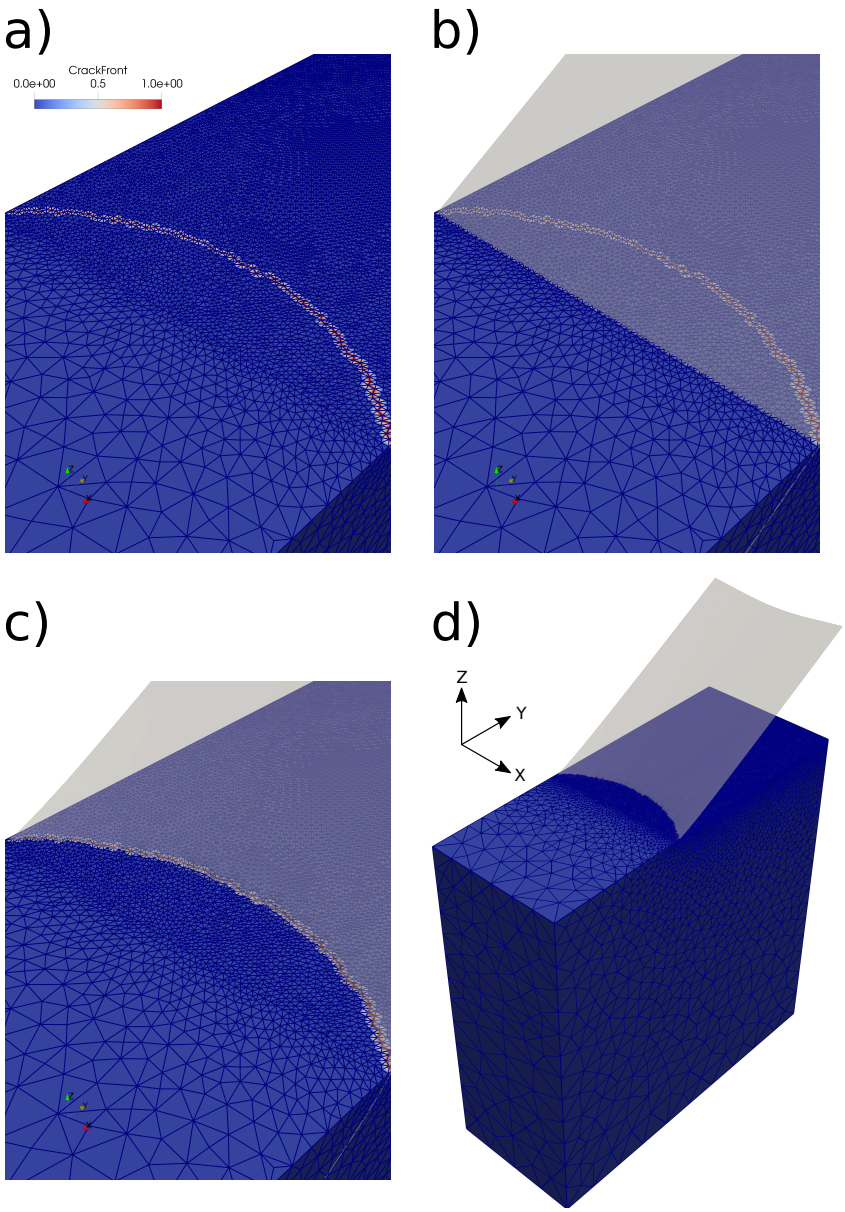

Figure 2.26: Detail top view close to the area of interest (i.e., crack front) of the example used as a test case for the implemented solver.

Figure 2.26 shows a detail view close to the area of interest (i.e., crack front) of the example used as a test case. Figure 2.26-**a** shows a top view where the circular crack front can be seen. Figure 2.26-**b** shows the initial plane (iso-zero value) which was used to compute the level-set function that was used as an initial solution of the problem. Figure 2.26-**c** shows the results where the iso-zero value of the obtained level-set function fits perfectly the circular crack front. Finally, Figure 2.26-**d** shows a zoom-out view of the problem. Now the mesh can be fit to the iso-zero value of the found level-set function using the remeshing procedures available at CEMEF [Shakoor et al., 2015].

2.6.3 Insertion process of cohesive elements

Once the remeshing has been performed, the insertion process of cohesive elements can take place. When either the crack tip in 2D or the crack front in 3D propagates through a finite element mesh, in order to simulate the fracture process taking place behind the crack tip or crack front, in this work cohesive elements will be used. They are going to be inserted over the crack path. Due to the fact that we are using only triangles (2D) and tetrahedra (3D), to completely separate two bulk or normal elements in 2D or 3D, two or three cohesive elements must be inserted between them respectively. This is illustrated in Figure 2.27, where cohesive elements are shown in red, blue and green.

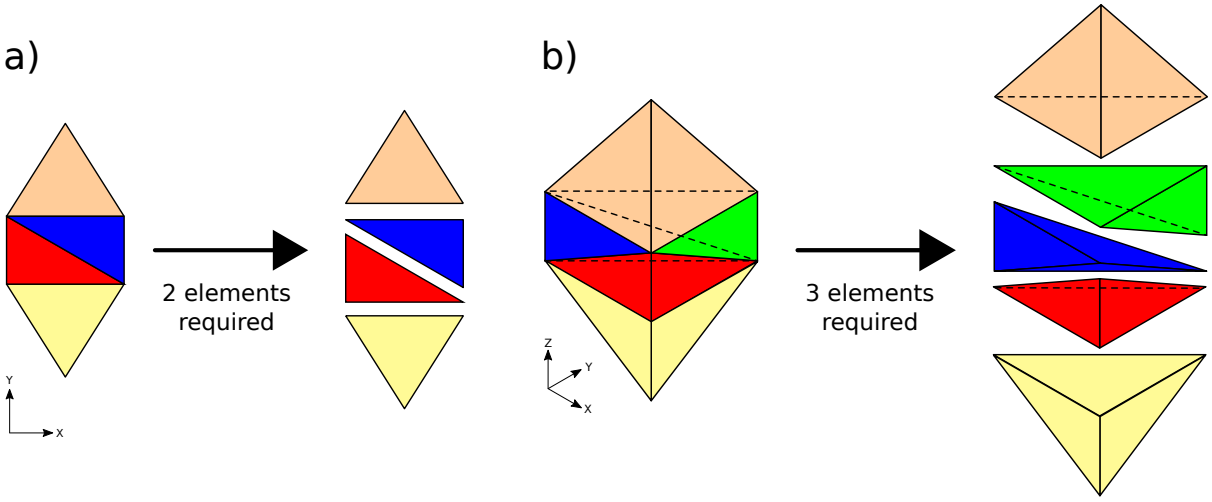

Figure 2.27: Schematic representation of the insertion process of cohesive elements in **a)** 2D and **b)** 3D.

Figure 2.28 depicts the insertion process of cohesive elements for the two-dimensional case. From this figure some important aspects must be noted. Two neighboring normal or bulk elements (i.e., non-cohesive) are connected through a shared edge (2D) or face (3D). In order to separate them, the shared edge should be tagged. When they are completely separated through the insertion of two cohesive elements between them, the inserted cohesive elements are said to belong to the same "family". For example, in Figure 2.28-**a)**, the edge shared by the elements E1 and E2 is shown in red. Once these elements are completely separated, two cohesive elements (C1 and C2) are inserted between them (Figure 2.28-**b)**). Elements C1 and C2 belong to the same cohesive "family".

Another important remark that has to be mentioned is the fact that the members of a cohesive "family" are limited, i.e., at some point the cohesive "family" will be completed. In 2D, the "family" is said to be completed when there are two cohesive elements separating two bulk elements that were initially adjacent (Figure 2.28-**b)**). All these explained concepts are very important in order to clearly understand the insertion process of cohesive elements that was performed in this PhD thesis and that will be explained later on.

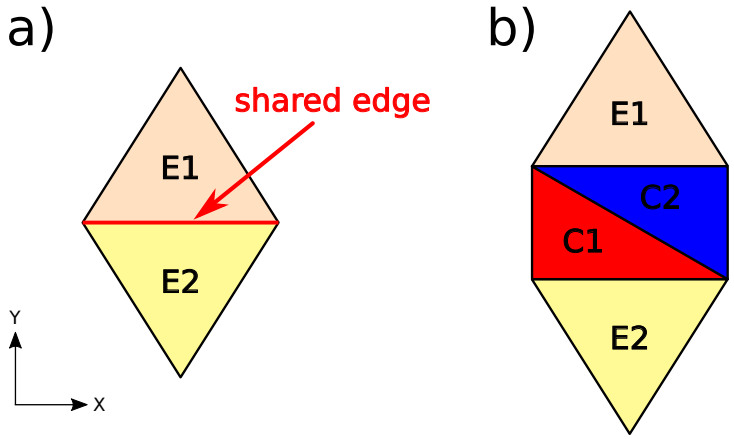

Figure 2.28: Configuration of two-dimensional bulk elements **a)** before and **b)** after the insertion of cohesive elements.

A graphical illustration of the insertion process implemented in this work is shown in Figure 2.29. Pragmatically, two neighboring bulk elements are separated by inserting a cohesive element at their shared face [†]. This insertion is carried out by duplicating the nodes that form the separating face and inserting new cohesive elements linking the original nodes to the new duplicated ones (Figure 2.29-**c**). In Figure 2.29-**a** the red dashed line showing the faces that will be split can be observed. Figure 2.29-**b** shows the blue dots corresponding to the nodes that have been duplicated (in this case there are two nodes at the same location). The red line corresponds to an initially flat cohesive elements. Finally, Figure 2.29-**c** shows that, after loading, the new inserted cohesive elements are open.

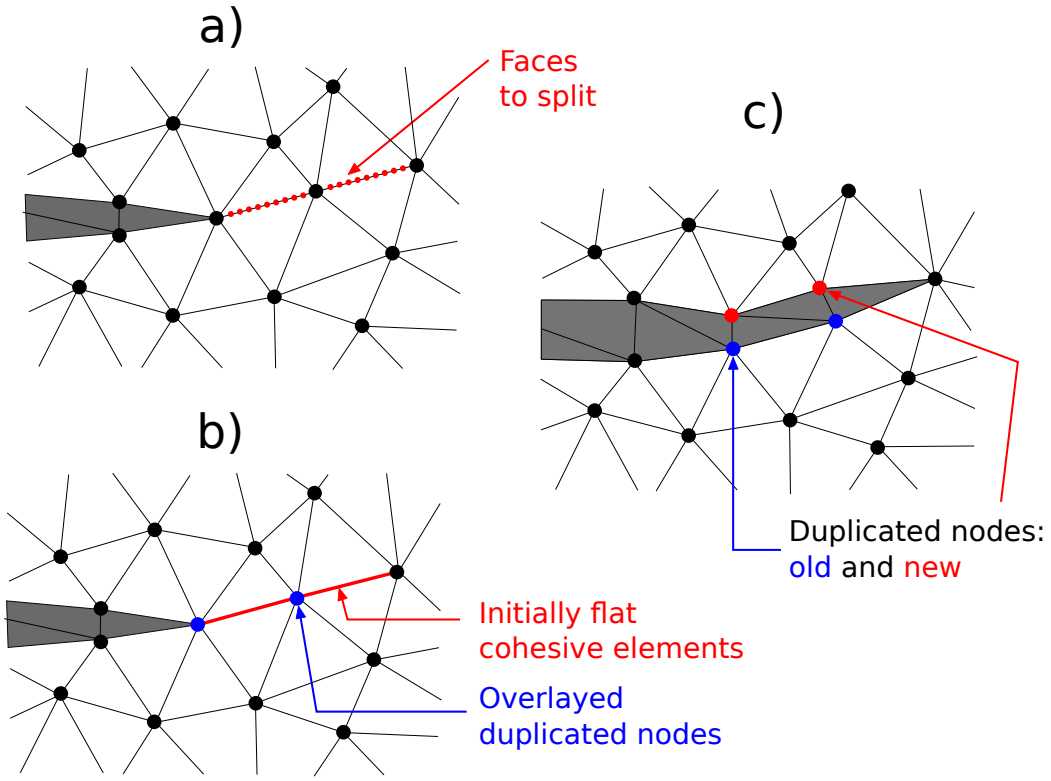

Figure 2.29: Schematic representation of the insertion of cohesive elements.

[†]We called it face because of 3D but in 2D it refers to an edge.

As it was already stated, in order to separate two neighboring normal or bulk elements by the insertion of cohesive elements, the nodes of the shared edge or face should be duplicated. To check whether or not a node should be duplicated, graph theory will be used. In practical terms, at each node of the mesh (node i) a graph is defined. To do so, all the elements of the mesh that contain the node of interest (i.e., patch of elements centered at node i) should be identified. Figure 2.30 shows an example of a graph that is built using the patch of elements centered at node i. In simple words, if after evaluating some conditions, the initial graph centered at node i can be split into two different graphs, node i should be duplicated. Once the graph of node i has been defined, in order to decide whether or not node i should be duplicated, the following conditions should be evaluated:

(i) If two neighboring bulk elements of the graph have an edge or face specifically marked to be separated, the graph should be split at this shared edge or face.

(ii) If there is an incomplete cohesive element (i.e., element belonging to an incomplete cohesive "family"), the graph should be split at this element.

If after evaluating these conditions, the graph can be split into two independent subgraphs, node i should be duplicated. Let's see some examples presented in Figure 2.30. Figure 2.30-**a** shows the case of a patch of elements composed only of bulk elements, in this case the edge shared by elements 3 and 4 is marked to be separated. Therefore, the graph should be split by this edge. Figure 2.30-**b** shows the case of a patch of elements composed of bulk elements and one incomplete cohesive element. As in the previous case, the edge shared by elements 3 and 4 is marked to be separated. Additionally, the graph should also be split at the incomplete cohesive element, and this cohesive element has to be added to any of the two subgraphs. Figure 2.30-**c** shows the case of a patch of elements composed of bulk elements and two incomplete cohesive elements from two different "families". None of the edges shared by the bulk elements is marked to be separated. But the graph should be split at both of the incomplete cohesive elements. The two cohesive elements have to be added to any of the two subgraphs. In the previous three cases, at the end, the initial graph built at node i is split into two independent subgraphs. Therefore, node i has to be duplicated. Conversely, Figure 2.30-**d** shows the case of a patch of elements composed of bulk elements and one incomplete cohesive element. In this case, none of the edges shared by the bulk elements is marked to be separated. Thus, the graph is only split at the incomplete cohesive element. But it is not possible to end up with two independent subgraphs, for this reason the node i must not be duplicated.

A schematic representation of the presented methodology (remeshing and insertion of cohesive elements) in a two-dimensional case is depicted in Figure 2.31. Figure 2.31-**a** shows the crack tip position at time step n. Also, a red line depicts the computed crack propagation direction. Figure 2.31-**b** shows the crack tip position after propagation at time step $n+1$. It also shows a magenta dashed line illustrating the performed remeshing operation and the previous crack tip position. Finally, Figure 2.31-**c** shows a zoomed-in view of the inserted cohesive elements (red) along the crack path.

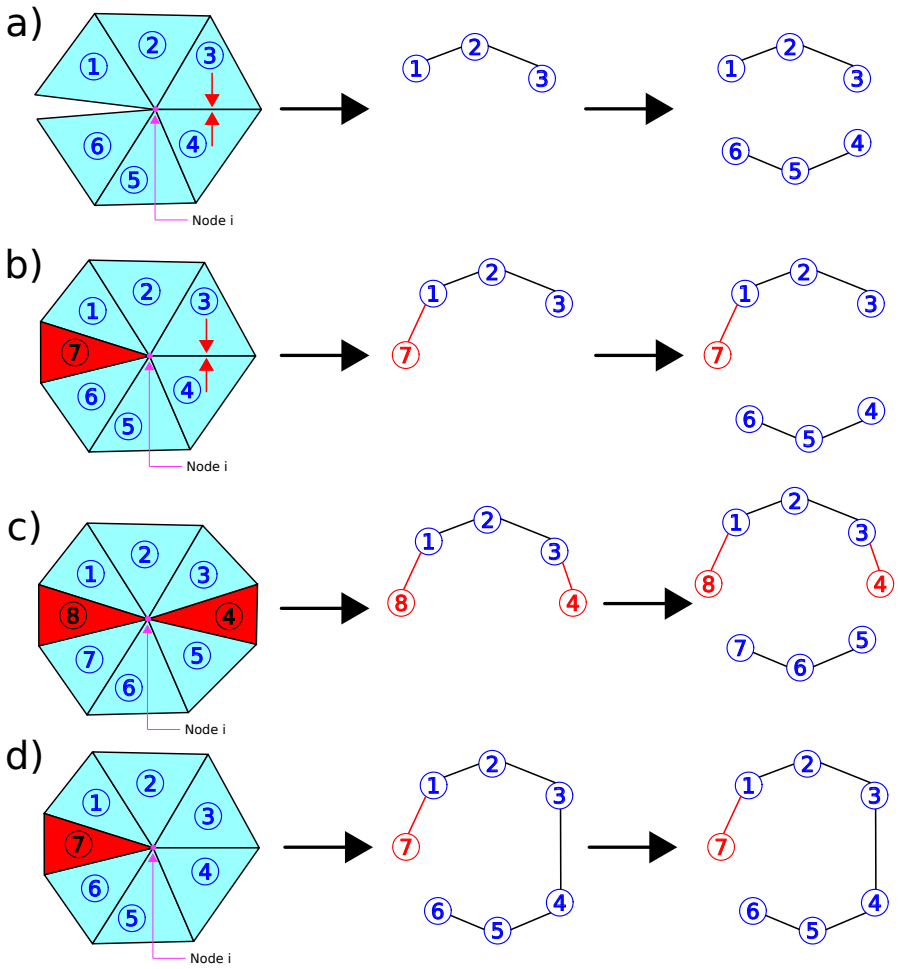

Figure 2.30: Graph at node i in 2D: **a)** Node i should be duplicated. **b)** Node i should be duplicated. **c)** Node i should be duplicated. **d)** Node i should not be duplicated.

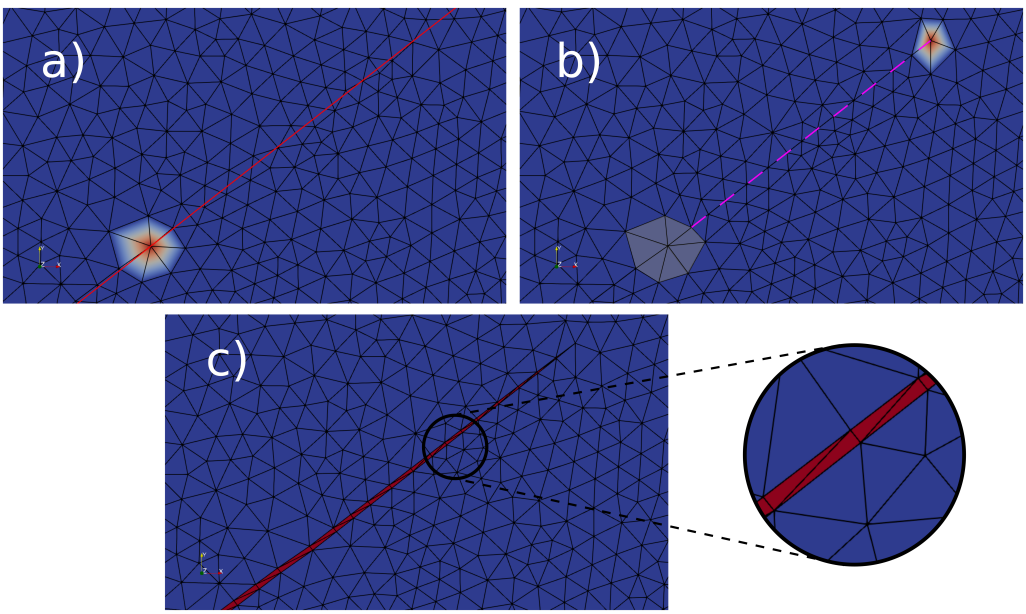

Figure 2.31: **a)** Crack tip position at time step n. **b)** Crack tip position at time step $n+1$. **c)** Inserted cohesive elements in red.

The presented methodology is also valid for three-dimensional problems, however the graphic representation is more complicated. For example, Figure 2.32 depicts the insertion process of cohesive elements for the three-dimensional case. The same important aspects highlighted in 2D can be extended to 3D. In Figure 2.32-**a)**, the face shared by the elements E1 and E2 is shown as a shaded triangle. Once these elements are completely separated, three cohesive elements (C1, C2 and C3) are inserted between them as shown in Figure 2.32-**a)**. Elements C1, C2 and C3 belong to the same cohesive "family". In the three-dimensional case, a cohesive "family" is said to be completed when there are three cohesive elements separating two bulk elements that were initially adjacent.

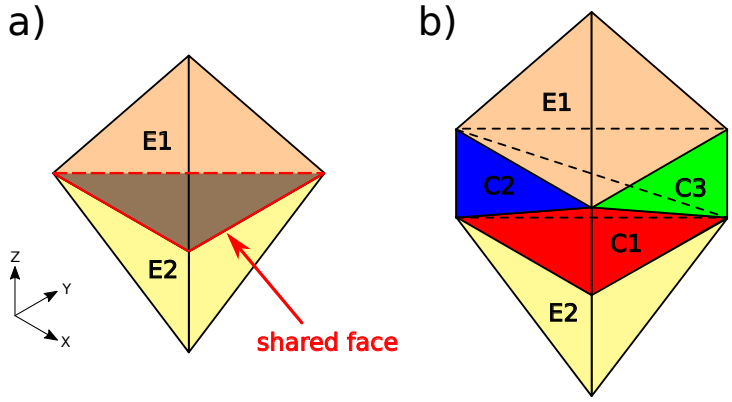

Figure 2.32: Configuration of three-dimensional bulk elements **a)** before and **b)** after the insertion of cohesive elements.

Representing a graph is more complex in 3D than in 2D. Figure 2.33 shows the comparison between the representation of a graph in 2D and 3D. Figure 2.33-**a)** shows that in 2D, the visual representation of the graph is simple. As triangle elements are used, the connectivity of the elements belonging to the patch is not difficult. The case is different in 3D where tetrahedral elements are used. In this case, as shown in Figure 2.33-**b)**, it is not simple to see the network formed by the elements belonging to the patch.

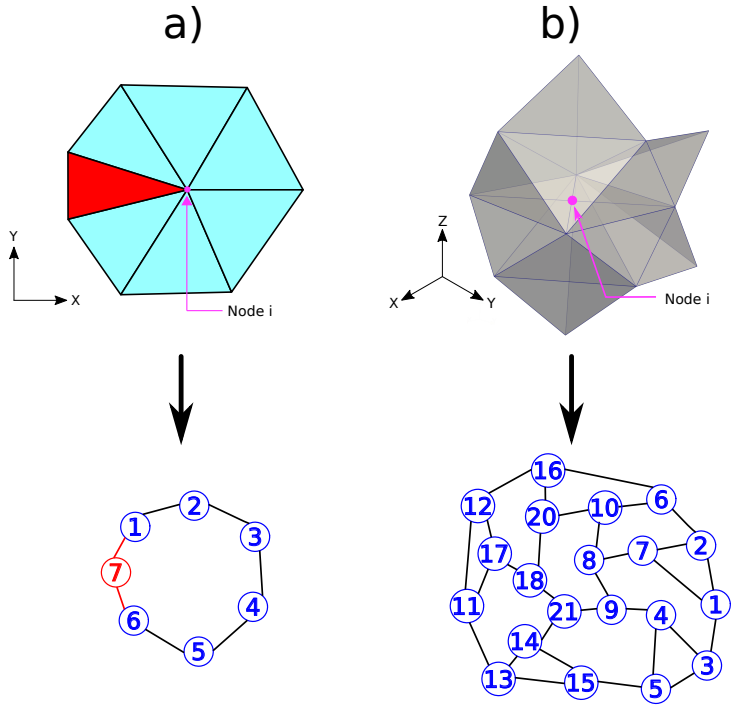

Figure 2.33: Graphic illustration of a graph at node i in both **a)** 2D and **b)** 3D.

Nevertheless, the procedure to check whether a node in a 3D mesh should be duplicated, is the same as the one explained for the 2D case. Figure 2.34-**a)** shows the case of a patch of elements composed only of normal or bulk elements. In this case the faces shared respectively, by elements 1 and 4 and by elements 6 and 5 are marked to be separated. Therefore, the graph should be split by these faces. Figure 2.34-**b)** shows the case of a patch of elements composed of normal or bulk elements and one incomplete cohesive group of elements from the same "family" (12 and 11). As in the previous case, the faces shared respectively, by elements 1 and 4 and by elements 6 and 5 are marked to be separated. Additionally, the graph should also be split at the incomplete cohesive group of elements, and this group has to be added to any of the two subgraphs. Figure 2.34-**c)** shows the case of a patch of elements composed of normal or bulk elements and two incomplete cohesive group of elements from two different "families" (i.e., 12-11 and 13). None of the faces shared by the normal or bulk elements is marked to be separated. But the graph should be split at both of the incomplete cohesive groups of elements. The two cohesive groups of elements have to be added to any of the two subgraphs. In the previous three cases, at the end, the initial graph built at node i is split into two independent subgraphs. Therefore, node i has to be duplicated.

Finally, Figure 2.34-**d)** shows the case of a patch of elements composed of normal elements and one incomplete cohesive group of elements from the same "family" (i.e., 12-11). None of the faces shared by the normal elements is marked to be separated. Thus, the graph is just split at the incomplete cohesive group of elements. But it is not possible to end up with two independent subgraphs, for this reason the node i must not be duplicated.

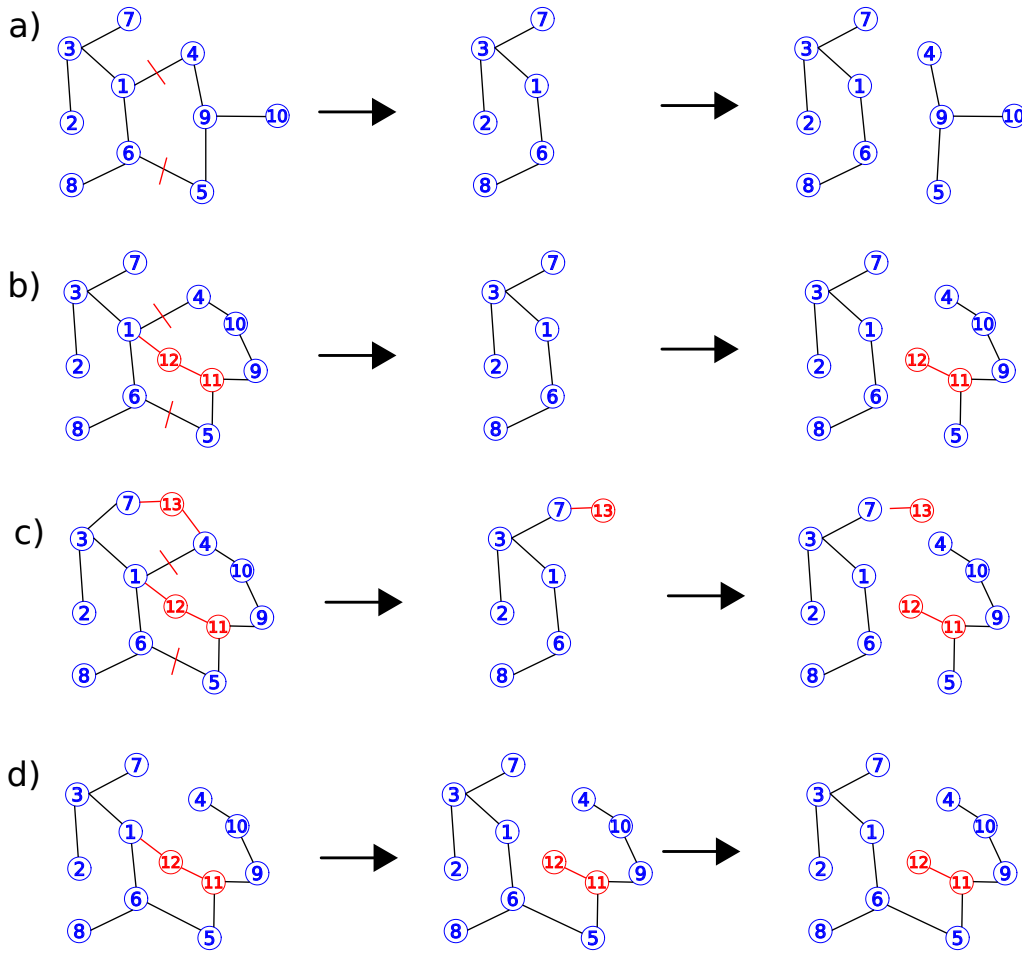

Figure 2.34: Graph at node i in 3D: **a)** Node i should be duplicated. **b)** Node i should be duplicated. **c)** Node i should be duplicated. **d)** Node i should not be duplicated.

2.7 Summary of Chapter 2

This chapter presents in detail all the implementations performed inside Cimlib, a C++ in-house finite element library [Digonnet et al., 2007] in order to achieve crack propagation in both 2D and 3D for arbitrary crack paths.

The first section presented the mechanical problem in which the current work is framed. This section also introduced the governing equations in terms of velocity and pressure. These equations will be solved through a mixed FE formulation detailed in the second section.

In the third section of this chapter, the cohesive zone models that were implemented in this work in order to simulate the fracture process were described: (i) Ortiz and Pandolfi's as well as, (ii) Xu and Needleman's cohesive laws. Additionally, the viscous regularization technique that was implemented in order to avoid convergence problem when using cohesive elements was described, specially in three-dimensional problems. Validations examples were presented.

Taking into account that one of the goals of this PhD thesis is to predict fracture propagation in the presence of thermal gradients generated by diurnal temperature cycling on solar system small bodies, the fourth section presented in detail the implemented thermoelasticity model in order to be able to account for thermal strain.

The fifth section presented in detail the numerical implementation of the $G\theta$ method. The methodology used in this work to compute the energy release rate in two-dimensional problems, and hence, the crack propagation direction. The implemented $G\theta$ method was validated under the presence of loadings of mechanical nature, as well as under the presence of loadings of thermal nature.

Finally, in the sixth section, the mesh modification strategies used in this work in order to achieve crack propagation through a finite element mesh were described. The methodology used to fit a finite element mesh to a given propagation direction in order to ensure crack propagation using remeshing operations and dynamic insertion of cohesive elements in a mesh-independent way was presented. Computation of the fracture surface was also described for both two- and three-dimensional problems. Lastly, the insertion process of cohesive elements was described.

2.8 Résumé en français

Ce chapitre présente en détail toutes les implémentations réalisées au sein de Cimlib, une librairie éléments-finis C++ interne au CEMEF [Digonnet et al., 2007], dans le but de simuler la propagation de fissures en 2D et 3D pour des directions arbitraires.

La première partie détaille le problème mécanique autour duquel ce travail est construit. Les équations définissant les évolutions de vitesse et pression qui seront résolues en utilisant une formulation éléments finis mixte sont présentées.

La troisème partie de ce chapitre décrit les modèles à zone cohésive implémentés puis utilisés pour simuler le processus de rupture: (i) la loi cohésive établie par Ortiz et Pandolfi et (ii) la loi cohésive établie par Xu et Needleman. De plus, la technique de régularisation visqueuse implémentée pour limiter les problèmes de convergence engendrés par l'utilisation d'éléments cohésifs est décrite, en particulier pour les problèmes à trois dimensions. Des cas de validations sont finalement explicités.

En considérant que l'un des objectifs de cette thèse de doctorat est de prédire la propagation de fissure en présence de gradients de température générés par des cycles thermiques jour-nuits dans des petits objets de notre système solaire, la quatrième partie présente en détails le modèle thermoélastique utilisé pour prendre en compte la déformation thermique.

La cinquième section, quant à elle, détaille l'implémentation de la méthode $G\theta$. La méthodologie utilisée dans ce travail pour calculer le taux de restitution d'énergie et la direction de propagation dans des problèmes à deux dimensions est détaillée. La méthode implémentée est validée dans le cas de chargements mécaniques mais aussi thermiques.

Finalement, la dernière partie décrit les stratégies de modification du maillage utilisées pour permettre la propagation de fissures dans un maillage éléments finis. La méthode utilisée pour ajuster un maillage éléments finis en fonction d'une direction de propagation de fissure donnée, à l'aide d'opérations de remaillages et d'insertion dynamique d'éléments cohésifs est présentée. Le calcul de la surface créée par la rupture est décrite pour des problèmes à deux et trois dimensions.

Chapter 3

Numerical modeling of crack propagation with remeshing and dynamic insertion of cohesive elements

Contents

One of the most challenging issues in computational fracture mechanics is the propagation of a crack through a finite element mesh for arbitrary crack paths. The methodology presented in this PhD thesis allows crack propagation through the combination of remeshing operations and dynamic insertion of cohesive elements in a mesh-independent way. This chapter presents the numerical results concerning crack propagation in both two- and three-dimensional scenarios. Section 3.1 is focused on the results already published in [Uribe-Suárez et al., 2020]. In this section, different benchmark problems are considered to assess the proposed crack propagation methodology. Additionally, the impact of different numerical and physical parameters on the crack path and fracture energy is studied. Then, in section 3.2, the results of a first three-dimensional crack propagation attempt through the application of the already validated two-dimensional methodology are shown. First, a three-dimensional interfacial debonding problem is depicted. Then a three dimensional single edge notched tensile test is presented. As in this case, the crack path is known a priori, initially, cohesive elements are inserted along the known trajectory since the beginning of the simulation to simulate the fracture process. Lastly, the previous example is used again, but in this case the crack front is propagated through arbitrary directions, bringing out the promising capabilities of the presented methodology when dealing with 3D configurations.

3.1 Two-dimensional crack propagation

In the two-dimensional case, the crack direction is computed using the maximal energy release rate criterion (MERRC) which is implemented using finite elements and the $G\theta$ method. The remeshing procedure used here is composed of two stages. In the first step, a conforming mesh is obtained in the computed crack direction, ensuring that edges are placed over the sought direction. In the second stage, cohesive elements are dynamically inserted at the conforming edges previously remeshed. The combination of this remeshing technique with dynamic insertion of cohesive elements, leads to a mesh-independent crack propagation method. In this section, different benchmark problems are considered to assess the proposed methodology.

In the work presented here, isotropic unstructured triangular meshes that are refined in the neighborhood of the crack tip are used. All the examples presented here consider an initial notch or a prescribed crack, initiation is not treated. The simulations performed are quasi-static, and a single crack is considered. To simulate the fracture process, the already presented Ortiz and Pandolfi's cohesive law [Ortiz and Pandolfi, 1999] is used. Although the crack propagation distance is indeed an important parameter involved in fracture process simulations, here, for the sake of simplicity, the crack growth distance is set to a fixed value equal to 8 times the average size of the elements attached to the crack tip. This length size remains small with respect to the process zone length ($PZL = \frac{G_c E}{\pi \sigma_c^2}$, see 3.1.4). The influence of this parameter will not be studied in this work.

In the first part of this section, an example regarding crack propagation under mixed-mode loading is examined to show the accuracy of the proposed method in terms of propagation direction. Then, another example that includes several holes, showing the influence of these on the crack path is subsequently addressed. Finally, the effects of different numerical and physical parameters regarding the fracture process are investigated.

3.1.1 Crack propagation of an edge-crack under mixed-mode loading

An edge crack geometry fixed at the bottom and subjected to a top unit shear load is considered here (Figure 3.1). Material properties are also given in Figure 3.1. This problem was also solved by [Nguyen-Xuan et al., 2012] and [Liao et al., 2018]. Through the solution of this benchmark example, it is intended to show the capabilities of the implemented methodology when calculating a crack path under mixed mode loading conditions. In this case, even though

the propagation process was carried out under quasi-static conditions, allowing the propagation only when the energy release rate exceeds its critical value, it can not be said that the propagation is stable. In order to verify the stability of the propagation (out of the scope of this work), the variation of the energy release rate with respect to the crack length ($\partial G/\partial a$) must be computed (see [Suo, 1990]).

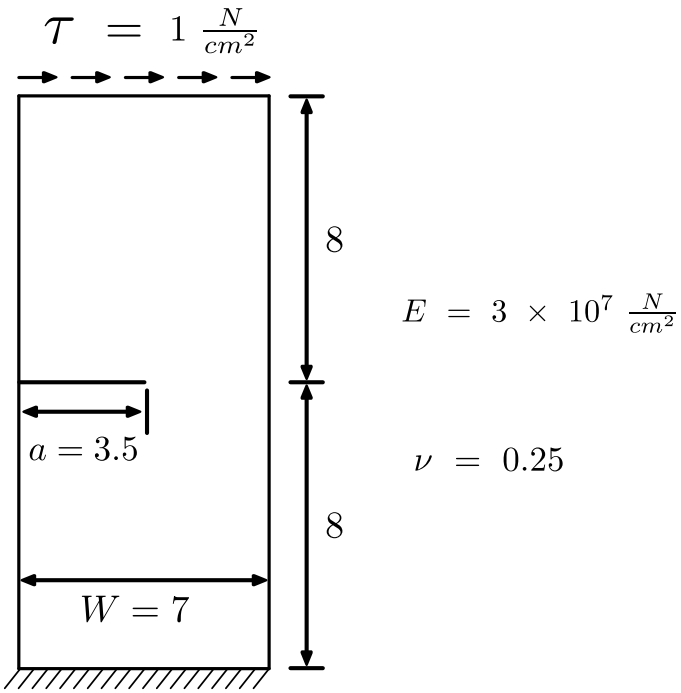

Figure 3.1: Geometry of the plate with an edge crack under shear (dimensions in cm)

Figure 3.2 shows the comparison in terms of crack path between 2 previous works and the approach presented here. It is shown that this work reproduces the crack path very well which means that, compared to the results presented in [Nguyen-Xuan et al., 2012, Liao et al., 2018], a good agreement is obtained here.

3.1.2 Cracked beam with three holes

This case consists in a cracked beam supported at two points and loaded at the center, as shown in Figure 3.3. The material properties are: Young's modulus $E = 29 \times 10^6$ psi, Poisson's ratio $\nu = 0.3$. The load P is equal to 1 lb. Here, three cases of the initial crack length a and its distance b from the left side of the beam are considered. The different values considered for these parameters are given in Table 3.1.

	a (*inches*)	**b** (*inches*)
Case I	1.0	4.0
Case II	1.5	5.0
Case III	1.5	6.0

Table 3.1: Gemetrical Configurations

In practical applications holes are common an can affect crack propagation. The proposed benchmark example aims at dealing with mixed-mode crack paths that are affected by the presence of holes. This problem has also been addressed by [Nguyen-Xuan et al., 2012, Azócar et al., 2010, Bittencourt et al., 1996], both numerically and experimentally. Again, in this example the propagation process was carried out under quasi-static conditions, allowing the

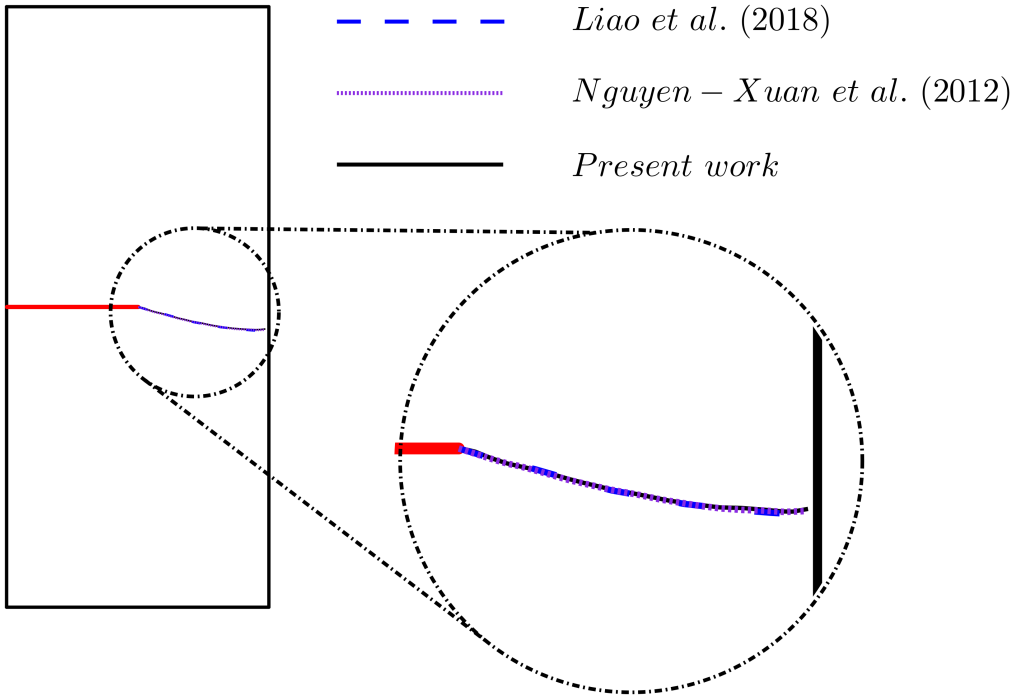

Figure 3.2: Comparison of crack path of the edge-cracked plate obtained here against different literature results.

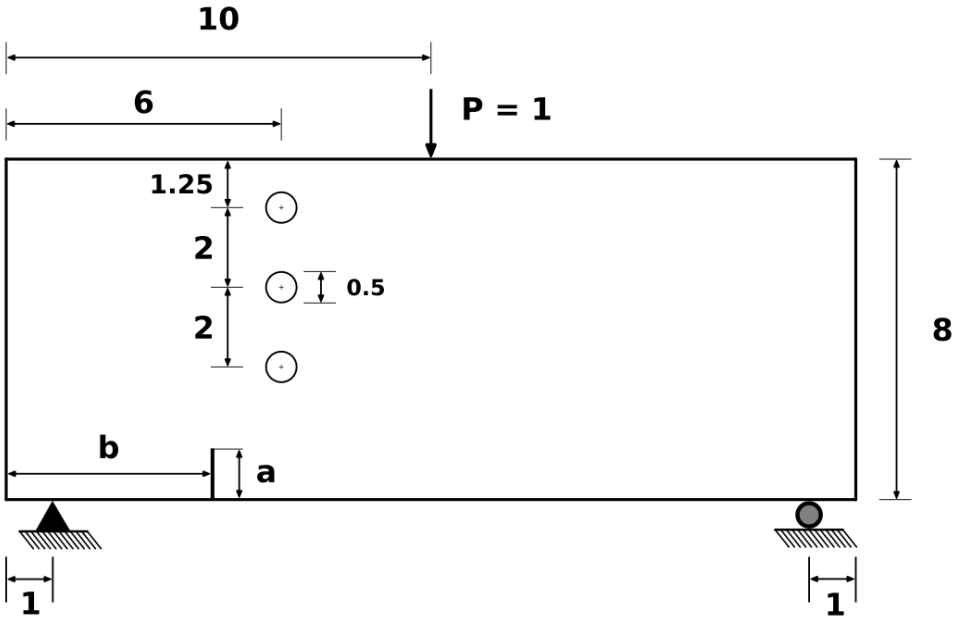

Figure 3.3: Cracked beam supported at two points and loaded at the center. The beam has three holes to create complex crack paths. (units in *inches*)

propagation only when the energy release rate exceeds its critical value. But, same as in the previous benchmark, it cannot be said that the propagation is stable. In order to check the stability of the propagation (out of the scope of this work), $\partial G/\partial a$ must computed [Suo, 1990].

Figure 3.4-**a** shows the complete crack path for Case I. The crack reaches the second hole from the lower left side. Figure 3.4-**b** shows the complete crack path for Case II. Crack propagation takes place through the material region between the first and second hole. The crack reaches the second hole from the lower right side. Finally, Figure 3.4-**c** shows the complete crack path

for Case III. In this situation the crack reaches the first hole from the lower right side. In all the three cases the comparison between this work and [Nguyen-Xuan et al., 2012] is shown. The crack paths predicted in this work show excellent agreement with cited work [Ingraffea and Grigoriu, 1990, Azócar et al., 2010, Bittencourt et al., 1996]. It is clear that, due to the presence of holes, the crack path experiences significant changes. The holes attract the crack path depending on the initial notch geometry.

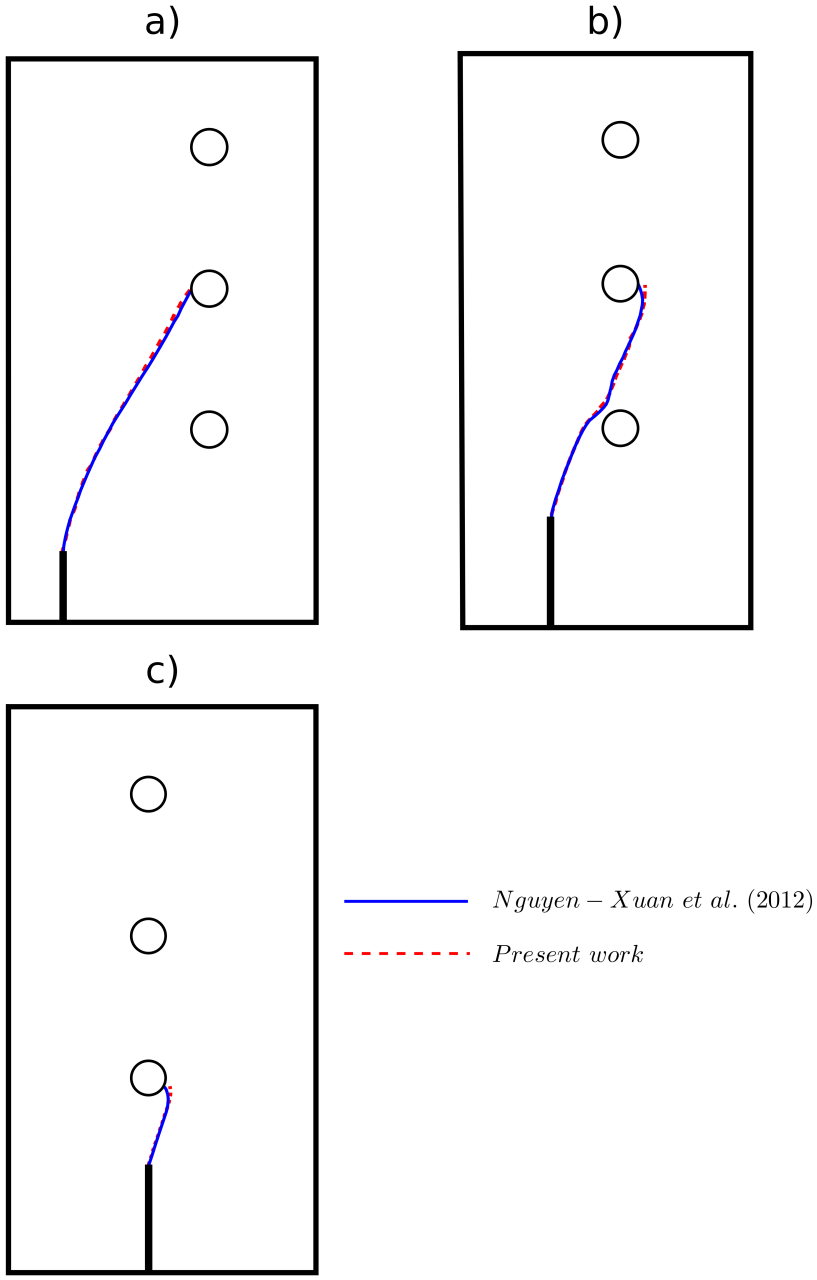

Figure 3.4: Comparison of the crack path between present work and [Nguyen-Xuan et al., 2012] for **a)** Case I, **b)** Case II and **c)** Case III. It is shown only a section of the beam in the region near the holes

These two mixed mode examples validate this new crack propagation method that combines (*i*) crack propagation direction ($G\theta$ method), (*ii*) automatic remeshing and (*iii*) dynamic insertion of cohesive elements on the crack path. In the following section, a simple mode-I example describes the ability of the proposed methodology to solve a fracture problem using the CZMs approach in the traditional way: cohesive elements are inserted over a predefined crack path

from the beginning of the simulation.

3.1.3 Cohesive elements inserted over a predefined crack path

This section aims at showing the accuracy of the proposed methodology when solving a fracture problem using the cohesive elements in the classical way they have been widely used in the literature. The pure mode-I problem whose geometry and boundary conditions are presented in Figure 3.5 is solved. This benchmark example is tackled using two different methodologies:

(i) Crack propagation using remeshing and dynamic insertion of cohesive elements.

(ii) Due to fact that the problem is pure mode-I, the crack path is known a priori, therefore, cohesive elements are placed from the beginning in the known direction (crack path is predefined).

Figure 3.5-**b)** shows the direction (red) in which the cohesive elements are inserted since the beginning of the simulation. The material properties are: Young's modulus $E = 3 \times 10^5\ MPa$, Poisson's ratio $\nu = 0.3$, critical cohesive stress $\sigma_c = 0.2\ MPa$ and critical opening displacement $\delta_c = 1.54 \times 10^{-6}\ mm$. The comparison between the two methodologies is performed using a *force-displacement* curve.

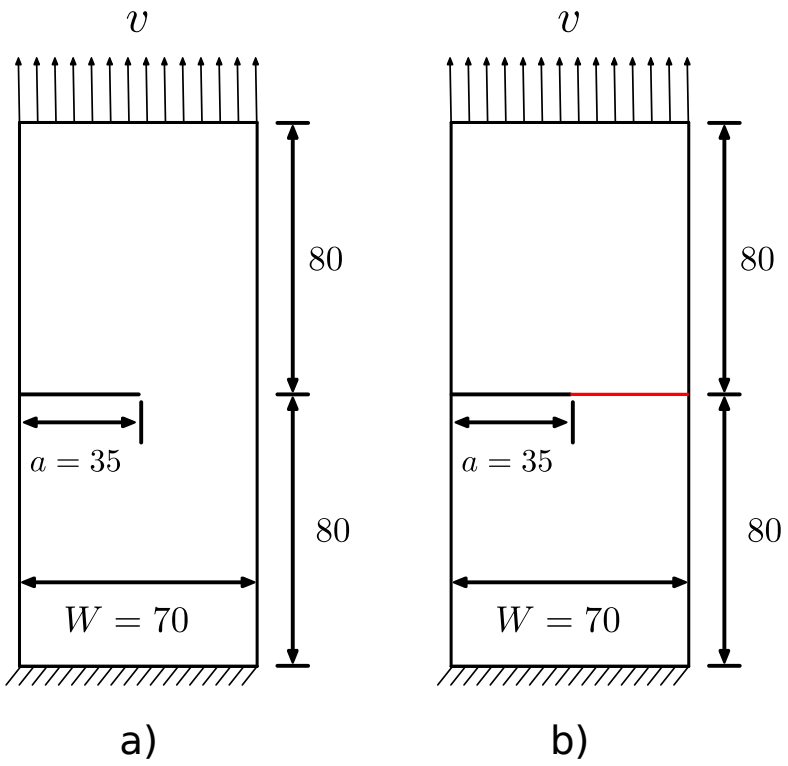

Figure 3.5: Geometry and boundary conditions for a pure Mode-I problem (dimensions in mm). The problem was solved using: **a)** dynamic insertion of cohesive elements and **b)** cohesive elements inserted since the beginning of the simulation over a predefined crack path (red).

Figure 3.6 shows the *force-displacement* curves for the two simulated cases. The black curve shows the case where cohesive elements are inserted dynamically as crack propagates. The red "+" indicates the start of the propagation process. The blue one depicts the case where the cohesive elements are inserted from the beginning of the simulation along the predefined crack path. Figure 3.6 clearly shows that when using the dynamic insertion of cohesive elements

(current approach), the artificial reduction of the stiffness of the material, one well-known drawback of using cohesive elements is avoided. This is observed in the difference of the slopes between the black curve and the blue one.

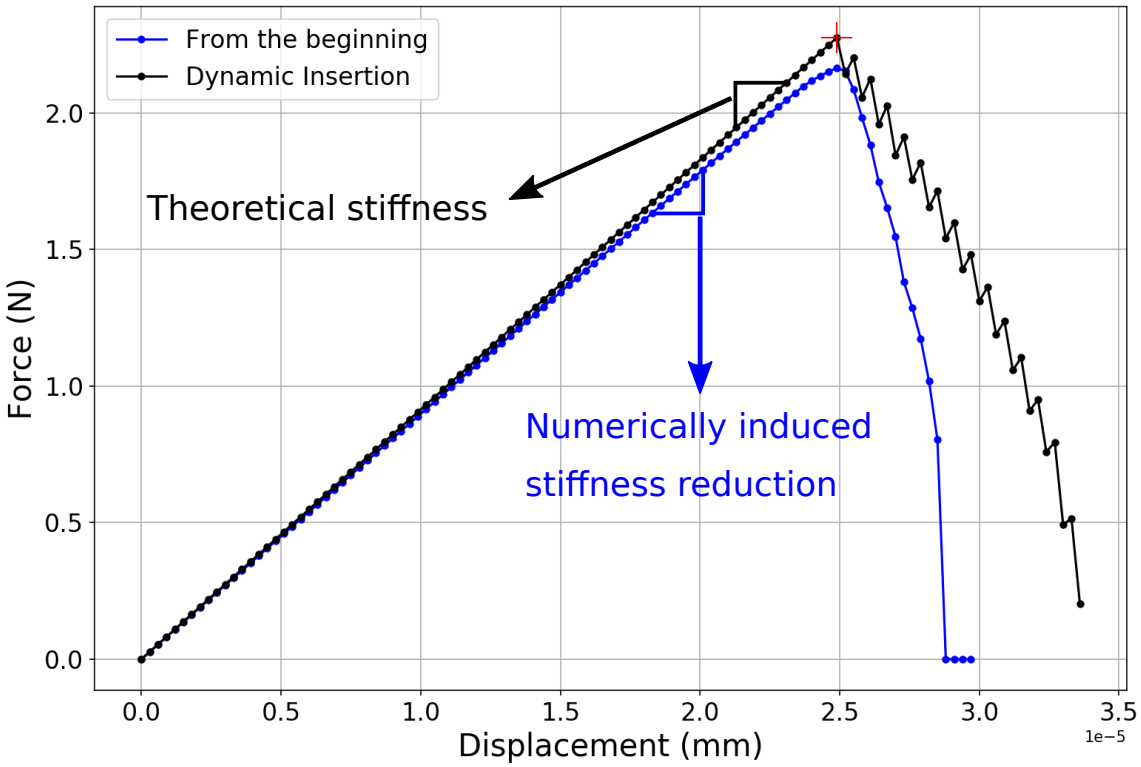

Figure 3.6: *Force-displacement* curve for the two applied methodologies.

As presented in the next section, the approach presented in this work has advantages compared to LEFM methodology as well as to classical CZM approach: respectively, fracture energy control and crack propagation through an arbitrary direction. But it also has disadvantages, such as a significant dependence on the time step, as well as on the crack growth distance. Nevertheless, when solving a fracture problem using the cohesive elements in the traditional way in which they have been used in the literature, the dependence on the time step disappears.

In the next section we address a topic which is rarely studied in the literature: the influence of time step on the numerical solution when performing dynamic insertion of cohesive elements. A sensitivity analysis to the cohesive law parameters is also presented and discussed.

3.1.4 Influence of numerical and physical parameters

In this section the influence of different numerical and physical parameters on the solution is studied. This influence is assessed in terms of either the force-displacement curve or the crack path comparison. Figure 3.7 shows the geometry, boundary conditions as well as material properties of the test example used in this section. The sensitivity to the mesh size and the time step are considered. First, aiming to prove the convergence of the solution in terms of the force-displacement curve as a function of the element size of the mesh, three different meshes are considered. Table 3.2 shows the element sizes of the different meshes used here. Simulations using these meshes are performed. Even though, in the present work for the sake of simplicity, the mesh size of the region containing the crack path is refined, it is worth mentioning that for more complex problems it is also possible to only remesh the neighborhood of the crack tip while it evolves.

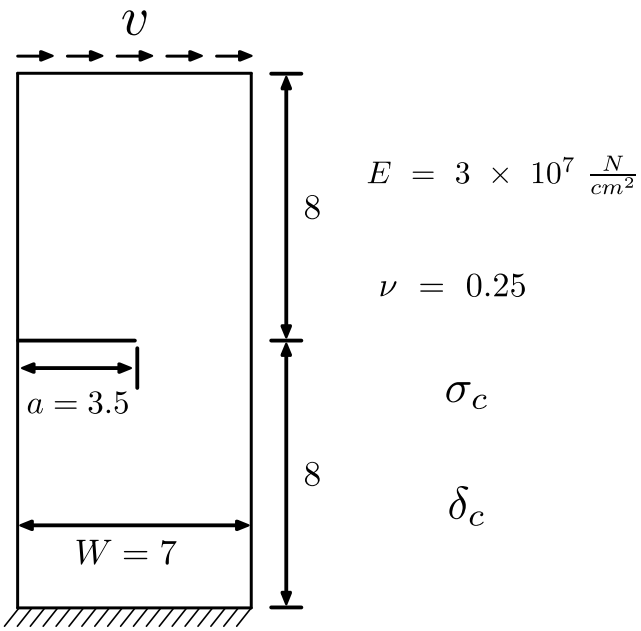

Figure 3.7: Geometry of a plate with an edge crack under shear (dimensions in cm)

	Far away from the crack tip	Crack tip neighborhood
Reference Mesh	1.850	0.231
Mesh 1	1.000	0.125
Mesh 2	0.541	0.068

Table 3.2: Elements size of the different meshes used (mm).

Figure 3.8 shows the force-displacement curve for a case where the mesh size changes. The red "+" indicates the start of the propagation process. Mesh convergence in the solution is obtained. The curve up to the red "+", i.e., when propagation process has not initiated, exhibits a totally linear relation between force and displacement. This behaviour is linear because cohesive elements have not been yet inserted into the mesh. Once they are inserted, the nonlinear behavior appears. Due to the presence of oscillations after the propagation process has started, the nonlinearity in the force-displacement curve after this point looks smoother.

Figure 3.8 exhibits oscillations after the crack starts its propagation. This is due to the fact that, in this work, once the energy released rate (G) exceeds its critical value (G_c, equation (2.37)), the propagation of the crack is allowed. After propagation, cohesive elements are inserted leading to a decrease of the stresses around the crack tip, leading to a drop in G. This drop of G eventually leads to a value lower than G_c and, thus, propagation is momentaneously stopped. Afterwards, an increase of the loading brings G to a value higher than G_c, the propagation then restarts. This is an essential point (rarely mentioned in the literature) which is directly related to the space and time discretizations associated with the FE method.

The curve describing the evolution of G through time for the three simulated cases (Reference Mesh, Mesh 1 and Mesh 2) is presented in Figure 3.9. The red "+" indicates the starts of the propagation process which is the same for all cases. This Figure shows that G varies from values close to $0.25G_c$ up to values greater than $2G_c$. This range of variation is thought to depend strongly on the time step. Therefore, the time step is the next numerical parameter studied.

Taking into account that mesh convergence is achieved, from now on, and for the sake of simplicity, the "Reference Mesh" case will be used as a reference for the upcoming comparisons. It will be referred to as "Reference".

Figure 3.10 shows the force-displacement curve obtained when the time step was decreased

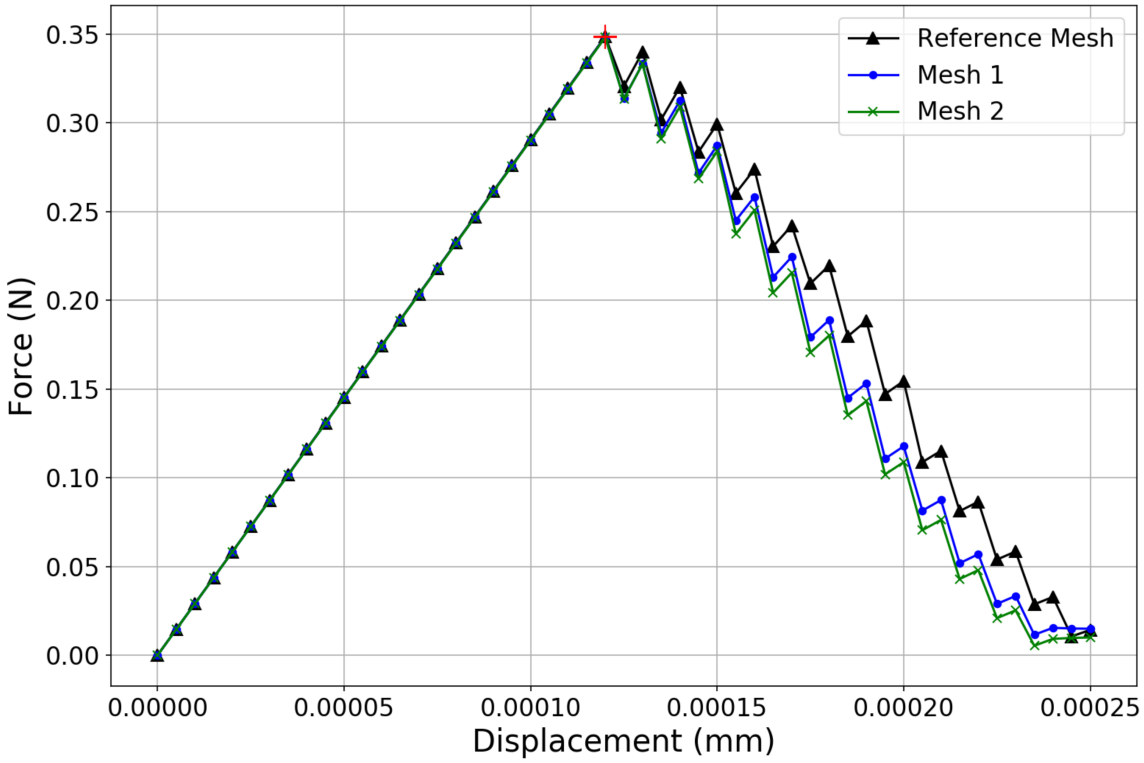

Figure 3.8: Force-displacement curve for different meshes

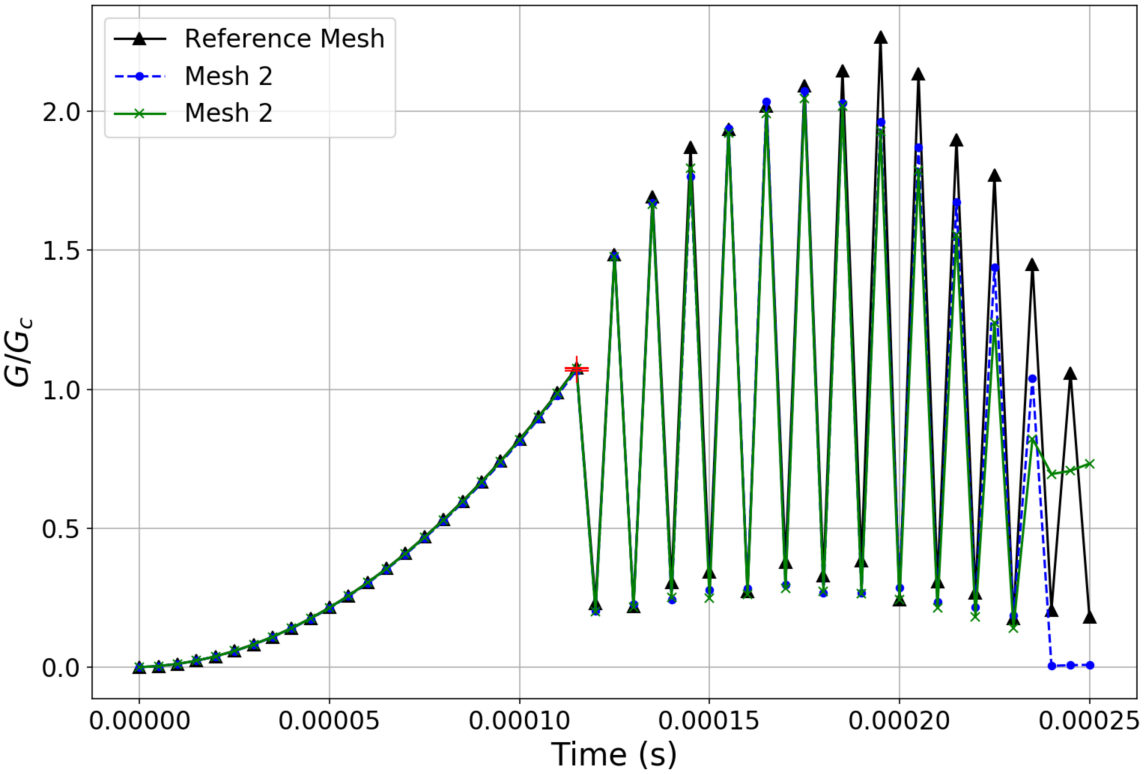

Figure 3.9: G-Time curve for different meshes

by half. In this case, the necessary force to start the propagation process (+) is less than the one required in the "Reference" case. In addition, when half of the time step is used, crack propagation starts sooner than in the "Reference" case. Also, after crack propagation has

started, for the same time, using half of the time step, the crack tip has propagated a greater distance than in the “Reference" case, so less force is needed to continue the propagation process.

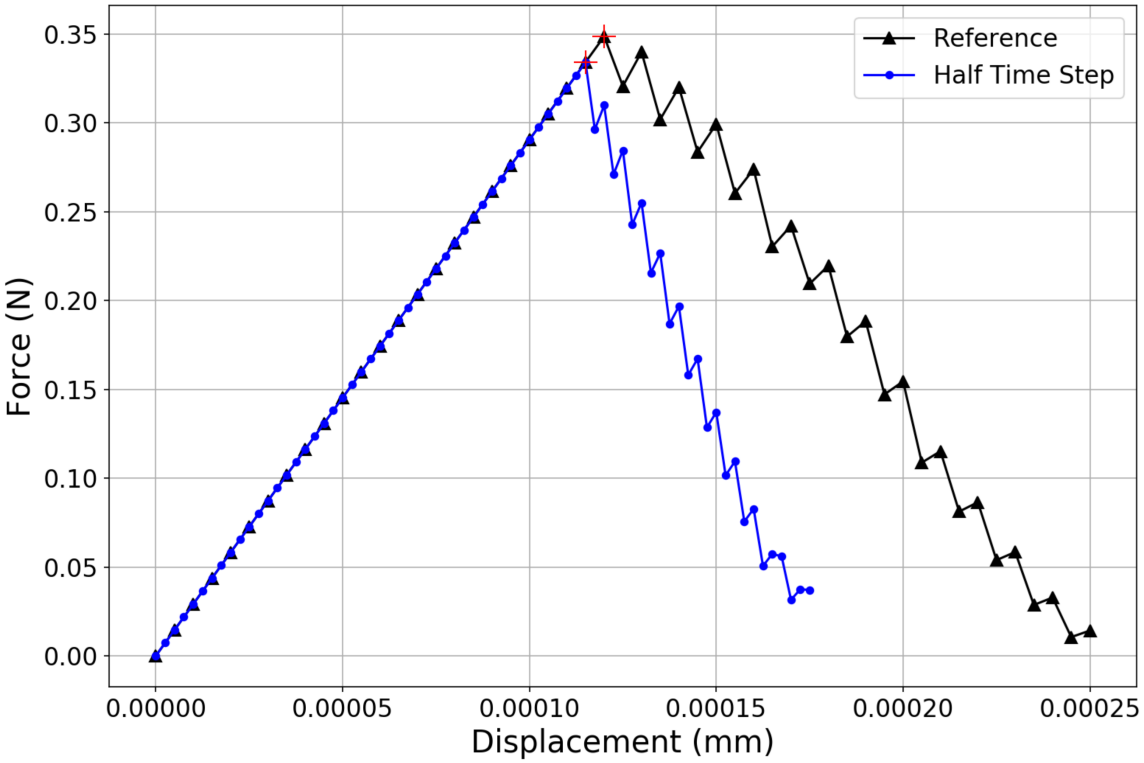

Figure 3.10: Force-displacement curve varying time step

The evolution of G through time is presented in Figure 3.11. As a result of using half of the time step value, the crack propagation process begins sooner and leads to faster propagation of the crack. It is also evident that decreasing the time step reduces the oscillation range of G. Thus, the crack propagation process has a strong dependence on the time step. This phenomenon is due to the fact that the same propagation distance is prescribed once G exceeds G_c, regardless of the time step used. In other words, this is due to the fact that the crack velocity is unknown in these computations. If the goal is to avoid time step dependence, methodologies such as the $\pi\theta$ method (crack growth stability) [Suo and Combescure, 1992a], that is an extension of the $G\theta$ method, and fatigue analysis (crack growth under cyclic conditions) [Lemaitre and Desmorat, 2005], that allow computation of the crack velocity, should be used.

In addition to the time step dependence, the current approach also depends on the crack growth distance. Even though the influence of this parameter was not studied here, the oscillations observed in the force-displacement curves (Figures 3.8 and 3.10) come from the fact that crack growth distance was set arbitrarily. The computation of the crack velocity is required if one wants to define the crack increment distance for a given time step. Compared to LEFM, the current approach has the advantage of allowing fracture energy control. Compared to CZMs, the main advantage is that crack propagation proceeds through an arbitrary direction. However it must be noted that the dynamic insertion of such cohesive elements introduces a numerical dependence of the crack increment and the associated time step.

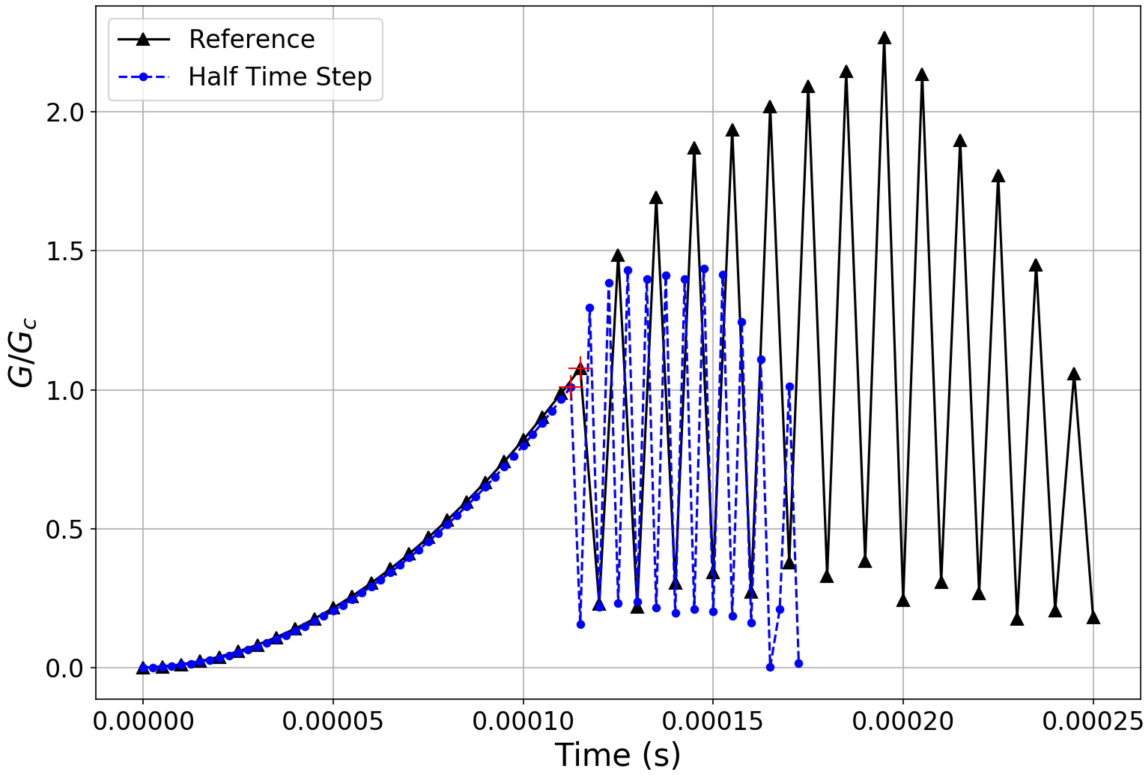

Figure 3.11: G-Time curve varying time step

According to the cohesive law implemented and used in this part of the work [Ortiz and Pandolfi, 1999], the relevant parameters involved in the model are the maximum cohesive stress (σ_c) and the critical opening displacement of the cohesive elements (δ_c). These values are directly related through the following equation describing the fracture energy:

$$G_c = e\sigma_c\delta_c \tag{3.1}$$

Equation (3.1) can also be related to equation (3.2), defining the process zone length (PZL), as follows [Turon et al., 2007, Hermes, 2010, Ha et al., 2015]:

$$PZL = \frac{G_c E}{\pi\sigma_c^2} \tag{3.2}$$

Aiming at finding the effect on the crack propagation process when the aforementioned cohesive parameters are varied, several simulations using different values are performed. Table 3.3 shows the different values that were tested for the cohesive parameters during the simulations. Apart from the reference case (A), five different simulations were performed. For the first three cases, B_1, B_2 and B_3 the critical cohesive stress (σ_c) is varied. The fracture energy (G) was kept constant, so the new critical opening displacement of the cohesive elements (δ_c) was computed in each case using equation (3.1). Variations of the critical cohesive stress (σ_c) were defined trying to keep a logical value for the process zone length (PZL).

In the remaining two cases, C_1 *and* C_2, the fracture energy was doubled. In the first case, the critical cohesive stress was doubled, while in the second one, the doubled parameter was the critical opening displacement. Figure 3.12 shows the different cohesive laws used in this work.

Figure 3.13 shows the different force-displacement curves obtained when cohesive parameters were varied. It is evident that the variation of these parameters did not lead to significant changes in the results. When fracture energy is kept constant, the influence of varying the maximum cohesive stress (σ_c) and the critical opening displacement (δ_c) is minimal. In the

Legend	$G\ [MPa.mm]$	$\sigma_c\ [MPa]$	$\delta_c\ [mm]$	$PZL\ [mm]$
A (Reference)	8.378×10^{-7}	0.200	1.541×10^{-6}	2.000
B_1	8.378×10^{-7}	0.141	2.179×10^{-6}	4.000
B_2	8.378×10^{-7}	0.282	1.089×10^{-6}	1.000
B_3	8.378×10^{-7}	0.400	7.705×10^{-7}	0.500
C_1	1.675×10^{-6}	0.400	1.541×10^{-6}	1.000
C_2	1.675×10^{-6}	0.200	3.081×10^{-6}	4.000

Table 3.3: Values of the different physical parameters used in the cohesive law.

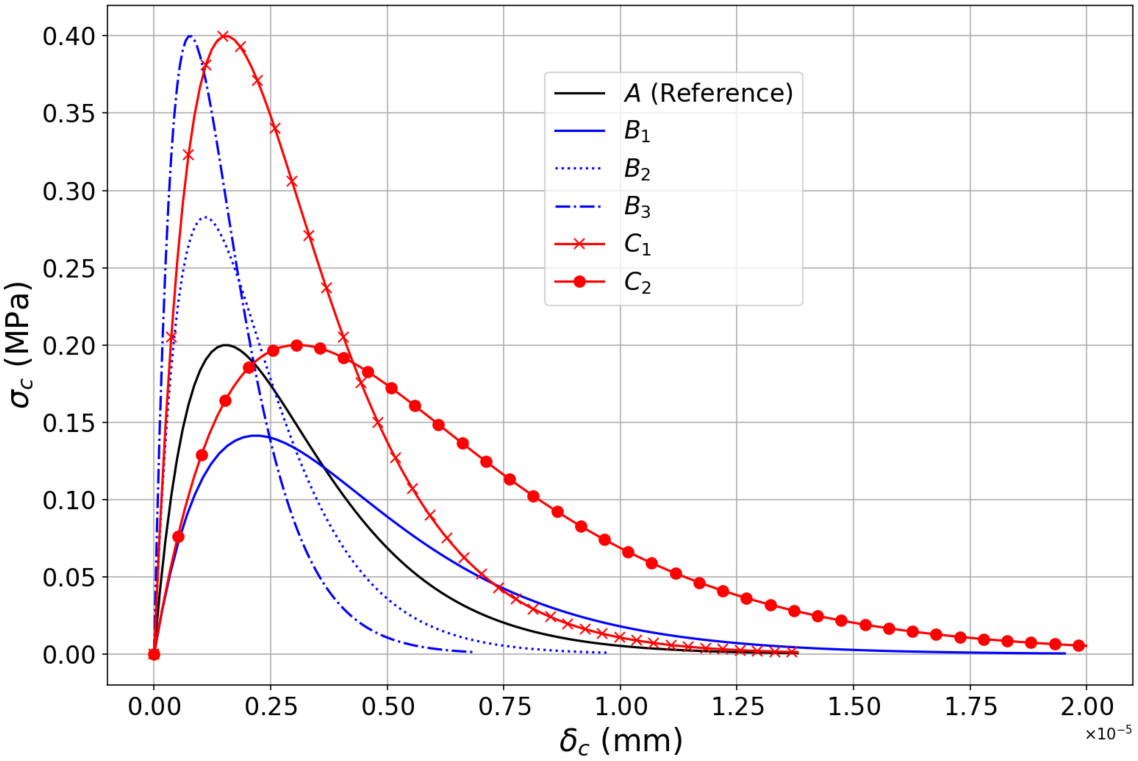

Figure 3.12: Different cohesive laws used here

other scenario, when fracture energy was doubled through the increasing of either the maximum cohesive stress or the critical opening displacement, the initiation of the propagation started later, and the required force for the fracture process was greater. The same remark can be asserted, if the fracture energy remains constant, variation of cohesive parameters do not lead to relevant changes in the solution.

When the critical opening displacement (δ_c) decreases while fracture energy is kept constant, the slope (stiffness) of the traction-separation law is significantly increased, as can be seen in Figure 3.12. Numerically, this high stiffness might heavily impact the conditioning of the linear system and, therefore impact the convergence of the numerical solver. Inversely, when δ_c increases, the stiffness is reduced.

The crack paths obtained using the studied cohesive parameters are shown in Figure 3.14. In terms of crack path, there are no significant differences. According to the results, the insertion of cohesive elements plays an important role in the crack propagation process. Its influence is in the energy involved in the propagation rather than in the crack path itself, allowing to simulate a more realistic fracture process.

Next section will be focused on the extension to 3D configurations of the already implemented and validated two-dimensional methodology.

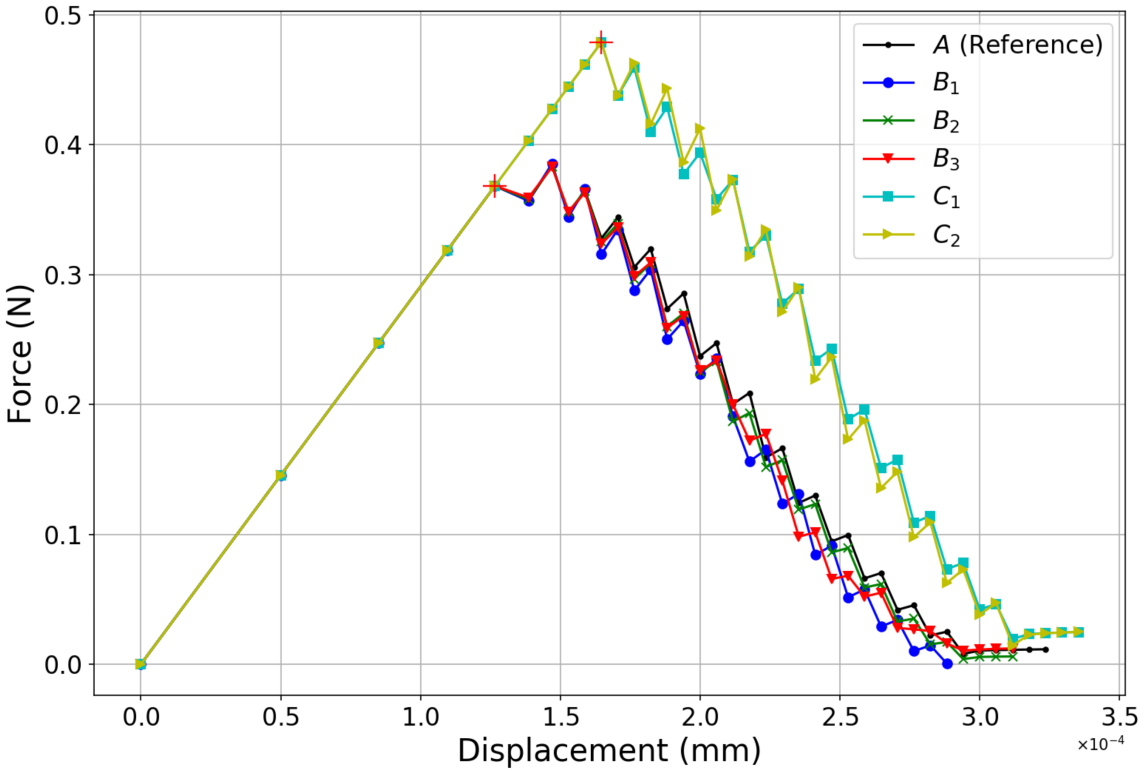

Figure 3.13: Force-displacement curves for different cohesive parameters

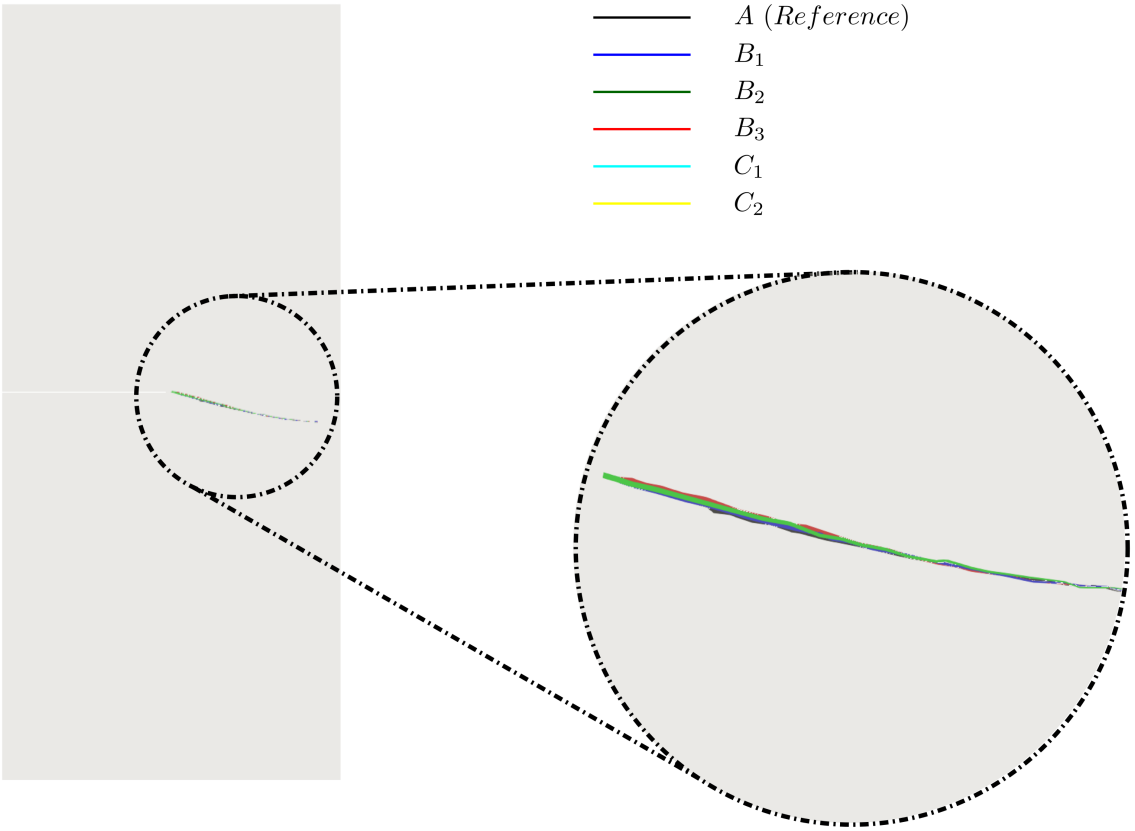

Figure 3.14: Crack paths comparison for different cohesive parameters.

3.2 Three-dimensional crack propagation

In order to illustrate the capabilities of the implemented methodology to tackle three-dimensional crack propagation, three benchmark examples will be presented. It is worth mentioning that in this work, an extension of the $G\theta$ method from 2D to 3D was not carried out due to lack of time. For this reason, this section will be focused in showing the ability of the proposed approach to propagate a crack front through arbitrarily predefined directions.

Here again, isotropic unstructured tetrahedral meshes that are refined in the neighborhood of the crack front are used. Unless otherwise said, all the examples presented here consider an initial notch or a prescribed crack front. The simulations performed are quasi-static. Multiple crack fronts are not considered. In order to simulate the fracture process, Xu and Needleman's cohesive law [Xu and Needleman, 1993] together with a viscous regularization technique [Gao and Bower, 2004] to avoid convergence issues were used. Same as in the two-dimensional cases of the previous section, for the sake of simplicity, the crack growth distance is set to a fixed value less than the process zone length ($PZL = \frac{G_c E}{\pi \sigma_c^2}$). Influence of this parameter on the simulations is not tackled here.

In the first part of this section, a three-dimensional interface debonding problem is presented to show the accuracy of the implemented cohesive law. Then, a three dimensional single edge notched tensile test is studied. Here, as the crack path is known a priori, cohesive elements are inserted since the beginning of the simulation over the crack path. Finally, the same three dimensional single edge notched tensile test is addressed, but in this case the crack front is propagated through arbitrary directions to show the robustness of the implemented methodology when tackling three-dimensional fracture propagation problems.

3.2.1 Interface debonding

To show the accuracy of the implemented Xu and Needleman's cohesive law [Xu and Needleman, 1993] (Chapter 2), the interfacial debonding of two solid parts joined by a cohesive interface is solved. Geometry, boundary conditions, as well as material properties are given in Figure 3.15.

Figure 3.16 shows the evolution of the stress (σ_{zz}) as well as of the opening displacement of the cohesive elements (δ) through the debonding process. It is possible to see that, initially the stress close to the interface starts to increase, and then when the critical cohesive stress (σ_c) is reached, the stress starts to decrease. Same figure also shows the evolution of the cohesive elements in terms of opening displacement. While the stress increases at the interface, cohesive elements open releasing the fracture energy. Looking at the bar scale, it is possible to see that when $u_z = 0.00045$ mm, the cohesive opening displacement (δ) is greater than the critical value showed in figure 3.15. Therefore, the cohesive elements have released much of the fracture energy and the two solid part are almost completely fractured.

Figure 3.17 presents the *force-displacement* curve describing the fracture process. The curves relating the force at the top boundary with both the top displacement and the opening displacement of the cohesive elements (δ) are also shown. In this figure it is possible to see that the theoretical cohesive law (blue dashed line) is almost perfectly reproduced. There is a small shift between the peaks of the two graphs (*force-displacement* and *force-opening displacement cohesive elements*). This is due to the fact that based on the imposed boundary conditions, the displacement at the top part of the domain is higher than in the middle.

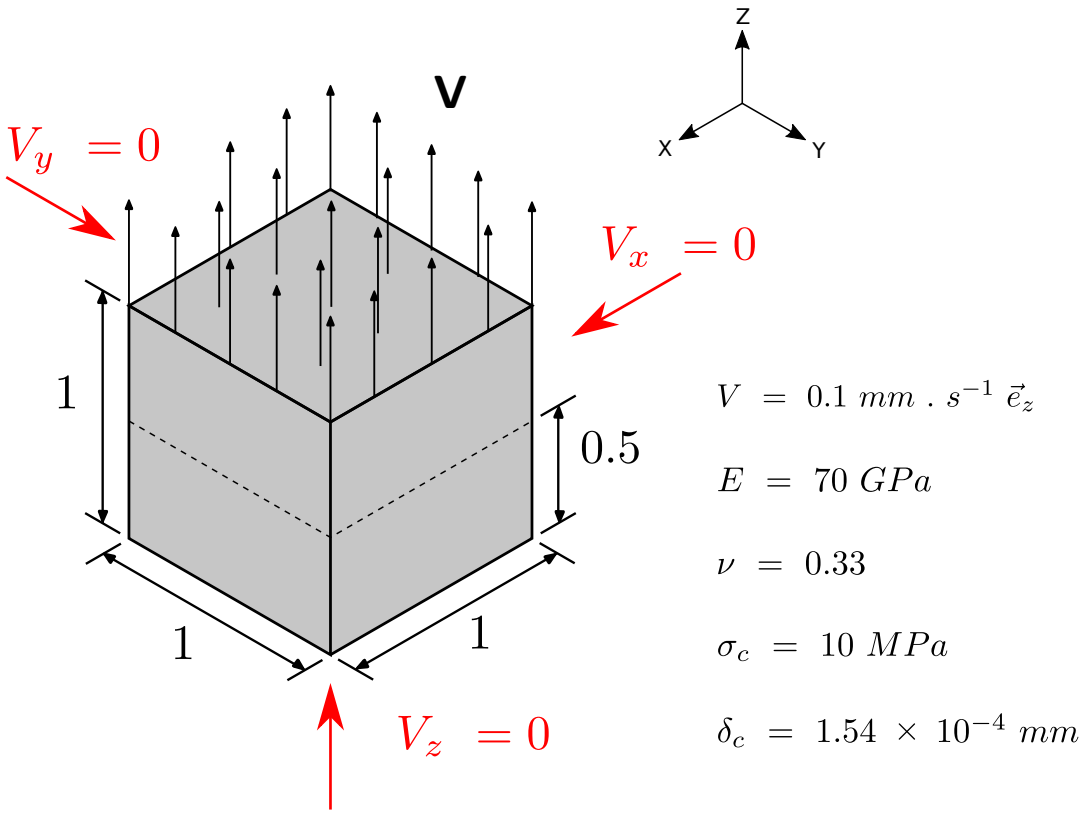

Figure 3.15: Geometry, boundary conditions and mechanical properties of the two solid parts joined by a cohesive interface (units in mm)

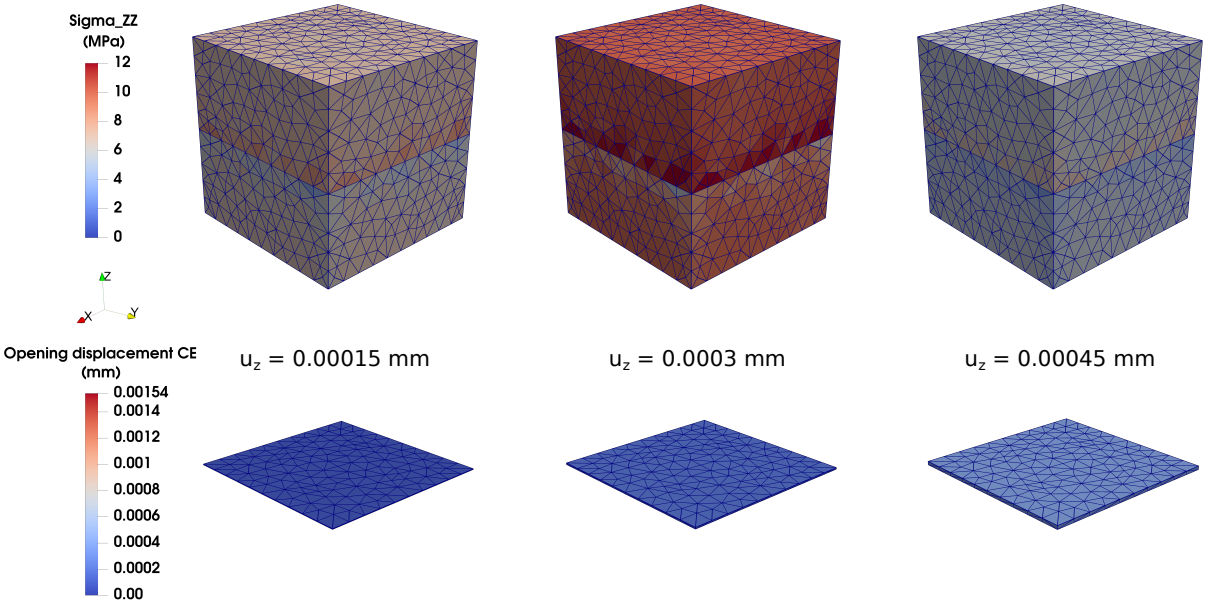

Figure 3.16: Evolution of the stress (σ_{zz}) and of the opening displacement of the cohesive elements (δ) for different displacement values (u_z) at the top part of the domain.

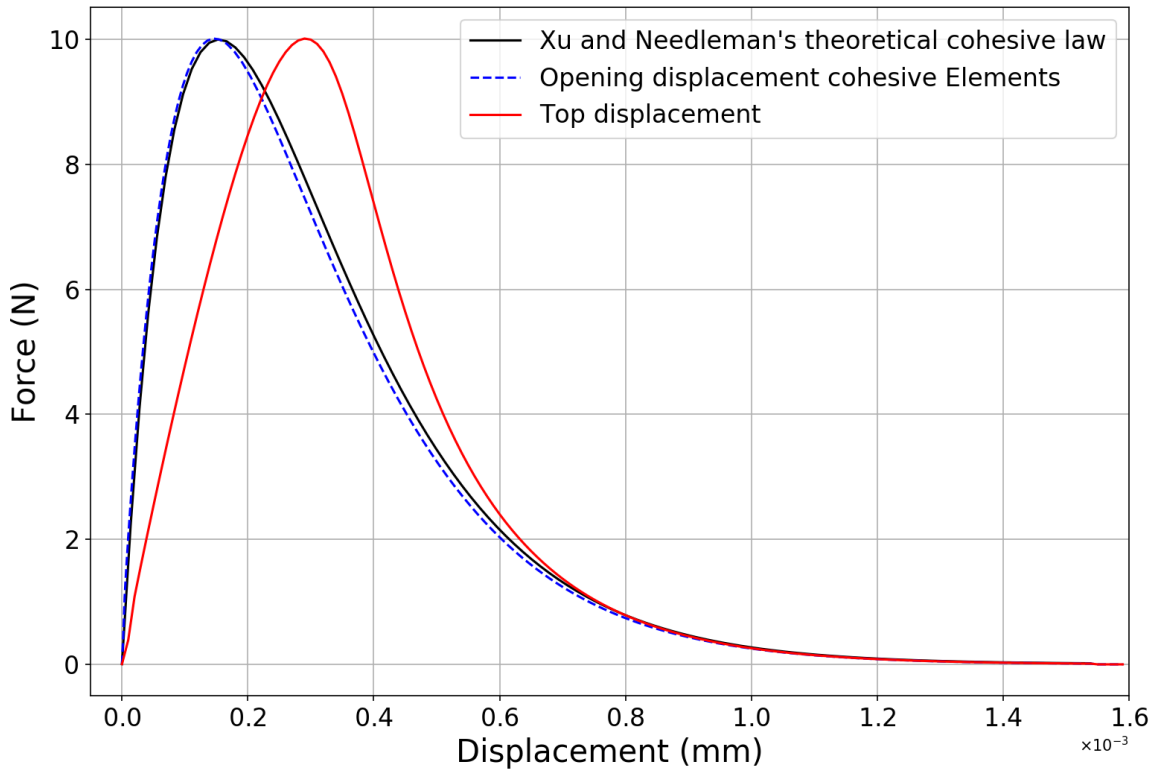

Figure 3.17: *Force-displacement* curve for the interfacial debonding of two solid parts joined by a cohesive interface.

3.2.2 Three dimensional single notched plate: predefined crack path

In this benchmark, taking advantage of the fact that the crack path under this loading configuration is known a priori, cohesive elements are inserted since the beginning of the simulation over the known direction. This example, like the previous one, helps us validating the implemented cohesive law. Figure 3.18 shows the geometry, boundary conditions, as well as material properties of a single edge notched specimen with a mode I crack. In this problem, the dimensionless constant Λ proposed by [Gao and Bower, 2004] is less than $\frac{1}{e}$ (Chapter 2), making necessary the use of a viscous regularization technique in order to avoid convergence problems.

The evolution of the crack front (i.e., the stress concentration) is depicted in Figure 3.19. In the same figure, the opening displacement of the cohesive elements (δ) for different top displacement values (u_z) is shown. It is worth noting that once the stress concentration at the crack front evolves, cohesive elements behind the front have an opening displacement greater than the critical value shown in Figure 3.18. According to this, those elements are almost broken, i.e., almost all the fracture energy has been released. On the other hand, the cohesive elements ahead of the crack front are still closed.

Introduction of cohesive elements since the beginning of the simulation induces one well-known drawback: reduction of the stiffness of the structure. Nevertheless, this is not a big issue here, because the goal of this example is to validate the implemented three-dimensional cohesive law and the insertion methodology of cohesive elements into a finite element mesh presented in section 2.6.3. This issue will be tackled in the next section. Figure 3.20 shows the *force-displacement* curve for the three dimensional single edge notched tensile test describing the fracture process. It is possible to see the force increase until it reaches the peak, then it gradually decreases following the post peak softening behaviour. Obtained results are in agreement with the expected behavior of crack propagation under mode-I.

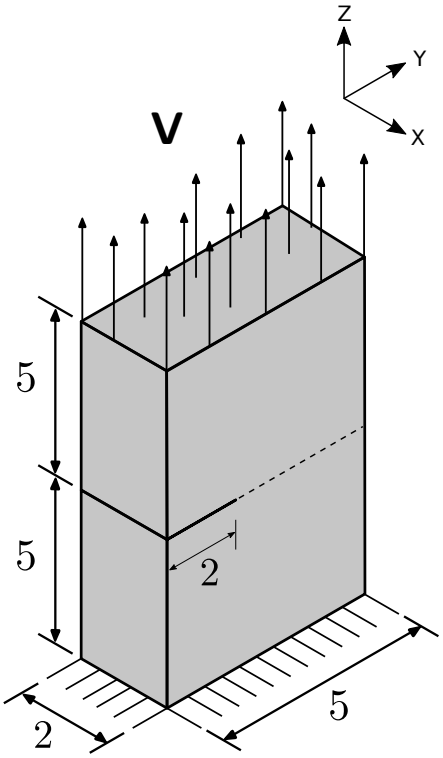

$V = 4\ mm\ .\ s^{-1}\ \vec{e}_z$ $\quad PZL = 0.1476\ mm$

$\Delta t = 0.5 \times 10^{-5}\ s$ $\quad G_c = 0.2229\ \frac{N}{mm}$

$E = 20800\ MPa$ $\quad \Lambda = \frac{E\delta_c}{2a\sigma_c} = 0.017056$

$\nu = 0.3$ $\quad \xi = 1 \times 10^{-5}$

$\sigma_c = 100\ MPa$

$\delta_c = 8.2 \times 10^{-4}\ mm$

Figure 3.18: Geometry, boundary conditions and mechanical properties for the three dimensional single edge notched tensile test (units in mm).

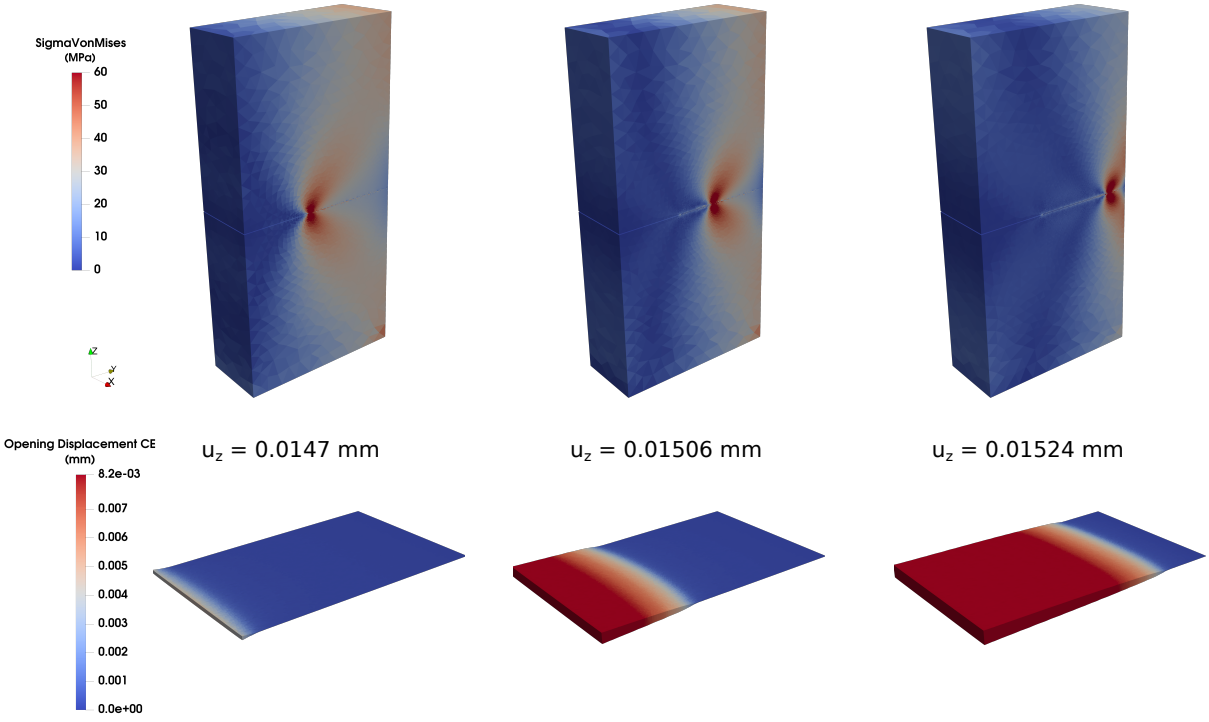

Figure 3.19: Evolution of the fracture process though the von Mises stress and the opening displacement of the cohesive elements (δ) for different displacement values (u_z) at the top part of the domain.

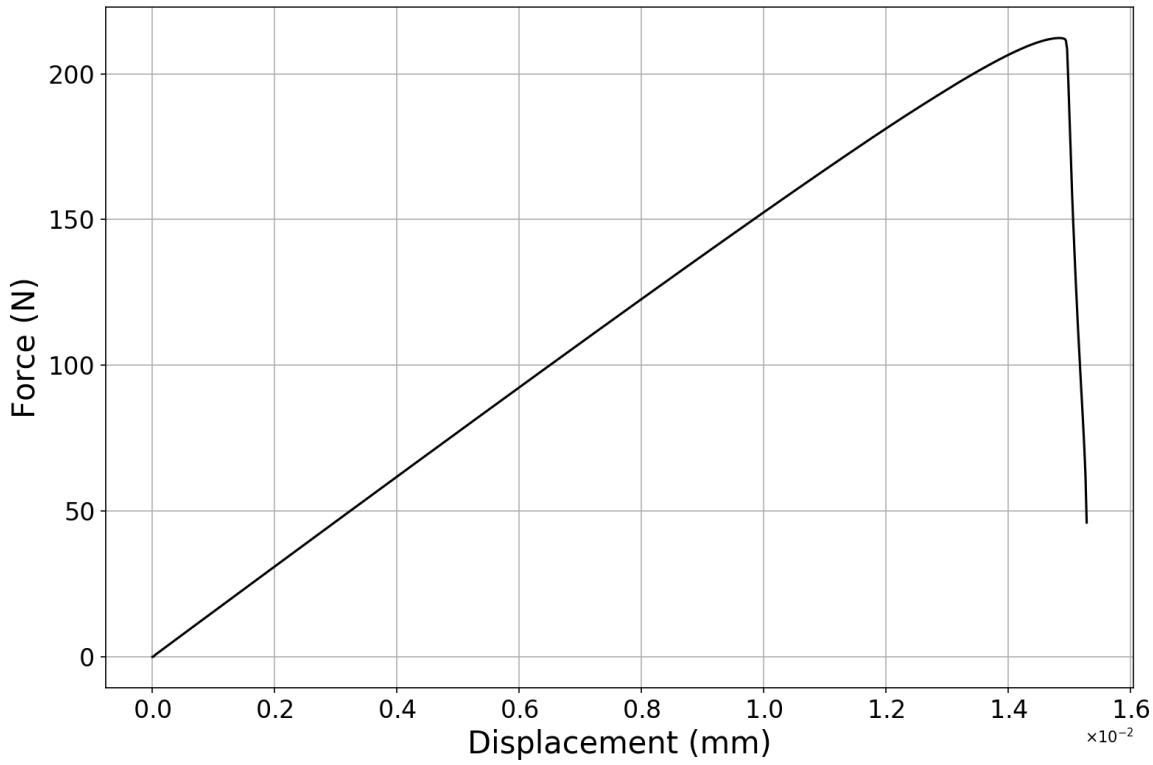

Figure 3.20: *Force-displacement* curve for the three dimensional single edge notched tensile test.

3.2.3 Three dimensional single notched plate: unknown crack path

In this section the capability of the implemented methodology to handle three-dimensional crack propagation through arbitrary directions is presented. At this point, some important details of the presented approach must be clarified:

- The extension of the $G\theta$ method to 3D was not carried out (lack of time).
- Consequently, crack propagation directions are arbitrarily prescribed, but cohesive elements are inserted *on the fly* once this direction is given.
- Definitely, the extension of the $G\theta$ method to 3D will be investigated in future work.

The benchmark example considered in previous section is used again. The main idea behind this benchmark is to show the promising capabilities of the already tested and validated two-dimensional approach presented in [Uribe-Suárez et al., 2020] when extending it to three-dimensional scenarios. Here some aspects of the performed propagation process must be clarified. For the sake of simplicity, at each propagation of the crack front, each one of the nodes belonging to the front will be propagated the same distance through the same direction. The propagation distance is set to a fixed value equal to 4 times the size of the elements close to the crack front ($\approx$ 0.089 mm). This value is less than the process zone length as normally recommended in the literature [Turon et al., 2007, Hermes, 2010, Ha et al., 2015].

In our three-dimensional case, directions over which the crack front propagates are defined arbitrarily. Figure 3.21 shows the geometry and boundary conditions of the benchmark case, as well as the aforementioned arbitrary directions. In order to define and compute the 3D surface over which the crack front evolves, the procedure described in section 2.6.2 is used. The remeshing procedure is the same that was previously described for the two-dimensional case. It is composed of two stages. In the first step, a conforming mesh is obtained in the defined

direction (surface), ensuring that faces of the tetrahedra are placed over the sought direction (surface). In the second stage, cohesive elements are dynamically inserted at the conforming faces previously remeshed. In this case, the crack front will follow a curvilinear trajectory composed of 6 propagations (i.e., numbers inside the circles in Figure 3.21).

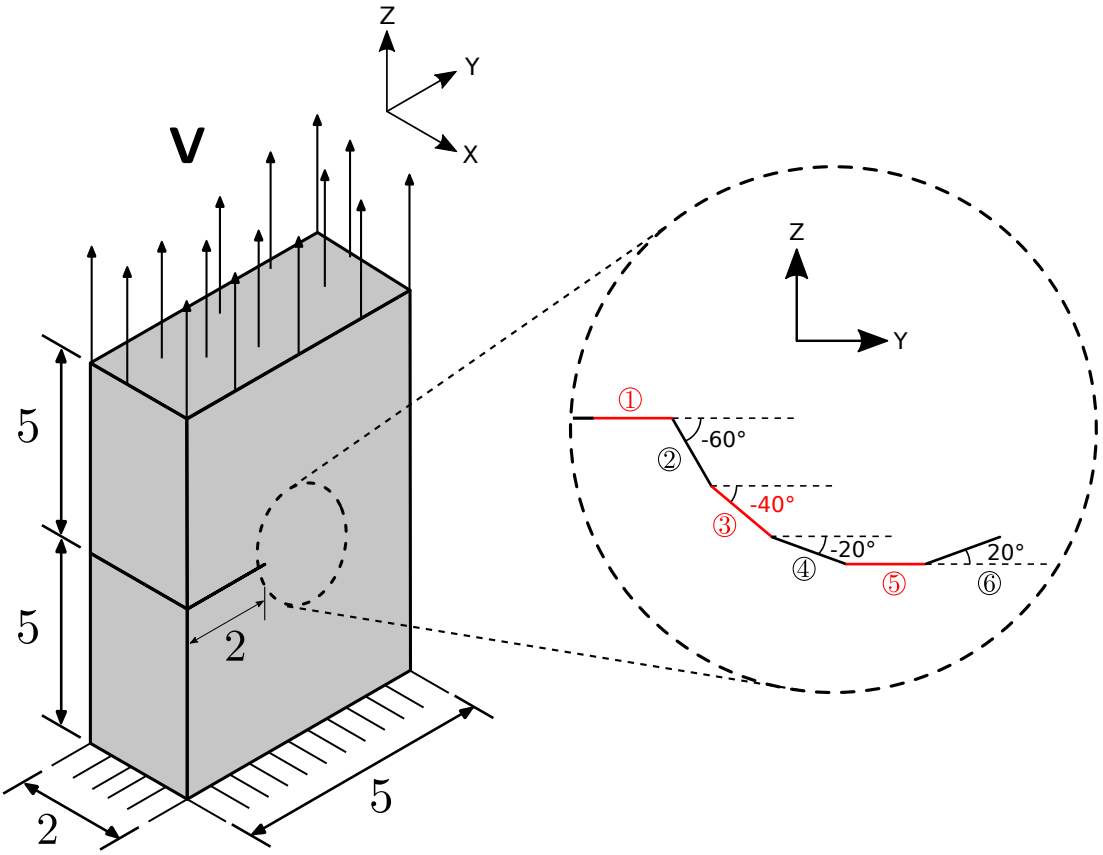

Figure 3.21: Geometry and boundary conditions for the three dimensional single edge notched tensile test. It is also shown a zoom view describing the arbitrary path over which the crack front will propagate.

Figure 3.22 shows the curvilinear crack path. The complexity of the crack path shows the capabilities of the proposed methodology to tackle three-dimensional crack propagation problems. It is also shown the opening displacement value of the cohesive elements forming the crack path, whose maximum value is around 0.0002 mm. This represents 2.44% of the critical value used in the cohesive law ($\delta_c = 8.2 \times 10^4\ mm$). It means that the inserted cohesive elements are practically still closed. They have released a tiny amount of the fracture energy, which is quite logical since the time at which they were inserted was arbitrarily defined without following any proper criteria. As the $G\theta$ method was not extended in this work, the energy release rate (G) can not be quantified. Therefore, there is no way to define a threshold value to decide when the cohesive elements must be inserted.

A detailed evolution of the crack front at different time steps is presented in Figure 3.23. It is worth mentioning that when propagating the crack front from its previous position to the next one, it is not possible to have anymore a straight line crack front. Some nodes propagate a distance greater than other nodes. Once the finite element mesh has been fit to the computed fracture surface in 3D (i.e., when faces of the tetrahedra are placed over the fracture surface), next step is to propagate over this surface the nodes belonging to the crack front to its new position. The distance that the nodes are propagated is dictated by the fixed propagation distance. Even though the mesh size is controlled during the remeshing process, there is not

way to guarantee that the new crack front is a straight line.

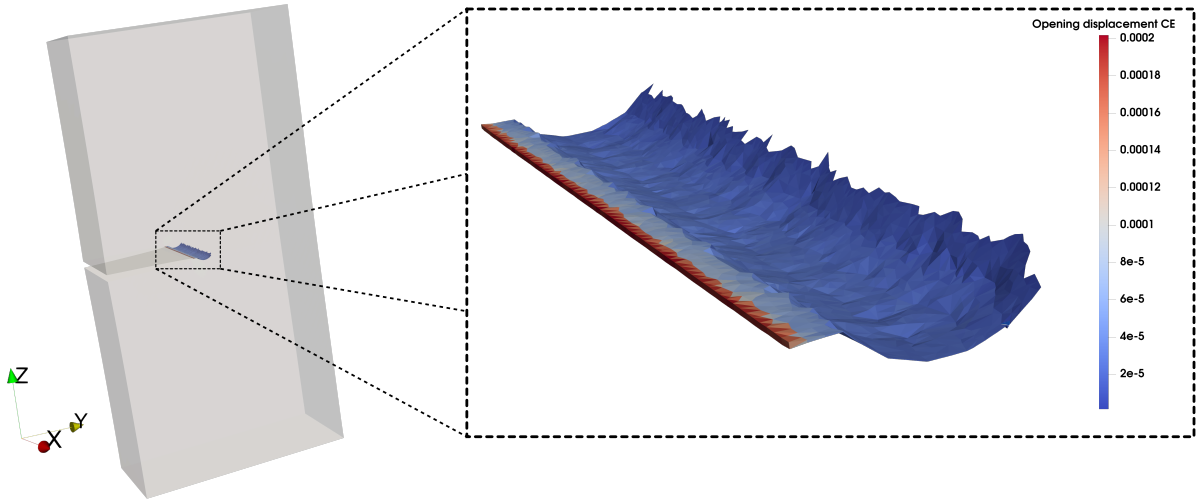

Figure 3.22: Final crack path after 6 propagations. The color map represents the opening displacement of the cohesive elements (mm) forming the crack path.

It can be seen that the crack front is quite irregular. This can generate some troubles that will be discussed in the perspectives section. A crack front smoothing technique could be necessary.

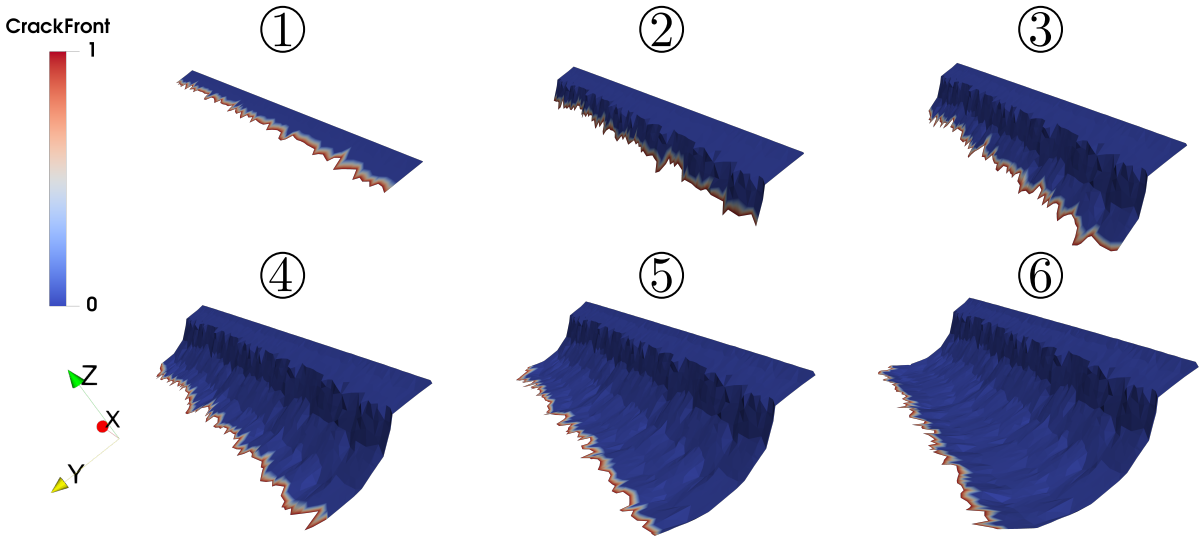

Figure 3.23: Detailed of the crack front propagation.

Due to the fact that the energy release rate is not being quantified and that cohesive elements are inserted without fulfilling any criterion, it is clear that this simulation does not have any physical meaning. This simulation is a merely representation of the capabilities of the presented methodology when simulating three-dimensional crack propagation using remeshing operations and dynamic insertion of cohesive elements. There are still some drawbacks or limitations that have to be faced in order to make this promising approach a really useful tool to handle fracture processes in three-dimensional problems:

(i) Application of a proper criterion to allow crack front propagation: in order to simulate appropriately the fracture process, a criterion to decide when to allow the propagation of the crack front (i.e., insertion of cohesive elements) must be defined. An energetic criterion as the one used in two-dimensional problems would be the most suitable ($G > G_c$).

(ii) Computation of the appropriate crack propagation direction: the most suitable technique to compute the direction of propagation is the $G\theta$ method. This is particularly true here since the available finite element framework (See Chapter 2) is not good enough at capturing the singularity of the stress field at the crack front. Thus, the use of an energetic approach may be more appropriate. Additionally, once G is known, it would be possible to compare it against G_c to decide whether or not, the crack front propagates.

(iii) Optimal propagation of the crack front: even if the propagation distance is fixed and equal for all the nodes belonging to the crack front, as shown in Figure 3.23, some nodes may propagate more than others, making the crack front quite irregular. To overcome this issue, a possible solution may be to develop a methodology that allows finding the intersection of the propagated crack front with the finite element mesh (not easy at all). Another solution could be the development of a crack front smoothing technique similar to that developed by [Shakoor et al., 2015], where the finite element meshes are adapted to level-set functions.

3.3 Summary of Chapter 3

This chapter is dedicated to the presentation of the numerical results regarding crack propagation using remeshing operations and dynamic insertion of cohesive elements in both two- and three-dimensional cases. Section 3.1 introduced the results already published in [Uribe-Suárez et al., 2020]. Two-dimensional crack propagation was achieved through the combination of a remeshing technique with dynamic insertion of cohesive elements, leading to a mesh-independent methodology. The effects of different numerical and physical parameters regarding the crack path and fracture energy were investigated. The accuracy of the proposed method when calculating the crack propagation direction under mixed-mode loading was presented. Additionally, through a cracked beam supported in two points and loaded in the center, the effects on mixed-mode crack paths due to the presence of holes was also assessed. In the same section, the impact of different numerical and physical parameters on the crack path and fracture energy was studied.

Then, section 3.2 presented the results regarding the first attempt to extend the already validated two-dimensional methodology to three-dimensional scenarios. Several cases were tackled there. First, the debonding of the cohesive interface joining two solid parts were presented. Then, the crack propagation process of a three dimensional single edge notched tensile test was shown. In this example, as the crack path was known a priori, cohesive elements were inserted from the beginning of the simulation over the whole crack path. Finally, in the last part of this section, the same three dimensional single edge notched tensile test was addressed, but in this case, the crack front was propagated in arbitrary directions. Latter was done in order to prove the promising capabilities of the proposed methodology to simulate three-dimensional crack propagation using remeshing operations and dynamic insertion of cohesive elements.

3.4 Résumé en français

Ce chapitre présente les résultats de simulation numérique de propagation de fissure en utilisant des opérations de remaillage et d'insertion dynamique d'éléments cohésifs pour des problèmes à deux et trois dimensions. La partie 3.1 introduit les résultats déjà publiés dans [Uribe-Suárez et al., 2020]. Dans des cas 2D, la propagation de fissure est réalisée en utilisant des techniques de remaillage et d'insertion dynamique d'éléments cohésifs, dans le but de développer une méthode indépendante du maillage. Les effets des paramètres numériques et physiques sur la direction de propagation et l'énergie de rupture sont étudiés. La précision de la méthode proposée pour le calcul de la direction de propagation de la fissure dans le cas de chargements

mixtes est discutée. De plus, en utilisant l'exemple d'une poutre fissurée, supportée en deux points et chargée en son centre, l'influence de la présence de trous sur la propagation des fissures est évaluée. L'effet de différents paramètres numériques et physiques sur la direction de propagation et l'énergie de rupture sont étudiés pour ce cas.

Puis, la section 3.2 présente les résultats concernant une première tentative d'extension de la méthode pour des cas en trois dimensions. Plusieurs exemples sont détaillés. Le premier traite de la décohésion d'une interface à la jonction entre deux pièces solides. Ensuite, un exemple d'une pièce entaillée soumise à un test de traction est présenté. Dans ce cas, la direction de propagation de la fissure étant connue, les éléments cohésifs sont introduits au début de la simulation, le long de la fissure. Finalement, dans la dernière partie de ce chapitre, ce cas test est repris dans le cas d'un front de fissure se propageant selon des directions arbitraires. Cet exemple a été défini afin d'illuster les capacités de la méthodologie proposée pour simuler des propagations de fissures en 3D.

Chapter 4

Diurnal temperature variation as the source of the preferential direction of fractures on asteroids: theoretical model for the case of the asteroid (101955) Bennu

Contents

It has been shown that temperature cycles on airless bodies of our Solar System can cause damaging of surface materials. These cycles are typically caused by the change between day and night. Nevertheless, propagation mechanisms in the case of space objects are still poorly understood. As it was mentioned in the beginning of this PhD thesis, one of the main ideas of this work is to numerically reproduce some observed fractures on space bodies which are thought to be induced by large amount of thermal cycles. In the present work, efforts are oriented to model the crack propagation direction in conditions similar to those existing on asteroid (101955) Bennu. The main motivation comes from the fact that theoretical foundation for analysis and interpretation of fracture directions on small asteroids with properties similar to those of Bennu is still lacking. The present chapter is based on the results already published in [Uribe-Suárez et al., 2021].

Aiming at predicting crack propagation in the presence of thermal gradients generated by diurnal temperature cycling and under conditions similar to those existing on the asteroid Bennu, the present work combines a thermoelasticity model together with linear elastic fracture mechanics theory. To facilitate the understanding of the results presented in this chapter, section 4.1 introduces the context of this study. Section 4.2 briefly describes the methodology followed in this work in order to perform a fracture mechanics analysis through the developed thermo-mechanical model. To show the accuracy of the proposed methodology when calculating the crack propagation direction due to the presence of thermal gradients, one simple example is presented in section 4.3. Obtained results are compared against observed crack propagation directions on asteroid Bennu. Then, a thermal fatigue analysis is performed in order to estimate the crack growth rate. Finally, section 4.4 discusses the computed crack propagation directions.

4.1 Introduction

The asteroid (101955) Bennu is the center of important studies because it is the target of the OSIRIS-REx mission [Lauretta et al., 2014, Lauretta et al., 2017]. Bennu is a near-Earth asteroid. This is a low-albedo B-type asteroid that has been linked to carbonaceous chondrites. Due to the fact that tremendous temperature variation have been reported on this asteroid, thermal fatigue is thought to play an important role in its landscape evolution [Ballouz et al., 2020, Molaro et al., 2020b]. Figure 4.1 shows the geomorphological diversity of the asteroid Bennu. Consistent with its characterization as a rubble-pile, it is cratered and covered by rocks with a wide range of sizes [DellaGiustina et al., 2019].

In the present study, the observational evidence reported by [Delbo et al., 2019] is used as reference. In this work, the authors used a series of images similar to the one presented in Figure 4.1-**b**. These images were obtained by the OSIRIS-REx Camera Suite (OCAMS), with a scale of 5-6 cm pix^{-1}, during the first and third "Baseball Diamond" flybys of the Detailed Survey mission phase, which occurred on 7 and 21 March 2019, respectively. The authors used different visualization tools to visually identify and map fractures on boulders. Then, as shown in Figure 4.2, they drew line segments along each identified fracture. [Delbo et al., 2019] found that the azimuthal distribution of the identified fractures on the asteroid (101955) Bennu displays a preferential North-West to South-East (NW-SE) direction. In this work, in order to be in accordance with the available observational evidence, all the computed crack propagation directions on Bennu are referenced to the azimuth angle.

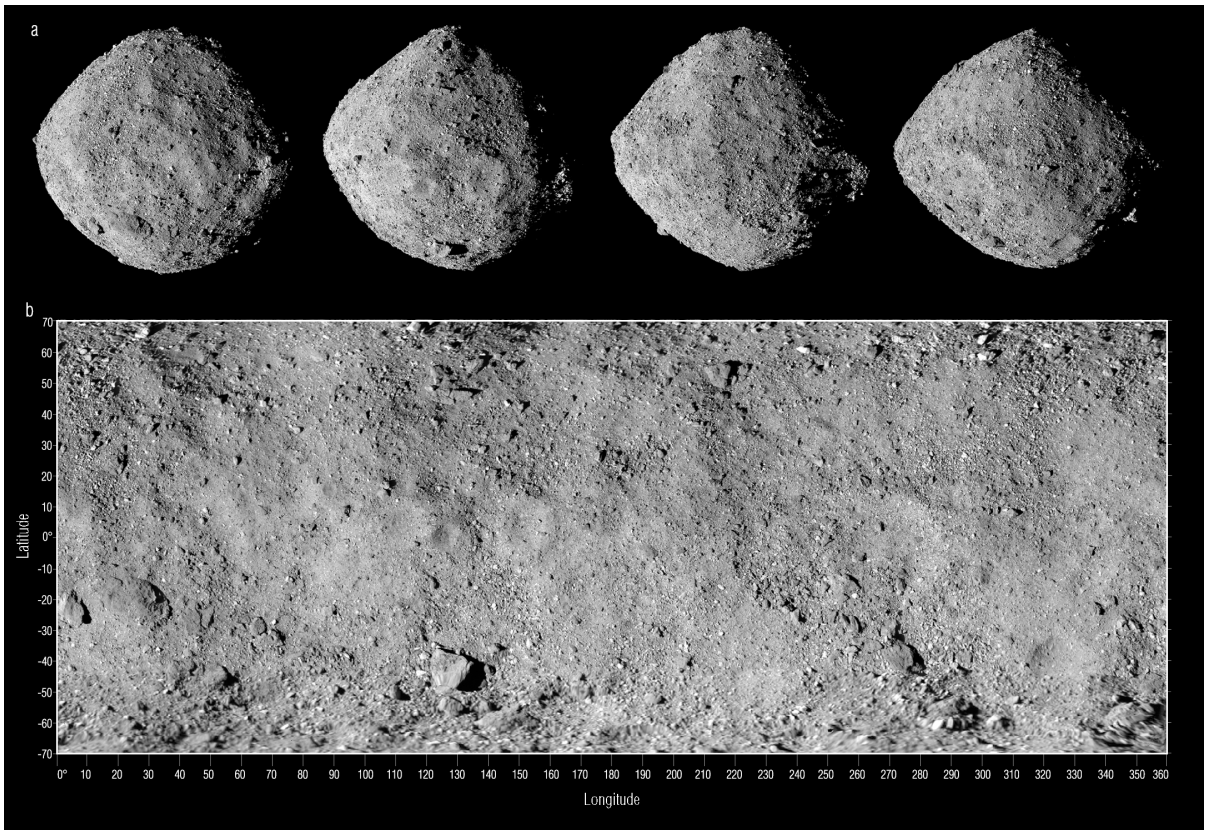

Figure 4.1: Asteroid Bennu imaged by the OSIRIS-REx Camera Suite. **a)** PolyCam images from 2 December, 2018 are combined to show four sides of Bennu. When viewed from left to right these data illustrate one rotation of the asteroid. **b)** PolyCam images acquired on 1 December, 2018 are combined with MapCam images from 13 December, 2018. These images are mosaicked into a global equirectangular map of Bennu. North points to the top of the image. Figure reproduced from [DellaGiustina et al., 2019].

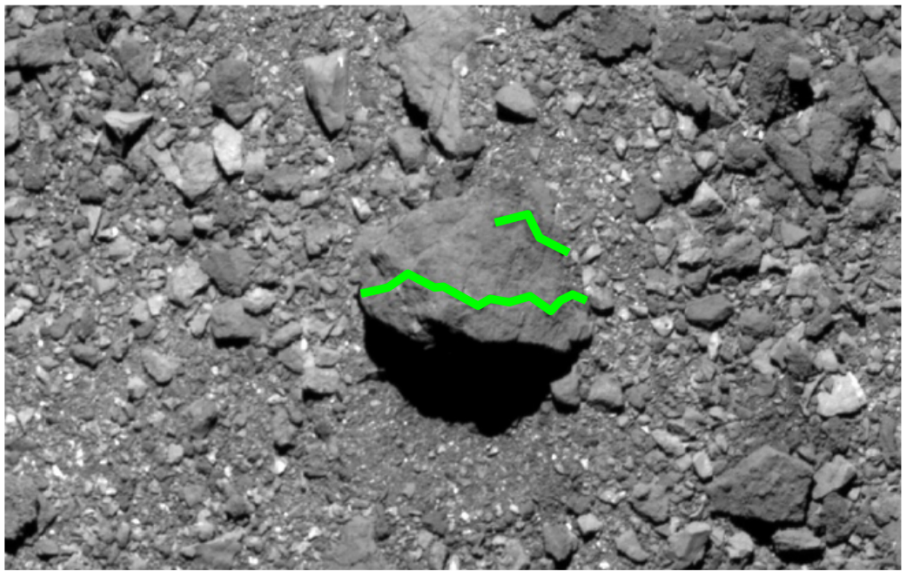

Figure 4.2: Example of fracture mapping on a boulder using a broken line made of several segments (green). Figure reproduced from [Delbo et al., 2019]

In order to have a better understanding of the results that will be presented in this chapter, the concept of azimuth angle is introduced. The azimuth is the angle formed between a reference direction (i.e., North) and a line from the observer (celestial body) to a point of interest on the same plane as the reference direction. A schematic representation of the azimuth angle is presented in Figure 4.3.

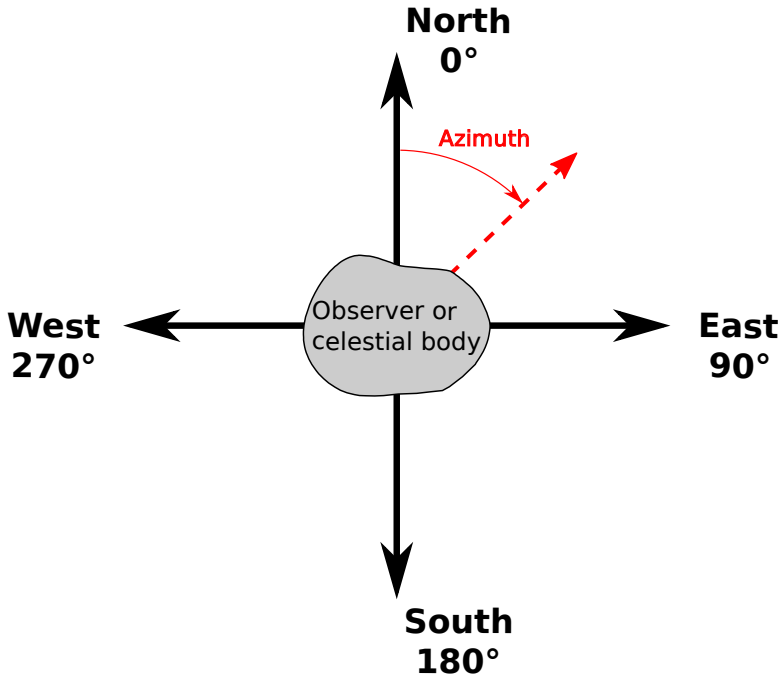

Figure 4.3: Schematic representation of the azimuth angle.

Aiming at a better understanding of one phenomenon (i.e., thermal cracking) that is thought to be highly important in the landscape evolution process of the asteroid Bennu (e.g., regolith production), the idea in the following is to try to quantify the predominant direction of the fractures associated with thermal stresses under fatigue on Bennu.

4.2 Methodology

Primary goal of this study is to compute the direction of crack propagation due to thermal strain in a geometry corresponding to a typical boulder on the surface of the asteroid (101955) Bennu, the target of NASA's sample return mission OSIRIS-REx. This work assumes the hypothesis that most of the fractures observed on the surface of the boulders by [Lauretta et al., 2019b], [DellaGiustina et al., 2019], and [Delbo et al., 2019] are due to the growth of surface cracks. [Molaro et al., 2020b] also discuss stresses inside boulders that could cause cracking deep inside the rock mass. These inside cracks, albeit possibly present, are not visible from spacecraft observations.

The geometry of the problem studied here is schematised in Figure 4.4. This Figure shows a cubic-like boulder extruding from the equator of the asteroid, of which only about half of the equatorial belt is simulated.

The mesh is divided in triangular facets. A thermophysical model [Delbo et al., 2015] is used to calculate the temperatures of all facets as a function of time, as described in the following sections. The temperatures of the boulder facets are then used in a thermoelastic model in order to compute the strain and stresses as a function of the position in the boulder and time. Next, fracture mechanics theory is used to estimate the propagation direction of a tiny notch that is placed on the horizontal (a', a") face of the cubic boulder. The crack direction is computed

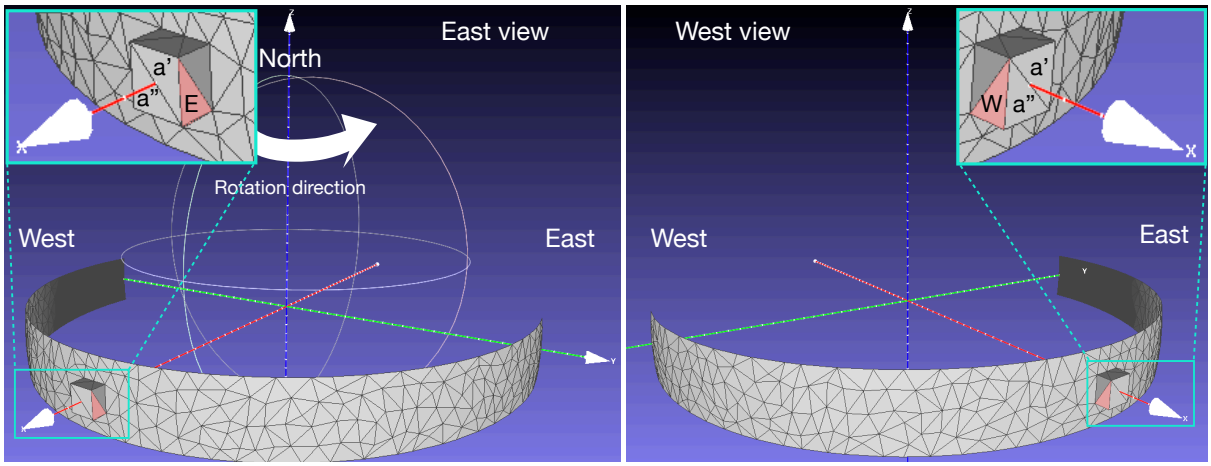

Figure 4.4: Schematic representation of the cubic-like boulder extruding from the equator of the asteroid, of which only about half of the equatorial belt is simulated to obtain the temperature distribution on faces **E** and **W**.

using the maximum energy release rate criterion (MERRC), which is implemented using finite elements and the $G\theta$ method (including thermal extension).

4.2.1 Thermo-physical model

The first step of the presented methodology consists in using a well-established thermophysical model [Spencer et al., 1989, Delbo et al., 2015] to solve the one-dimensional heat diffusion problem. Temperature is calculated as a function of time for all the surface elements of the mesh depicted in Figure 4.4. Boundary conditions are given by the variable day/night illumination including the shadows cast by the local terrain of the mesh on itself, radiation of the heat in space, conduction in the sub surface, and mutual heating [Rozitis and Green, 2011]. The physical parameters of the material used in this work are given in Table 4.1. These properties were taken from [Delbo et al., 2014]. They correspond to the Carbonaceous Chondrite sub-type CM2 Murchison meteorite. This is considered to be a good analog of asteroids belonging to the C-complex broad spectroscopic class [DeMeo et al., 2009]. The asteroid Bennu also belongs to the C-complex class [Hamilton et al., 2019]. This study assumes that the material is homogeneous and isotropic.

4.2.2 Thermoelastic model

[Delbo et al., 2019] observed and mapped cracks on boulders on the surface of the asteroid Bennu using OSIRIS-REx images that can be approximated as parallel to the local surface of the asteroid. On the other hand [Delbo et al., 2014], [Ravaji et al., 2019] and [El Mir et al., 2019] considered cracks propagating perpendicularly to the local surface (i.e., fragmentation or breakdown of asteroid rocks). For this reason, current work is interested in the component of the crack growth parallel to the local surface of the asteroid, namely the plane perpendicular to the X-axis of the mesh of Figure 4.4. To study this case, a 2-D model where the initial crack is placed on the a' and a" facets of Figure 4.4 is used. These two facets are treated together in the following as the single planar face that is called "a-face" (Figure 4.5). The separation of the a-face in two facets is required to make the implemented thermo-phyisical model, that uses triangular facets only, compatible with the meshing algorithm. The vertical E and W facets of the 3D mesh of the thermo-physical model (Figure 4.4) are respectively mapped to the vertical right and left sides of the beam simulated by the proposed thermoelastic and fracture mechanics model (Figure 4.5). The crack propagation on the a-face is essentially driven by

Quantity name, symbol	Units	Value	Reference
Rotational period, P	s	15,469.2	[1]
Bulk modulus, K	MPa	29,000	[2]
Shear modulus, μ	MPa	18,000	[2]
Young modulus, E	MPa	44,742.857	[2]
Poisson's ratio, ν		0.2428	[2]
Bulk density, ρ	kg m^{-3}	1,662	[2]
Thermal conductivity, λ	W mm^{-1} K^{-1}	5×10^{-4}	[2]
Thermal expansion coefficient, α	K^{-1}	8.5×10^{-6}	[2]
Specific heat capacity, c	J kg^{-1} K^{-1}	500	[2]
Reference temperature, T_{ref}	K	250	[3]
Paris pre-factor, C	m [MPa $\sqrt{\text{m}}$]$^{-n}$	3×10^{-4}	[2]
Paris exponent, n		3.84	[2]

Table 4.1: Thermal and mechanical properties and their default values used in this work for the simulations of the crack propagation directions on asteroid Bennu. References: [1] = [Barnouin et al., 2019], [2] = [Delbo et al., 2014], [3] = this work.

the 2D temperature gradient created by the strong temperature mismatch between the E- and W-face (See section 4.3).

These temperature gradients exist throughout the whole day/night cycles and strongly depend on time. There is also a component of the temperature gradient perpendicular to the a-face, which causes crack propagation in the sub-surface. This component has been studied by [Delbo et al., 2014], [El Mir et al., 2019] and [Ravaji et al., 2019] providing laws to estimate the crack growth rate in that direction.

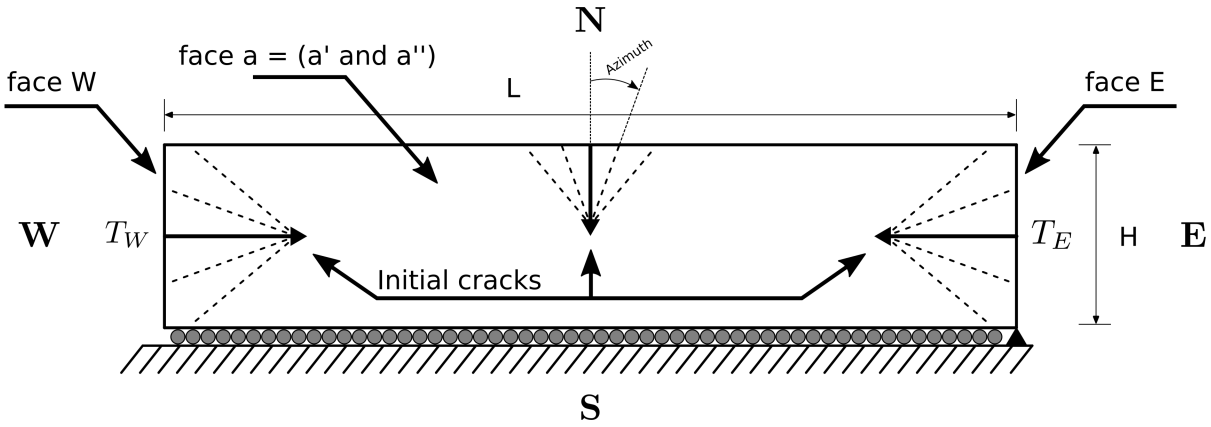

Figure 4.5: Geometry and boundary conditions for the face of the boulder parallel to the surface. Crack tip position and crack axis were varied. The length of the a-face is also varied in our simulations.

Therefore, only the temperature gradient is considered in the a-face in this study. To do so, the heat diffusion equation is used to calculate the temperature as a function of space and time in the a-face given as boundary conditions the temperatures on the E- and W-faces, which are determined by the asteroid thermo-physical model. Once the thermal problem has been solved, the effect of the temperature variation on the mechanical response of the body (thermal stresses) is computed through the implemented thermeolasticity model described in section 2.4. In this model the computation of the thermal strain presented in equation (2.55) requires the use of a reference temperature (i.e., temperature where there is no strain). The current work assumes that the reference temperature is the average of the temperatures given in Section 4.3.

As it was already said in section 2.4, in the presented method a weak thermomechanical coupling is assumed. This means that the temperature is initially obtained from the heat problem and then introduced into the mechanics computation. This is possible since the characteristic time scale of the thermal problem is several orders of magnitude greater than the characteristic time scale of the crack propagation problem. For the solution of a thermoelastic problem, first, the temperature distribution inside the body is computed by solving the heat transfer problem. Then, the resulting temperature distribution is used as an input initial strain to the mechanical problem.

4.2.3 Fracture analysis

Once the thermomechanical problem is solved, the fracture mechanics analysis is carried out. To compute the crack propagation direction, a criterion based on the azimuthal distribution of the energy release rate around the crack tip is used. Multiple crack propagation directions are tested and then the one that maximises G is selected. Namely, in the plane of the a-face, the azimuth of the maximum energy release rate is identified, as it is known that crack propagation will take place in that direction. Since thermal strain is accounted for, the $G\theta$ method including thermal strain (as described in section 2.5) is used to compute the crack propagation direction. A schematic representation of the sequential solution of the thermomechanical problem presented in this work is provided in Figure 4.6.

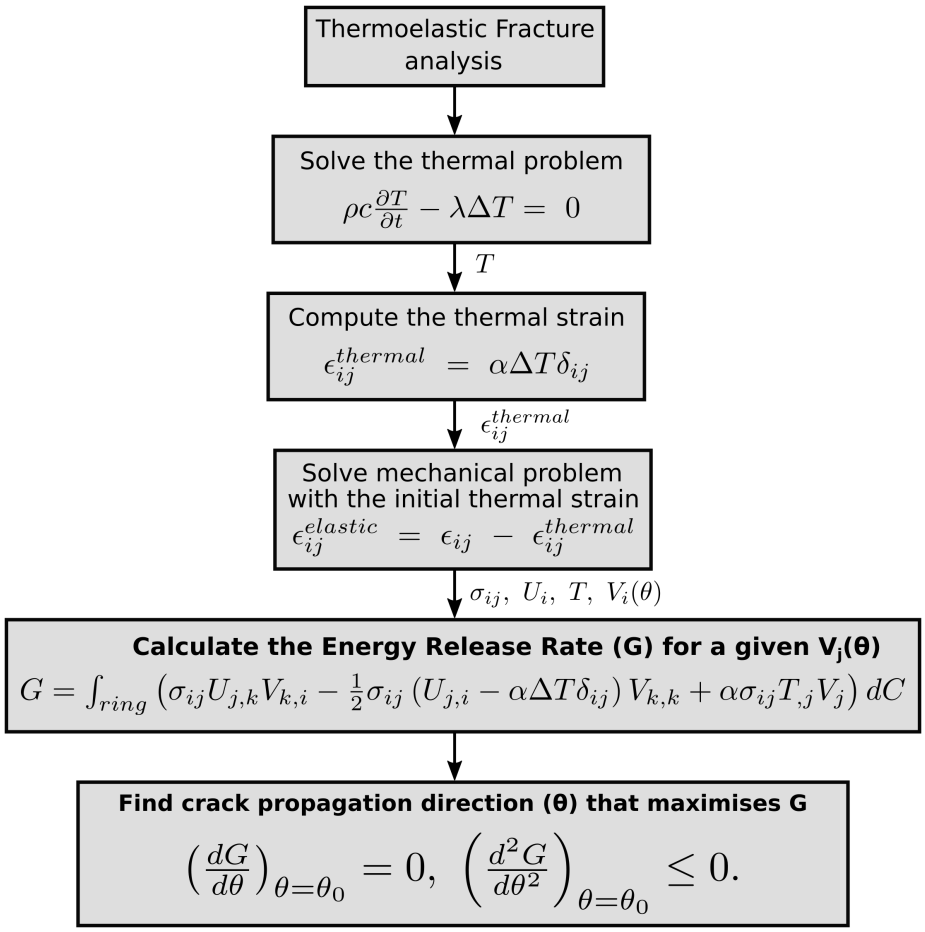

Figure 4.6: Schematic representation for the thermoelastic fracture analysis performed in this work.

Due to the fact that the present work deals with thermal cyclic stress (tension-compression), only mode I loading is assumed. Once the energy release rate (G) is known, it is possible to

compute the stress intensity factor (K_I). Assuming plane strain conditions, a relation between G and K_I can be stated from equation (1.12):

$$K_I = \sqrt{\frac{G\ E}{1-\nu^2}} \tag{4.1}$$

where K_I is the mode I stress intensity factor, G is the energy release rate, E is the Young modulus and ν is the Poisson's ratio. In order to perform a thermal fatigue analysis in the case of asteroid Bennu, Paris's Law (See section 1.2.3.1) is used.

The beam presented in Figure 4.5, also referred as the a-face in this work, is embedded in a mesh that is different from the one showed in Figure 4.4. The aforementioned mesh is an isotropic unstructured triangular mesh, that is refined in the neighborhood of the crack tip. The thermoelasticity problem is solved on this mesh through the finite element method (FEM). The developed thermoelastic model has been implemented in Cimlib [Digonnet et al., 2007]. Regarding the thermal problem, the available finite element framework in Cimlib is a classic one where the variable temperature (T) is solved through an implicit formulation [Ryan et al., 2020]. The mechanical problem is solved using a mixed implicit formulation (see section 2.2).

4.3 Results

In this work, the simulations begin by calculating temperatures for the mesh of Figure 4.4 using the asteroid thermophysical model described in section 4.2. The asteroid is placed at a distance of 1.12 au from the sun. This corresponds to the semi major axis of the orbit of the asteroid Bennu. The resulting temperatures of the E- and W-faces are shown in Figure 4.7. Next, these temperatures are used as inputs into the thermo-mechanical model. This second model predicts the stress over the domain of the a-face as a function of space and time. Since the presence of cracks highly affects the stress field, different simulations for different crack positions and orientations for the same temperature fields are run.

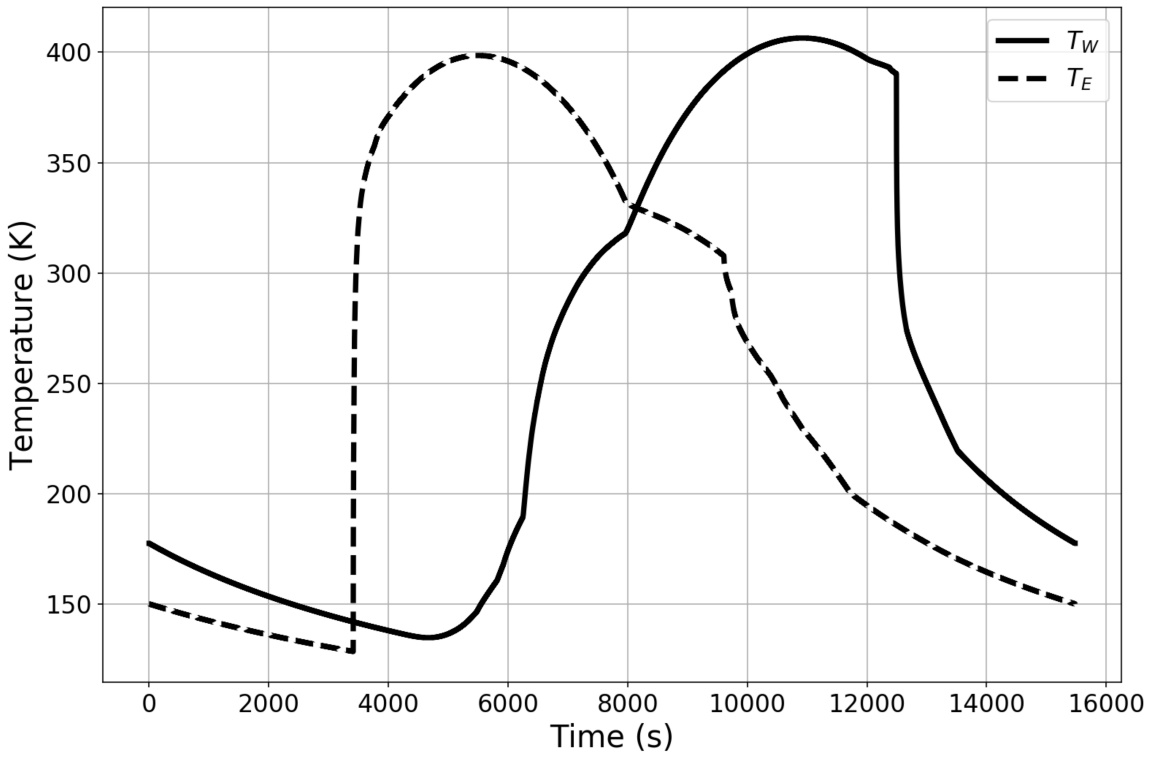

Figure 4.7: Temperatures T_W (W-face) and T_E (E-face) used as thermal boundary conditions.

The propagation direction for an initial crack in different positions inside the domain of the a-face is computed, as shown in Figure 4.5. In addition, for each position of each initial crack, its orientation is varied. When the crack is attached to the W-face the crack propagation direction is computed for different initial orientations with azimuth angles ranging from 46° to 134°. Azimuth angle is increasing clockwise (i.e. from the north to the east) and is equal to zero when it is pointing vertical up (i.e. to the north). When the crack is attached to the E-face, the crack propagation direction is simulated for different initial crack orientations having azimuth angles ranging from 226° to 314°. Finally, when the crack is attached to the north (top) side of the a-face (also called beam), the crack propagation direction is simulated for different initial crack orientations with azimuth angles ranging from 136° to 224°. In all the described cases, the length and the width of the a-face were fixed to 100 mm and 4 mm respectively. These values were chosen after studying: (i) the characteristic time of the thermal problem as well as (ii) the minimum required width of the a-face in order to avoid the boundary effects on the results and (iii) to avoid a high computational cost. The characteristic time mentioned in (i) was computed using:

$$\tau = \frac{L^2}{d} \tag{4.2}$$

where L is the characteristic length of the direction in which the thermal gradient takes place and d is the thermal diffusivity, which is given by:

$$d = \frac{\lambda}{\rho c} \tag{4.3}$$

with λ the thermal conductivity, c the specific heat capacity and ρ the density. Item (ii) was determined using trial and error method. In order to keep a low computational cost as indicated in item (iii), appropriate values for mesh size and time step were defined based on items (i) and (ii). Due to the fact that there is no temperature gradient in the vertical direction in the aforementioned simulations, a larger height of the domain does not affect initial crack propagation direction. Similarly, this work does not intend to study crack evolution with time.

The results are presented using the so-called windrose diagrams, which can be considered as circular histograms that represent the distribution of the computed crack propagation directions. When working with angle values, the usual summary statistics, such as the mean or the standard deviation, may not be the most suitable to present the data. In this case, windrose diagrams or circular histograms are a powerful tool. In these graphs, the usual histogram is wrapped around a circle. The windrose diagrams presented in this study are sorted into sixteen equal arc segments, 22.5° each segment. The radius of each of the sixteen segments represents the amount of cracks that grow in the direction represented by each of these segments. It should be noticed that the windrose circular histograms are identical for a rotation of 180°. This is due to the fact that crack propagation direction (azimuthal angle) has to be independent of the beginning and ending point of a crack. This means that for each one of the computed crack propagation directions θ counted in the histogram, the direction $\theta + 180°$ is also included. For the scenario where crack propagation direction is computed for an initial crack tip placed in different positions inside the domain of the a-face and for different crack orientations, the windroses are presented separately.

In all the simulations carried out in this study, the position of the crack tip inside the domain (beam) is fixed. Therefore, when talking about different crack orientations, it refers to the different cracks showed in dashed lines in Figure 4.5. If the crack tip is fixed inside the domain, obviously by varying the orientation of the crack, its length will vary. As the variation of the orientation of the cracks is determined by the $azimuth$ angle, their lengths are given by $\frac{a}{|\sin azimuth|}$.

Figure 4.8a shows the windrose diagram for the case of a crack attached to the W-face. Computed crack propagation directions are preferentially oriented in the North-West to South-East (NW-SE) direction, regardless of the initial different orientations of the cracks taken into account. Furthermore, a minimum number of computed crack propagation directions are oriented East (E) to West (W). In Figure 4.8b shows the windrose diagram for the case of a crack attached to the E-face. In this case the preferential orientation of the computed crack propagation directions is in the North-East to South-West (NE-SW) direction. There are also few cracks propagating in a direction aligned East (E) - West (W). The last case, where the crack is attached to the north (top) is shown in Figure 4.8c. According to the windrose diagram, the preferential orientation of the computed crack propagation directions is in the North to South (N-S) direction.

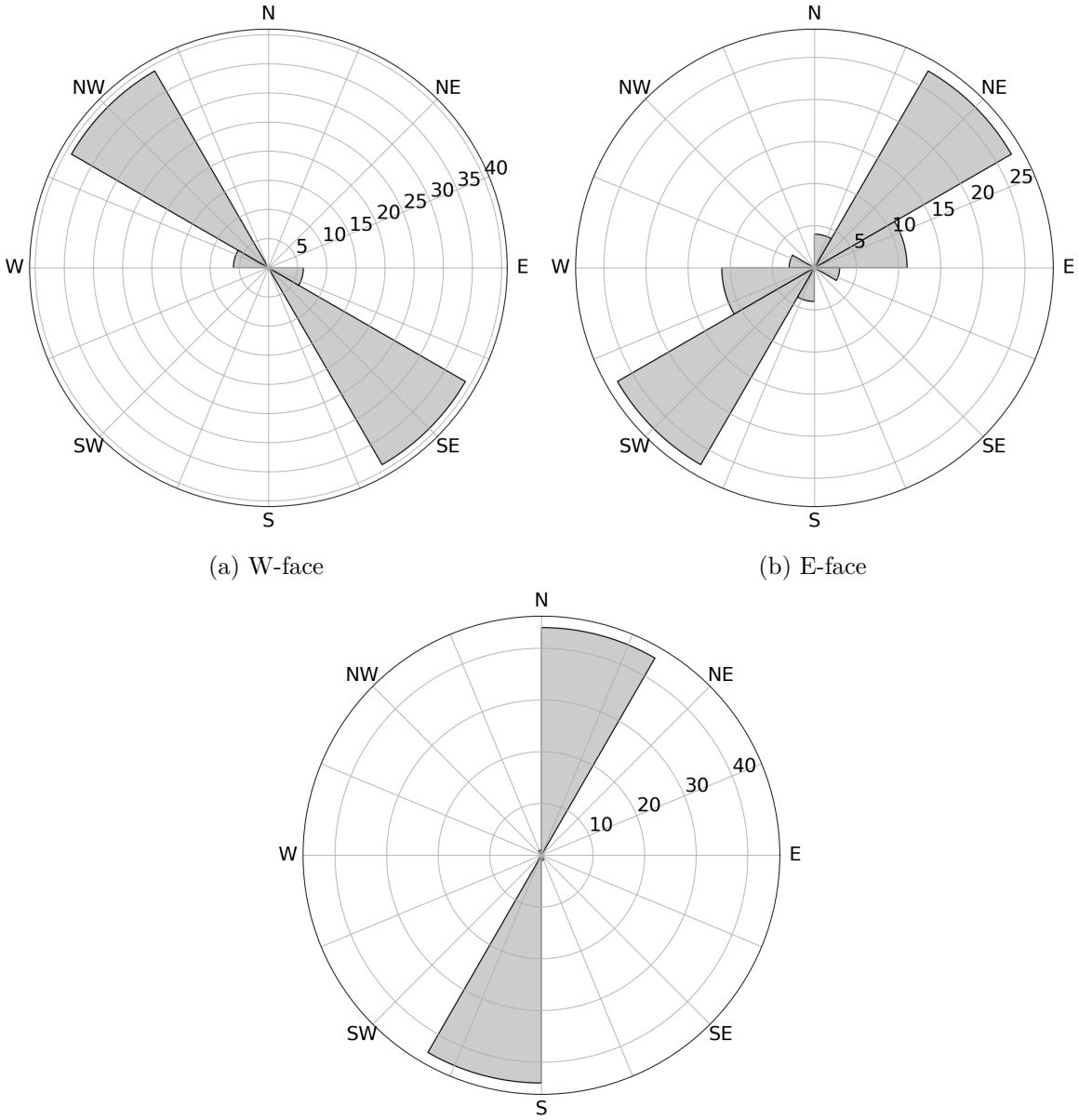

(a) W-face

(b) E-face

(c) north (top)

Figure 4.8: Windrose diagrams for different crack orientations and cracks attached to **a)** the W-face, **b)** the E-face and to **c)** the north.

Finally, in Figure 4.9 a windrose diagram that gathers all the cases described above is presented. In summary, the distribution of all the computed crack propagation directions are preferentially oriented in a higher concentration in the North to South (N-S), in the North-West to South-East (NW-SE) and in the North-East to South-West (NE-SW) directions as it was already described.

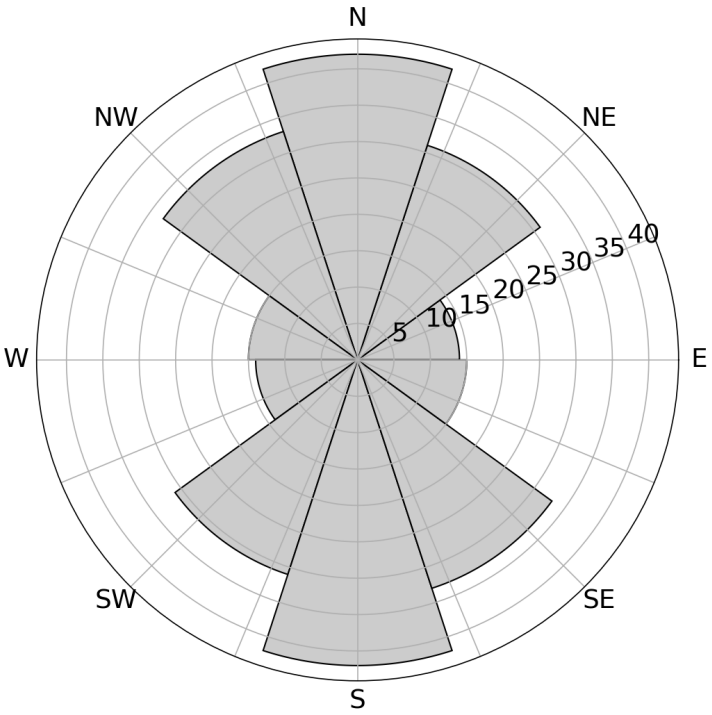

Figure 4.9: Windrose diagram gathering the cases where crack is attached to the W-face, to the E-face and to the north (top) for different crack orientations.

It must be noted that the cracks simulated up to now have a length considerably smaller than the ones observed on the boulders on the surface of Bennu [Molaro et al., 2020a, Lauretta et al., 2019b, DellaGiustina et al., 2019, Walsh et al., 2019, Delbo et al., 2019]. In the following, the crack propagation direction is studied as a function of the initial crack size. From the different configurations shown in Figure 4.5, the case for the crack attached to the E-face was selected. For this, crack propagation direction is computed by placing the crack tip at 3 different positions inside the domain of the a-face (i.e., the crack length was varied); for each one of this positions 3 different lengths of the a-face were used; for each one of these cases the orientation of the crack was varied as it was done in the previous simulations. Figure 4.10 shows that for a small crack length ($\frac{2}{|\sin azimuth|}$ mm), increasing the length of the a-face does not play an important role in the distribution of the computed crack propagation directions. No changes are observed in the windrose diagrams for these cases. Computed crack propagation directions are preferentially oriented in the North-East to South-West (NE-SW) direction, with a few amount of computed crack propagation directions going to the East (E) and to the West (W).

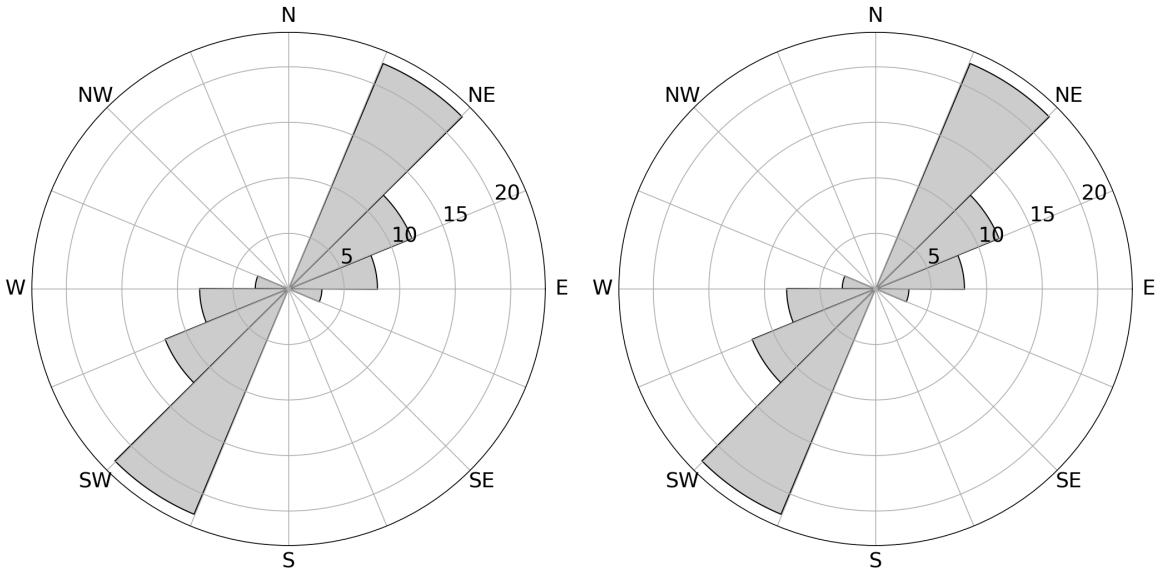

(a) a-face length: 200 mm

(b) a-face length: 500 mm

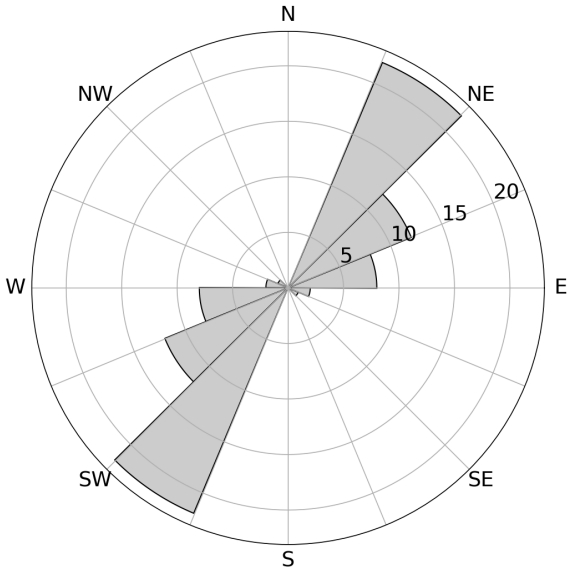

(c) a-face length: 1000 mm

Figure 4.10: Windrose diagrams for a crack attached to the E-face when crack length equals to $\frac{2}{|\sin azimuth|}$ mm and the length of the beam was varied for different crack orientations.

In Figure 4.11, it is possible to see that when increasing the length of the a-face for cracks whose lengths are $\frac{20}{|\sin azimuth|}$ mm, the distribution of the computed crack propagation directions oriented in the North to South (N-S) direction decreases, while the cracks oriented in the North-East to South-West (NE-SW) direction increase. It should also be noted that the amount of cracks directed to the East (E) and the West (W) decreases when increasing the length of the a-face from 500 mm to 1000 mm.

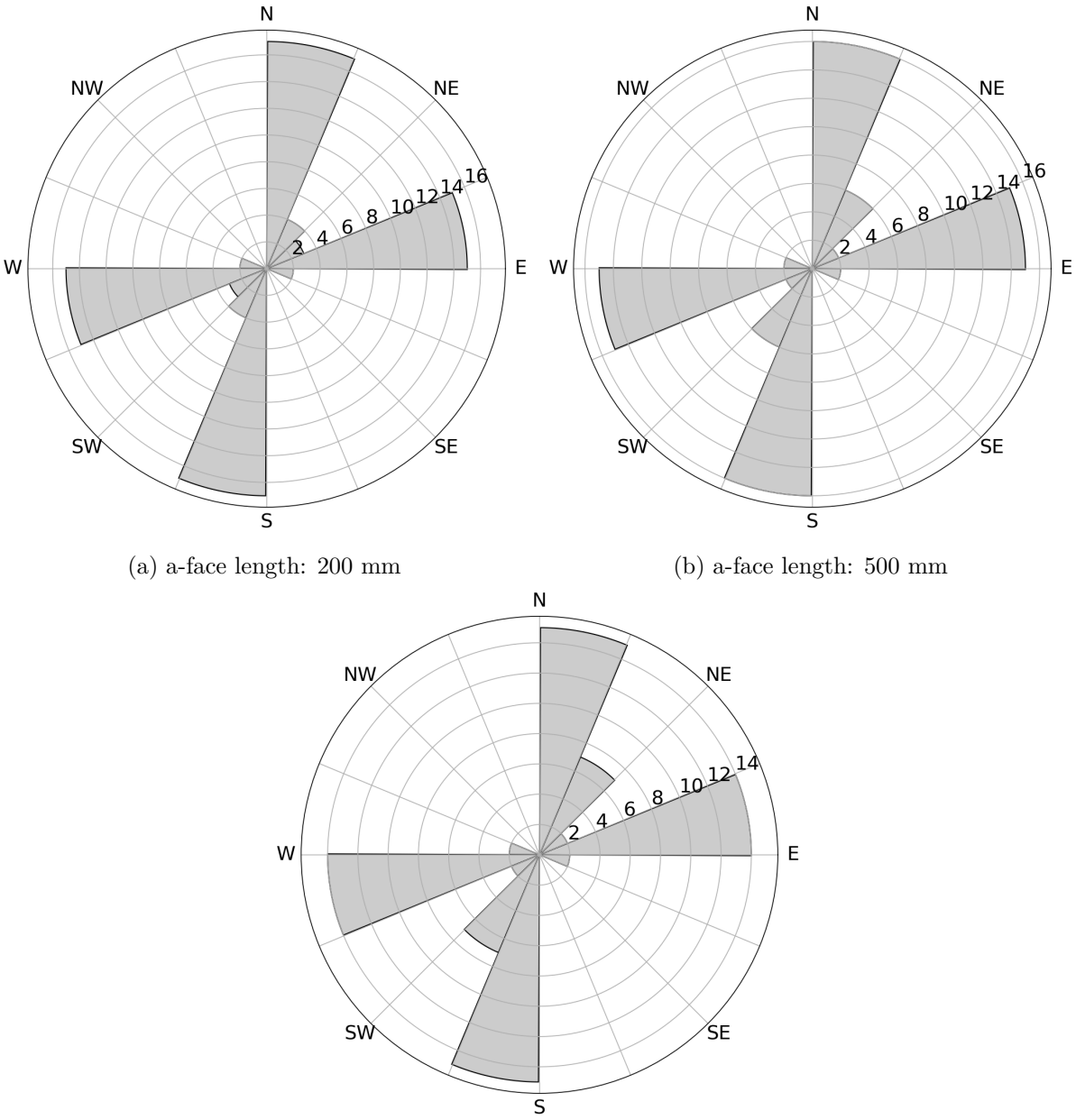

(a) a-face length: 200 mm

(b) a-face length: 500 mm

(c) a-face length: 1000 mm

Figure 4.11: Windrose diagrams for a crack attached to the E-face when crack length equals to $\frac{20}{|\sin azimuth|}$ mm and the length of the beam was varied for different crack orientations.

Finally, Figure 4.12 presents the windrose diagrams for a configuration where crack length is equal to $\frac{200}{|\sin azimuth|}$ mm. Taking into account that the length of the a-face took the values of 200 mm, 500 mm and 1000 mm, for this last case, the configuration of the a-face with a length equal to 200 mm was not simulated because the length of the a-face and the crack length would be the same, something without sense. Figure 4.12 shows that when increasing the length of the a-face from 500 mm to 1000 mm, a redistribution of the computed crack propagation directions takes place. The initial cracks preferentially oriented in the North-East to South-West (NE-SW) direction changed their orientation into the North-West to South-East (NW-SE) direction.

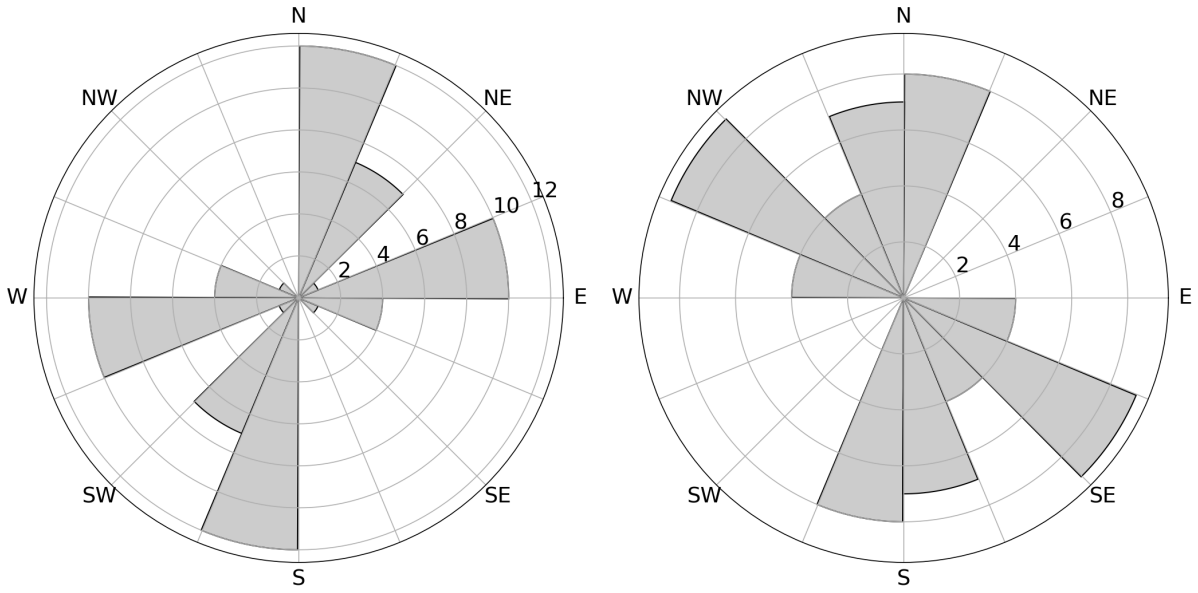

(a) a-face length: 500 mm

(b) a-face length: 1000 mm

Figure 4.12: Windrose diagrams for a crack attached to the E-face when crack length equals to $\frac{200}{|\sin azimuth|}$ mm and the length of the beam was varied for different crack orientations.

Figure 4.13 shows the maximum principal stress for three cracks with different orientations: attached to the W-face and directed to the East, attached to the north face of the boulder and directed to the South, and attached to the E-face of the boulder and directed to the West. It is worth noting that in all the cases, the computed crack propagation direction (black dashed line), the one that maximises G, is perpendicular to the direction in which the maximum principal stress takes place (white dashed line). For all cases, the maximum stress near the crack tip over a temperature cycle exceeds some MPa, which is a significant fraction of the typical strength of carbonaceous chondrites and even comparable to the strength of boulders on Bennu [Ballouz et al., 2020]. The stress at the crack tip highly depends on the element size since it is, in fact, a point where, according to linear elastic fracture mechanics, stress goes to infinity (∞). When possibly, the use of quarter-point elements [Barsoum, 1976] is recommended for better accuracy of the stress field.

Another option to study crack propagation can be the typical approach of thermal fatigue. In this case, the crack growth length per cycle is determined using the Paris' law. To do so, the configuration in which the crack is attached to the W-face was chosen. Additionally, it was selected an orientation of the crack (azimuthal angle) equal to 90°, i.e. pointing to the east. In this case, as the maximum energy release rate (G_{max}) is known, and assuming plane strain conditions, it is possible to compute the maximum stress intensity factor (K_{Imax}) using equation (4.1). In this case, G_{max} in the thermal cycle is equal to 5.15×10^{-4} $[MPa \,.\, mm]$, therefore, using equation (4.1), K_I is equal to 4.95 $[MPa \,.\, mm^{0.5}]$. Due to the fact that this work deals with stresses generated by thermal cycles, the crack tip is subjected to both tensile and compressive stresses over a full cycle. Thus, ignoring crack closure [Suresh, 1998, Boussattine, 2018], the lowest stress intensity factor experienced by the crack tip is simply zero. According to this, it follows that ΔK_I is equal to 4.95 $[MPa \,.\, mm^{0.5}]$. The value of the material's properties required when using Paris' law (C, n) was the same used in [Delbo et al., 2014] (Table 4.1). In this work, fatigue crack growth data obtained from experiments performed on two meteorites (carbonaceous chondrite and ordinary chondrite), were satisfactorily predicted using the physical parameters computed in Carrara marble by [Migliazza et al., 2011].

For the case where constant crack growth is assumed, it can be computed that for the

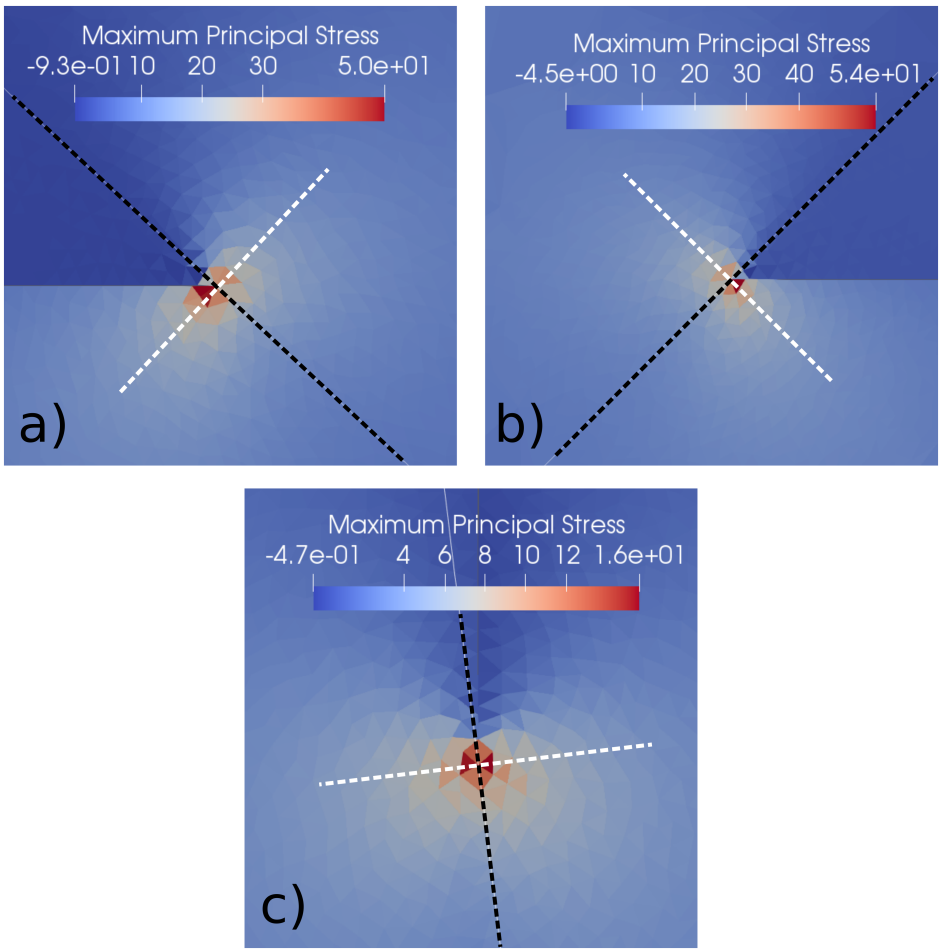

Figure 4.13: Maximum principal stress (MPa) for a crack attached to **a)** the W-face, **b)** the E-face and to **c)** the north (top). In all cases, the black dashed line represents the computed crack propagation direction, while the white dashed line represents the axis associated with the maximum principal stress.

presented thermal cycle, the crack growth rate is 2.42×10^{-4} $[mm \,.\, cycle^{-1}]$, which is of the order of 0.5 $[mm \,.\, yr^{-1}]$ (or $\sim 0.5[m]$ in thousand years), in good agreement with previous studies [Delbo et al., 2014]. This indicates that cracks would propagate on Bennu's boulders solely due to diurnal thermal stresses. It is cautioned here that crack propagation is a non linear process, where the rate of propagation is among other parameters a function of the position of the crack tip with respect to the temperature gradient. This means that a full simulation of the crack growth from the beginning until its size is comparable to the size of the hosting boulder should be carried out in order to estimate the time required to fracture the boulder, which is beyond the scope of this work.

4.4 Discussion

We begin to notice that in Figure 4.8a, 4.8b and 4.8c, the range of computed crack propagation directions is preferentially concentrated in some sectors of the windrose diagrams. This could be explained by the fact that when a crack orientation is defined, the range of possible crack propagation directions, is determined by the limit angle corresponding to pure shear defined in the work of [Erdogan and Sih, 1963]. This value is approximately $\pm 70°$ with respect to the crack axis orientation. It should also be noted that the crack was only placed at three different places inside the domain, i.e. attached to the East, the West faces and attached to the

North rim of the domain. This means that not all the angles belonging to the range $[0°, 360°]$ were taken into account. For example, in Figure 4.8b, i.e., for the case of a crack attached to the E-face, the computed crack propagation directions range from 202.5° to 292.5°. From this figure, it is worth noting that most of the computed direction are oriented to the South-West (SW), and due to the already explained symmetry of the wind rose, the preferential orientation of the computed crack propagation directions is in the North-East to South-West (NE-SW) direction.

When plotting the windrose diagrams for the three evaluated cases (crack attached to the E-, W-face and the north rim of the domain) in the same graph, as shown in Figure 4.9, the sector grouping the majority of the computed directions is the one oriented in the North to South (N-S) direction, followed by the groups oriented in the North-West to South-East (NW-SE) and in the North-East to South-West (NE-SW) directions, respectively. Looking at the results of the three simulated cases, it is worth noting that cracks on asteroid Bennu propagate mainly in the North-South (N-S) direction.

In Figure 4.13 it should be noticed that the computed crack propagation directions in the three cases presented here are perpendicular to the axis of the maximum principal stresses, as stated by the literature. This makes us feel confident about the results coming out from the coupled thermoelastic model with the linear elastic fracture mechanics approach that was implemented in this work.

From Figure 4.10 it can be noticed that for short crack lengths, the increasing of the length of the a-face does not highly affect the tendency of the distribution of the computed crack propagation directions. Cracks mainly continue propagating oriented in the North-East to South-West (NE-SW) direction. When increasing the length of the a-face from 500 mm to 1000 mm, a few amount of cracks changed their orientation into the North-West to South-East (NW-SE) direction. It tells us that even if the temperature gradient along the a-face changes, cracks of short length are not affected.

According to Figure 4.11, when crack length increases, a redistribution of the computed directions takes place. It is possible to see two main groups, one oriented almost in the North to South (N-S) direction and another one oriented almost in the West to East (W-E) direction. Meanwhile, for the case when the crack length is very long compared with the length of the a-face, as depicted in Figure 4.12, a marked tendency is clearly observed. Computed crack propagation directions are preferentially oriented in the North-West to South-East (NW-SE) direction, which is consistent with the observations performed by [Delbo et al., 2019].

Taking into account that the duration of the thermal cycle used in this work is 4.3 h, and assuming a constant crack propagation rate, the crack growth rate computed here, whose value is 2.42×10^{-4} $[mm \,.\, cycle^{-1}]$, is equivalent to a crack growth rate of about 0.5 $[mm \,.\, year^{-1}]$. This value is not very different from the one measured by [Delbo et al., 2014] through laboratory experiments on two meteorites: a carbonaceous chondrite and an ordinary chondrite. However, as stated in the same study, the crack propagation rate is typically a nonlinear function between the crack size, the maximum variation of the stress intensity factor over the whole cycle and material properties. However, considering that this work is a first attempt to describe crack growth due to thermal fatigue, the results are promising.

4.5 Summary of Chapter 4

One of the main goals of this PhD was to numerically reproduce some observed fractures on solar system small bodies induced by large amount of thermal cycles. Here, the efforts were oriented to model the crack propagation direction in conditions similar to those existing on the asteroid (101955) Bennu. This motivation arose because there is a lack of a theoretical foundation that allows to carry out analysis and interpretations of fracture directions on small asteroids with properties similar to those of Bennu. This chapter presented the obtained results

when applying the developed and implemented thermo-elastic fracture mechanics model for the case of Bennu. Those results were already published in [Uribe-Suárez et al., 2021].

In section 4.2 the methodology followed in this work to achieve the fracture mechanics analysis in the asteroid Bennu was described. Using the implemented methodology, crack propagation direction for an initial crack tip in different positions and for different orientations was computed. Through the comparison against available observational evidence, the accuracy of the proposed methodology when calculating the crack propagation direction due to the presence of thermal gradients was shown in section 4.3. It was found that cracks preferentially propagate in the North to South (N-S), in the North-East to South-West (NE-SW) and in the North-West to South-East (NW-SE) directions. In the same section, a thermal fatigue analysis was performed in order to estimate the crack growth rate. Computed value is in good agreement with available experimental evidence. Finally, in Section 4.4 the computed crack propagation directions were discussed.

4.6 Résumé en français

L'un des objectifs premiers de ce projet de thèse était de reproduire à l'aide de simulations numériques des fissures observées sur des corps célestes dont on suppose qu'elles ont été causées par la répétition d'un grand nombre de cycles thermiques. Dans ce chapitre, un intérêt particulier a été apporté à la modélisation de la propagation de fissures dans des conditions représentatives de celles existantes sur l'astéroïde (101955) Bennu. Cet intérêt est motivé par le manque de bases théoriques permettant d'interpréter les directions de fissures sur des petits astéroïdes présentant des propriétés similaires à celles de Bennu. Ce chapitre présente les résultats obtenus via l'application du modèle de fracture mécanique thermoélastique. Ces résultats ont déjà été publiés dans [Uribe-Suárez et al., 2021].

Dans la section 4.2, la méthodologie utilisée pour réaliser l'analyse mécanique de la rupture dans le cas de l'astéroïde Bennu est décrite. A l'aide de cette méthodologie, la direction de propagation pour un début de fissure présent à différentes positions et suivant différentes orientations est calculée. En comparant ces résultats à d'autres observations, la précision de la méthode peut être évaluée comme cela est montré en section 4.3. Cela a permis de déterminer que les fissures se propagent de préférence suivant les directions suivantes : Nord vers Sud, Nord-Est vers Sud-Est et Nord-Ouest vers Sud-Est. Puis, une analyse de fatigue est réalisée afin d'estimer la vitesse de croissance de la fissure. Les résultats de cette analyse sont en bon accord avec les observations expérimentales. Finalement, la section 4.4 discute la pertinence des résultats concernant les directions de propagation des fissures.

Chapter 5

Conclusions and Perspectives

Contents

5.1 Conclusions

Fracture mechanics is in charge of the prediction of the conditions when failure is likely to occur inside a material containing cracks. Numerical simulations are often an effective strategy to study these problems. Particularly, numerical simulation of crack propagation through a finite element mesh for arbitrary crack paths has been a challenging issue in computational fracture mechanics for decades. For this reason, one of the goals of this PhD was focused in developing a methodology allowing crack propagation in brittle materials through arbitrary directions combining remeshing operations and dynamic insertion of cohesive elements either in two- or three-dimensional scenarios.

Regarding the two-dimensional case, a new methodology for crack growth simulations under mixed-mode loading in brittle materials has been developed and presented. It combines an advanced remeshing technique, that enables remeshing exactly in a computed direction, with dynamic insertion of cohesive elements in the remeshed zone. Additionally, the method presented here allows for an accurate modeling of the energy dissipation rate through a traction-separation law. It also enables crack propagation using remeshing operations and cohesive elements in a mesh-independent way. Over the various applications presented in this work, the robustness and the accuracy of the proposed approach in terms of crack path was shown.

The impact of different numerical and physical parameters on the crack path and fracture energy was studied. First, by varying the mesh size, it was found that the presented approach exhibits mesh convergence. Compared to classical crack propagation techniques based on linear elastic fracture mechanics (LEFM), the current approach offers the possibility of controlling fracture energy (i.e., modeling the energy dissipation rate due to the fracture process). This approach improves on classical cohesive zone model (CZM) approaches since it enables to model configurations with arbitrary crack paths. However, as shown in this work, the dynamic insertion of cohesive elements introduces oscillations in the post-peak regime. These oscillations are merely due to the crack increment length and the time step. The aforementioned oscillations are the result of a dependence of the current approach on the time step, as well as on the constant crack increment used once G exceeds G_c. In order to overcome this problem, methodologies that allow for the computation of the crack velocity should be used.

Then, after performing a sensitivity analysis to the cohesive law parameters, an interesting remark must be stated. Variation of the maximum cohesive stress (σ_c) and of the critical opening displacement (δ_c) while the fracture energy was kept constant, showed that these parameters play a purely numerical role. Thus, the fracture energy is the most important parameter to take into account when tuning the model. The results of this first part of the thesis were published in [Uribe-Suárez et al., 2020].

With respect to the three-dimensional crack propagation, the great capabilities of the implemented approach to propagate a crack front through arbitrary directions was extended to three-dimensional scenarios. Although the crack front propagations were performed through arbitrarily predefined directions because the $G\theta$ method has not yet been extended to 3D, the promising capabilities of current approach to follow complex crack paths (e.g., curvilinear paths) were shown. The effectiveness of the implemented three-dimensional cohesive zone model, as well as of the implemented viscous regularization technique in order to avoid convergence problems when simulating 3D fracture problems was also proved. Nevertheless, there are still a lot of work to do regarding three-dimensional problems. Attention should be paid to how to compute the crack propagation direction, as well as how to control the fracture energy. Not less important, the methodology to propagate the crack front through the finite element mesh must be improved (see next section).

Due to the recent importance that the asteroid (101955) Bennu has gained by being the target of the OSIRIS-REx mission, many studies trying to explain different surface processes

affecting the landscape evolution of Bennu have appeared. One of the most important phenomena that is thought to be responsible of such processes is thermal cracking. The second major objective of this PhD thesis was, therefore, focused on the development of a methodology able to numerically reproduce some observed crack patterns on solar system small bodies induced by a large amount of thermal cycles. Here, efforts were oriented to reproduce observed directions in which some cracks propagated in asteroid (101955) Bennu.

Regarding this goal, an approach to compute two-dimensional crack propagation direction under the presence of thermal gradients has been presented. This methodology combines thermoelasticity and linear elastic fracture mechanics theories in order to compute crack propagation directions driven by diurnal temperature cycling and under conditions similar to those existing on the asteroid (101955) Bennu. Through the different scenarios simulated in this work, the robustness and the accuracy of the proposed approach in terms of crack propagation direction was shown.

It was found that the distribution of the computed crack propagation directions for different configurations on a simple domain simulating Bennu's boulders, show a preferential direction from North to South (N-S) and from North-East to South-West (NE-SW) for shorter cracks. For longer cracks, the preferential direction is from North to South (N-S) and from North-West to South-East (NW-SE). This conclusion is supported by observations performed by [Delbo et al., 2019].

Additionally, and according to the results obtained by means of our thermomechanical model combined with a well-known fatigue model (i.e., Paris's law) and assuming constant crack growth length, it was found that on asteroid Bennu cracks grow at rate approximately equal to 0.5 $[mm \ . \ year^{-1}]$. This is a value very similar to the one found on experiments performed in the work of [Delbo et al., 2014], giving us a good insight of the promising approach proposed. However, it is cautioned that crack propagation is a highly non-linear process. In order to estimate the time to fracture Bennu's meter-sized rocks a full-blown simulation shall be performed to calculate the crack growth rate at different crack growth stages. This is really important because crack growth rate highly depends on the geometry and on the stress intensity factor at the crack tip, and those will change as the crack tip evolves trough the domain.

It must also be noted that boulders' heterogeneity was not accounted for in this study. Material's heterogeneity definitely plays a role on local bifurcations and cracks kinematics.

The findings of this PhD can be understood as a theoretical foundation for some fracture processes that are thought to be the result of a thermal fatigue induced by the temperature changes driven by the day/night cycles on asteroid (101955) Bennu. Results from this second part of the PhD were published in [Uribe-Suárez et al., 2021].

The developed methodology also opens new opportunities, as it can be applied to other applications than thermal fatigue of solar system small bodies, applications such as composites cracking at the meso-scale.

5.2 Perspectives

Although in the present PhD thesis, comprehensive studies have been performed on numerical modeling of crack propagation in both two- and three-dimensional scenarios, as well as on thermal cracking on solar system small bodies such as the asteroid (101955) Bennu, there are still some topics of prime interest that must be faced to enhance the presented methodologies.

Some of these topics are: (i) the inclusion of fatigue phenomenon in the cohesive law, (ii) evaluation of crack propagation stability, (iii) extension of the $G\theta$ method to 3D, (iv) improvement of the methodology developed to propagate crack fronts through a finite element mesh in 3D and (v) 3D thermal cracking on airless bodies. These topics are presented in more details below.

5.2.1 Fatigue cohesive law

When working with cyclic loading such as thermal fatigue, the working loads are generally less than the critical values of the cohesive zone model. In the present study, when solving the thermal problem on airless bodies, it was observed that if the crack tip was propagated, and cohesive elements were immediately inserted, these elements were not able to release energy due to the low level of the cyclic loading. To account for a more realistic simulation of the fracture process under fatigue, the inclusion of a cohesive zone degradation law (i.e., cyclic cohesive zone model) is necessary.

For the case of monotonic cohesive zone models (MCZMs), the damage (i.e., material degradation) initiates only when the peak of the traction-separation law (σ_c) is reached. In the case of fatigue applications, the cohesive behavior of the material under cyclic loading is of primary concern because if for example, monotonic CZMs are used under cyclic loading with constant separation amplitude, an infinite number of repetitions without any accumulation of damage would be allowed [Nguyen et al., 2001, Roth et al., 2014]. [Springer et al., 2019] developed a cyclic cohesive zone model (CCZM) based on a hysteresis loop damage formulation to account for variable amplitude loading. [Springer et al., 2019] used an exponential traction–separation law to describe the interface behavior. In this work, to develop the cyclic cohesive model, an energy based damage variable was defined. The evolution of the energy damage variable accounts for cyclic damage by a Paris' law like approach.

Mixed–mode delamination growth under cyclic loading was simulated by [Springer et al., 2019]. In this case, the loading-unloading process may cause some damage at the interface. At each point ahead of the crack tip, the energy dissipated will be equal to the sum of the energy dissipated due to the quasi-static loading to reach the maximum load, and the energy dissipated due to the cyclic loading ($G_c = W_s + W_f$). The cohesive zone under fatigue loading is shown in Figure 5.1.

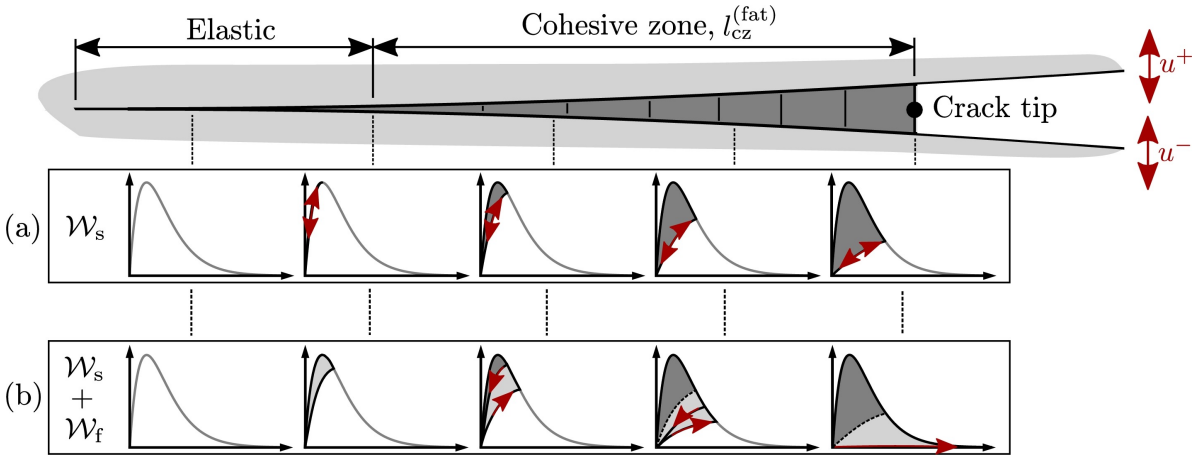

Figure 5.1: Subcritical delamination growth obtained by cycling loading. The dark grey area depicts the dissipated energy due to monotonic interface opening, W_s. The light–grey area indicates the additionally dissipated energy, W_f, caused by the fatigue damage formulation. Figure reproduced from [Springer et al., 2019].

When implementing this method, the effect on the fracture process of cyclic loads whose value is below the critical values of the cohesive law will be taken into account. Therefore, "real" crack propagation through finite element meshes that represent small celestial bodies could begin to be studied.

5.2.2 Stability assessment of crack growth ($\pi\theta$ method)

To study the stability of the crack propagation process and to overcome the time step dependence observed in this work, a possible solution is the implementation of a methodology such as the $\pi\theta$ method, which is an extension of the $G\theta$ method. The $\pi\theta$ method allows to assess the stability of crack growth as well as to calculate its velocity.

According to the Griffith energy criterion, crack growth can occur if the energy required to form an additional crack of size da can just be delivered by the system [Broek, 1982b]. Mathematically, crack extension occurs when $G = G_c$; but crack growth may be stable or unstable, depending on how the energy release rate (G) and the fracture energy (G_c) vary with crack size. Depending on the material, the plastic, viscoelastic, or viscoplastic effects could be included in the fracture energy. Increasing of the surface area due to crack meandering and branching can also influence the fracture energy. To clarify stable and unstable behavior, conveniently G_c can be replaced by R, the material resistance to crack extension. A plot of the material resistance to crack extension against the crack size (R vs a) is called a resistance curve or *R-curve*. The corresponding plot of the energy release rate against the crack size (G vs a) is known as the driving force curve [Anderson, 2005].

The *R-curve* of some materials is flat, while others materials exhibit a rising *R-curve*. The shape of his curve depends on the material behavior and, to a lesser extent, on the configuration of the cracked structure. Experiments have shown that the crack resistance (R) can be considered independent of crack length for cracks under plane strain conditions. While in the case of plane stress, the crack resistance (R) varies with the amount of crack growth [Broek, 1982b]. For a perfectly brittle material the fracture energy is constant and equal to the surface energy (2γ). For the case of metals, the energy required for a crack to grow is much larger than the surface energy to create the new free surfaces. In this case, plastic deformation takes place in front of the crack tip and during the crack growth, energy is consumed by the formation of a new plastic zone at the tip of the advanced crack [Anderson, 2005]. The *R-curve* produced by a crack in a thin sheet tends to be steeper than in a thick plate because there is a low degree of stress triaxiality (i.e., plane stress) at the crack tip in the thin sheet. In the case of the thick plate, the material near the tip of the crack may be in a plane strain condition.

Consider a wide plate with a through crack of initial length $2a_o$ as the one shown in Figure 1.6. At a fixed remote stress σ, the energy release rate (G) varies linearly with crack size according to:

$$G = \frac{\pi\sigma^2 a}{E} \tag{5.1}$$

Figure 5.2 shows the resistance curve or *R-curve* (R vs a) and the driving force curve (G vs a) for two types of material behavior. The first case shown in Figure 5.2-**a)** corresponds to a flat *R-curve*, where the material resistance (R) is constant with crack growth. When the remote stress is equal to σ_1, the crack growth does not occur. Contrary, when the remote stress is equal to σ_2 or higher, the crack propagation is unstable because the driving force increases with crack growth, but the material resistance (R) remains constant. Figure 5.2-**b)** illustrates the case with a material with a rising *R-curve*. When the remote stress is equal to σ_1, the crack growth does not occur. If the stress is equal to σ_2, the crack grows a small amount but cannot grow further unless the stress increases. In this case, the driving force increases at a slower rate than R. The stable crack propagation continues as the stress increases to σ_3. Finally, when the remote stress is equal to σ_4, the driving force curve is tangent to the *R-curve*. In this case, the crack propagation in the plate is unstable with further crack growth because the rate of change in the driving force exceeds the slope of *R-curve*. Mathematically, the above can be written as follows:

$$\begin{cases} G < R & \text{no propagation} \\ G = R \text{ and } \frac{\partial G}{\partial a} < \frac{\partial R}{\partial a} & \text{stable propagation} \\ G = R \text{ and } \frac{\partial G}{\partial a} \geq \frac{\partial R}{\partial a} & \text{unstable propagation} \end{cases} \tag{5.2}$$

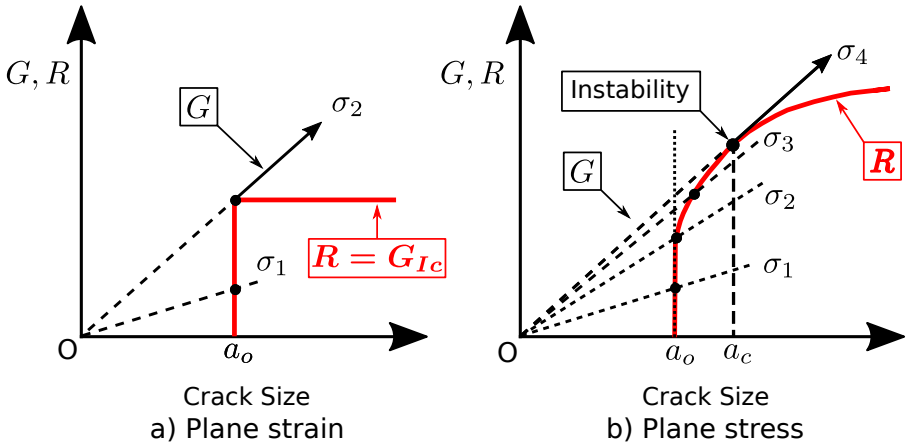

Figure 5.2: Schematic driving force vs *R-curve* diagrams for: **a)** flat *R-curve* (plane strain) and **b)** rising *R-curve* (plane stress).

Based on the continuum mechanics model, and in order to analyze the stability of a cracked system, [Suo and Combescure, 1989, Suo, 1990] performed a mathematical formulation for the second derivative of potential energy with respect to the crack length ($\partial W_p^2/\partial a^2$), or the first derivative of the energy release rate with respect to the crack length ($\partial G/\partial a$) in the framework of linear elasticity. The term $\partial G/\partial a$ can be computed using the $\pi\theta$ method proposed by [Suo and Combescure, 1989, Suo, 1990]. For this, two crowns together with two virtual displacements fields (θ, π) must be defined around the crack tip as shown in Figure 5.3. The first ring of elements (θ_c) is used to compute $G = -\partial W_p/\partial a$ while the second ring of elements (π_c), is used to compute $\partial G/\partial a$.

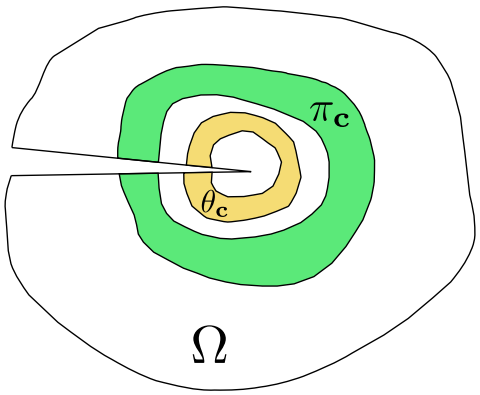

Figure 5.3: Schematic representation of the domains (crowns) used to implement the $\pi\theta$ method.

According to [Suo and Combescure, 1989, Suo, 1990]:

$$\frac{\partial G}{\partial a} = \int_\Omega Tr(\sigma^\pi \nabla U \nabla \theta) d\Omega + \int_\Omega Tr(\sigma \nabla U^\pi \nabla \theta) d\Omega - \int_\Omega Tr(\sigma \nabla U^\pi) div(\theta) d\Omega \tag{5.3}$$

where (σ^π, U^π) represent the variation of the solution (σ, U) during an evolution of the crack. σ^π and U^π are the unique solution of the variational problem presented in 5.4. Details of the

solution of this problem using the finite element method can be found in [Suo, 1990].

$$\begin{cases} \sigma_{ij}^{\pi} = C_{ijkl}\left[\frac{1}{2}\left(U_{k,l}^{\pi} + U_{l,k}^{\pi}\right) - \frac{1}{2}\left(U_{k,i}\pi_{i,l} + \pi_{l,i}U_{i,k}\right)\right] \\ \int_{\Omega} \sigma_{ij}^{\pi} V_{j,i}\ d\Omega = \int_{\Gamma} \sigma_{ij} V_{j,k}\pi_{k,i}\ d\Omega - \int_{\Omega} \sigma_{ij} V_{j,i}\pi_{k,k}\ d\Omega \end{cases} \tag{5.4}$$

Once $\partial G/\partial a$ is computed, we can check whether the propagation is stable or not. Additionally, as presented in section 1.2.3.1, under stable propagation the crack propagation velocity is given by:

$$\dot{a} = \left[-\frac{\frac{\partial^2 W_p}{\partial a \partial u}\dot{u}}{\frac{\partial^2 W_p}{\partial a^2}}\right]^{+} = \left[-\frac{\frac{\partial G}{\partial u}\dot{u}}{\frac{\partial G}{\partial a}}\right]^{+} \tag{5.5}$$

where $\frac{\partial G}{\partial u}\dot{u}$ is given by:

$$\frac{\partial G}{\partial u}\dot{u} = \int_{\Omega} Tr(\dot{\sigma}\nabla U \nabla\theta)d\Omega + \int_{\Omega} Tr(\sigma\nabla\dot{U}\nabla\theta)d\Omega + \int_{\Omega} Tr(\sigma\nabla\dot{U})div(\theta)d\Omega \tag{5.6}$$

This outlook will allow the analysis of crack growth stability, as well as the computation of the crack velocity.

To the best of our knowledge, this kind of velocity computation has never been done for practical applications. In addition, crack propagation in brittle materials can be extremely fast, which would require a very small time step. In the case of fatigue analysis, crack propagation laws such as the Paris' law are preferred and easier to use.

5.2.3 Extension of the $G\theta$ method to 3D

As already mentioned in this work, due to the lack of time, the $G\theta$ method was not extended to three-dimensional configurations. The $G\theta$ method extended to 3D will allow, first, the quantification of the energy release rate (G). Therefore, the application of an appropriate criterion ($G > G_c$) to decide when to allow the propagation of the crack front (i.e., insertion of cohesive elements) will be possible. Additionally, as done in the two-dimensional problems, the $G\theta$ method will allow the computation of the appropriate crack propagation direction.

According to [Brochard and Suo, 1994], in the analysis of structures presenting cracks of any shape, the knowledge of G at particular points of the crack front where the crack is likely to start (local value of G) is often required. In two-dimensional problems, G is constant along the front and is defined by:

$$G = -\frac{1}{B}\frac{\partial W_p}{\partial a} \tag{5.7}$$

where $B = 1$ because the calculation is carried out for a unit crack width, and ∂a is the increase of the crack length. [Brochard and Suo, 1994] generalized this definition to three-dimensional crack fronts. A planar three-dimensional crack is shown in Figure 5.4. In this Figure S, represents the curvilinear abscissa along the crack front.

The reduction of the total potential energy for a crack advance located on a segment L_c of the front is related with the local value of the energy release rate $G(S)$ as follows:

$$\delta W_p = -\int_{L_c} G(S)\delta l(S) dS \tag{5.8}$$

where $\delta l(S)$ is the virtual crack increment normal to the front at the local level. Given a local displacement field (θ) representing the virtual propagation of the crack shown in previous diagram (Figure 5.4), the integration over the volume (Ω) using the $G\theta$ method allows the computation

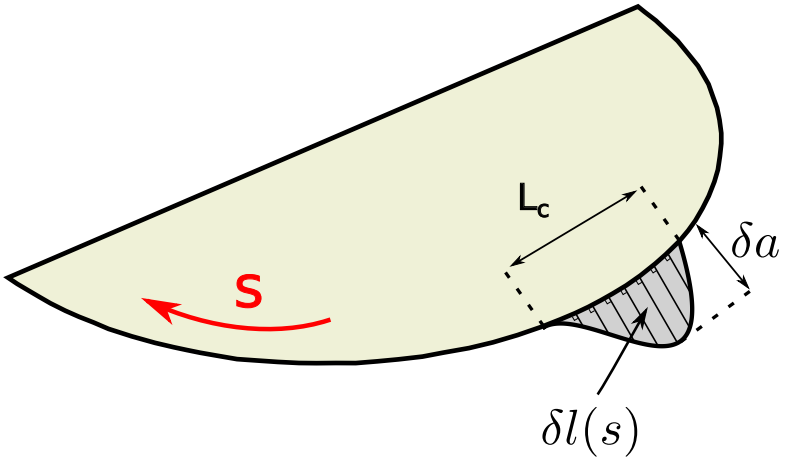

Figure 5.4: Schematic representation of the virtual crack increment normal to the crack front at the local level.

of the variation of the total potential energy (δW_p) during a crack growth corresponding to the shaded gray area (δA) in Figure 5.4:

$$-\delta W_p = -\int_\Omega \left[Tr(\sigma \nabla U \nabla \theta) - \frac{1}{2} Tr(\sigma \nabla U) div(\theta) \right] d\Omega \tag{5.9}$$

$$\delta A = \int_{L_c} \delta l(S) dS = \int_{L_c} \theta(S) dS \tag{5.10}$$

The average value of G on the segment L_c is then:

$$G = -\frac{\delta W_p}{\delta A} \tag{5.11}$$

Therefore, a piecewise constant function $G(S)$ along the front is obtained. Following the approaches proposed by [Li et al., 1985, Martin et al., 2019], to define the crack propagation direction, a possible solution would be to determine at each point of the crack front (e.g., $M_o(S)$ in Figure 5.5), the direction which would maximize the local value of the energy release rate, $G(s)$). The virtual displacement field θ would be defined in the X_1-X_2 plane. θ depends on the distance to the crack front r, the angle ϕ and the curvilinear abscissa S.

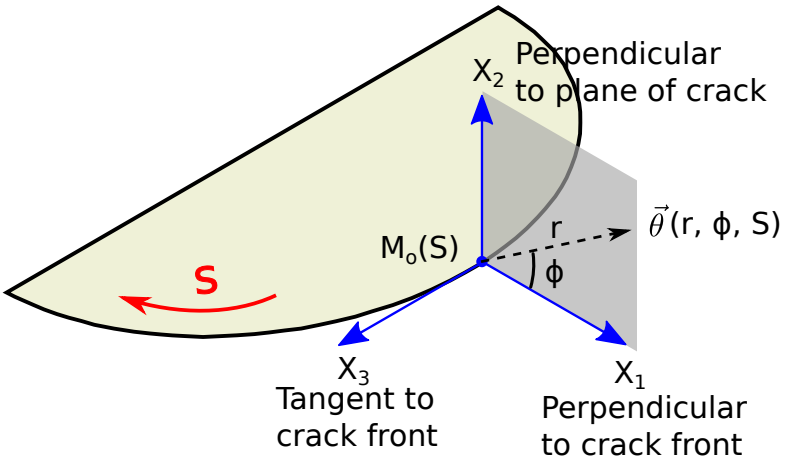

Figure 5.5: Definition of local orthogonal Cartesian coordinates at the point $M_o(S)$ on the crack front. The crack plane is the X_1-X_3 plane.

5.2.4 Propagation of the crack front through the finite element mesh

Even though this work presented the promising capabilities of the implemented methodology to perform three-dimensional crack propagation, as said in Chapter 3 there are still some issues that must be solved to enhance the methodology. The approach followed in this work is simple. First, the direction in which the crack front evolves is defined. Then, the finite element mesh is fitted to the defined direction. After this, the current crack front is updated to its new position, which is determined by the fixed crack propagation length. The developed methodology to propagate the crack front sometimes presented some drawbacks. For example, Figure 5.6 shows a crack path formed by the inserted cohesive elements after several propagations. Some holes highlighted with red circles can be observed. The origin of these holes could be because, at some point, some auxiliary variables that are required by the remeshing procedure as input parameters are not being defined properly. So if the remeshing does not work well, neither does the insertion of cohesive elements.

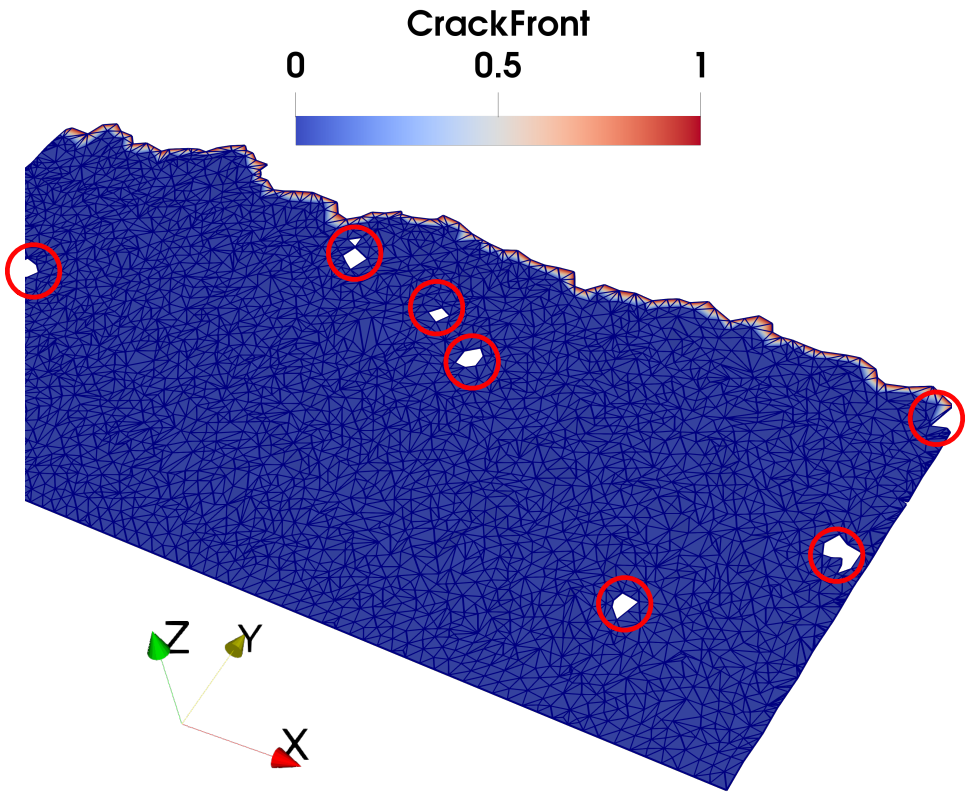

Figure 5.6: Crack path with some issues in the remeshing process and in the insertion of cohesive elements process.

The circumstances under which this problem occurs have not yet been identified. Additionally as mentioned before, Figure 5.6 shows that even if the propagation distance is fixed and equal for all the nodes belonging to the crack front, some of them may propagate more than others, making the crack front very irregular. A methodology allowing a smoother propagation of the crack front must be developed. The combination of methodologies where the fracture surface is defined by level-set functions with body-fitted mesh adaption techniques could be a solution [Shakoor et al., 2015, Shakoor et al., 2017].

5.2.5 3D thermal cracking on airless bodies

Until now, most studies of thermal cracking on airless bodies have been performed in simple geometries such as two-dimensional planar faces, or spherical boulders. Studies on more complex

geometries are scarce. See for example [Liang et al., 2020], who were among the first that incorporated a realistic 3D microstructure of an asteroidal rock to study fracture. For this reason, once the three-dimensional crack propagation methodology is completely tested and validated, the most logical next step is to tackle the thermal cracking problem on celestial bodies in 3D.

Due to the fact that the internal structure of space objects is not well known, a big hypothesis of the current work is that the material was assumed to be homogeneous and isotropic, and it is well known that asteroidal rocks contain inclusions that have different thermomechanical properties [El Mir et al., 2019]. This leads to the generation of additional stresses between the inclusion and the matrix, which in general can affect the stress field, a variable of primary importance when studying the fracture process. From this and depending on the availability of information, a possible outlook could be the assumption that the material is heterogeneous and anisotropic.

Additionally, to perform more accurate simulations regarding thermal fatigue analysis, there is a need to measure thermomechanical and fracture mechanical properties of space materials. Analysis of returned samples from different space missions that are currently in progress (e.g., NASA's OSIRIS-REx mission or NASA's Perseverance Mars Rover mission) will be of great help to improve this aspect.

References

[Al-Mukhtar and Merkel, 2015] Al-Mukhtar, A. and Merkel, B. (2015). Simulation of the crack propagation in rocks using fracture mechanics approach. *Journal of Failure Analysis and Prevention*, 15:90–100. (Cited on page 2.)

[Alessi et al., 2015] Alessi, R., Marigo, J.-J., and Vidoli, S. (2015). Gradient damage models coupled with plasticity: Variational formulation and main properties. *Mechanics of Materials*, 80:351 – 367. Materials and Interfaces. (Cited on pages xxiii and 21.)

[Alessi et al., 2018] Alessi, R., Ambati, M., Gerasimov, T., Vidoli, S., and De Lorenzis, L. (2018). *Comparison of Phase-Field Models of Fracture Coupled with Plasticity*, pages 1–21. Springer International Publishing, Cham. (Cited on page 26.)

[Alfano et al., 2007] Alfano, M., Furgiuele, F., Leonardi, A., Maletta, C., and Paulino, G. H. (2007). Cohesive zone modeling of mode i fracture in adhesive bonded joints. In *Advances in Fracture and Damage Mechanics VI*, volume 348 of *Key Engineering Materials*, pages 13–16. Trans Tech Publications. (Cited on page 26.)

[Alí-Lagoa et al., 2013] Alí-Lagoa, V., de León, J., Licandro, J., Delbó, M., Campins, H., Pinilla-Alonso, N., and Kelley, M. (2013). Physical properties of b-type asteroids from wise data. *A&A*, 554:A71. (Cited on page 6.)

[Alí-Lagoa et al., 2015] Alí-Lagoa, V., Delbó, M., and Libourel, G. (2015). Rapid temperature changes and the early activity on comet 67p/churyumov-gerasimenko. *The Astrophysical Journal Letters*, 810(2):L22. (Cited on pages xxvi and 3.)

[Aliaga, 2000] Aliaga, C. (2000). *Simulation numérique par éléments finis en 3D du comportement thermomécanique au cours du traitement thermique d'aciers: application à la trempe de pièces forgées ou coulées*. PhD thesis, Ecole Nationale Supérieure des Mines de Paris. (Cited on pages 42 and 44.)

[Anderson, 2005] Anderson, T. (2005). *Fracture Mechanics: Fundamentals and Applications, Third Edition*. Taylor & Francis. (Cited on pages xv, 8, 9, 10, and 121.)

[Arnold et al., 1984] Arnold, D., Brezzi, F., and Fortin, M. (1984). A stable finite element for the stokes equations. *Calcolo*, 21:337–344. (Cited on page 40.)

[Atkinson, 1982] Atkinson, B. K. (1982). Subcritical crack propagation in rocks: theory, experimental results and applications. *Journal of Structural Geology*, 4(1):41 – 56. (Cited on page 2.)

[Atkinson, 1984] Atkinson, B. K. (1984). Subcritical crack growth in geological materials. *Journal of Geophysical Research: Solid Earth*, 89(B):4077–4114. (Cited on page 3.)

[Attree et al., 2018] Attree, N., Groussin, O., Jorda, L., Rodionov, S., Auger, A. T., Thomas, N., Brouet, Y., Poch, O., Kührt, E., Knapmeyer, M., Preusker, F., Scholten, F., Knollenberg, J., Hviid, S., and Hartogh, P. (2018). Thermal fracturing on comets. Applications to 67P/Churyumov-Gerasimenko. *Astronomy and Astrophysics*, 610:A76. (Cited on pages xxiv, 2, and 3.)

[Azócar et al., 2010] Azócar, D., Elgueta, M., and Rivara, M. C. (2010). Automatic lefm crack propagation method based on local lepp–delaunay mesh refinement. *Advances in Engineering Software*, 41(2):111 – 119. (Cited on pages 79 and 81.)

[Ballouz et al., 2020] Ballouz, R.-L., Walsh, K. J., Barnouin, O., Dellagiustina, D. N., Al Asad, M., Jawin, E. R., Daly, M. G., Bottke, W. F., Michel, P., Avdellidou, C., Delbo, M., Daly, R. T., Asphaug, E., Bennett, C. A., Bierhaus, E. B., Connolly, H. C., Golish, D. R., Molaro, J. L., Nolan, M. C., Pajola, M., Rizk, B., Schwartz, S. R., Trang, D., Wolner, C. W. V., and Lauretta, D. S. (2020). Bennu's near-Earth lifetime of 1.75 million years inferred from craters on its boulders. *Nature*, 587:205–209. (Cited on pages xxv, 6, 100, and 112.)

[Barenblatt, 1962] Barenblatt, G. I. (1962). The mathematical theory of equilibrium cracks in brittle fracture. In Dryden, H. L., von Kármán, T., Kuerti, G., van den Dungen, F. H., and Howarth, L., editors, *Advances in Applied Mechanics*, volume 7, pages 55–129. Elsevier. (Cited on pages xvi, 26, 44, and 45.)

[Barnouin et al., 2019] Barnouin, O. S., Daly, M. G., Palmer, E. E., Gaskell, R. W., Weirich, J. R., Johnson, C. L., Al Asad, M. M., Roberts, J. H., Perry, M. E., Susorney, H. C. M., Daly, R. T., Bierhaus, E. B., Seabrook, J. A., Espiritu, R. C., Nair, A. H., Nguyen, L., Neumann, G. A., Ernst, C. M., Boynton, W. V., Nolan, M. C., Adam, C. D., Moreau, M. C., Rizk, B., Drouet d'Aubigny, C. Y., Jawin, E. R., Walsh, K. J., Michel, P., Schwartz, S. R., Ballouz, R. L., Mazarico, E. M., Scheeres, D. J., McMahon, J. W., Bottke, W. F., Sugita, S., Hirata, N., Watanabe, S. i., Burke, K. N., DellaGiustina, D. N., Bennett, C. A., Lauretta, D. S., and Team, O.-R. (2019). Shape of (101955) Bennu indicative of a rubble pile with internal stiffness. *Nature Geoscience*, 12(4):247–252. (Cited on pages xxi, 6, and 104.)

[Barsoum, 1976] Barsoum, R. S. (1976). On the use of isoparametric finite elements in linear fracture mechanics. *International Journal for Numerical Methods in Engineering*, 10(1):25–37. (Cited on pages 17 and 112.)

[Bathe, 2001] Bathe, K.-J. (2001). The inf–sup condition and its evaluation for mixed finite element methods. *Computers & Structures*, 79(2):243 – 252. (Cited on page 40.)

[Beden et al., 2009] Beden, S. M., Abdullah, S., and Ihsan, A. (2009). Review of fatigue crack propagation models for metallic components. *European journal of scientific research*, 28:364–397. (Cited on page 15.)

[Belytschko et al., 1994a] Belytschko, T., Lu, Y. Y., and Gu, L. (1994a). Element-free Galerkin methods. *International Journal for Numerical Methods in Engineering*, 37(2):229–256. (Cited on pages 22 and 23.)

[Belytschko et al., 1994b] Belytschko, T., Gu, L., and Lu, Y. Y. (1994b). Fracture and crack growth by element free galerkin methods. *Modelling and Simulation in Materials Science and Engineering*, 2(3A):519–534. (Cited on page 23.)

[Belytschko et al., 1996] Belytschko, T., Krongauz, Y., Organ, D., Fleming, M., and Krysl, P. (1996). Meshless methods: An overview and recent developments. *Computer Methods in Applied Mechanics and Engineering*, 139(1):3 – 47. (Cited on pages xv and 23.)

[Belytschko and Black, 1999] Belytschko, T. and Black, T. (1999). Elastic crack growth in finite elements with minimal remeshing. *International Journal for Numerical Methods in Engineering*, 45(5):601–620. (Cited on pages xvi, xxiv, and 25.)

[Belytschko et al., 2009] Belytschko, T., Gracie, R., and Ventura, G. (2009). A review of extended/generalized finite element methods for material modeling. *Modelling and Simulation in Materials Science and Engineering*, 17(4):043001. (Cited on page 25.)

[Bittencourt et al., 1996] Bittencourt, T., Wawrzynek, P., Ingraffea, A., and Sousa, J. (1996). Quasi-automatic simulation of crack propagation for 2d lefm problems. *Engineering Fracture Mechanics*, 55(2):321 – 334. (Cited on pages xxiv, 29, 79, and 81.)

[Blackburn et al., 1977] Blackburn, W., Jackson, A., and Hellen, T. (1977). An integral associated with the state of a crack tip in a non-elastic material. *International Journal of Fracture*, 13:183–199. (Cited on page 58.)

[Blal et al., 2012] Blal, N., Daridon, L., Monerie, Y., and Pagano, S. (2012). Artificial compliance inherent to the intrinsic cohesive zone models: Criteria and application to planar meshes. *International Journal of Fracture*, 178:71–83. (Cited on page 26.)

[Blandford et al., 1981] Blandford, G. E., Ingraffea, A. R., and Liggett, J. A. (1981). Two-dimensional stress intensity factor computations using the boundary element method. *International Journal for Numerical Methods in Engineering*, 17(3):387–404. (Cited on page 10.)

[Borden et al., 2012] Borden, M. J., Verhoosel, C. V., Scott, M. A., Hughes, T. J., and Landis, C. M. (2012). A phase-field description of dynamic brittle fracture. *Computer Methods in Applied Mechanics and Engineering*, 217-220:77 – 95. (Cited on page 28.)

[Bouchard et al., 2000] Bouchard, P.-O., Bay, F., Chastel, Y., and Tovena, I. (2000). Crack propagation modelling using an advanced remeshing technique. *Computer Methods in Applied Mechanics and Engineering*, 189(3):723 – 742. (Cited on pages xvi, 24, and 29.)

[Bouchard et al., 2003] Bouchard, P.-O., Bay, F., and Chastel, Y. (2003). Numerical modelling of crack propagation: automatic remeshing and comparison of different criteria. *Computer Methods in Applied Mechanics and Engineering*, 192(35):3887 – 3908. (Cited on pages xxiv, 17, 18, 22, 29, 32, and 57.)

[Bourdin et al., 2000] Bourdin, B., Francfort, G., and Marigo, J.-J. (2000). Numerical experiments in revisited brittle fracture. *Journal of the Mechanics and Physics of Solids*, 48(4):797 – 826. (Cited on page 26.)

[Bourdin et al., 2008] Bourdin, B., Francfort, G., and Marigo, J.-J. (2008). The variational approach to fracture. *Journal of Elasticity*, 91(1 - 3):5 – 148. (Cited on pages 26 and 28.)

[Boussattine, 2018] Boussattine, Z. (2018). *Consequences of the thermal effects generated during fatigue crack growth on the mode one stress intensity factor*. PhD thesis, Ecole nationale supérieure d'arts et métiers-ENSAM. (Cited on page 112.)

[Branco et al., 2015] Branco, R., Antunes, F., and Costa, J. (2015). A review on 3d-fe adaptive remeshing techniques for crack growth modelling. *Engineering Fracture Mechanics*, 141:170 – 195. (Cited on pages xxiv and 29.)

[Brezzi and Fortin, 1991] Brezzi, F. and Fortin, M. (1991). *Mixed and Hybrid Finite Element Methods*. Springer series in computational mathematics. Springer. (Cited on page 40.)

[Brochard and Suo, 1994] Brochard, J. and Suo, X. (1994). Le taux de restitution d'énergie G en mécanique de la rupture non-linéaire, formulation de la méthode *G-θ* et description de la programmation dans castem 2000. Technical report, C.E.A. Rapport DMT/94-640. (Cited on page 123.)

[Brocks, 2018] Brocks, W. (2018). *Concepts of Fracture Mechanics*, pages 5–21. Springer International Publishing, Cham. (Cited on page 9.)

[Broek, 1982a] Broek, D. (1982a). *Determination of stress intensity factors*, pages 328–346. Springer Netherlands, Dordrecht. (Cited on page 9.)

[Broek, 1982b] Broek, D. (1982b). *The energy principle*, pages 115–141. Springer Netherlands, Dordrecht. (Cited on page 121.)

[Burbine, 2014] Burbine, T. (2014). 2.14 - asteroids. In Holland, H. D. and Turekian, K. K., editors, *Treatise on Geochemistry (Second Edition)*, pages 365–415. Elsevier, Oxford, second edition edition. (Cited on page 4.)

[Camacho and Ortiz, 1996] Camacho, G. and Ortiz, M. (1996). Computational modelling of impact damage in brittle materials. *International Journal of Solids and Structures*, 33(20):2899 – 2938. (Cited on pages xvi, 26, 27, 45, and 148.)

[Cao et al., 2019] Cao, R.-H., Cao, P., Lin, H., Fan, X., Zhang, C., and Liu, T. (2019). Crack initiation, propagation, and failure characteristics of jointed rock or rock-like specimens: A review. *Advances in Civil Engineering*, 2019:1–31. (Cited on page 2.)

[Cao, 2013] Cao, T. S. (2013). *Modeling ductile damage for complex loading paths*. PhD thesis, Ecole Nationale Supérieure des Mines de Paris. (Cited on page 43.)

[Carter et al., 2000] Carter, B., Wawrzynek, P., and Ingraffea, A. (2000). Automated 3-d crack growth simulation. *International Journal for Numerical Methods in Engineering*, 47(1-3):229–253. (Cited on pages xxiv and 29.)

[Cellino, 2021] Cellino, A. (2021). Asteroids. In Alderton, D. and Elias, S. A., editors, *Encyclopedia of Geology (Second Edition)*, pages 141 – 149. Academic Press, Oxford, second edition edition. (Cited on page 4.)

[Chaboche et al., 2001] Chaboche, J., Feyel, F., and Monerie, Y. (2001). Interface debonding models: a viscous regularization with a limited rate dependency. *International Journal of Solids and Structures*, 38(18):3127 – 3160. (Cited on pages 26 and 50.)

[Chiaruttini et al., 2012] Chiaruttini, V., Geoffroy, D., Riolo, V., and Bonnet, M. (2012). An adaptive algorithm for cohesive zone model and arbitrary crack propagation. *Revue Européenne de Mécanique Numérique/European Journal of Computational Mechanics*, 21:208–218. (Cited on pages xvi, 30, 31, and 61.)

[Choi and Park, 2019] Choi, H. and Park, K. (2019). Removing mesh bias in mixed-mode cohesive fracture simulation with stress recovery and domain integral. *International Journal for Numerical Methods in Engineering*, 0(0):1–24. (Cited on page 30.)

[Clark et al., 2011] Clark, B. E., Binzel, R. P., Howell, E. S., Cloutis, E. A., Ockert-Bell, M., Christensen, P., Barucci, M. A., DeMeo, F., Lauretta, D. S., Connolly, H., Soderberg, A., Hergenrother, C., Lim, L., Emery, J., and Mueller, M. (2011). Asteroid (101955) 1999 rq36: Spectroscopy from 0.4 to 2.4μm and meteorite analogs. *Icarus*, 216(2):462–475. (Cited on page 6.)

[Collins and Stock, 2016] Collins, B. D. and Stock, G. M. (2016). Rockfall triggering by cyclic thermal stressing of exfoliation fractures. *Nature Geoscience*, 9:395–400. (Cited on pages xxiii, xxiv, and 2.)

[Collins et al., 2018] Collins, B. D., Stock, G. M., Eppes, M.-C., Lewis, S. W., Corbett, S. C., and Smith, J. B. (2018). Thermal influences on spontaneous rock dome exfoliation. *Nature Communications*, 9:1–12. (Cited on pages xxiii, xxiv, and 2.)

[Coupez, 1996] Coupez, T. (1996). Stable-stabilized finite element for 3d forming calculation. Technical report, CEMEF, Ecole des Mines de paris. (Cited on page 41.)

[Coupez et al., 2013] Coupez, T., Digonnet, H., Hachem, E., Laure, P., Silva, L., and Valette, R. (2013). *Multidomain Finite Element Computations*, chapter 5, pages 221–290. John Wiley & Sons, Ltd. (Cited on pages 29 and 32.)

[Crouzeix and Raviart, 1973] Crouzeix, M. and Raviart, P.-A. (1973). Conforming and non-conforming finite element methods for solving the stationary stokes equations i. *R.A.I.R.O.*, 7(R3):33–75. (Cited on page 40.)

[Dai et al., 2015] Dai, S., Augarde, C., Du, C., and Chen, D. (2015). A fully automatic polygon scaled boundary finite element method for modelling crack propagation. *Engineering Fracture Mechanics*, 133:163 – 178. (Cited on page 29.)

[Dally et al., 2020] Dally, T., Bilgen, C., Werner, M., and Weinberg, K. (2020). Cohesive elements or phase-field fracture: Which method is better for dynamic fracture analyses? In Valdman, J. and Marcinkowski, L., editors, *Modeling and Simulation in Engineering*, chapter 1. IntechOpen, Rijeka. (Cited on page 28.)

[de Borst, 2018] de Borst, R. (2018). Chapter 3 - fracture mechanics. In de Borst, R., editor, *Computational Methods for Fracture in Porous Media*, pages 35 – 45. Elsevier. (Cited on page 44.)

[de Pater and Lissauer, 2015] de Pater, I. and Lissauer, J. J. (2015). *Solar Heating and Energy Transport*, page 56–75. Cambridge University Press, 2 edition. (Cited on page 6.)

[Delbo et al., 2014] Delbo, M., Libourel, G., Wilkerson, J., Murdoch, N., Michel, P., Ramesh, K. T., Ganino, C., Verati, C., and Marchi, S. (2014). Thermal fatigue as the origin of regolith on small asteroids. *Nature*, 508(7495):233–236. (Cited on pages xxi, xxiv, xxvi, xxvii, 2, 3, 21, 103, 104, 112, 113, 114, and 119.)

[Delbo et al., 2015] Delbo, M., Mueller, M., Emery, J. P., Rozitis, B., and Capria, M. T. (2015). Asteroid Thermophysical Modeling. *in Asteroids IV (P. Michel, et al. eds.) University of Arizona Press, Tucson.*, pages 107–128. (Cited on pages 102 and 103.)

[Delbo et al., 2019] Delbo, M., Walsh, K., Molaro, J., Al Asad, M., DellaGiustina, D., Pajola, M., Bennett, C., Jawin, E., Ballouz, R., Schwartz, S., Rizk, B., and Lauretta, D. (2019). Distribution of fractures on boulders on (101955) Bennu: OSIRIS-REx searching for evidence of thermal cracking. In *EPSC-DPS Joint Meeting 2019*, volume 2019, pages EPSC–DPS2019–176. (Cited on pages xviii, 4, 32, 33, 100, 101, 102, 103, 109, 114, and 119.)

[DellaGiustina et al., 2019] DellaGiustina, D. N., Emery, J. P., Golish, D. R., Rozitis, B., Bennett, C. A., Burke, K. N., Ballouz, R. L., Becker, K. J., Christensen, P. R., Drouet d'Aubigny, C. Y., Hamilton, V. E., Reuter, D. C., Rizk, B., Simon, A. A., Asphaug, E., Bandfield, J. L., Barnouin, O. S., Barucci, M. A., Bierhaus, E. B., Binzel, R. P., Bottke, W. F., Bowles, N. E., Campins, H., Clark, B. C., Clark, B. E., Connolly, H. C., Daly, M. G., Leon, J. D., Delbo, M., Deshapriya, J. D. P., Elder, C. M., Fornasier, S., Hergenrother, C. W., Howell, E. S.,

Jawin, E. R., Kaplan, H. H., Kareta, T. R., Le Corre, L., Li, J. Y., Licandro, J., Lim, L. F., Michel, P., Molaro, J., Nolan, M. C., Pajola, M., Popescu, M., Garcia, J. L. R., Ryan, A., Schwartz, S. R., Shultz, N., Siegler, M. A., Smith, P. H., Tatsumi, E., Thomas, C. A., Walsh, K. J., Wolner, C. W. V., Zou, X. D., Lauretta, D. S., and Team, O.-R. (2019). Properties of rubble-pile asteroid (101955) Bennu from OSIRIS-REx imaging and thermal analysis. *Nature Astronomy*, 3:341–351. (Cited on pages xviii, xxiv, xxvi, 2, 100, 101, 102, and 109.)

[DeLorenzi, 1982] DeLorenzi, H. G. (1982). On the energy release rate and the J-integral for 3-D crack configurations. *International Journal of Fracture*, 19:183–193. (Cited on page 18.)

[Delorenzi, 1985] Delorenzi, H. G. (1985). Energy release rate calculations by the finite element method. *Engineering Fracture Mechanics*, 21(1):129 – 143. (Cited on page 18.)

[DeMeo et al., 2009] DeMeo, F. E., Binzel, R. P., Slivan, S. M., and Bus, S. J. (2009). An extension of the Bus asteroid taxonomy into the near-infrared. *Icarus*, 202(1):160–180. (Cited on page 103.)

[Destuynder et al., 1983] Destuynder, P., Djaoua, M., and Lescure, S. (1983). Quelques remarques sur la mécanique de la rupture élastique. *J. Méca. Théo. Appl.*, 2(1):113–135. (Cited on pages 18, 20, and 21.)

[Digonnet et al., 2007] Digonnet, H., Silva, L., and Coupez, T. (2007). Cimlib: A Fully Parallel Application For Numerical Simulations Based On Components Assembly. In Cesar de Sa, J. M. A. and Santos, A. D., editors, *Materials Processing and Design; Modeling, Simulation and Applications; NUMIFORM '07*, volume 908 of *American Institute of Physics Conference Series*, pages 269–274. (Cited on pages xxvii, 38, 40, 67, 74, and 106.)

[Dombard et al., 2010] Dombard, A. J., Barnouin, O. S., Prockter, L. M., and Thomas, P. C. (2010). Boulders and ponds on the Asteroid 433 Eros. *Icarus*, 210(2):713–721. (Cited on pages xxiv, xxvi, 2, and 3.)

[Dowling, 2013] Dowling, N. E. (2013). *Mechanical Behavior of Materials: Engineering Methods for Deformation, Fracture, and Fatigue*. Pearson Education, 4 edition. (Cited on pages 14 and 16.)

[Duarte and Oden, 1996] Duarte, C. and Oden, J. (1996). An h-p adaptive method using clouds. *Computer Methods in Applied Mechanics and Engineering*, 139(1):237 – 262. (Cited on page 25.)

[Dugdale, 1960] Dugdale, D. (1960). Yielding of steel sheets containing slits. *Journal of the Mechanics and Physics of Solids*, 8(2):100–104. (Cited on pages xvi, 44, and 45.)

[Egger et al., 2019] Egger, A., Pillai, U., Agathos, K., Kakouris, E., Chatzi, E., Aschroft, I. A., and Triantafyllou, S. P. (2019). Discrete and phase field methods for linear elastic fracture mechanics: A comparative study and state-of-the-art review. *Applied Sciences*, 9(12). (Cited on page 28.)

[El Khaoulani, 2010] El Khaoulani, R. (2010). *Prédiction fiable de l'endommagement ductile par la méthode des éléments finis mixtes : endommagement non local et adaptation de maillage*. PhD thesis, Ecole Nationale Supérieure des Mines de Paris. (Cited on page 44.)

[El Maarry et al., 2] El Maarry, M., Thomas, N., Gracia Berná, A., Marschall, R., Auger, A., Groussin, O., Mottola, S., Pajola, M., Massironi, M., Marchi, S., Höfner, S., Preusker, F., Scholten, F., Jorda, L., Kührt, E., Keller, H., Sierks, H., A'Hearn, M., Barbieri, C., Barucci, M., Bertaux, J., Bertini, I., Cremonese, G., Da Deppo, V., Davidsson, B., Debei, S., De Cecco, M., Deller, J., Güttler, C., Fornasier, S., Fulle, M., Gutierrez, P., Hofmann, M., Hviid,

S., Ip, W., Knollenberg, J., Koschny, D., Kovacs, G., Kramm, J., Küppers, M., Lamy, P., Lara, L., Lazzarin, M., Lopez, M. J., Marzari, F., Michalik, H., Naletto, G., Oklay, N., Pommerol, A., Rickman, H., Rodrigo, R., Tubiana, C., and Vincent, J. (2). Fractures on comet 67p/churyumov-gerasimenko observed by rosetta/osiris. *Geophysical Research Letters*, 42(13):5170–5178. (Cited on pages xxiv, xxvi, 2, and 3.)

[El Mir et al., 2019] El Mir, C., Ramesh, K. T., and Delbo, M. (2019). The efficiency of thermal fatigue in regolith generation on small airless bodies. *Icarus*, 333:356–370. (Cited on pages xxvii, 3, 103, 104, and 126.)

[Eldahshan et al., 2021] Eldahshan, H., Bouchard, P.-O., Alves, J., Perchat, E., and Pino-Muñoz, D. (2021). Phase field modeling of ductile fracture at large plastic strains using adaptive isotropic remeshing. *Computational Mechanics*, 67(3):763–783. (Cited on pages xxiii and 28.)

[Eppes et al., 2015] Eppes, M.-C., Willis, A., Molaro, J., Abernathy, S., and Zhou, B. (2015). Cracks in Martian boulders exhibit preferred orientations that point to solar-induced thermal stress. *Nature Communications*, 6:6712. (Cited on pages xxiv, 2, and 3.)

[Erdogan and Sih, 1963] Erdogan, F. and Sih, G. C. (1963). On the crack extension in plates under plane loading and transverse shear. *Journal of Basic Engineering*, 85(4):519–525. (Cited on pages 16, 56, and 113.)

[Erdogan, 2000] Erdogan, F. (2000). Fracture mechanics. *International Journal of Solids and Structures*, 37(1):171–183. (Cited on page xxiii.)

[Falk et al., 2001] Falk, M., Needleman, A., and Rice, J. (2001). A critical evaluation of cohesive zone models of dynamic fracture. *Journal De Physique Iv*, 11. (Cited on page 44.)

[Farahmand, 2001] Farahmand, B. (2001). *Fatigue Crack Growth and Applications*, pages 118–179. Springer US, Boston, MA. (Cited on page 14.)

[Fayolle, 2008] Fayolle, S. (2008). *Modélisation numérique de la mise en forme et de la tenue mécanique des assemblages par déformation plastique: application au rivetage auto-poinçonneur*. PhD thesis, Ecole Nationale Supérieure des Mines de Paris. (Cited on page 44.)

[Fischer-Cripps, 2007] Fischer-Cripps, A. (2007). *Linear Elastic Fracture Mechanics*, pages 31–48. Mechanical Engineering Series. Springer, New York. (Cited on pages xv, 11, and 12.)

[Forman and Mettu, 1990] Forman, R. and Mettu, S. (1990). Behavior of surface and corner cracks subjected to tensile and bending loads in ti-6al-4v alloy. (Cited on page 16.)

[Fortin, 1981] Fortin, M. (1981). Old and new finite elements for incompressible flows. *International Journal for Numerical Methods in Fluids*, 1(4):347–364. (Cited on page 40.)

[Francfort and Marigo, 1998] Francfort, G. and Marigo, J.-J. (1998). Revisiting brittle fracture as an energy minimization problem. *Journal of the Mechanics and Physics of Solids*, 46(8):1319 – 1342. (Cited on pages 26 and 28.)

[Fries and Belytschko, 2010] Fries, T.-P. and Belytschko, T. (2010). The extended/generalized finite element method: An overview of the method and its applications. *International Journal for Numerical Methods in Engineering*, 84(3):253–304. (Cited on pages xxiv and 24.)

[Gao and Bower, 2004] Gao, Y. and Bower, A. (2004). A simple technique for avoiding convergence problems in finite element simulations of crack nucleation and growth on cohesive interfaces. *Modelling and Simulation in Materials Science and Engineering*, 12(3):453 – –463. (Cited on pages 50, 52, 90, 92, and 154.)

[Garikipati, 1996] Garikipati, K. (1996). *On strong discontinuities in inelastic solids and their numerical simulations*. PhD thesis, Stanford University. (Cited on page 25.)

[Geißler et al., 2010] Geißler, G., Netzker, C., and Kaliske, M. (2010). Discrete crack path prediction by an adaptive cohesive crack model. *Engineering Fracture Mechanics*, 77(18):3541 – 3557. Computational Mechanics in Fracture and Damage: A Special Issue in Honor of Prof. Gross. (Cited on pages 30 and 61.)

[Geubelle and Baylor, 1998] Geubelle, P. H. and Baylor, J. S. (1998). Impact-induced delamination of composites: a 2d simulation. *Composites Part B: Engineering*, 29(5):589–602. (Cited on pages xvi and 45.)

[Griggs, 1936] Griggs, D. T. (1936). The Factor of Fatigue in Rock Exfoliation. *The Journal of Geology*, 44(7):783–796. (Cited on page 2.)

[Gruau and Coupez, 2005] Gruau, C. and Coupez, T. (2005). 3d tetrahedral, unstructured and anisotropic mesh generation with adaptation to natural and multidomain metric. *Computer Methods in Applied Mechanics and Engineering*, 194(48):4951 – 4976. Unstructured Mesh Generation. (Cited on page 61.)

[Ha et al., 2015] Ha, K., Baek, H., and Park, K. (2015). Convergence of fracture process zone size in cohesive zone modeling. *Applied Mathematical Modelling*, 39(19):5828 – 5836. (Cited on pages 44, 87, and 94.)

[Hadamard, 1902] Hadamard, J. (1902). Sur les problemes aux derivees partielles et leur signification physique. *Princeton university bulletin*, pages 49–52. (Cited on page 40.)

[Hall, 2004] Hall, K. (2004). Evidence for freeze-thaw events and their implications for rock weathering in northern Canada. *Earth Surface Processes and Landforms*, 29:43–57. (Cited on page 2.)

[Hamilton et al., 2019] Hamilton, V. E., Simon, A. A., Christensen, P. R., Reuter, D. C., Clark, B. E., Barucci, M. A., Bowles, N. E., Boynton, W. V., Brucato, J. R., Cloutis, E. A., Connolly, H. C., Donaldson Hanna, K. L., Emery, J. P., Enos, H. L., Fornasier, S., Haberle, C. W., Hanna, R. D., Howell, E. S., Kaplan, H. H., Keller, L. P., Lantz, C., Li, J. Y., Lim, L. F., McCoy, T. J., Merlin, F., Nolan, M. C., Praet, A., Rozitis, B., Sandford, S. A., Schrader, D. L., Thomas, C. A., Zou, X. D., Lauretta, D. S., and Team, O.-R. (2019). Evidence for widespread hydrated minerals on asteroid (101955) Bennu. *Nature Astronomy*, 3(4):332–340. (Cited on page 103.)

[Hamitouche et al., 2008] Hamitouche, L., Tarfaoui, M., and Vautrin, A. (2008). An interface debonding law subject to viscous regularization for avoiding instability: Application to the delamination problems. *Engineering Fracture Mechanics*, 75(10):3084 – 3100. (Cited on page 50.)

[Hazeli et al., 2018] Hazeli, K., El Mir, C., Papanikolaou, S., Delbo, M., and Ramesh, K. T. (2018). The origins of Asteroidal rock disaggregation: Interplay of thermal fatigue and microstructure. *Icarus*, 304:172–182. (Cited on page 3.)

[Hegen, 1997] Hegen, D. (1997). *An element-free Galerkin method for crack propagation in brittle materials*. PhD thesis, Department of Mechanical Engineering. (Cited on page 24.)

[Hellen, 1975] Hellen, T. (1975). On the method of virtual crack extensions. *International Journal for Numerical Methods in Engineering*, 9(1):187–207. (Cited on pages 18 and 58.)

[Hellen and Cesari, 1979] Hellen, T. and Cesari, F. (1979). On the solution of the centre cracked plate with a quadratic thermal gradient. *Engineering Fracture Mechanics*, 12(4):469 – 478. (Cited on pages 58 and 59.)

[Hellen et al., 1982] Hellen, T., Cesari, F., and Maitan, A. (1982). The application of fracture mechanics in thermally stressed structures. *International Journal of Pressure Vessels and Piping*, 10(3):181 – 204. (Cited on pages 58 and 59.)

[Hergenrother et al., 2013] Hergenrother, C. W., Nolan, M. C., Binzel, R. P., Cloutis, E. A., Barucci, M. A., Michel, P., Scheeres, D. J., d'Aubigny, C. D., Lazzaro, D., Pinilla-Alonso, N., Campins, H., Licandro, J., Clark, B. E., Rizk, B., Beshore, E. C., and Lauretta, D. S. (2013). Lightcurve, color and phase function photometry of the osiris-rex target asteroid (101955) bennu. *Icarus*, 226(1):663–670. (Cited on page 6.)

[Hermes, 2010] Hermes, F. (2010). Process zone and cohesive element size in numerical simulations of delamination in bi-layers. Master's thesis, Eindhoven University of Technology. (Cited on pages 44, 87, and 94.)

[Hood and Taylor, 1974] Hood, P. and Taylor, C. (1974). Navier-stokes equations using mixed-interpolation. In Oden, J. T., Zienkiewicz, O. C., Gallagher, R., and Taylor, C., editors, *Finite Element Methods in Flow Problems*, pages 57–66. UAH Press. (Cited on page 40.)

[Hussain et al., 1973] Hussain, M., Pu, S., and Underwood, J. (1973). Strain energy release rate for a crack under combined mode i and mode ii. *Fracture Analysis, Proc. 1973 National Symposium on Fracture Mechanics, Part II, ASTM STP 560, Amer. Soc. Testing Mater*, pages 2–28. (Cited on pages 16 and 18.)

[Inglis, 1913] Inglis, C. E. (1913). Stresses in a plate due to the presence of cracks and sharp corners. *Transactions of the Institute of Naval Architects*, 55:219–242. (Cited on page 11.)

[Ingraffea and Grigoriu, 1990] Ingraffea, A. and Grigoriu, M. (1990). Probabilistic fracture mechanics: a validation of predictive capability. Technical report, Department of Structural Engineering, Cornell University. (Cited on page 81.)

[Ingraffea and de Borst, 2017] Ingraffea, A. R. and de Borst, R. (2017). *Computational Fracture Mechanics*. Encyclopedia of Computational Mechanics Second Edition (Ed. E. Stein, R. de Borst and T.J.R. Hughes), John Wiley and Sons. (Cited on page 24.)

[Irwin, 1957] Irwin, G. R. (1957). Analysis of stresses and strains near the end of a crack transversing a plate. *Trans. ASME, Ser. E, J. Appl. Mech.*, 24:361–364. (Cited on page 9.)

[Janssen et al., 2004] Janssen, M., Zuidema, J., and Wanhill, R. (2004). *Fracture Mechanics - 2nd Edition*. Spon Press, 2^{nd} edition. (Cited on pages xv, 14, and 15.)

[Jiang, 2010] Jiang, H. (2010). *Cohesive zone model for carbon nanotube adhesive simulation and fracture/fatigue crack growth*. PhD thesis, The University of Akron. (Cited on pages 26 and 50.)

[Jirásek, 2000] Jirásek, M. (2000). Comparative study on finite elements with embedded discontinuities. *Computer Methods in Applied Mechanics and Engineering*, 188(1):307 – 330. (Cited on pages xxiv and 24.)

[Kobayashi et al., 1964] Kobayashi, A. S., Cherepy, R. D., and Kinsel, W. C. (1964). A numerical procedure for estimating the stress intensity factor of a crack in a finite plate. *Journal of Basic Engineering*, 86(4):681–684. (Cited on page 10.)

[Krysl and Belytschko, 1999] Krysl, P. and Belytschko, T. (1999). The element free galerkin method for dynamic propagation of arbitrary 3-d cracks. *International Journal for Numerical Methods in Engineering*, 44(6):767–800. (Cited on page 23.)

[Kuhn and Müller, 2010] Kuhn, C. and Müller, R. (2010). A continuum phase field model for fracture. *Engineering Fracture Mechanics*, 77(18):3625 – 3634. (Cited on page 28.)

[Lauretta et al., 2014] Lauretta, D. S., Bartels, A. E., Barucci, M. A., Bierhaus, E. B., Binzel, R. P., Bottke, W. F., Campins, H., Chesley, S. R., Clark, B. C., Clark, B. E., Cloutis, E. A., Connolly, H. C., Crombie, M. K., Delbo, M., Dworkin, J. P., Emery, J. P., Glavin, D. P., Hamilton, V. E., Hergenrother, C. W., Johnson, C. L., Keller, L. P., Michel, P., Nolan, M. C., Sandford, S. A., Scheeres, D. J., Simon, A. A., Sutter, B. M., Vokrouhlický, D., and Walsh, K. J. (2014). The OSIRIS-REx target asteroid (101955) Bennu: Constraints on its physical, geological, and dynamical nature from astronomical observations. *Meteoritics & Planetary Science*, page 113. (Cited on pages xxvi, 3, and 100.)

[Lauretta et al., 2017] Lauretta, D. S., Balram-Knutson, S. S., Beshore, E., Boynton, W. V., Drouet d'Aubigny, C., DellaGiustina, D. N., Enos, H. L., Golish, D. R., Hergenrother, C. W., Howell, E. S., Bennett, C. A., Morton, E. T., Nolan, M. C., Rizk, B., Roper, H. L., Bartels, A. E., Bos, B. J., Dworkin, J. P., Highsmith, D. E., Lorenz, D. A., Lim, L. F., Mink, R., Moreau, M. C., Nuth, J. A., Reuter, D. C., Simon, A. A., Bierhaus, E. B., Bryan, B. H., Ballouz, R., Barnouin, O. S., Binzel, R. P., Bottke, W. F., Hamilton, V. E., Walsh, K. J., Chesley, S. R., Christensen, P. R., Clark, B. E., Connolly, H. C., Crombie, M. K., Daly, M. G., Emery, J. P., McCoy, T. J., McMahon, J. W., Scheeres, D. J., Messenger, S., Nakamura-Messenger, K., Righter, K., and Sandford, S. A. (2017). Osiris-rex: Sample return from asteroid (101955) bennu. *Space Science Reviews*, 212. (Cited on pages xxvi and 100.)

[Lauretta et al., 2019a] Lauretta, D. S., Hergenrother, C. W., Chesley, S. R., Leonard, J. M., Pelgrift, J. Y., Adam, C. D., Al Asad, M., Antreasian, P. G., Ballouz, R. L., Becker, K. J., Bennett, C. A., Bos, B. J., Bottke, W. F., Brozovic, M., Campins, H., Connolly, H. C., Daly, M. G., Davis, A. B., de León, J., DellaGiustina, D. N., Drouet d'Aubigny, C. Y., Dworkin, J. P., Emery, J. P., Farnocchia, D., Glavin, D. P., Golish, D. R., Hartzell, C. M., Jacobson, R. A., Jawin, E. R., Jenniskens, P., Kidd, J. N., Lessac-Chenen, E. J., Li, J. Y., Libourel, G., Licandro, J., Liounis, A. J., Maleszewski, C. K., Manzoni, C., May, B., McCarthy, L. K., McMahon, J. W., Michel, P., Molaro, J. L., Moreau, M. C., Nelson, D. S., Owen, W. M., Rizk, B., Roper, H. L., Rozitis, B., Sahr, E. M., Scheeres, D. J., Seabrook, J. A., Selznick, S. H., Takahashi, Y., Thuillet, F., Tricarico, P., Vokrouhlický, D., and Wolner, C. W. V. (2019a). Episodes of particle ejection from the surface of the active asteroid (101955) Bennu. *Science*, 366(6). (Cited on page 3.)

[Lauretta et al., 2019b] Lauretta, D. S., DellaGiustina, D. N., Bennett, C. A., Becker, K. J., Barnouin, O. S., Bottke, W. F., Drouet d'Aubigny, C. Y., Dworkin, J. P., Emery, J. P., Hamilton, V. E., Hergenrother, C. W., Izawa, M. R. M., Rizk, B., Walsh, K. J., Wolner, C. W. V., Team, O.-R., Connolly, H. C., Clark, B. E., Campins, H., Becker, T. L., Boynton, W. V., d'Aubigny, C. Y. D., Enos, H. L., Golish, D. R., Howell, E. S., Balram-Knutson, S. S., Nolan, M. C., Roper, H. L., Smith, P. H., Scheeres, D. J., and Kaplan, H. H. (2019b). The unexpected surface of asteroid (101955) Bennu. *Nature*, 568(7):55–60. (Cited on pages xxiv, xxvi, 2, 3, 6, 102, and 109.)

[Lemaitre and Desmorat, 2005] Lemaitre, J. and Desmorat, R. (2005). *Engineering Damage Mechanics: Ductile, Creep, Fatigue and Brittle Failures*. Springer Berlin Heidelberg, Berlin, Heidelberg. (Cited on page 86.)

[Li et al., 1985] Li, F., Shih, C., and Needleman, A. (1985). A comparison of methods for calculating energy release rates. *Engineering Fracture Mechanics*, 21(2):405 – 421. (Cited on page 124.)

[Li et al., 2017] Li, Y., Basilevsky, A. T., Xie, M., and Ip, W.-H. (2017). Shape of boulders ejected from small lunar impact craters. *Planetary and Space Science*, 145:71–77. (Cited on pages xxiv and 2.)

[Liang et al., 2020] Liang, B., Cuadra, J., Hazeli, K., and Soghrati, S. (2020). Stress field analysis in a stony meteorite under thermal fatigue and mechanical loadings. *Icarus*, 335:113381. (Cited on pages 3 and 126.)

[Liao et al., 2018] Liao, M., Deng, X., and Guo, Z. (2018). Crack propagation modelling using the weak form quadrature element method with minimal remeshing. *Theoretical and Applied Fracture Mechanics*, 93:293–301. (Cited on pages xxiii, 78, and 79.)

[Libourel et al., 2019] Libourel, G., Nakamura, A. M., Beck, P., Potin, S., Ganino, C., Jacomet, S., Ogawa, R., Hasegawa, S., and Michel, P. (2019). Hypervelocity impacts as a source of deceiving surface signatures on iron-rich asteroids. *Science Advances*, 5(8). (Cited on page xxiv.)

[Lorentz, 2008] Lorentz, E. (2008). A mixed interface finite element for cohesive zone models. *Computer Methods in Applied Mechanics and Engineering*, 198(2):302 – 317. (Cited on page 26.)

[Lu et al., 1995] Lu, Y., Belytschko, T., and Tabbara, M. (1995). Element-free galerkin method for wave propagation and dynamic fracture. *Computer Methods in Applied Mechanics and Engineering*, 126(1):131–153. (Cited on page 24.)

[Maiti and Smith, 1984] Maiti, S. K. and Smith, R. A. (1984). Comparison of the criteria for mixed mode brittle fracture based on the preinstability stress-strain field. *International Journal of Fracture*, 24(1):5–22. (Cited on page 16.)

[Marigo et al., 2016] Marigo, J.-J., Maurini, C., and Pham, K. (2016). An overview of the modelling of fracture by gradient damage models. *Meccanica*, 51(12):3107–3128. (Cited on pages xxiii and 21.)

[Martin et al., 2019] Martin, A., LE CREN, M., and Stolz, C. (2019). Analyse de la méthode G – θ en 3D : cas des fissures planes à front droit. In *CSMA 2019, 14ème Colloque National en Calcul des Structures*, CSMA-2019, Giens (Var), France. (Cited on page 124.)

[Matonti et al., 2019] Matonti, C., Attree, N., Groussin, O., Jorda, L., Viseur, S., Hviid, S. F., Bouley, S., Nébouy, D., Auger, A. T., Lamy, P. L., Sierks, H., Naletto, G., Rodrigo, R., Koschny, D., Davidsson, B., Barucci, M. A., Bertaux, J. L., Bertini, I., Bodewits, D., Cremonese, G., Da Deppo, V., Debei, S., De Cecco, M., Deller, J., Fornasier, S., Fulle, M., Gutiérrez, P. J., Güttler, C., Ip, W. H., Keller, H. U., Lara, L. M., La Forgia, F., Lazzarin, M., Lucchetti, A., Lopez Moreno, J. J., Marzari, F., Massironi, M., Mottola, S., Oklay, N., Pajola, M., Penasa, L., Preusker, F., Rickman, H., Scholten, F., Shi, X., Toth, I., Tubiana, C., and Vincent, J. B. (2019). Bilobate comet morphology and internal structure controlled by shear deformation. *Nature Geoscience*, 12(3):157–162. (Cited on pages xxiv and 2.)

[McCoy, 2021] McCoy, T. J. (2021). Meteorites. In Alderton, D. and Elias, S. A., editors, *Encyclopedia of Geology (Second Edition)*, pages 174 – 184. Academic Press, Oxford, second edition edition. (Cited on pages xv, 4, 5, and 6.)

[McFadden et al., 2005] McFadden, L. D., Eppes, M. C., Gillespie, A. R., and Hallet, B. (2005). Physical weathering in arid landscapes due to diurnal variation in the direction of solar heating. *Geological Society of America Bulletin*, 117:161. (Cited on page 3.)

[Melenk, 1995] Melenk, J. (1995). On generalized finite element methods. *Ph. D. dissertation, University of Maryland*. (Cited on page 25.)

[Melenk and Babuška, 1996] Melenk, J. and Babuška, I. (1996). The partition of unity finite element method: Basic theory and applications. *Computer Methods in Applied Mechanics and Engineering*, 139(1):289 – 314. (Cited on page 25.)

[Meng et al., 2019] Meng, Z. J., Cheng, H., Ma, L. D., and Cheng, Y. M. (2019). The hybrid element-free galerkin method for three-dimensional wave propagation problems. *International Journal for Numerical Methods in Engineering*, 117(1):15–37. (Cited on page 24.)

[Miehe et al., 2010] Miehe, C., Hofacker, M., and Welschinger, F. (2010). A phase field model for rate-independent crack propagation: Robust algorithmic implementation based on operator splits. *Computer Methods in Applied Mechanics and Engineering*, 199(45):2765 – 2778. (Cited on pages xvi and 28.)

[Migliazza et al., 2011] Migliazza, M., Ferrero, A. M., and Spagnoli, A. (2011). Experimental investigation on crack propagation in carrara marble subjected to cyclic loads. *International Journal of Rock Mechanics and Mining Sciences*, 48(6):1038–1044. (Cited on pages 21 and 112.)

[Millar, 2013] Millar, S. (2013). 8.23 mass movement processes in the periglacial environment. In Shroder, J. F., editor, *Treatise on Geomorphology*, pages 374–391. Academic Press, San Diego. (Cited on page 3.)

[Moës et al., 1999] Moës, N., Dolbow, J., and Belytschko, T. (1999). A finite element method for crack growth without remeshing. *International Journal for Numerical Methods in Engineering*, 46(1):131–150. (Cited on pages xxiv and 25.)

[Molaro et al., 2015] Molaro, J. L., Byrne, S., and Langer, S. A. (2015). Grain-scale thermoelastic stresses and spatiotemporal temperature gradients on airless bodies, implications for rock breakdown. *Journal of Geophysical Research: Planets*, 120(2):255–277. (Cited on page 2.)

[Molaro et al., 2017] Molaro, J. L., Byrne, S., and L, L. J. (2017). Thermally induced stresses in boulders on airless body surfaces, and implications for rock breakdown. *Icarus*, 294:247–261. (Cited on pages 2 and 3.)

[Molaro et al., 2020a] Molaro, J. L., Walsh, K. J., Jawin, E. R., Ballouz, R. L., Bennett, C. A., DellaGiustina, D. N., Golish, D. R., Drouet d'Aubigny, C., Rizk, B., Schwartz, S. R., Hanna, R. D., Martel, S. J., Pajola, M., Campins, H., Ryan, A. J., Bottke, W. F., and Lauretta, D. S. (2020a). In situ evidence of thermally induced rock breakdown widespread on Bennu's surface. *Nature Communications*, 11(1):2913–11. (Cited on pages xxiv, 2, 3, 6, and 109.)

[Molaro et al., 2020b] Molaro, J. L., Hergenrother, C. W., Chesley, S. R., Walsh, K. J., Hanna, R. D., Haberle, C. W., Schwartz, S. R., Ballouz, R. L., Bottke, W. F., Campins, H. J., and Lauretta, D. S. (2020b). Thermal Fatigue as a Driving Mechanism for Activity on Asteroid Bennu. *Journal of Geophysical Research: Planets*, 125(8):e06325. (Cited on pages xxvii, 3, 6, 100, and 102.)

[Murdoch et al., 2015] Murdoch, N., Sánchez, P., Schwartz, S. R., and Miyamoto, H. (2015). Asteroid Surface Geophysics. *in Asteroids IV (P. Michel, et al. eds.) University of Arizona Press, Tucson.*, pages 767–792. (Cited on pages xxvi and 3.)

[Muskhelishvili, 1977] Muskhelishvili, N. (1977). *Some Basic Problems of the mathematical theory of elasticity*. Number 1. Springer Netherlands. (Cited on page 58.)

[NASGRO, 2010] NASGRO (2010). *NASGRO, Fracture mechanics and fatigue crack growth analysis*. NASA Johnson Space Center and Southwest Research Institute. (version 6.0), reference manual. (Cited on page 16.)

[Needleman, 1987] Needleman, A. (1987). A Continuum Model for Void Nucleation by Inclusion Debonding. *Journal of Applied Mechanics*, 54(3):525–531. (Cited on pages xvi and 45.)

[Needleman, 1990] Needleman, A. (1990). An analysis of decohesion along an imperfect interface. *International Journal of Fracture*, 42:21–40. (Cited on page 45.)

[Needleman, 2014] Needleman, A. (2014). Some issues in cohesive surface modeling. *Procedia IUTAM*, 10:221 – 246. Mechanics for the World: Proceedings of the 23rd International Congress of Theoretical and Applied Mechanics, ICTAM2012. (Cited on page 50.)

[Newman, 1984] Newman, J. (1984). A crack opening stress equation for fatigue crack growth. *International Journal of Fracture*, 24(4):R131–R135. (Cited on page 16.)

[Nguyen et al., 2001] Nguyen, O., Repetto, E., Ortiz, M., and Radovitzky, R. (2001). A cohesive model of fatigue crack growth. *International Journal of Fracture*, 110:351–369. (Cited on page 120.)

[Nguyen et al., 2015] Nguyen, T., Yvonnet, J., Zhu, Q.-Z., Bornert, M., and Chateau, C. (2015). A phase field method to simulate crack nucleation and propagation in strongly heterogeneous materials from direct imaging of their microstructure. *Engineering Fracture Mechanics*, 139:18 – 39. (Cited on page 28.)

[Nguyen-Xuan et al., 2012] Nguyen-Xuan, H., Liu, G., Nourbakhshnia, N., and Chen, L. (2012). A novel singular es-fem for crack growth simulation. *Engineering Fracture Mechanics*, 84:41 – 66. (Cited on pages xvii, 17, 57, 78, 79, and 81.)

[Nolan et al., 2013] Nolan, M. C., Magri, C., Howell, E. S., Benner, L. A., Giorgini, J. D., Hergenrother, C. W., Hudson, R. S., Lauretta, D. S., Margot, J.-L., Ostro, S. J., and Scheeres, D. J. (2013). Shape model and surface properties of the osiris-rex target asteroid (101955) bennu from radar and lightcurve observations. *Icarus*, 226(1):629–640. (Cited on page 6.)

[Nuismer, 1975] Nuismer, R. (1975). An energy release rate criterion for mixed mode fracture. *International Journal of Fracture*, 11:245–250. (Cited on pages 16 and 18.)

[Oliver and Huespe, 2004] Oliver, J. and Huespe, A. (2004). Continuum approach to material failure in strong discontinuity settings. *Computer Methods in Applied Mechanics and Engineering*, 193(30):3195 – 3220. Computational Failure Mechanics. (Cited on page 25.)

[Oliver et al., 2006] Oliver, J., Huespe, A., and Sánchez, P. (2006). A comparative study on finite elements for capturing strong discontinuities: E-fem vs x-fem. *Computer Methods in Applied Mechanics and Engineering*, 195(37):4732 – 4752. John H. Argyris Memorial Issue. Part I. (Cited on pages xxiv and 24.)

[Ooi et al., 2013] Ooi, E., Shi, M., Song, C., Tin-Loi, F., and Yang, Z. (2013). Dynamic crack propagation simulation with scaled boundary polygon elements and automatic remeshing technique. *Engineering Fracture Mechanics*, 106:1 – 21. (Cited on pages xvi, 29, and 30.)

[Ortiz and Pandolfi, 1999] Ortiz, M. and Pandolfi, A. (1999). Finite-deformation irreversible cohesive elements for three-dimensional crack-propagation analysis. *Int J Numer Methods Eng*. (Cited on pages xvi, 26, 27, 46, 47, 78, and 87.)

[Osher and Sethian, 1988] Osher, S. and Sethian, J. A. (1988). Fronts propagating with curvature-dependent speed: Algorithms based on hamilton-jacobi formulations. *Journal of Computational Physics*, 79(1):12 – 49. (Cited on page 61.)

[Pandolfi and Ortiz, 1998] Pandolfi, A. and Ortiz, M. (1998). Solid modeling aspects of three-dimensional fragmentation. *Engineering with Computers*, 14(4):287–308. (Cited on page 30.)

[Pandolfi and Ortiz, 2002] Pandolfi, A. and Ortiz, M. (2002). An efficient adaptive procedure for three-dimensional fragmentation simulations. *Engineering with Computers*, 18:148–159. (Cited on pages xvi, 30, and 31.)

[Paris et al., 1961] Paris, P., Gomez, M., and Anderson, W. (1961). A rational analytic theory of fatigue. *The Trend of Engineering*, 13:9–14. (Cited on page 15.)

[Paris and Erdogan, 1963] Paris, P. and Erdogan, F. (1963). A Critical Analysis of Crack Propagation Laws. *Journal of Basic Engineering*, 85(4):528–533. (Cited on page 15.)

[Paris and Sih, 1965] Paris, P. and Sih, G. (1965). Stress analysis of cracks. In *Fracture Toughness Testing and its Applications*, pages 30–81. ASTM STP 381, American Society for Testing and Materials, Philadelphia. (Cited on page 11.)

[Parks, 1974] Parks, D. M. (1974). A stiffness derivative finite element technique for determination of crack tip stress intensity factors. *International Journal of Fracture*, 10(4):487–502. (Cited on pages 18 and 58.)

[Perchat, 2000] Perchat, E. (2000). *MINI-élément et factorisation incomplètes pour la parallelisation d'un solveur de Stokes 2D: application au forgeage*. PhD thesis, Ecole Nationale Supérieure des Mines de Paris. (Cited on page 44.)

[Pook, 2000] Pook, L. (2000). *Linear Elastic Fracture Mechanics for Engineers: Theory and Applications*. WIT Press. (Cited on page 11.)

[Pook, 2015] Pook, L. P. (2015). The linear elastic analysis of cracked bodies and crack paths. *Theoretical and Applied Fracture Mechanics*, 79:34–50. (Cited on page 11.)

[Poulet et al., 2016] Poulet, F., Lucchetti, A., Bibring, J.-P., Carter, J., Gondet, B., Jorda, L., Langevin, Y., Pilorget, C., Capanna, C., and Cremonese, G. (2016). Origin of the local structures at the Philae landing site and possible implications on the formation and evolution of 67P/Churyumov-Gerasimenko. *Monthly Notices of the Royal Astronomical Society*, 462(Suppl1):S23–S32. (Cited on pages xv and xxvi.)

[Rabczuk et al., 2010] Rabczuk, T., Bordas, S., and Zi, G. (2010). On three-dimensional modelling of crack growth using partition of unity methods. *Computers & Structures*, 88(23):1391 – 1411. Special Issue: Association of Computational Mechanics – United Kingdom. (Cited on page 25.)

[Radaj, 2013a] Radaj, D. (2013a). *Extended Stress Intensity Factor Concepts*, pages 101–265. Springer Berlin Heidelberg, Berlin, Heidelberg. (Cited on page 9.)

[Radaj, 2013b] Radaj, D. (2013b). State-of-the-art review on extended stress intensity factor concepts. *Fatigue & Fracture of Engineering Materials & Structures*, 37(1):1–28. (Cited on page 9.)

[Rahulkumar et al., 2000] Rahulkumar, P., Jagota, A., Bennison, S., and Saigal, S. (2000). Cohesive element modeling of viscoelastic fracture: application to peel testing of polymers. *International Journal of Solids and Structures*, 37(13):1873 – 1897. (Cited on page 48.)

[Rashid, 1998] Rashid, M. (1998). The arbitrary local mesh replacement method: An alternative to remeshing for crack propagation analysis. *Computer Methods in Applied Mechanics and Engineering*, 154(1):133 – 150. (Cited on pages xv and 24.)

[Ravaji et al., 2019] Ravaji, B., Ali-Lagoa, V., Delbo, M., and Wilkerson, J. W. (2019). Unraveling the Mechanics of Thermal Stress Weathering: Rate-Effects, Size-Effects, and Scaling Laws. *Journal of Geophysical Research: Planets*, 124(1):3304–3328. (Cited on pages 3, 103, and 104.)

[Rice, 1968a] Rice, J. R. (1968a). Mathematical analysis in the mechanics of fracture. In Liebowitz, H., editor, *Fracture : An Advanced Treatise.*, chapter 3, pages 191–311. Academic Press, N.Y. (Cited on page 44.)

[Rice, 1968b] Rice, J. R. (1968b). A path independent integral and the approximate analysis of strain concentration by notches and cracks. *Journal of Applied Mechanics*, 35(2):379–386. (Cited on pages 18, 26, and 44.)

[Roe and Siegmund, 2003] Roe, K. and Siegmund, T. (2003). An irreversible cohesive zone model for interface fatigue crack growth simulation. *Engineering Fracture Mechanics*, 70(2):209 – 232. (Cited on pages 47, 48, and 49.)

[Roth et al., 2014] Roth, S., Hütter, G., and Kuna, M. (2014). Simulation of fatigue crack growth with a cyclic cohesive zone model. *International Journal of Fracture*, 188:23–45. (Cited on page 120.)

[Rozitis and Green, 2011] Rozitis, B. and Green, S. F. (2011). Directional characteristics of thermal-infrared beaming from atmosphereless planetary surfaces - a new thermophysical model. *Monthly Notices of the Royal Astronomical Society*, 415(3):2042–2062. (Cited on page 103.)

[Rozitis et al., 2020] Rozitis, B., Ryan, A. J., Emery, J. P., Christensen, P. R., Hamilton, V. E., Simon, A. A., Reuter, D. C., Al Asad, M., Ballouz, R.-L., Bandfield, J. L., Barnouin, O. S., Bennett, C. A., Bernacki, M., Burke, K. N., Cambioni, S., Clark, B. E., Daly, M. G., Delbo, M., DellaGiustina, D. N., Elder, C. M., Hanna, R. D., Haberle, C. W., Howell, E. S., Golish, D. R., Jawin, E. R., Kaplan, H. H., Lim, L. F., Molaro, J. L., Munoz, D. P., Nolan, M. C., Rizk, B., Siegler, M. A., Susorney, H. C. M., Walsh, K. J., and Lauretta, D. S. (2020). Asteroid (101955) bennu's weak boulders and thermally anomalous equator. *Science Advances*, 6(41). (Cited on pages xv, xxv, 2, and 6.)

[Ruesch et al., 2020] Ruesch, O., Sefton-Nash, E., Vago, J. L., Küppers, M., Pasckert, J. H., Krohn, K., and Otto, K. (2020). In situ fragmentation of lunar blocks and implications for impacts and solar-induced thermal stresses. *Icarus*, 336:113431. (Cited on pages xxiv and 2.)

[Ryan et al., 2020] Ryan, A. J., Pino Muñoz, D., Bernacki, M., and Delbo, M. (2020). Full-field modeling of heat transfer in asteroid regolith: Radiative thermal conductivity of polydisperse particulates. *Journal of Geophysical Research: Planets*, 125(2). (Cited on page 106.)

[Schijve, 2009] Schijve, J., editor (2009). *Fatigue as a Phenomenon in the Material*, pages 13–58. Springer Netherlands, Dordrecht. (Cited on page 14.)

[Sepasdar and Shakiba, 2020] Sepasdar, R. and Shakiba, M. (2020). Overcoming the convergence difficulty of cohesive zone models through a newton-raphson modification technique. *Engineering Fracture Mechanics*, 233:107046. (Cited on pages 50, 51, and 153.)

[Shakoor et al., 2015] Shakoor, M., Bernacki, M., and Bouchard, P.-O. (2015). A new body-fitted immersed volume method for the modeling of ductile fracture at the microscale: Analysis of void clusters and stress state effects on coalescence. *Engineering Fracture Mechanics*, 147:398 – 417. (Cited on pages 32, 61, 62, 68, 97, and 125.)

[Shakoor et al., 2017] Shakoor, M., Bouchard, P.-O., and Bernacki, M. (2017). An adaptive level-set method with enhanced volume conservation for simulations in multiphase domains. *International Journal for Numerical Methods in Engineering*, 109(4):555–576. (Cited on pages 32 and 125.)

[Shakoor et al., 2018] Shakoor, M., Navas, V. T., Muñoz, D. P., Bernacki, M., and Bouchard, P.-O. (2018). Computational methods for ductile fracture modeling at the microscale. *Archives of Computational Methods in Engineering*, pages 1–40. (Cited on pages 22, 25, 33, 61, and 62.)

[Shet and Chandra, 2002] Shet, C. and Chandra, N. (2002). Analysis of Energy Balance When Using Cohesive Zone Models to Simulate Fracture Processes . *Journal of Engineering Materials and Technology*, 124(4):440–450. (Cited on page 45.)

[Shoemaker, 2003] Shoemaker, C. S. (2003). Asteroid impacts and extinctions. In Meyers, R. A., editor, *Encyclopedia of Physical Science and Technology (Third Edition)*, pages 647–663. Academic Press, New York, third edition edition. (Cited on page 4.)

[Sih, 1973] Sih, G. (1973). Some basic problems in fracture mechanics and new concepts. *Engineering Fracture Mechanics*, 5(2):365 – 377. (Cited on page 16.)

[Sih and Macdonald, 1974] Sih, G. and Macdonald, B. (1974). Fracture mechanics applied to engineering problems-strain energy density fracture criterion. *Engineering Fracture Mechanics*, 6(2):361 – 386. (Cited on page 16.)

[Simo and Taylor, 1985] Simo, J. and Taylor, R. (1985). Consistent tangent operators for rate-independent elastoplasticity. *Computer Methods in Applied Mechanics and Engineering*, 48(1):101–118. (Cited on page 43.)

[Simo et al., 1993] Simo, J., Oliver, J., and Armero, F. (1993). An analysis of strong discontinuities induced by strain-softening in rate-independent inelastic solids. *Computational Mechanics*, 12(5):277–296. (Cited on page 25.)

[Simo and Taylor, 1986] Simo, J. C. and Taylor, R. L. (1986). A return mapping algorithm for plane stress elastoplasticity. *International Journal for Numerical Methods in Engineering*, 22(3):649–670. (Cited on page 43.)

[Song et al., 2008] Song, J.-H., Wang, H., and Belytschko, T. (2008). A comparative study on finite element methods for dynamic fracture. *Computational Mechanics*, 42(2):239–250. (Cited on pages xv and 22.)

[Spencer et al., 1989] Spencer, J. R., Lebofsky, L. A., and Sykes, M. V. (1989). Systematic biases in radiometric diameter determinations. *Icarus*, 78(2):337–354. (Cited on page 103.)

[Springer et al., 2019] Springer, M., Turon, A., and Pettermann, H. (2019). A thermo–mechanical cyclic cohesive zone model for variable amplitude loading and mixed–mode behavior. *International Journal of Solids and Structures*, 159:257–271. (Cited on pages xix and 120.)

[Stern et al., 1976] Stern, M., Becker, E., and Dunham, R. (1976). A contour integral computation of mixed-mode stress intensity factors. *International Journal of Fracture*, 12:359–368. (Cited on page 57.)

[Strobl and Seelig, 2018] Strobl, M. and Seelig, T. (2018). Restrictions in phase field modeling of brittle fracture. *Proc. Appl. Math. Mech. (PAMM)*, 18(1):e201800157. (Cited on page 28.)

[Sun and Jin, 2012a] Sun, C. and Jin, Z.-H. (2012a). Chapter 3 - the elastic stress field around a crack tip. In Sun, C. and Jin, Z.-H., editors, *Fracture Mechanics*, pages 25 – 75. Academic Press, Boston. (Cited on page 9.)

[Sun and Jin, 2012b] Sun, C. and Jin, Z.-H. (2012b). Chapter 9 - cohesive zone model. In Sun, C. and Jin, Z.-H., editors, *Fracture Mechanics*, pages 227–246. Academic Press, Boston. (Cited on page 46.)

[Suo and Combescure, 1989] Suo, X.-Z. and Combescure, A. (1989). $\pi - \theta$ method: a new method for the stability assessment of crack growth. In *International conference on Structural Mechanics in Reactor Technology (SMIRT); Anaheim, CA (USA); 14-18 Aug.* (Cited on page 122.)

[Suo, 1990] Suo, X.-Z. (1990). *Analyse Mathématique et Numérique de la propagation des Fissures par le Modèle De Multi-Couronnes*. PhD thesis, Ecole Nationale des Ponts et chaussées. (Cited on pages 14, 21, 79, 80, 122, and 123.)

[Suo and Combescure, 1992a] Suo, X.-Z. and Combescure, A. (1992a). Double virtual crack extension method for crack growth stability assessment. *International Journal of Fracture*, 57(2):127–150. (Cited on page 86.)

[Suo and Combescure, 1992b] Suo, X.-Z. and Combescure, A. (1992b). On the application of g(θ) method and its comparison with de lorenzi's approach. *Nuclear Engineering and Design*, 135(2):207 – 224. (Cited on pages 20 and 21.)

[Suo and Combescure, 1993] Suo, X.-Z. and Combescure, A. (1993). Energy release rate and J integral for cracks propagating in nonhomogeneous media. *Revue Européenne des Éléments Finis*, 2(1):75–93. (Cited on page 21.)

[Suresh, 1998] Suresh, S. (1998). *Fatigue of Materials*. Cambridge University Press, 2^{nd} edition. (Cited on page 112.)

[Tanné et al., 2018] Tanné, E., Li, T., Bourdin, B., Marigo, J.-J., and Maurini, C. (2018). Crack nucleation in variational phase-field models of brittle fracture. *Journal of the Mechanics and Physics of Solids*, 110:80 – 99. (Cited on pages xxiii and 21.)

[Terzaghi, 1962] Terzaghi, K. (1962). Dam foundation on sheeted granite. *Géotechnique*, 12(3):199–208. (Cited on page xxiv.)

[Tijssens et al., 2000] Tijssens, M. G., Sluys, B. L., and van der Giessen, E. (2000). Numerical simulation of quasi-brittle fracture using damaging cohesive surfaces. *European Journal of Mechanics - A/Solids*, 19(5):761 – 779. (Cited on page 61.)

[Tomar et al., 2004] Tomar, V., Zhai, J., and Zhou, M. (2004). Bounds for element size in a variable stiffness cohesive finite element model. *International Journal for Numerical Methods in Engineering*, 61(11):1894–1920. (Cited on page 26.)

[Tracey, 1971] Tracey, D. M. (1971). Finite elements for determination of crack tip elastic stress intensity factors. *Engineering Fracture Mechanics*, 3(3):255–265. (Cited on page 10.)

[Troutman, 1996] Troutman, J. L. (1996). *Sufficient Conditions for a Minimum*, pages 282–337. Springer New York, New York, NY. (Cited on page 65.)

[Turon et al., 2007] Turon, A., Dávila, C., Camanho, P., and Costa, J. (2007). An engineering solution for mesh size effects in the simulation of delamination using cohesive zone models. *Engineering Fracture Mechanics*, 74(10):1665–1682. (Cited on pages 44, 87, and 94.)

[Turon et al., 2010] Turon, A., Camanho, P., Costa, J., and Renart, J. (2010). Accurate simulation of delamination growth under mixed-mode loading using cohesive elements: Definition of interlaminar strengths and elastic stiffness. *Composite Structures*, 92(8):1857 – 1864. (Cited on page 26.)

[Tvergaard and Hutchinson, 1992] Tvergaard, V. and Hutchinson, J. W. (1992). The relation between crack growth resistance and fracture process parameters in elastic-plastic solids. *Journal of the Mechanics and Physics of Solids*, 40(6):1377–1397. (Cited on pages xvi and 45.)

[Uribe-Suárez et al., 2020] Uribe-Suárez, D., Bouchard, P.-O., Delbo, M., and Pino-Muñoz, D. (2020). Numerical modeling of crack propagation with dynamic insertion of cohesive elements. *Engineering Fracture Mechanics*, 227:106918. (Cited on pages 78, 94, 97, and 118.)

[Uribe-Suárez et al., 2021] Uribe-Suárez, D., Delbo, M., Bouchard, P.-O., and Pino-Muñoz, D. (2021). Diurnal temperature variation as the source of the preferential direction of fractures on asteroids: Theoretical model for the case of bennu. *Icarus*, 360:114347. (Cited on pages 100, 115, and 119.)

[Vastola, G., 2011] Vastola, G. (2011). Asymmetric crack propagation near waterfall cliff and its influence on the waterfall lip shape. *EPL*, 96(4):49002. (Cited on page 2.)

[Veverka et al., 2001] Veverka, J., Thomas, P. C., Robinson, M., Murchie, S., Chapman, C., Bell, M., Harch, A., Merline, W. J., Bell, J. F., Bussey, B., Carcich, B., Cheng, A., Clark, B., Domingue, D., Dunham, D., Farquhar, R., Gaffey, M. J., Hawkins, E., Izenberg, N., Joseph, J., Kirk, R., Li, H., Lucey, P., Malin, M., McFadden, L., Miller, J. K., Owen, W. M., Peterson, C., Prockter, L., Warren, J., Wellnitz, D., Williams, B. G., and Yeomans, D. K. (2001). Imaging of small-scale features on 433 eros from near: Evidence for a complex regolith. *Science*, 292(5516):484–488. (Cited on pages xxvi and 3.)

[Viles et al., 2010] Viles, H., Ehlmann, B., Wilson, C. F., Cebula, T., Page, M., and Bourke, M. (2010). Simulating weathering of basalt on Mars and Earth by thermal cycling. *Geophysical Research Letters*, 37(1):18201. (Cited on pages xxiv and 2.)

[Volokh, 2004] Volokh, K. Y. (2004). Comparison between cohesive zone models. *Communications in Numerical Methods in Engineering*, 20(11):845–856. (Cited on page 50.)

[Wada et al., 2018] Wada, K., Grott, M., Michel, P., Walsh, K. J., Barucci, A. M., Biele, J., Blum, J., Ernst, C. M., Grundmann, J. T., Gundlach, B., Hagermann, A., Hamm, M., Jutzi, M., Kim, M.-J., Kührt, E., Corre, L. L., Libourel, G., Lichtenheldt, R., Maturilli, A., Messenger, S. R., Michikami, T., Miyamoto, H., Mottola, S., Nakamura, A. M., Müller, T., Nittler, L. R., Ogawa, K., Okada, T., Palomba, E., Sakatani, N., Schröder, S., Senshu, H., Takir, D., and Zolensky, M. E. (2018). Asteroid ryugu before the hayabusa2 encounter. *Progress in Earth and Planetary Science*, 5(82). (Cited on pages xxiv and 6.)

[Walker, 1970] Walker, K. (1970). The effect of stress ratio during crack propagation and fatigue for 2024-t3 and 7075-t6 aluminum. pages 1–14, Philadelphia, Pa, USA. American Society for Testing and Materials. (Cited on page 15.)

[Walsh et al., 2019] Walsh, K. J., Jawin, E. R., Ballouz, R. L., Barnouin, O. S., Bierhaus, E. B., Connolly, H. C., Molaro, J. L., McCoy, T. J., Delbo, M., Hartzell, C. M., Pajola, M., Schwartz, S. R., Trang, D., Asphaug, E., Becker, K. J., Beddingfield, C. B., Bennett, C. A.,

Bottke, W. F., Burke, K. N., Clark, B. C., Daly, M. G., DellaGiustina, D. N., Dworkin, J. P., Elder, C. M., Golish, D. R., Hildebrand, A. R., Malhotra, R., Marshall, J., Michel, P., Nolan, M. C., Perry, M. E., Rizk, B., Ryan, A., Sandford, S. A., Scheeres, D. J., Susorney, H. C. M., Thuillet, F., Lauretta, D. S., and Team, O.-R. (2019). Craters, boulders and regolith of (101955) Bennu indicative of an old and dynamic surface. *Nature Geoscience*, 12(4):242–246. (Cited on pages xxiv, 2, 6, and 109.)

[Wang et al., 2019] Wang, M., Wang, F., Zhu, Z., Dong, Y., Mousavi Nezhad, M., and Zhou, L. (2019). Modelling of crack propagation in rocks under shpb impacts using a damage method. *Fatigue & Fracture of Engineering Materials & Structures*, 42(8):1699–1710. (Cited on page 2.)

[Watwood, 1970] Watwood, V. (1970). The finite element method for prediction of crack behavior. *Nuclear Engineering and Design*, 11(2):323–332. (Cited on page 18.)

[Weiss, 2004] Weiss, J. (2004). Subcritical crack propagation as a mechanism of crevasse formation and iceberg calving. *Journal of Glaciology*, 50(168):109–115. (Cited on page 3.)

[Westergaard, 1939] Westergaard, H. M. (1939). Bearing pressures and cracks. *Trans AIME, J. Appl. Mech.*, 6:49–53. (Cited on page 9.)

[Wilson, 1969] Wilson, W. (1969). *Combined mode fracture mechanics*. PhD thesis, University of Pittsburgh. (Cited on page 57.)

[Wu, 1974] Wu, H. (1974). Dual failure criterion for plain concrete. *Journal of the Engineering Mechanics Division*, 100:1167–1181. (Cited on page 16.)

[Wulf et al., 1993] Wulf, J., Schmauder, S., and Fischmeister, H. (1993). Finite element modelling of crack propagation in ductile fracture. *Computational Materials Science*, 1(3):297 – 301. (Cited on page 22.)

[Wulf et al., 1996] Wulf, J., Steinkopff, T., and Fischmeister, H. (1996). Fe-simulation of crack paths in the real microstructure of an Al(6061)/SiC composite. *Acta Materialia*, 44(5):1765 – 1779. (Cited on pages xxiv and 22.)

[Xu and Needleman, 1993] Xu, X. P. and Needleman, A. (1993). Void nucleation by inclusion debonding in a crystal matrix. *Modelling and Simulation in Materials Science and Engineering*, 1(2):111–132. (Cited on pages 47, 50, 52, 90, 153, and 154.)

[Xu and Needleman, 1994] Xu, X.-P. and Needleman, A. (1994). Numerical simulations of fast crack growth in brittle solids. *Journal of the Mechanics and Physics of Solids*, 42(9):1397 – 1434. (Cited on page 61.)

[Yang and Jewitt, 2010] Yang, B. and Jewitt, D. (2010). IDENTIFICATION OF MAGNETITE IN b-TYPE ASTEROIDS. *The Astronomical Journal*, 140(3):692–698. (Cited on page 6.)

[Yano et al., 2006] Yano, H., Kubota, T., Miyamoto, H., Okada, T., Scheeres, D., Takagi, Y., Yoshida, K., Abe, M., Abe, S., Barnouin-Jha, O., Fujiwara, A., Hasegawa, S., Hashimoto, T., Ishiguro, M., Kato, M., Kawaguchi, J., Mukai, T., Saito, J., Sasaki, S., and Yoshikawa, M. (2006). Touchdown of the hayabusa spacecraft at the muses sea on itokawa. *Science*, 312(5778):1350–1353. (Cited on pages xxvi and 3.)

[Ye, 2018] Ye, Q.-Z. (2018). Meteor showers from active asteroids and dormant comets in near-earth space: A review. *Planetary and Space Science*, 164:7 – 12. (Cited on page 4.)

[Zerbst et al., 2015] Zerbst, U., Klinger, C., and Clegg, R. (2015). Fracture mechanics as a tool in failure analysis — prospects and limitations. *Engineering Failure Analysis*, 55:376 – 410. (Cited on page xxiii.)

[Zhou et al., 2018] Zhou, S., Zhuang, X., Zhu, H., and Rabczuk, T. (2018). Phase field modelling of crack propagation, branching and coalescence in rocks. *Theoretical and Applied Fracture Mechanics*, 96:174 – 192. (Cited on page 28.)

[Zhuang et al., 2014] Zhuang, Z., Liu, Z., Cheng, B., and Liao, J. (2014). Chapter 2 - fundamental linear elastic fracture mechanics. In Zhuang, Z., Liu, Z., Cheng, B., and Liao, J., editors, *Extended Finite Element Method*, pages 13–31. Academic Press, Oxford. (Cited on page 13.)

Appendix A

Appendix

A.1 Tangent stiffness matrix for Ortiz and Pandolfi's cohesive law

Let be d_i the opening displacement defined as follow:

$$d_i = d_i^t + d_i^n \tag{A.1}$$

Where d_i is the opening displacement vector, d_i^t and d_i^n are respectively, the tangential and normal vectors forming d_i. From basic math one knows that the dot product between d_i^t and d_i^n is equal to:

$$d_i^t d_i^n = 0 \tag{A.2}$$

It is also known that the vector magnitudes of d_i^t and d_i^n are given by:

$$d^n = \sqrt{d_i^n d_i^n} \tag{A.3}$$

$$d^t = \sqrt{d_i^t d_i^t} \tag{A.4}$$

d_i^t and d_i^n are given by:

$$d_i^n = d_k n_k n_i \tag{A.5}$$

$$d_i^t = d_i - d_k n_k n_i \tag{A.6}$$

$\frac{\partial d_i^t}{\partial d_j}$ is computed:

$$\begin{aligned} \frac{\partial d_i^t}{\partial d_j} &= \frac{\partial}{\partial d_j}\left[d_i - d_k n_k n_i\right] \\ &= \frac{\partial d_i}{\partial d_j} - \frac{\partial}{\partial d_j}\left[d_k n_k n_i\right] \\ &= \delta_{ij} - \delta_{kj} n_k n_i \\ \frac{\partial d_i^t}{\partial d_j} &= \delta_{ij} - n_j n_i \end{aligned} \tag{A.7}$$

$\frac{\partial d_i^n}{\partial d_j}$ is computed:

$$\begin{aligned}\frac{\partial d_i^n}{\partial d_j} &= \frac{\partial}{\partial d_j}\left[d_k n_k n_i\right] \\ &= \delta_{kj} n_k n_i \\ \frac{\partial d_i^n}{\partial d_j} &= n_j n_i\end{aligned} \tag{A.8}$$

To further simplify the formulation of mixed-mode cohesive laws, we follow [Camacho and Ortiz, 1996] and introduce an effective opening displacement (d):

$$d = \sqrt{\beta^2 (d^t)^2 + (d^n)^2} \tag{A.9}$$

Where d^t and d^n are respectively, the sliding (tangential) and normal opening displacements, β is a factor that assigns different weights to them. Replacing equations (A.3) and (A.4) in (A.9) it follows:

$$d = \sqrt{\beta^2 d_i^t d_i^t + d_i^n d_i^n} \tag{A.10}$$

As already said in section 2.3.1, in the case of contact ($d < 0$) a penalization technique is implemented as shown in equation (2.44).

$\frac{\partial d}{\partial d_j}$ is computed:

$$\begin{aligned}\frac{\partial d}{\partial d_j} &= \frac{\partial}{\partial d_j}\left[\sqrt{\beta^2 d_i^t d_i^t + d_i^n d_i^n}\right] \\ &= \frac{1}{2}\left(\beta^2 d_i^t d_i^t + d_i^n d_i^n\right)^{-\frac{1}{2}} \frac{\partial}{\partial d_j}\left[\beta^2 d_i^t d_i^t + d_i^n d_i^n\right] \\ &= \frac{1}{2d}\left[\beta^2 \frac{\partial d_i^t}{\partial d_j} d_i^t + \beta^2 d_i^t \frac{\partial d_i^t}{\partial d_j} + \frac{\partial d_i^n}{\partial d_j} d_i^n + d_i^n \frac{\partial d_i^n}{\partial d_j}\right] \\ &= \frac{1}{2d}\left[2\beta^2 \frac{\partial d_i^t}{\partial d_j} d_i^t + 2\frac{\partial d_i^n}{\partial d_j} d_i^n\right] \\ \frac{\partial d}{\partial d_j} &= \frac{1}{d}\left[\beta^2 \frac{\partial d_i^t}{\partial d_j} d_i^t + \frac{\partial d_i^n}{\partial d_j} d_i^n\right]\end{aligned} \tag{A.11}$$

Replacing equations (A.7) and (A.8) in (A.11) leads to:

$$\begin{aligned}\frac{\partial d}{\partial d_j} &= \frac{1}{d}\left[\beta^2 \left(\delta_{ij} - n_j n_i\right) d_i^t + \left(n_j n_i\right) d_i^n\right] \\ &= \frac{1}{d}\left[\beta^2 \left(d_i^t \delta_{ij} - n_j n_i d_i^t\right) + n_j n_i d_i^n\right] \\ &= \frac{1}{d}\left[\beta^2 \left(d_j^t - d_i^t n_i n_j\right) + d_i^n n_i n_j\right] \\ \frac{\partial d}{\partial d_j} &= \frac{1}{d}\left(\beta^2 d_j^t + d_j^n\right)\end{aligned} \tag{A.12}$$

Using equation (A.12), it is possible to calculate $\frac{\partial^2 d}{\partial d_j \partial d_i}$:

$$\begin{aligned}\frac{\partial^2 d}{\partial d_j \partial d_i} &= \frac{\partial}{\partial d_i}\left[\frac{\partial d}{\partial d_j}\right] \\ &= \frac{\partial}{\partial d_i}\left[\frac{1}{d}\left(\beta^2 d_j^t + d_j^n\right)\right] \\ &= \frac{1}{d}\frac{\partial}{\partial d_i}\left[\beta^2 d_j^t + d_j^n\right] + \frac{\partial}{\partial d_i}\left[d^{-1}\right]\left(\beta^2 d_j^t + d_j^n\right) \\ \frac{\partial^2 d}{\partial d_j \partial d_i} &= \frac{1}{d}\left[\beta^2 \frac{\partial d_j^t}{\partial d_i} + \frac{\partial d_j^n}{\partial d_i}\right] - \frac{1}{d^2}\frac{\partial d}{\partial d_i}\left(\beta^2 d_j^t + d_j^n\right)\end{aligned} \tag{A.13}$$

Replacing equations (A.7), (A.8) and (A.11) in (A.13) it follows:

$$\begin{aligned}\frac{\partial^2 d}{\partial d_j \partial d_i} &= \frac{1}{d}\left[\beta^2\left(\delta_{ji} - n_i n_j\right) + n_i n_j\right] - \frac{1}{d^2}\left[\frac{1}{d}\left(\beta^2 d_i^t + d_i^n\right)\left(\beta^2 d_j^t + d_j^n\right)\right] \\ \frac{\partial^2 d}{\partial d_j \partial d_i} &= \frac{1}{d}\left[\beta^2\left(\delta_{ij} - n_i n_j\right) + n_i n_j\right] - \frac{1}{d^3}\left(\beta^2 d_i^t + d_i^n\right)\left(\beta^2 d_j^t + d_j^n\right)\end{aligned} \tag{A.14}$$

Let t be the effective traction defined as:

$$t = e\sigma_c \frac{d}{\delta_c} e^{-\frac{d}{\delta_c}} \tag{A.15}$$

where t is the effective cohesive traction, d is the effective opening displacement, σ_c is the maximun cohesive normal traction and δ_c is the characteristic opening displacement. The individual traction (t_i) components can be expressed as:

$$t_i = \frac{t}{d}\left(\beta^2 d_i^t + d_i^n\right) \tag{A.16}$$

Using equation (A.15) in (A.16) it follows that:

$$t_i = \frac{e\sigma_c \frac{d}{\delta_c} e^{-\frac{d}{\delta_c}}}{d}\left(\beta^2 d_i^t + d_i^n\right) = \frac{e\sigma_c}{\delta_c} e^{-\frac{d}{\delta_c}}\left(\beta^2 d_i^t + d_i^n\right) \tag{A.17}$$

The tangent modulus matrix (D_{ij}) can be derived as:

$$D_{ij} = \frac{\partial t_i}{\partial d_j} \tag{A.18}$$

Using equation (A.17) in (A.19) it follows that:

$$\begin{aligned}D_{ij} &= \frac{\partial}{\partial d_j}\left[\frac{e\sigma_c}{\delta_c} e^{-\frac{d}{\delta_c}}\left(\beta^2 d_i^t + d_i^n\right)\right] \\ &= \frac{\partial}{\partial d_j}\left[\frac{e\sigma_c}{\delta_c} e^{-\frac{d}{\delta_c}}\right]\left(\beta^2 d_i^t + d_i^n\right) + \frac{e\sigma_c}{\delta_c} e^{-\frac{d}{\delta_c}}\frac{\partial}{\partial d_j}\left[\beta^2 d_i^t + d_i^n\right] \\ D_{ij} &= \left(-\frac{e\sigma_c}{\delta_c^2} e^{-\frac{d}{\delta_c}}\frac{\partial d}{\partial d_j}\right)\left(\beta^2 d_i^t + d_i^n\right) + \frac{e\sigma_c}{\delta_c} e^{-\frac{d}{\delta_c}}\left(\beta^2 \frac{\partial d_i^t}{\partial d_j} + \frac{\partial d_i^n}{\partial d_j}\right)\end{aligned} \tag{A.19}$$

Replacing equations (A.12), (A.7), (A.8) in (A.19):

$$\begin{aligned}D_{ij} = &\left(-\frac{e\sigma_c}{\delta_c^2} e^{-\frac{d}{\delta_c}}\right)\frac{1}{d}\left(\beta^2 d_j^t + d_j^n\right)\left(\beta^2 d_i^t + d_i^n\right) \\ &+ \frac{e\sigma_c}{\delta_c} e^{-\frac{d}{\delta_c}}\left(\beta^2\left(\delta_{ij} - n_i n_j\right) + n_i n_j\right)\end{aligned} \tag{A.20}$$

Where (A.20) is the cohesive stiffness matrix.

A.2 Tangent stiffness matrix for Xu and Needleman's cohesive law

Tangential and normal tractions are defined as follows:

$$\begin{aligned} T^n(d^n,d^t) &= \left(\frac{\phi_n}{\delta_{cn}}\right) e^{-\left(\frac{d^n}{\delta_{cn}}\right)} \left\{ \left(\frac{d^n}{\delta_{cn}}\right) e^{-\left(\frac{d^t}{\delta_{ct}}\right)^2} + \left[\frac{1-q}{r-1}\right] \left[1 - e^{-\left(\frac{d^t}{\delta_{ct}}\right)^2}\right] \left[r - \frac{d^n}{\delta_{cn}}\right] \right\} \\ T^t(d^n,d^t) &= \left(\frac{\phi_n}{\delta_{cn}}\right) \left(\frac{2\delta_{cn}}{\delta_{ct}}\right) \left(\frac{d^t}{\delta_{ct}}\right) \left\{ q + \left[\frac{r-q}{r-1}\right] \frac{d^n}{\delta_{cn}} \right\} e^{-\left(\frac{d^n}{\delta_{cn}}\right)} e^{-\left(\frac{d^t}{\delta_{ct}}\right)^2} \end{aligned} \tag{A.21}$$

The traction vector is given by:

$$T_i = T^n(d^n,d^t)n_i + T^t(d^n,d^t)t_i \tag{A.22}$$

Where n_i and t_i are the normal and tangential vectors to the cohesive surface. For the sake of simplicity from now on in this work: $T^n(d^n,d^t) = T^n$ and $T^t(d^n,d^t) = T^t$. The tangent stiffness matrix is given by:

$$D_{ij} = \frac{\partial T_i}{\partial d_j} = \frac{\partial T^n}{\partial d^n}\frac{\partial d^n}{\partial d_j}n_i + \frac{\partial T^n}{\partial d^t}\frac{\partial d^t}{\partial d_j}n_i + \frac{\partial T^t}{\partial d^n}\frac{\partial d^n}{\partial d_j}t_i + \frac{\partial T^t}{\partial d^t}\frac{\partial d^t}{\partial d_j}t_i \tag{A.23}$$

In order to calculated the tangent stiffness matrix presented in equation (A.23), it should be computed the following derivatives: $\frac{\partial d^n}{\partial d_j}$, $\frac{\partial d^t}{\partial d_j}$, $\frac{\partial T^n}{\partial d^n}$, $\frac{\partial T^n}{\partial d^t}$, $\frac{\partial T^t}{\partial d^n}$ and $\frac{\partial T^t}{\partial d^t}$. Let be d_i the opening displacement defined as follow:

$$d_i = d_i^t + d_i^n \tag{A.24}$$

Where d_i is the opening displacement vector, d_i^t and d_i^n are respectively, the tangential and normal vectors forming d_i. From basic math one knows that the dot product between d_i^t and d_i^n is equal to:

$$d_i^t d_i^n = 0 \tag{A.25}$$

d_i^n is given by:

$$d_i^n = d_k n_k n_i \tag{A.26}$$

It is also known that the vector magnitud of d_i^n is given by:

$$d^n = d_k n_k \tag{A.27}$$

As already said in section 2.3.2, if there is contact between the cohesive interfaces ($d^n < 0$), a penalization term will be added as shown in equation (2.50).

The derivative of equation (A.27) with respect to d_j is computed:

$$\begin{aligned} \frac{\partial d^n}{\partial d_j} &= \frac{\partial}{\partial d_j}\left[d_k n_k\right] \\ &= \delta_{kj} n_k \\ \frac{\partial d^n}{\partial d_j} &= n_j \end{aligned} \tag{A.28}$$

The magnitud of d_i is given by:

$$\begin{aligned} \|d_i\|^2 &= \|d_i^n\|^2 + \|d_i^t\|^2 \\ \|d_i^t\| &= \sqrt{\|d_i\|^2 - \|d_i^n\|^2} \end{aligned} \tag{A.29}$$

d_i^t is given by:

$$d_i^t = d_i - d_k n_k n_i \tag{A.30}$$

The magnitud of d_i^t is given by:

$$d^t = \|d_i^t\| \tag{A.31}$$

In order to find $\|d_i^t\|$, first, it should be computed $\|d_i\|^2$ and $\|d_i^n\|^2$:

$$\begin{aligned} \|d_i\|^2 &= \left[(d_i d_i)^{\frac{1}{2}}\right]^2 = d_i d_i \\ \|d_i^n\|^2 &= \left[(d_k n_k d_m n_m)^{\frac{1}{2}}\right]^2 = d_k n_k d_m n_m \end{aligned} \tag{A.32}$$

Finally by replacing equation (A.29) and (A.32) in (A.31), the magnitud of d^t is obtanied:

$$d^t = \sqrt{d_i d_i - d_k n_k d_m n_m} \tag{A.33}$$

After this, the derivative of equation (A.33) with respect to d_j is computed:

$$\begin{aligned} \frac{\partial d^t}{\partial d_j} &= \frac{\partial}{\partial d_j}\left[\sqrt{d_i d_i - d_k n_k d_m n_m}\right] \\ &= \frac{1}{2d^t}\left[\frac{\partial}{\partial d_j}(d_i d_i) - \frac{\partial}{\partial d_j}(d_k n_k d_m n_m)\right] \\ &= \frac{1}{2d^t}\left[\delta_{ij} d_i + \delta_{ij} d_i - \delta_{kj} n_k d_m n_m - d_k n_k \delta m j n_m\right] \\ &= \frac{1}{2d^t}\left[2d_j - 2d_z n_z n_j -\right] \\ &= \frac{1}{d^t}\left[d_j - d_j^n -\right] \\ &= \frac{d_j - d_j^n}{d^t} \\ \frac{\partial d^t}{\partial d_j} &= t_j \end{aligned} \tag{A.34}$$

where t_j is the tangential vector already introduced in equation (A.22). The derivative of T^n with respect to d^n is also computed:

$$
\begin{aligned}
\frac{\partial T^n}{\partial d^n} &= \frac{\partial}{\partial d^n}\left\{\left(\frac{\phi_n}{\delta_{cn}}\right)e^{-\frac{d^n}{\delta_{cn}}}\left\{\left(\frac{d^n}{\delta_{cn}}\right)e^{-\frac{d^{2t}}{\delta_{ct}^2}}+\left[\frac{1-q}{r-1}\right]\left[1-e^{-\frac{d^{2t}}{\delta_{ct}^2}}\right]\left[r-\frac{d^n}{\delta_{cn}}\right]\right\}\right\} \\
&= \left(\frac{\phi_n}{\delta_{cn}}\right)\left(-\frac{1}{\delta_{cn}}\right)e^{-\frac{d^n}{\delta_{cn}}}\left\{\left(\frac{d^n}{\delta_{cn}}\right)e^{-\frac{d^{2t}}{\delta_{ct}^2}}+\left[\frac{1-q}{r-1}\right]\left[1-e^{-\frac{d^{2t}}{\delta_{ct}^2}}\right]\left[r-\frac{d^n}{\delta_{cn}}\right]\right\} \\
&+ \left(\frac{\phi_n}{\delta_{cn}}\right)e^{-\frac{d^n}{\delta_{cn}}}\left\{\left(\frac{1}{\delta_{cn}}\right)e^{-\frac{d^{2t}}{\delta_{ct}^2}}+\left[\frac{1-q}{r-1}\right]\left[1-e^{-\frac{d^{2t}}{\delta_{ct}^2}}\right]\left(-\frac{1}{\delta_{cn}}\right)\right\} \\
&= \left(\frac{\phi_n}{\delta_{cn}}\right)\left(\frac{1}{\delta_{cn}}\right)e^{-\frac{d^n}{\delta_{cn}}}\left\{\left(-\frac{d^n}{\delta_{cn}}\right)e^{-\frac{d^{2t}}{\delta_{ct}^2}}-\left[\frac{1-q}{r-1}\right]\left[1-e^{-\frac{d^{2t}}{\delta_{ct}^2}}\right]\left[r-\frac{d^n}{\delta_{cn}}\right]\right\} \\
&+ \left(\frac{\phi_n}{\delta_{cn}}\right)\left(\frac{1}{\delta_{cn}}\right)e^{-\frac{d^n}{\delta_{cn}}}\left\{e^{-\frac{d^{2t}}{\delta_{ct}^2}}-\left[\frac{1-q}{r-1}\right]\left[1-e^{-\frac{d^{2t}}{\delta_{ct}^2}}\right]\right\} \\
\frac{\partial T^n}{\partial d^n} &= \left(\frac{\phi_n}{\delta_{cn}^2}\right)e^{-\frac{d^n}{\delta_{cn}}}\left\{\left(1-\frac{d^n}{\delta_{cn}}\right)e^{-\frac{d^{2t}}{\delta_{ct}^2}}-\left[\frac{1-q}{r-1}\right]\left[1-e^{-\frac{d^{2t}}{\delta_{ct}^2}}\right]\left[1+r-\frac{d^n}{\delta_{cn}}\right]\right\}
\end{aligned}
\tag{A.35}
$$

Then the derivative of T^n with respect to d^t is computed:

$$
\begin{aligned}
\frac{\partial T^n}{\partial d^t} &= \frac{\partial}{\partial d^t}\left\{\left(\frac{\phi_n}{\delta_{cn}}\right)e^{-\frac{d^n}{\delta_{cn}}}\left\{\left(\frac{d^n}{\delta_{cn}}\right)e^{-\frac{d^{2t}}{\delta_{ct}^2}}+\left[\frac{1-q}{r-1}\right]\left[1-e^{-\frac{d^{2t}}{\delta_{ct}^2}}\right]\left[r-\frac{d^n}{\delta_{cn}}\right]\right\}\right\} \\
&= \left(\frac{\phi_n}{\delta_{cn}}\right)e^{-\frac{d^n}{\delta_{cn}}}\left\{\left(\frac{d^n}{\delta_{cn}}\right)e^{-\frac{d^{2t}}{\delta_{ct}^2}}\left(-\frac{2d^t}{\delta_{ct}^2}\right)+\left[\frac{1-q}{r-1}\right]\left[\frac{d^n}{\delta_{cn}}-r\right]e^{-\frac{d^{2t}}{\delta_{ct}^2}}\left(-\frac{2d^t}{\delta_{ct}^2}\right)\right\} \\
\frac{\partial T^n}{\partial d^t} &= 2\left(\frac{\phi_n}{\delta_{cn}\delta_{ct}}\right)\left(\frac{d^t}{\delta_{ct}}\right)e^{-\frac{d^n}{\delta_{cn}}}e^{-\frac{d^{2t}}{\delta_{ct}^2}}\left\{-\frac{d^n}{\delta_{cn}}+\left[\frac{1-q}{r-1}\right]\left[r-\frac{d^n}{\delta_{cn}}\right]\right\}
\end{aligned}
\tag{A.36}
$$

Next, the derivative of T^t with respect to d^t is computed:

$$
\begin{aligned}
\frac{\partial T^t}{\partial d^t} &= \frac{\partial}{\partial d^t}\left\{\left(\frac{\phi_n}{\delta_{cn}}\right)\left(\frac{2\delta_{cn}}{\delta_{ct}}\right)\left(\frac{d^t}{\delta_{ct}}\right)\left\{q+\left[\frac{r-q}{r-1}\right]\frac{d^n}{\delta_{cn}}\right\}e^{-\frac{d^n}{\delta_{cn}}}e^{-\frac{d^{2t}}{\delta_{ct}^2}}\right\} \\
&= \left(\frac{\phi_n}{\delta_{cn}}\right)\left(\frac{2\delta_{cn}}{\delta_{ct}}\right)\left(\frac{1}{\delta_{ct}}\right)e^{-\frac{d^n}{\delta_{cn}}}\left\{q+\left[\frac{r-q}{r-1}\right]\frac{d^n}{\delta_{cn}}\right\}e^{-\frac{d^{2t}}{\delta_{ct}^2}} \\
&+ \left(\frac{\phi_n}{\delta_{cn}}\right)\left(\frac{2\delta_{cn}}{\delta_{ct}}\right)\left(\frac{d^t}{\delta_{ct}}\right)e^{-\frac{d^n}{\delta_{cn}}}\left\{q+\left[\frac{r-q}{r-1}\right]\frac{d^n}{\delta_{cn}}\right\}e^{-\frac{d^{2t}}{\delta_{ct}^2}}\left(-\frac{2d^t}{\delta_{ct}^2}\right) \\
\frac{\partial T^t}{\partial d^t} &= \left(\frac{2\phi_n}{\delta_{ct}^2}\right)\left\{q+\left[\frac{r-q}{r-1}\right]\frac{\delta_n}{\delta_{cn}}\right\}e^{-\frac{d^n}{\delta_{cn}}}e^{-\frac{d^{2t}}{\delta_{ct}^2}}\left\{1-\frac{2d^{2t}}{\delta_{ct}^2}\right\}
\end{aligned}
\tag{A.37}
$$

As well as the derivative of T^t with respect to d^n:

$$
\begin{aligned}
\frac{\partial T^t}{\partial d^n} &= \frac{\partial}{\partial d^n}\left\{\left(\frac{\phi_n}{\delta_{cn}}\right)\left(\frac{2\delta_{cn}}{\delta_{ct}}\right)\left(\frac{d^t}{\delta_{ct}}\right)\left\{q+\left[\frac{r-q}{r-1}\right]\frac{d^n}{\delta_{cn}}\right\}e^{-\frac{d^n}{\delta_{cn}}}e^{-\frac{d^{2t}}{\delta_{ct}^2}}\right\} \\
&= \left(\frac{\phi_n}{\delta_{cn}}\right)\left(\frac{2\delta_{cn}}{\delta_{ct}}\right)\left(\frac{d^t}{\delta_{ct}}\right)e^{-\frac{d^{2t}}{\delta_{ct}^2}}\left[\frac{r-q}{r-1}\right]\frac{1}{\delta_{cn}}e^{-\frac{d^n}{\delta_{cn}}} \\
&+ \left(\frac{\phi_n}{\delta_{cn}}\right)\left(\frac{2\delta_{cn}}{\delta_{ct}}\right)\left(\frac{d^t}{\delta_{ct}}\right)e^{-\frac{d^{2t}}{\delta_{ct}^2}}\left\{q+\left[\frac{r-q}{r-1}\right]\frac{d^n}{\delta_{cn}}\right\}e^{-\frac{d^n}{\delta_{cn}}}\left(-\frac{1}{\delta_{cn}}\right) \\
&= \left(\frac{2\phi_n}{\delta_{cn}\delta_{ct}}\right)\left(\frac{d^t}{\delta_{ct}}\right)e^{-\frac{d^n}{\delta_{cn}}}e^{-\frac{d^{2t}}{\delta_{ct}^2}}\left\{\left(\frac{r-q}{r-1}\right)-\left[q+\left(\frac{r-q}{r-1}\right)\frac{d^n}{\delta_{cn}}\right]\right\} \\
\frac{\partial T^t}{\partial d^n} &= \left(\frac{2\phi_n}{\delta_{cn}\delta_{ct}}\right)\left(\frac{d^t}{\delta_{ct}}\right)e^{-\frac{d^n}{\delta_{cn}}}e^{-\frac{d^{2t}}{\delta_{ct}^2}}\left\{\left(\frac{r-q}{r-1}\right)\left(1-\frac{d^n}{\delta_{cn}}\right)-q\right\}
\end{aligned}
\tag{A.38}
$$

Finally, by replacing (A.28), (A.34), (A.35), (A.36), (A.37) and (A.38) in equation (A.23), it is possible to compute the tangent stiffness matrix (D_{ij}) that should be used when using the cohesive law proposed by [Xu and Needleman, 1993].

A.3 Tangent stiffness matrix for Ortiz and Pandolfi's cohesive law when including viscous dissipation

When using this kind of exponential cohesive law, [Sepasdar and Shakiba, 2020] proposed the addition of the following viscosity term:

$$
t = e\sigma_c\frac{d}{\delta_c}e^{-\frac{d}{\delta_c}} + \xi\frac{\sigma_c}{\delta_c}\dot{d} \tag{A.39}
$$

where ξ is a viscosity-like parameter that governs viscous energy dissipation and $\dot{d}$ is the derivative of the effective opening displacement (d) with respect to the time ($\mathbf{t}$): $\dot{d} = \frac{dd}{d\mathbf{t}}$. Starting from the fact that $d = \sqrt{\beta^2(d^t)^2 + (d^n)^2}$, equation (A.9), it will be computed $\frac{dd}{dt}$:

$$
\begin{aligned}
\frac{\partial d}{\partial t} &= \frac{\partial}{\partial t}\left[\sqrt{\beta^2 d_i^t d_i^t + d_i^n d_i^n}\right] \\
&= \frac{1}{2d}2\beta^2 d_i^t\dot{d}_i^t + \frac{1}{2d}2d_i^n\dot{d}_i^n \\
\frac{\partial d}{\partial t} &= \frac{1}{d}\left[\beta^2 d_i^t\dot{d}_i^t + d_i^n\dot{d}_i^n\right] = \dot{d}
\end{aligned}
\tag{A.40}
$$

The definition of the cohesive tangent stiffness matrix (D_{ij}) presented in equation (A.19) taking into account viscosity term is given by:

$$
\begin{aligned}
D_{ij} &= \frac{\partial}{\partial d_j}\left[\frac{1}{d}\left\{e\sigma_c\frac{d}{\delta_c}e^{-\frac{d}{\delta_c}} + \xi\frac{\sigma_c}{\delta_c}\dot{d}\right\}\left(\beta^2 d_i^t + d_i^n\right)\right] \\
D_{ij} &= \frac{\partial}{\partial d_j}\left[\frac{e\sigma_c}{\delta_c}e^{-\frac{d}{\delta_c}} + \xi\frac{\sigma_c}{\delta_c\Delta t}\dot{d}\right]\left(\beta^2 d_i^t + d_i^n\right) \\
&+ \frac{\partial}{\partial d_j}\left[\left(\beta^2 d_i^t + d_i^n\right)\right]\left(\frac{e\sigma_c}{\delta_c}e^{-\frac{d}{\delta_c}} + \xi\frac{\sigma_c}{\delta_c\Delta t}\dot{d}\right)
\end{aligned}
\tag{A.41}
$$

Replacing equation (A.40) into equation (A.41) leads to:

$$
\begin{aligned}
D_{ij} &= \frac{\partial}{\partial d_j}\left[\frac{1}{d}\left\{e\sigma_c\frac{d}{\delta_c}e^{-\frac{d}{\delta_c}}+\xi\frac{\sigma_c}{\delta_c d}\left(\beta^2 d_i^t\dot{d}_i^t+d_i^n\dot{d}_i^n\right)\right\}\left(\beta^2 d_i^t+d_i^n\right)\right]\\
&= \frac{\partial}{\partial d_j}\left[\frac{e\sigma_c}{\delta_c}e^{-\frac{d}{\delta_c}}+\xi\frac{\sigma_c}{\delta_c d^2}\left(\beta^2 d_i^t\dot{d}_i^t+d_i^n\dot{d}_i^n\right)\right]\left(\beta^2 d_i^t+d_i^n\right)\\
&+\frac{\partial}{\partial d_j}\left[\left(\beta^2 d_i^t+d_i^n\right)\right]\left(\frac{e\sigma_c}{\delta_c}e^{-\frac{d}{\delta_c}}+\xi\frac{\sigma_c}{\delta_c d^2}\left(\beta^2 d_i^t\dot{d}_i^t+d_i^n\dot{d}_i^n\right)\right)\\
&= \left(-\frac{e\sigma_c}{\delta_c^2}e^{-\frac{d}{\delta_c}}\frac{\partial d}{\partial d_j}+\frac{\partial}{\partial d_j}\left[\xi\frac{\sigma_c}{\delta_c d^2}\left(\beta^2 d_i^t\dot{d}_i^t+d_i^n\dot{d}_i^n\right)\right]\right)\left(\beta^2 d_i^t+d_i^n\right)\\
&+\left(\beta^2\frac{\partial d_i^t}{\partial d_j}+\frac{\partial d_i^n}{\partial d_j}\right)\left(\frac{e\sigma_c}{\delta_c}e^{-\frac{d}{\delta_c}}+\xi\frac{\sigma_c}{\delta_c d^2}\left(\beta^2 d_i^t\dot{d}_i^t+d_i^n\dot{d}_i^n\right)\right)\\
D_{ij} &= \left(-\frac{e\sigma_c}{\delta_c^2}e^{-\frac{d}{\delta_c}}\frac{\partial d}{\partial d_j}+\frac{\partial}{\partial d_j}\left[\frac{\sigma_c\xi}{\delta_c}d^{-2}\right]\left(\beta^2 d_i^t\dot{d}_i^t+d_i^n\dot{d}_i^n\right)\right.\\
&\left.+\frac{\sigma_c\xi}{\delta_c}d^{-2}\frac{\partial}{\partial d_j}\left[\left(\beta^2 d_i^t\dot{d}_i^t+d_i^n\dot{d}_i^n\right)\right]\right)\left(\beta^2 d_i^t+d_i^n\right)\\
&+\left(\beta^2\frac{\partial d_i^t}{\partial d_j}+\frac{\partial d_i^n}{\partial d_j}\right)\left(\frac{e\sigma_c}{\delta_c}e^{-\frac{d}{\delta_c}}+\xi\frac{\sigma_c}{\delta_c d^2}\left(\beta^2 d_i^t\dot{d}_i^t+d_i^n\dot{d}_i^n\right)\right)
\end{aligned}
\tag{A.42}
$$

Using equations (A.7) and (A.8) and the fact that $\dot{d}_i^n=\frac{dd_i^n}{dt}$, we have that:

$$
\begin{cases}
\frac{\partial \dot{d}_i^n}{\partial d_j}=\frac{n_j n_i}{\Delta t}\\
\frac{\partial \dot{d}_i^t}{\partial d_j}=\frac{\delta_{ij}-n_j n_i}{\Delta t}
\end{cases}
\tag{A.43}
$$

Replacing equations (A.7), (A.8), (A.12) and (A.43) in (A.42) leads to:

$$
\begin{aligned}
D_{ij} &= \left(-\frac{e\sigma_c}{d\delta_c^2}e^{-\frac{d}{\delta_c}}\left(\beta^2 d_j^t+d_j^n\right)-\frac{2\sigma_c\xi}{\delta_c d^3}\left(\beta^2 d_i^t\dot{d}_i^t+d_i^n\dot{d}_i^n\right)\frac{1}{d}\left(\beta^2 d_j^t+d_j^n\right)+\frac{\sigma_c\xi}{\delta_c d^2}\beta^2\dot{d}_i^t\left(\delta_{ij}-n_i n_j\right)\right.\\
&\left.+\frac{\sigma_c\xi}{\delta_c d^2}\beta^2\frac{d_i^t}{\Delta t}\left(\delta_{ij}-n_i n_j\right)+\frac{\sigma_c\xi}{\delta_c d^2}\dot{d}_i^n n_i n_j+\frac{\sigma_c\xi}{\delta_c d^2}\frac{d_i^n}{\Delta t}n_i n_j\right)\left(\beta^2 d_i^t+d_i^n\right)\\
&+\left(\beta^2\left(\delta_{ij}-n_j n_i\right)+n_j n_i\right)\left(\frac{e\sigma_c}{\delta_c}e^{-\frac{d}{\delta_c}}+\xi\frac{\sigma_c}{\delta_c d^2}\left(\beta^2 d_i^t\dot{d}_i^t+d_i^n\dot{d}_i^n\right)\right)
\end{aligned}
\tag{A.44}
$$

In equation (A.44) the terms that should be added in order to take into account viscous dissipation are shown in red.

A.4 Tangent stiffness matrix for Xu and Needleman's cohesive law when including viscous dissipation

When using the exponential cohesive law presented by [Xu and Needleman, 1993], [Gao and Bower, 2004] proposed the addition of some viscosity term in the following way:

$$
\begin{aligned}
T^{*n}(d^n,d^t) &= \left(\frac{\phi_n}{\delta_{cn}}\right)e^{-\frac{d^n}{\delta_{cn}}}\left\{\left(\frac{d^n}{\delta_{cn}}\right)e^{-\frac{d^{2t}}{\delta_{ct}^2}}+\left[\frac{1-q}{r-1}\right]\left[1-e^{-\frac{d^{2t}}{\delta_{ct}^2}}\right]\left[r-\frac{d^n}{\delta_{cn}}\right]\right\}\left\{1+\xi_n\frac{d}{dt}\left(\frac{d^n}{\delta_{cn}}\right)\right\}\\
T^{*t}(d^n,d^t) &= \left(\frac{\phi_n}{\delta_{cn}}\right)\left(\frac{2\delta_{cn}}{\delta_{ct}}\right)\left(\frac{d^t}{\delta_{ct}}\right)\left\{q+\left[\frac{r-q}{r-1}\right]\frac{d^n}{\delta_{cn}}\right\}e^{-\frac{d^n}{\delta_{cn}}}e^{-\frac{d^{2t}}{\delta_{ct}^2}}\left\{1+\xi_t\frac{d}{dt}\left(\frac{d^t}{\delta_{ct}}\right)\right\}
\end{aligned}
\tag{A.45}
$$

Where $T^{*n}(d^n, d^t)$ and $T^{*t}(d^n, d^t)$ are the interfacial tractions when adding some viscosity terms. ξ_n and ξ_t are viscosity-like parameters that govern viscous energy dissipation under normal and tangential loading, respectively. Using the relations presented in equation (A.21), (A.45) can be arranged as follow:

$$\begin{aligned} T^{*n}(d^n, d^t) &= T^n(d^n, d^t)\left\{1 + \xi_n \frac{d}{dt}\left(\frac{d^n}{\delta_{cn}}\right)\right\} \\ T^{*t}(d^n, d^t) &= T^t(d^n, d^t)\left\{1 + \xi_t \frac{d}{dt}\left(\frac{d^t}{\delta_{ct}}\right)\right\} \end{aligned} \tag{A.46}$$

Following equation (A.23), the tangent stiffness matrix when including viscous dissipation terms is given by:

$$D_{ij} = \frac{\partial T_i}{\partial d_j} = \frac{\partial T^{*n}}{\partial d^n}\frac{\partial d^n}{\partial d_j}n_i + \frac{\partial T^{*n}}{\partial d^t}\frac{\partial d^t}{\partial d_j}n_i + \frac{\partial T^{*t}}{\partial d^n}\frac{\partial d^n}{\partial d_j}t_i + \frac{\partial T^{*t}}{\partial d^t}\frac{\partial d^t}{\partial d_j}t_i \tag{A.47}$$

The derivative of T^{*n} with respect to d^n needs to be computed:

$$\begin{aligned} \frac{\partial T^{*n}}{\partial d^n} &= \frac{\partial}{\partial d^n}\left\{T^n\left[1 + \xi_n \frac{d}{dt}\left(\frac{d^n}{\delta_{cn}}\right)\right]\right\} \\ &= \frac{\partial}{\partial d^n}\left\{T^n + T^n\xi_n \frac{d}{dt}\left(\frac{d^n}{\delta_{cn}}\right)\right\} \\ &= \frac{\partial T^n}{\partial d^n} + \frac{\partial T^n}{\partial d^n}\xi_n \frac{d}{dt}\left(\frac{d^n}{\delta_{cn}}\right) + T^n \frac{\partial}{\partial d^n}\left\{\xi_n \frac{d}{dt}\left(\frac{d^n}{\delta_{cn}}\right)\right\} \\ \frac{\partial T^{*n}}{\partial d^n} &= \frac{\partial T^n}{\partial d^n}\left\{1 + \frac{\xi_n}{\delta_{cn}}\frac{d}{dt}\left[d^n\right]\right\} + T^n\xi_n \frac{1}{\Delta t \delta_{cn}} \end{aligned} \tag{A.48}$$

Following a similar procedure, they are computed $\frac{\partial T^{*n}}{\partial d^t}$, $\frac{\partial T^{*t}}{\partial d^n}$ y $\frac{\partial T^{*t}}{\partial d^t}$:

$$\frac{\partial T^{*n}}{\partial d^t} = \frac{\partial T^n}{\partial d^t}\left\{1 + \frac{\xi_n}{\delta_{cn}}\frac{d}{dt}\left[d^n\right]\right\} \tag{A.49}$$

$$\frac{\partial T^{*t}}{\partial d^t} = \frac{\partial T^t}{\partial d^t}\left\{1 + \frac{\xi_t}{\delta_{ct}}\frac{d}{dt}\left[d^t\right]\right\} + T^t\xi_t \frac{1}{\Delta t \delta_{ct}} \tag{A.50}$$

$$\frac{\partial T^{*t}}{\partial d^n} = \frac{\partial T^t}{\partial d^n}\left\{1 + \frac{\xi_t}{\delta_{ct}}\frac{d}{dt}\left[d^t\right]\right\} \tag{A.51}$$

Finally, by replacing equations (A.21), (A.28), (A.34), (A.35), (A.36), (A.37), (A.38), (A.48), (A.49), (A.50) and (A.51) into (A.47), it is possible to compute the tangent stiffness matrix (D_{ij}) including viscous dissipation terms (red ones).

A.5 Validation case for the thermolasticity model: a fully constrained specimen

In order to validate the implemented thermoelasticity model, a specimen which deformations are fully constrained as depicted in Figure A.1 is considered. For this case the material behavior is considered isotropic linear elastic with E and ν being the elastic constants, the Young's modulus and Poisson's ratio, respectively. A temperature change (ΔT) is prescribed on the specimen. Geometry, boundary conditions as well as material properties are given in Figure A.1.

The analytical solution to this problem in terms of stress is given by equation (2.56), showing that the theoretical stress in the specimen is equal to:

$$\sigma_{ij} = -65\ \delta_{ij}\ [\text{MPa}] \tag{A.52}$$

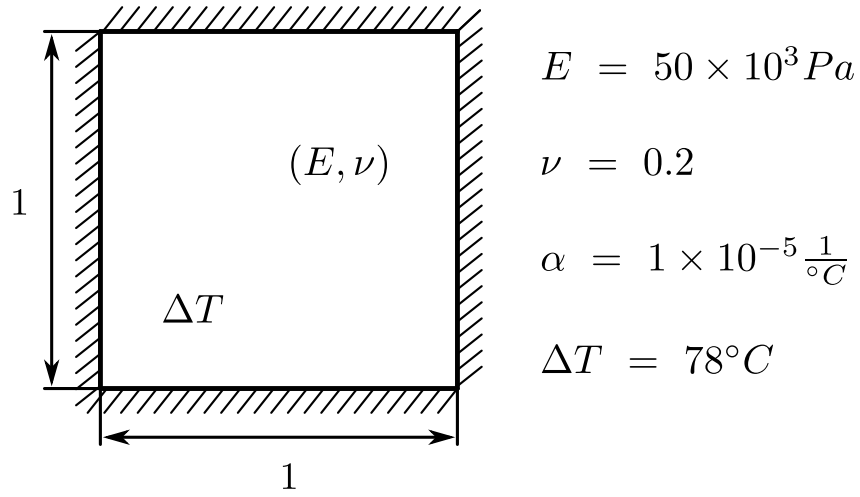

Figure A.1: Geometry and boundary conditions (units in m)

To find the pressure it should be recalled that by definition it is equal to the trace of the stress tensor:

$$P = -\frac{1}{3}\sigma_{ii} = 65 \text{ [MPa]} \tag{A.53}$$

Figure A.2 shows the results obtained using the implemented thermoelasticity model. Obtained results perfectly fit the presented theory. In the results showed in this figure, as well as in the benchmark example, the only non-zero stresses are the ones related to volume changes. The stresses related to shape changes are null. The results in terms of pressure also agree perfectly.

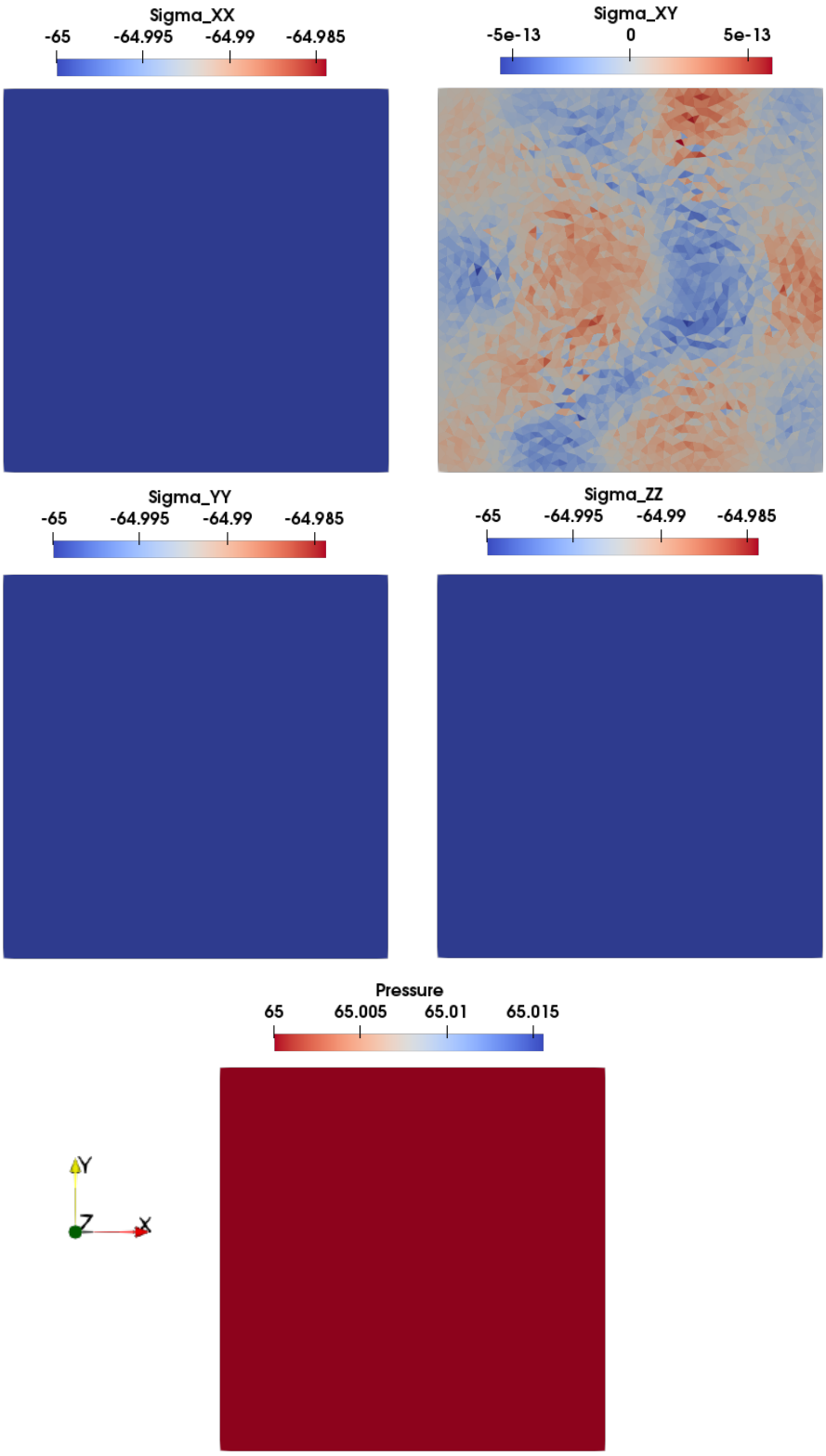

Figure A.2: Numerical solution in terms of stress (σ_{ij}) and pressure (P) of the problem presented in Figure A.1

A.6 Hessian matrix of the problem of computing the fracture surface in 3D

The term $\frac{\partial g(\phi^*)}{\partial \phi^*}$ needs to be computed:

$$\begin{aligned}
\frac{\partial g(\phi^*)}{\partial \phi^*} &= \frac{\partial}{\partial \phi^*}\left[\int_\Omega \frac{2\left(|\nabla\phi^*|-1\right)}{|\nabla\phi^*|}\nabla\hat{\phi}\nabla\phi^* d\Omega + 2\alpha\int_\Omega \vec{d}.\nabla\phi^*\vec{d}.\nabla\hat{\phi}d\Omega\right] \\
&= 2\int_\Omega\left\{\frac{\partial}{\partial\phi^*}\left[|\nabla\phi^*|-1\right]\frac{\nabla\hat{\phi}\nabla\phi^*}{|\nabla\phi^*|} + \left(|\nabla\phi^*|-1\right)\frac{\partial}{\partial\phi^*}\left[\frac{\nabla\hat{\phi}\nabla\phi^*}{|\nabla\phi^*|}\right]\right\}d\Omega \\
&+ 2\alpha\int_\Omega\left\{\frac{\partial}{\partial\phi^*}\left[\vec{d}.\phi^*\right]\vec{d}.\hat{\phi} + \vec{d}.\phi^*\frac{\partial}{\partial\phi^*}\left[\vec{d}.\hat{\phi}\right]\right\}d\Omega \qquad \text{(A.54)} \\
\frac{\partial g(\phi^*)}{\partial \phi^*} &= \int_\Omega \frac{2\nabla\hat{\phi}\nabla\phi^*}{|\nabla\phi^*|}\frac{\nabla\hat{\phi}\nabla\phi^*}{|\nabla\phi^*|}d\Omega + \int_\Omega 2\left(|\nabla\phi^*|-1\right)\frac{\nabla\hat{\phi}\nabla\hat{\phi}}{|\nabla\phi^*|}d\Omega \\
&- \int_\Omega 2\left(|\nabla\phi^*|-1\right)\nabla\hat{\phi}\nabla\phi^*\frac{\nabla\hat{\phi}\nabla\phi^*}{|\nabla\phi^*|^3}d\Omega + 2\alpha\int_\Omega \vec{d}.\nabla\hat{\phi}\ \vec{d}.\nabla\hat{\phi}\ d\Omega
\end{aligned}$$

Equation (A.54) can be also written as:

$$\frac{\partial g(\phi^*)}{\partial \phi^*} = \int_\Omega \left(2\left(|\nabla\phi^*|-1\right)|\nabla\phi^*|^2\mathbf{I} + 2\nabla\phi^*\otimes\nabla\phi^* + 2\alpha|\nabla\phi^*|^3\vec{d}\otimes\vec{d}\right) : \left(\frac{\nabla\hat{\phi}\otimes\nabla\hat{\phi}}{|\nabla\phi^*|^3}\right)d\Omega \qquad \text{(A.55)}$$